INSTABILITY MEASUREMENTS ON TWO CONE-CYLINDER-FLARES AT MACH 6

by

Elizabeth K. Benitez

A Dissertation

Submitted to the Faculty of Purdue University

In Partial Fulfillment of the Requirements for the degree of

Doctor of Philosophy

School of Aeronautics and Astronautics

West Lafayette, Indiana

August 2021

THE PURDUE UNIVERSITY GRADUATE SCHOOL
STATEMENT OF COMMITTEE APPROVAL

Dr. Steven Schneider, Co-Chair

School of Aeronautics and Astronautics

Dr. Joseph Jewell, Co-Chair

School of Aeronautics and Astronautics

Dr. Sally Bane

School of Aeronautics and Astronautics

Dr. Matthew Borg

Air Force Research Laboratory

Approved by:

Dr. Gregory Blaisdell

To Michael, the best husband ever, and our daughter Cassandra.

Also Patches and Tigger, who kept me company while working from home.

ACKNOWLEDGMENTS

This dissertation would not have been possible without the help and support of numerous people. I would like to start by thanking my co-advisors, Prof. Steven Schneider and Prof. Joseph Jewell. Their guidance and advice was essential to putting this work together. Thanks also to Dr. Brandon Chynoweth, who has answered my many questions and provided lodging during the pandemic so I could safely keep testing. I would also like to thank my committee members, Prof. Sally Bane and Dr. Matthew Borg. Dr. Borg also graciously provided time in the AFRL Mach-6 Ludwieg Tube for initial schlieren testing and will be my advisor while I am an NRC postdoc. I am looking forward to working with him.

My labmates made my time at Purdue both educational and fun. Alumni Greg McKiernan, Josh Edelman, Mark Wason, Varun Viswanathan, Phil Portoni, and Scott Gleason and current students Katie Gray, Drew Turbeville, Carson Lay, Chris Yam, Derek Mamrol, Hunter Ahlquist, Lauren Wagner, Mark Noftz, Sam Overpeck, Nate Lavery, and Bethany Price, were all helpful and fun to be around. Welcome also to the new students, Samantha Miller, Zachary McDaniel, Zach Lawless, and Trey Francis, as well as the undergraduate researchers Cassandra Butler and Colin Rhodes.

The perturber electronics were provided by Prof. Sally Bane. I would like to especially thank Lalit Rajendran and Bhavini Singh from her lab for setting up and running the electronics to generate the controlled disturbances. Lalit was always willing to help with any schlieren or other optical questions I had, and I am very grateful for the assistance.

Thanks to Dr. Sebastien Esquieu for designing the cone-cylinder-flare geometry and providing computational results for comparison. In addtion, I would like to thank Daniel Mullen and Dr. Pedro Paredes, who are also doing computational comparisons, along with Dr. Jean-Philippe Brazier, Dr. Joseph Kuehl, Dr. Koen Groot, and Dr. Helen Reed.

This work was supported by the Department of Defense (DoD) through the National Defense Science & Engineering Graduate Fellowship (NDSEG) Program. Materials for this work were purchased through the U.S. Air Force Office of Scientific Research grant FA9550-17-1-0419 (Program Officer: Dr. Sarah Popkin). I would like to thank Jerry Hahn, Robin Snodgrass, and Jim Younts of the department machine shop for their help in designing

and fabricating the models and support structures for this research. Without them, no experiments would have taken place. Additional thanks to John Phillips for assistance with electrical aspects of this research.

I would especially like to thank my family. My amazing husband, Michael, who supported me quitting my job to go and get a doctorate and encouraged me all the way. Thanks for the friendly arguments about whether air or space is better, and for listening to me practice presentations and prep for meetings while working at home. Thanks also to my parents for their love and support, particularly to Mom, who helped with Cassandra during her first several weeks. I additionally want to thank my sister, Sarah, for all her help with editing my writing. Everything always sounds better after she goes through it. Finally, thanks to my Lord Jesus, who was there through all the challenges and achievements that came during the past four years.

TABLE OF CONTENTS

LIST OF TABLES

LIST OF FIGURES

LIST OF SYMBOLS

A	Disturbance amplitude
A_0	Initial disturbance amplitude
C_p	Specific heat (J/(kg*K))
f	Frequency (kHz)
f_{Az}	Peak frequency at azimuthal angle (kHz) Az
K	Gladstone-Dale constant (m^3/kg)
L	Optical path length (m)
M	Mach number
N	Growth factor
n	Index of refraction
p	Pressure (psi)
q	Heat transfer (W/m^2)
Re	Freestream unit Reynolds number (m^{-1})
Re_x	Axial length Reynolds number based on sensor streamwise position and freestream conditions
Re_δ	Boundary-layer Reynolds number based on computed boundary-layer thickness δ and freestream conditions
St	Stanton number
T	Temperature (K)
t	Time (s)
V	Voltage (V)
V_0	Baseline voltage magnitude (V)
x	vertical location measured from laser focal point perpendicular to the flow and optical axis (m)
y	horizontal location measured from laser focal point parallel to the flow and perpendicular to optical axis (m)
z	horizontal location measured from laser focal point perpendicular to the flow but along optical axis (m)

Greek Symbols

α	Angle of attack (degrees)
β	Pitch percent
δ	Boundary-layer edge thickness (computed in DPLR using return from enthalpy overshoot to 100.5% of the freestream total enthalpy) (m)
Δ	Change in a quantity
ϕ	Beam phase (radians)
φ	Flow angle (degrees)
γ	Ratio of specific heats
κ	Thermal conductivity (W/(m*K)
λ	Wavelength (m)
μ	Dynamic viscosity (Pa*s)
Ψ	Wave propagation angle (degrees)
ρ	Density (kg/m^3)
θ	Compression corner angle (degrees)
Θ	Cone half-angle (degrees)
ω	Angular frequency (radians/s)

Subscripts

$'$	(Superscript) fluctuation
∞	Freestream condition
0	Stagnation condition
e	Boundary-layer edge conditions
i	Initial condition
ref	Reference condition
rms	Integrated root mean square value
$wall$	Model surface condition

ABBREVIATIONS

AFOSR	Air Force Office of Scientific Research
ASL	Aerospace Sciences Laboratory
BAM6QT	Boeing/AFOSR Mach-6 Quiet Tunnel
CCD	Charge-Coupled Device
CCF	Cone-cylinder-flare
DNS	Direct Numerical Simulation
DPLR	Data-Parallel Line Relaxation (Navier-Stokes flow solver)
D-FLDI	Double FLDI
FFT	Fast Fourier Transform
FLDI	Focused Laser Differential Interferometer/Interferometry
GUI	Graphical User Interface
HeNe	Helium-Neon Laser
IR	Infrared
LDI	Laser Differential Interferometer/Interferometry
LED	Light Emitting Diode
LST	Linear Stability Theory
NASA	National Aeronautics and Space Administration
PCB	PCB Piezotronics (pressure transducer manufacturer)
PEEK	Poly-Ether Ether Ketone
PIRANHA	Purdue Infrared Registration ANd Heat transfer App
PQFLT	Purdue Quiet Flow Ludwieg Tube (decommissioned Mach-4 quiet tunnel)
PSD	Power Spectral Density
PSE	Parabolized Stability Equations
RMS	Root Mean Square
SB	Schmidt-Boelter Heat Transfer Gauge
SNR	Signal-to-Noise Ratio
STABL	Stability and Transition Analysis for Hypersonic Boundary Layers
TSP	Temperature Sensitive Paint

ABSTRACT

This research focuses on measurements of a convective shear-layer instability seen naturally in quiet hypersonic flow. Experiments were carried out in the Boeing/AFOSR Mach 6 Quiet Tunnel (BAM6QT) at Purdue University. The BAM6QT provides low-disturbance hypersonic flow with freestream noise levels similar to what would be experienced by a flight vehicle. To obtain high-speed, off-the-surface measurements of the instability, a modified focused laser differential interferometer (FLDI) was first designed to work with the contoured Plexiglas windows available in the tunnel.

A cone-cylinder-flare geometry was then selected to study the instabilities related to an axisymmetric separation bubble at Mach 6. The sharp cone had a 5° half-angle, while flare angles of 10° and 3.5° were tested to compare axisymmetric compression with and without separation, respectively. Under quiet flow, laminar separation and reattachment was confirmed by schlieren and surface pressure-fluctuation measurements. Coherent traveling waves were observed. These were attributed to both the second-mode instability, as well as a shear-generated instability from the separation bubble. The symmetry of the bubble was found to be highly sensitive to angle of attack. Additionally, by introducing controlled disturbances on the cone upstream of the separation, larger-amplitude shear-generated waves were measured while the second-mode amplitudes remained unchanged. Therefore, the shear-generated waves were amplified moving through the shear layer, while the second mode remained neutrally stable. These appear to be the first measurements of traveling waves that are generated in the shear layer of a separation bubble in hypersonic flow.

1. INTRODUCTION

The hypersonic regime (generally defined by flow with a Mach number greater than 5) is of growing interest to our nation and the world, with hypersonic vehicles being developed by the US, China, and Russia for scientific and defense purposes. However, despite the large interest, transition in hypersonic flow is not well understood. In particular, separated flow due to shock-boundary layer interactions in a compression corner may create or amplify instabilities in high speed flow, which can lead to transition. This scenario is a common occurrence on control surfaces, and understanding instabilities on such surfaces is important for computing heating and other aerodynamic properties that affect controllability and material survivability.

Conventional high-speed wind tunnels are frequently used in hypersonic research, but are not entirely accurate representations of real flight. Turbulent boundary layers on the tunnel wall radiate noise onto the model being tested, causing early transition and ultimately altering the heating and separation conditions on the model. The Boeing/AFOSR Mach-6 Quiet Tunnel (BAM6QT) at Purdue maintains a laminar boundary layer on the tunnel wall, producing results that better match flight noise levels. This unique facility provides the low-disturbance hypersonic environment used for this research.

Low-speed separation studies have shown that traveling instabilities created by the separation bubble can be the dominant mechanism of transition for those geometries. Hypersonic experiments so far have not verified that traveling instabilities naturally exist in high-speed flow. This study utilizes an axisymmetric cone-cylinder-flare geometry to demonstrate the existence of these traveling waves in Mach-6 quiet flow.

1.1 Hypersonic Laminar-Turbulent Transition

At the surface of a hypersonic vehicle, the air velocity decelerates to zero in the vehicle frame to meet the no-slip boundary condition. This region is known as the boundary layer. Initially, the boundary layer of a vehicle is laminar, with nearly parallel streamlines. Moving downstream, the boundary layer reacts to surface disturbances (such as roughness) and environmental disturbances (such as freestream noise) through receptivity. Instabilities are

generated by these disturbances, which can amplify or diminish depending on several conditions (like the pressure gradient). If the instabilities grow, the amplification will become nonlinear and intermittent turbulent spots appear. These spots eventually merge and the boundary layer becomes fully turbulent. [1]

The boundary layer of a hypersonic vehicle can affect all aspects of that vehicle. Laminar flow means a thin boundary layer that is more prone to separation, but yields less surface heat transfer. Turbulent flow, on the other hand, results in a thicker boundary layer that is capable of remaining attached despite large turning angles, but has higher heat transfer. Transitional flow, where laminar flow begins to break down into turbulence, has its own unique properties that could have a large effect on vehicle design. For example, heat transfer drastically changes depending on transition. Figure 1.1 is a plot of heat transfer data from Martellucci et al. [2] with comparison to a finite-difference code [3]. The plot shows the nondimensional heat transfer (the Stanton number, St) as a function of nondimensional downstream distance (the actual distance x divided by the model length L) for a 7.2° half-angle blunt cone at Mach 8. The solid line represents the purely laminar solution, while the dashed line displays the purely turbulent solution. The dash-dotted line is the computational results for transition, fitted to the experimental data (plotted by squares). Up until $x/L = 0.5$, the experimental results follow the laminar solution, but at $x/L = 0.5$, transition begins and the heat transfer rises dramatically. Around $x/L = 0.8$, the heat transfer peaks nearly 25% above the turbulent solution before it starts to decrease towards the turbulent value. This localized heating spike is just one example of why transition is important in hypersonic vehicle design.

Despite its significance to vehicle design, transition is difficult to predict. Semi-empirical methods are available for some subsonic, transonic, and supersonic flows, but a general hypersonic model has not yet been developed. Therefore, experimental testing is still a requirement to determine transition. Flight tests are expensive and risky, so ground tests are necessary. However, most hypersonic wind tunnels have turbulent boundary layers along the nozzle and test section. These boundary layers radiate noise into the test section, which impinges on the model and changes the flow field being studied. Figure 1.2 shows an example of transition and of noise radiating from a turbulent boundary layer. It is a shadowgraph of 5° half-angle sharp cone at Mach 4 in free flight at the Naval Ordnance Laboratory ballistic

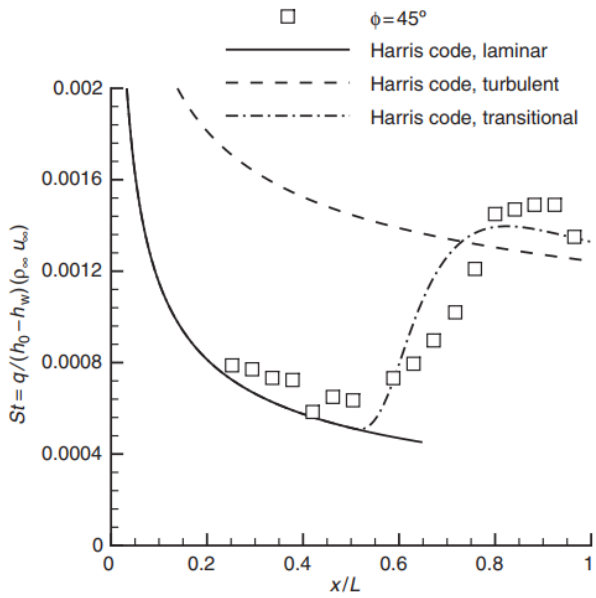

Figure 1.1. Heat transfer through transition [3]

range [4]. On the upper surface, a laminar boundary layer (the thin white line along the model) is seen with two turbulent spots. In front of the turbulent spots a compression wave can be seen. On the lower surface is a turbulent boundary layer (thicker white and gray region along the model). Noise can be seen radiating from that boundary layer into the flow. That noise radiation is the same phenomenon that occurs in conventional hypersonic tunnels.

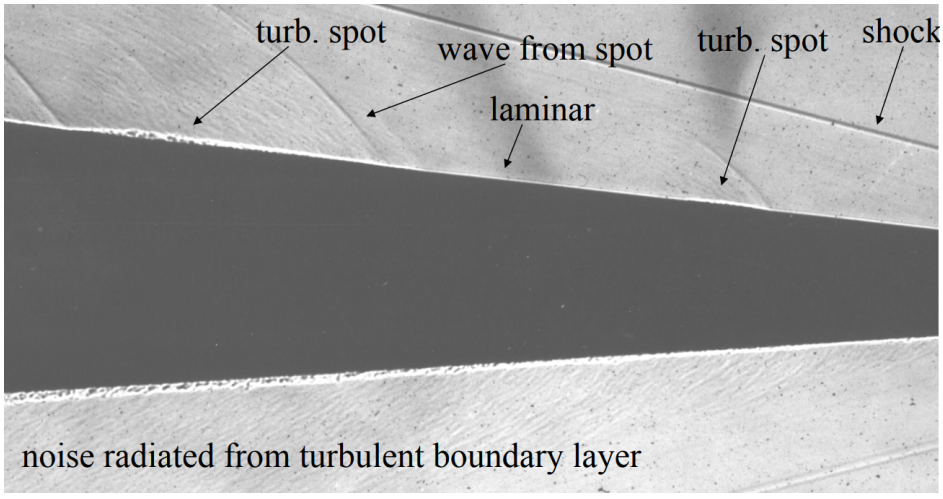

Figure 1.2. Transition and noise radiated off turbulent boundary layer [4]

Radiated noise causes transition to move upstream along a model [5]–[7]. Conventional tunnels therefore yield inaccurate transition estimates; quiet tunnels designed to have laminar boundary layers along the nozzle can reduce this problem. Freestream pitot fluctuations in conventional hypersonic tunnels can vary between 1-4% of the mean. Quiet tunnels have freestream noise levels below 0.1%, which is much closer to (although still higher than) free-air noise during flight. Therefore, quiet tunnels have managed to measure similar transition Reynolds numbers to flight tests in some instances [5]. However, these tunnels are difficult to construct, as they have very small tolerances for roughnesses in the nozzle near the throat. Additionally, they generally only provide quiet flow for a limited range of freestream unit Reynolds numbers and Mach numbers. They also do not emulate chemical processes actually encountered in high-hypersonic flight. No single ground test facility can accurately simulate all aspects of flight, but quiet tunnels can help to study hypersonic instability and transition.

1.2 Hypersonic Separation

1.2.1 Shock-Boundary Layer Interactions (SBLIs)

Shock-boundary layer interactions (SBLIs) are common occurrences on supersonic vehicles. They can happen in external as well as internal flows, and result in complex flow structures that are difficult to compute. When a shock encounters a boundary layer, it is affected by the viscous and rotational properties of that layer, while the boundary layer must traverse a strong adverse pressure gradient upon encountering the shock. [8]

When a supersonic flow encounters a compression corner, an oblique shock is formed above the ramp. This shock results in an adverse pressure gradient that decelerates the flow going through it; this deceleration causes a thickening of the boundary layer. As the boundary layer gets larger, it can act as a further source of compression, forming compression waves in the flow, which join to form the shock in the first place. [8]

While in general information in supersonic flows cannot propagate upstream, the presence of the boundary layer with its reduced velocity and subsonic sublayer allow an upstream interaction length to exist. The length of this upstream influence region (L) can be affected by a variety of properties, such as the upstream Mach number M (increasing M decreases

L/δ), flow deflection angle $\Delta\varphi_1$ (increasing $\Delta\varphi_1$ increases L/δ), or Reynolds number Re_δ. Re_δ has an interesting relationship on the upstream influence region in that it influences two competing physical effects. Increasing the Reynolds number means viscous forces are less influential than inertial forces, implying an increase in upstream influence as the boundary layer can better resist the adverse pressure gradient. However, it also means the boundary layer profile tends to be more full, implying a smaller subsonic sublayer with which to transmit the upstream influence. Therefore, L/δ tends to increase with increasing Re_δ for lower Reynolds numbers, while it decreases with increasing Re_δ at higher ones in laminar flows. [8], [9]

When the shock to be traversed is sufficiently strong, the boundary layer can become separated from the wall. The flow is decelerated through stagnation to reversal. The result is similar whether the SBLI was caused by an incident shock or a compression corner, as long as the pressure rise is the same. Figure 1.3 shows an illustration of the flow above a ramp. Above the separation bubble, a shear layer exists where mixing with the high speed freestream occurs; this mixing causes the flow in the separation streamline to accelerate until it is decelerated by reattachment. The pressure at the wall at the separation point increases rapidly, followed by a decrease in slope or a plateau of the wall pressure inside the separation bubble. The pressure rises at a higher rate again at reattachment. [10]

Separation in supersonic flows is explained by a free-interaction process as the boundary layer interacts with the inviscid freestream. Chapman, Kuehn, and Larson coined the term "free interaction" in their 1958 report, where they confirmed the independence of the flow solution from direct influences such as downstream geometry and source of separation [11].

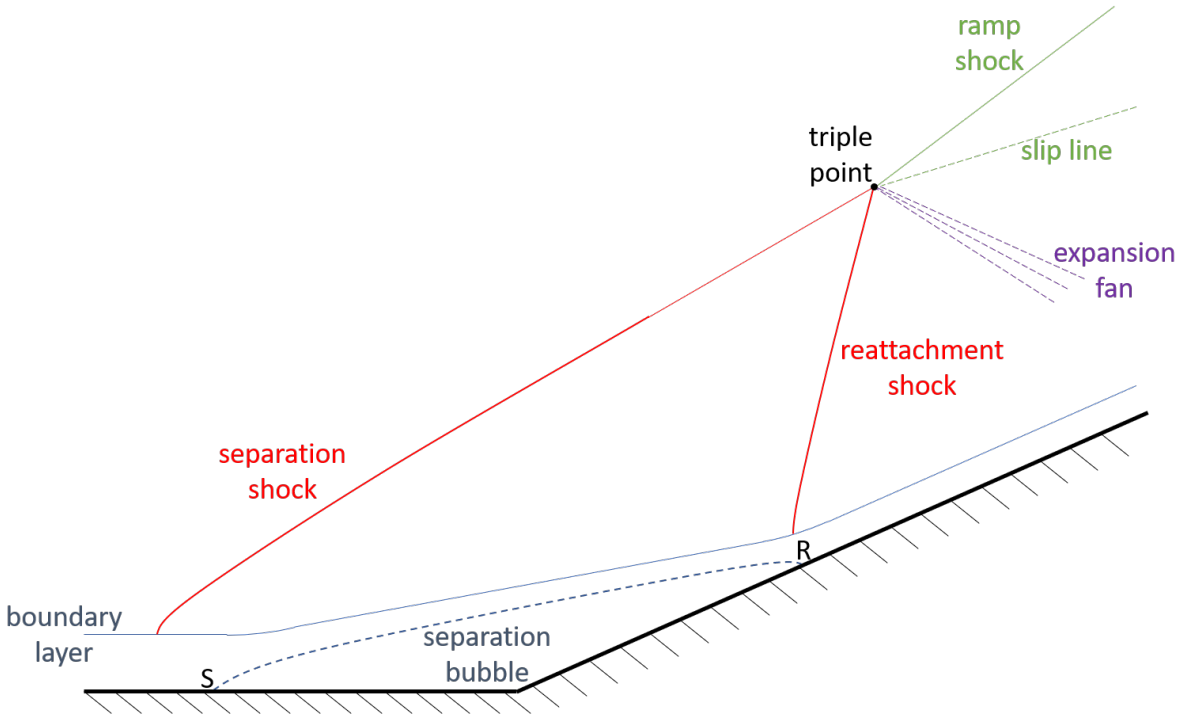

Figure 1.3. Illustration of supersonic separated ramp flow. The separation and reattachment points are denoted by S and R, respectively.

1.2.2 Hypersonic Transitional Separation

1.2.2.1 Separation Bubble Geometry and Mean Flow Trends

Initial supersonic and hypersonic research focused on the factors that affected the size and extent of the separation bubble. A 1956 report by Becker and Korycinski was the first to focus on the effects of transition on SBLI separation. They performed a study on ogive-cylinder-flare models with 10° or 30° flare angles at Mach 6.8 in the Langley 11-inch hypersonic tunnel [12]. Their experiment covered a variety of Reynolds numbers such that transition was located either prior to separation, above the separation bubble, or after reattachment. They observed that the separation point moved upstream with increasing Reynolds numbers, but as transition moved forward the separation point moved downstream again. Once transition was upstream of the separation point, the boundary layer was turbulent at the corner and only minimal separation was seen. Additionally, Becker and Korycinski saw rapid fluctuation

in the separation point location when the transition point was nearby. Their report remained classified until 1961.

Chapman, Kuehn, and Larson conducted an experimental and theoretical study of separated flows at NACA in 1958 [11]. They were the first to look at "free interaction" of the boundary layer with the external flow in supersonic cases as they relate to separation. They also compared at a large number of freestream conditions. While they did not specifically study the hypersonic regime, they did cover Mach numbers from 0.4 to 3.6 and a large range of Reynolds numbers. Their work pointed out the Mach number effect on separated laminar boundary layer stability, with higher Mach numbers increasing the stability of a separated laminar mixing layer.

Larson and Keating performed experiments at NASA in 1960 to document transition Reynolds numbers of separated flows between Mach 2.06 and 4.24 [13]. They used an ogive-stepped cylinder model, and noted that the transition Reynolds number decreased with increasing wall cooling, and increased with increasing Mach number and unit Reynolds number, in supersonic separated flow. In 1962, Schaefer and Ferguson conducted experiments with a cone-cylinder-flare model at Mach 4.98 [14]. Their research found that the heat transfer at reattachment was dependent on whether the boundary layer was laminar or transitional; with laminar reattachment, low heat transfer rates were measured, while with transitional reattachment high values were found with peak heating near the location of reattachment.

In 1966, Needham and Stollery conducted a series of hypersonic experiments on laminar boundary layer separation at Imperial College in London [15]. Looking at flows between Mach 2 and 16 with both compression corners as well as flat plates with incident shocks, they confirmed Chapman et al.'s theory of free interaction. They also found that increasing the Mach number of the flow resulted in decreasing pressure coefficients at the separation point and pressure plateau, but also an increasing pressure coefficient at incipient separation (with incipient separation defined as "the maximum overall pressure rise which can be imposed on the boundary layer without causing separation" [15]). While not focused on transition, Needham and Stollery determined that the location of transition was critical for the conditions of incipient separation and the length of the separated region. They found

that laminar and transitional flow separation data tend to display opposite trends when varying Reynolds number or when looking at the length of separation.

Demetriades in 1990 wrote a review on high-speed shear-layer transition [16]. He included several correlations displaying good qualitative agreement between experimental observations and linear stability theory. However, he also noted that more work is needed to determine the effect of wind-tunnel noise on shear-layer transition. Demetriades also stated that more measurements are needed of laminar instabilities that are present in the shear layer and their effect on transition.

1.2.2.2 Streamwise Vortices

As high-speed separation-bubble experiments were conducted, researchers began to notice Görtler-like vortices present in the boundary layer downstream of reattachment. Ginoux in 1965 conducted an experimental investigation primarily to determine the effect of transition location on separation extent [17]. He used 2 different models, a flat plate with a flap and a hollow cylinder with a flare, and he also looked at attaching a sharp nose cap to the front of the cylinder-flare model. Ginoux saw striations in oil flow on the ramp of the flat plate-ramp model and the flare of the hollow cylinder-flare model that were indicative of strong streamwise vortices. These striations were not present when the sharp cone was included with the cylinder and flare. He concluded that sharp-nosed axisymmetric bodies should be used for transitional reattaching flow studies with compression corners to reduce streamwise vortex amplification related to leading edge irregularities.

Heffner, Chpoun, and Lengrand in 1993 studied hypersonic transition on a sharp hollow cylinder-flare model in Mach 5 flow [18]. Their measurements showed transition occuring in the region of separation, and found the length of separation decreased with increasing Reynolds number, similar to Needham and Stollery in 1966 [15]. They also found that a sharp leading edge on their cylinder contributed to streamwise vortices, like those from Ginoux's study [17].

Dwivedi, Gs, Candler, Nichols, and Jovanovic in 2018 looked at receptivity of an SBLI on a slender double wedge [19]. They performed a computational analysis that looked at

how disturbances amplified downstream, both with and without the separation bubble. Their research found that the streamwise streaks commonly seen in geometries like a flat-plate with a ramp or a hollow cylinder-flare are the result of amplification of low-frequency streamwise perturbations. They also found that the separation bubble is essential for that amplification; when it is removed from the dynamics of the simulation, the amplification decreases by over an order of magnitude.

The next year, Leinemann et al. published an experimental and computational study with a hollow cylinder-flare model [20]. The model had a 15° flare and was tested at Mach 6 in the Hypersonic Ludwieg Tube Braunschweig. They noted the appearance of Görtler vortices in the reattached boundary layer via infrared thermography. The study included both natural and triggered transition using notched tape upstream of the separation. In the triggered transition case, the vortices were much stronger than in the natural transition case. However, Leinemann et al. did not believe that these stationary vortices were the dominant instability under natural transition.

Lugrin et al. performed a detailed computational study of transition on an axisymmetric compression ramp at Mach 5 in 2021 [21]. They found that as the oblique first modes amplified, they began to interact nonlinearly. This nonlinear interaction created streamwise vortices that amplify moving downstream until they break down at reattachment, triggering transition. The streamwise vortices are what have been observed as streaks in similar geometries in previous experimental and computational studies. Their study found that the nonlinear interaction of the first modes was essential for transition to occur with the given conditions.

Further investigation is needed to determine the significance of these streamwise vortices on transition. While this work includes some experimental measurements of the vortices in Section 5.4, Lauren Wagner is currently using controlled roughnesses to study this instability in more detail [22].

1.2.2.3 Separation-Induced Instabilities

Unsteadiness related to supersonic separated flow began being studied in earnest in the early 1980s. Inger in 1981 began investigating the source of three-dimensional spanwise disturbances often seen in reattaching separated flows [23]. He was able to create updated theories on viscous-inviscid interactions with separation as well as on three-dimensional effects in high speed flows with the help of experimental data from the Princeton University Gas Dynamics Laboratory. The next year, Dolling and Murphy published their experimental research on wall pressure fluctuations in two-dimensional turbulent shock-boundary layer interactions [24]. Their measurements found significant pressure fluctuations throughout the flowfield, although they were especially present at the point of separation due to unsteadiness in the shock causing streamwise oscillations of the shock itself.

A review of instabilities associated with laminar boundary-layer separation in low-speed flows was written by Dovgal et al. in 1994 [25]. While not covering high-speed separation, the review did include several studies and noted that traveling instabilities generated in or amplified by the shear layer over the separation bubble were significant for transition.

In 2003, Vandomme, Chanetz, Benay, and Perraud at ONERA reported an experimental and numerical study on transitional shock/boundary-layer interactions at Mach 5 [26]. They used a hollow cylinder-flare model with pressure and heat flux wall measurements, laser doppler velocimetry (LDV), pitot probe measurements, oil flow visualization, and schlieren photography. They compared the experimental results to numerical calculations. To distinguish transition as the result of separation from natural unseparated transition, they also used a cylindrical attachment to the base of the model, replacing the flare; from this configuration, they determined that separation does not seem to induce transition on the model at high Reynolds numbers. This conclusion was drawn due to the similar transition locations as determined by heat flux measurements between the model with and without the flare. This work was followed up by Benay, Chanetz, Mangin, and Vandomme in 2006 looking at more numerical results to compare with additional experimental data taken at ONERA [27].

Balakumar, Zhao, and Atkins performed a numerical study in 2005 on hypersonic boundary layer stability with a compression corner [28]. They simulated the lower surface of the

Hyper-X model as well as the experimental conditions it was subject to at the NASA LaRC 20-Inch Mach 6 Wind Tunnel. Their study found that second-mode disturbances amplified at the rate suggested by linear stability theory in the region prior to separation, then maintained their amplitude over the separated region (without entering the separation bubble), and finally proceeded to amplify after reattachment. In the region of separation, several unstable modes were seen, and the second mode was found to have a lower frequency than in the regions around it. They concluded that transition due to the second mode was unlikely to occur before the second corner (that is, at the downstream end of the separation bubble).

In 2012, Estruch-Samper, Ganapathisubramani, Vanstone, and Hillier performed an experimental study of a blunted cylinder-flare model in Mach 8.9 flow [29]. They used heat transfer measurements and high-speed Schlieren photography to visualize the flow both with and without roughness trips inserted. They used flares of angles between 4° and 14° to measure separation lengths, and selected the 8° for more detailed testing. With that model, they were able to vary roughness inserts until they obtained an intermittent stream of turbulent spots, which resulted in an alternating state of attached and separated flow as the turbulent spots passed by the compression corner. Vanstone, Estruch-Samper, Hillier, and Banapathisubramani continued this work with a focus on pressure results in 2013 [30]. They looked at a particular run to see the time scales necessary for a turbulent spot to pass a given point and for it to collapse the separated region. In 2017, Vanstone, Estruch-Samper, and Ganapathisubramani published a study detailing intermittancy establishment criteria and predictive methodologies that came out of their work with the blunted cylinder-flare model [31]. Two years later, Vanstone and Clemens did similar work in intermittancy on a 2D compression corner in Mach 2 flow [32].

In 2016 through 2020, a series of tests were conducted by McKiernan in the Boeing/AFOSR Mach 6 Quiet Tunnel (BAM6QT) at Purdue [33]–[36]. A variation on the Oberkampf cone-with-slice-and-flap model [37] with a sharp 7° half-angle cone was used as the base shape. Flaps with deflection angles of 10°, 20° and 30° were installed in the slice and the modular compression corner was run at a variety of unit Reynolds numbers. PCB and Kulite surface pressure measurements, temperature sensitive paint (TSP), IR thermography, and oil flow visualization were used to understand the flowfield in both quiet and noisy flow.

Higher reattachment heating was seen in quiet flow than in the equivalent noisy case. The second mode was damped on the slice, but lower frequency absolute (as opposed to convective) instabilities developed in the same region. No frequency peaks were seen downstream of reattachment, where broadband increases of the power spectra of the surface pressure fluctuations occurred as transition happened. However, with the introduction of artificial disturbances to the boundary layer upstream of the separation, a convective instability was observed in the reattached boundary layer.

Leinemann et al.'s study from 2019 included runs from the BAM6QT, in addition to the Hypersonic Ludwieg Tube Braunschweig [20]. Their experimental and numerical studies of a hollow cylinder-flare with a 15° deflection angle focused on Reynolds number and leading edge effects. They found that as the Reynolds number increased, transition moved upstream, and the length of separation decreased. Additionally, they discovered that increasing the leading edge radius lead to an increase in separation length. Second-mode fluctuations were measured in the 170-190 kHz range, while the separated region had pressure fluctuations in the 30-70 kHz range.

In 2020, Butler et al. studied axisymmetric compression and expansion corners in the University of Maryland HyperTERP hypersonic shock tunnel [38]. A 5° half-angle cone with flares of either 0° (for the expansion) or 15° (for the compression) was run with high-speed schlieren and surface pressure fluctuation measurements. They found that energy was being radiated away from the second-mode instability in the shear layer over the separation bubble. At low unit Reynolds number, the second mode was able to retain its periodic structure downstream of reattachment, but as Re increased, transition began to occur at reattachment instead. The reattachment process was found to create lower-frequency fluctuations as well.

1.3 Research Objectives

The purpose of this research is to examine the onset of instabilities in hypersonic flow initiated or amplified by a separation bubble. In particular, traveling waves generated in the shear layer of the bubble are studied. These waves have been seen with low-speed separation,

where they can break down and cause transition to turbulence [25], [39]. This work provides the first experimental evidence of these waves naturally occurring in quiet hypersonic flow.

To study this instability, the waves must first be observed and measured using a variety of techniques to help capture the physics. A focused laser differential interferometer (FLDI) was developed and validated to make non-intrusive, off-the-surface measurements. The FLDI was then used, along with other measurement techniques, to study traveling instabilities that occurred with boundary-layer separation. Specific objectives designed to achieve the goal of this research are summarized below:

1. Build an FLDI system that has a spatial sensitivity (as defined by a 1/e falloff of signal amplitude) of less than 100 mm in the optical axis direction and 0.30 mm perpendicular to the optical axis, as well as a frequency sensitivity (as defined by a 3 dB falloff) of at least 2 MHz. Confirm the performance of the FLDI by bench tests.

2. Demonstrate that the FLDI functions in the BAM6QT by running it with a simple 7° sharp cone. Obtain density-fluctuation measurements off the model surface and compare to computed eigenfunctions.

3. Characterize flow instabilities along an axisymmetric compression corner without boundary-layer separation. Study Reynolds number effects by capturing pressure and heat transfer data along the surface with PCB pressure transducers and IR thermography. Make measurements in both quiet and conventional noise to capture laminar, transitional, and turbulent flow. This provides a baseline to compare to instability measurements made with a separation bubble.

4. Characterize flow instabilities along an axisymmetric compression corner with boundary-layer separation. Study Reynolds number effects by obtaining surface pressure fluctuations and heat transfer. Make measurements in both quiet and conventional noise flow to again capture laminar, transitional, and turbulent flow. Capture off-the-surface density measurements inside and around the bubble with FLDI to determine if instabilities can be seen in the shear layer.

5. Study how the natural instabilities from the separating axisymmetric model react to controlled perturbations generated in the boundary layer upstream of the separation. To do this, run the model in quiet flow with a plasma perturber installed. Use the FLDI to observed the artificial disturbance in the shear layer above the separation bubble.

Ultimately, the design of hypersonic vehicles will need to take into account transition. To do so, a solid understanding of the flow instabilities needs to be established. Hypersonic vehicles will have separation bubbles, so studying shear-layer instabilities is essential to this understanding. This dissertation aims to provide the initial measurements for the future development of a physics-based prediction of transition in the presence of SBLI separation.

2. FACILITIES AND APPARATUS

2.1 Boeing/AFOSR Mach 6 Quiet Tunnel (BAM6QT)

Experiments were conducted in the Boeing/AFOSR Mach 6 Quiet Tunnel (BAM6QT) at Purdue University. The BAM6QT is a Ludweig tube that is capable of running with conventional noise or quiet flow with run times of up to 6 seconds. The test section is located in the downstream end of the diverging section of the nozzle and includes optical access with a variety of windows. Contoured Plexiglas™ windows were the largest option available for most of the experiments and were used for most FLDI measurements, but smaller porthole windows for IR measurements were also available. Large flat sapphire windows were purchased later and used for schlieren imaging. A diagram of the tunnel can be found in Figure 2.1.

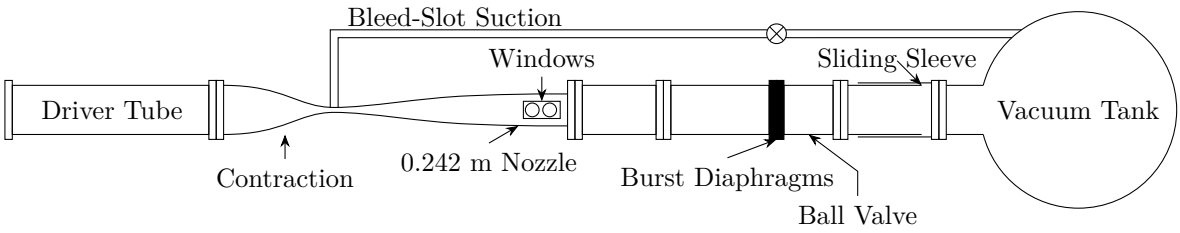

Figure 2.1. BAM6QT diagram [40].

The BAM6QT consists of a 37.3 meter driver tube connected to a converging-diverging nozzle that exhausts into a 113 cubic meter vacuum tank. The air is heated and dried to prevent condensation. Downstream of the test section, the tunnel uses a diaphragm system consisting of two thin aluminum sheets separated by an air gap. Prior to a run, the tunnel is filled to the desired stagnation pressure everywhere upstream of the two diaphragms. While filling, a gap pressure is maintained between the diaphragms of approximately half the upstream pressure. Once full, if a quiet run is desired, a minimum of ten minutes is allowed to pass for the air to settle. The diaphragms are then burst by evacuating the pressure in the gap; this allows the full pressure difference between the tunnel and the vacuum tank to be carried by the upstream diaphragm, causing it to burst, shortly followed by the downstream diaphragm bursting. A shock is sent towards the vacuum tank, while an expansion wave

propagates upstream. After the expansion wave passes through the throat, the air in the driver tube begins accelerating through the nozzle and the tunnel starts.

After about 200 ms, the expansion wave completes a reflection cycle between the upstream and downstream ends of the driver tube, and the stagnation pressure is lowered by approximately 1%. The stagnation temperature is also reduced. The expansion wave can reflect back and forth several times during a run before the tunnel unstarts, reducing the stagnation pressure (and therefore the unit Reynolds number) each time. During the time between reflections, steady Mach 5.8 (for noisy runs) or 6.0 (for quiet runs) flow is achieved. Because of this, it is possible to obtain data from a variety of unit Reynolds numbers in one run.

To obtain quiet flow, a combination of several features are implemented to reduce disturbances and keep the boundary layer on the nozzle laminar. The nozzle of the BAM6QT is polished to a mirror finish to reduce the presence of roughness on the surface. Additionally, the nozzle itself is long so that the radius of curvature in the streamwise direction is large, reducing amplification of the Görtler instability. Air travels through a particle filter before entering the driver tube to remove most particles such that the air is similar to that in a clean room. Finally, bleed slots are located at the throat of the nozzle. These slots use suction to remove the boundary layer from the contraction so it begins again at the throat with a laminar boundary layer, thereby removing any disturbances that might convect from the contraction section. Together, these features allow the tunnel to operate with very low freestream noise levels (less than 0.02%) [41]. However, at high enough unit Reynolds numbers the flow will still be noisy. During most entries, the tunnel was able to operate quietly at up to 155 psia stagnation pressure (about $Re = 12 \times 10^6/\text{m}$); due to a nozzle swap, later entries were limited to a maximum quiet stagnation pressure of 135 psia (about $Re = 10 \times 10^6/\text{m}$).

To use the tunnel for a noisy run, the same steps are followed as for a quiet run except the suction at the bleed slots is disabled. The bleed lips then trip the flow along the nozzle wall, resulting in a noisy run. Since a turbulent boundary layer along the diverging portion of the nozzle is thicker than a laminar one, the effective diameter of that part of the nozzle

is smaller, resulting in Mach 5.8 flow, as opposed to the Mach 6.0 achieved during a quiet run.

A Model 55R45 Dantec single-element hot-film array, located on the nozzle wall upstream of the model, is used to determine when the flow is quiet or noisy. Figure 2.2b shows stagnation pressures and hot-film voltages for typical noisy and quiet runs. The quiet run has much lower hot-film voltage fluctuations, despite being at a higher stagnation pressure than the noisy run; however, the duration of usable data only lasts about 3 seconds for the quiet run, while it continues for more than 6 for the noisy one. A few turbulent bursts can also be seen between 2.5 and 3.3 seconds during the quiet portion of the flow. During data analysis, those bursts need to be excluded to determine true quiet flow performance.

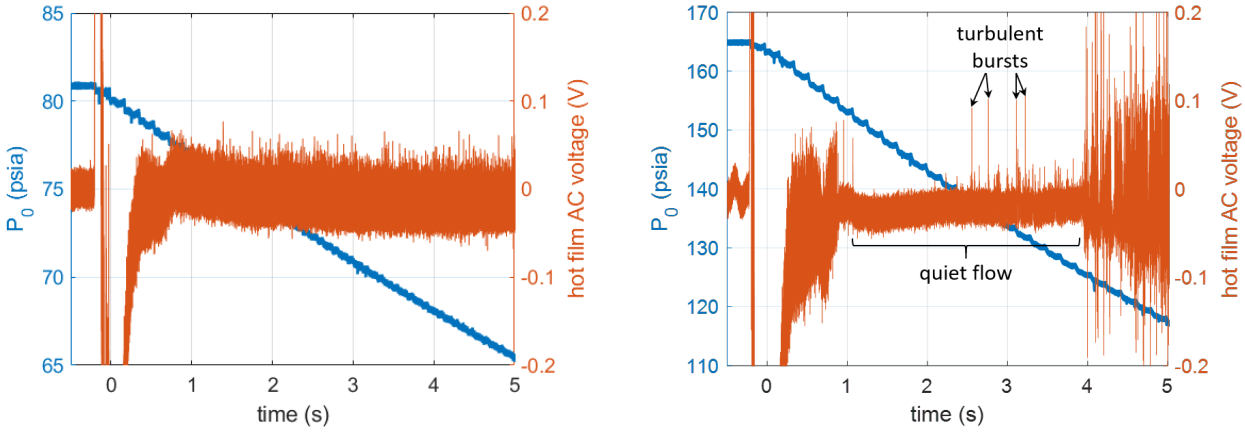

(a) Noisy run (Run 1039)

(b) Quiet run (Run 1040)

Figure 2.2. Stagnation pressures and hot film AC voltages during 2 typical runs

2.1.1 Run Condition Calculation

A Kulite XTEL-190-500A pressure transducer located at the upstream end of the contraction section of the nozzle and mounted flush with the wall is used to determine the stagnation pressure during a run. It is calibrated at the beginning of each tunnel entry by using a 300 psia Paroscientific Inc. Model 740 Digiquartz Portable Standard pressure gauge. The Kulite voltage scales linearly with the stagnation pressure, and the correlation

found from the calibration is used to convert voltages to stagnation pressures during the run. Figure 2.3 shows a typical result for a Kulite calibration performed for this research.

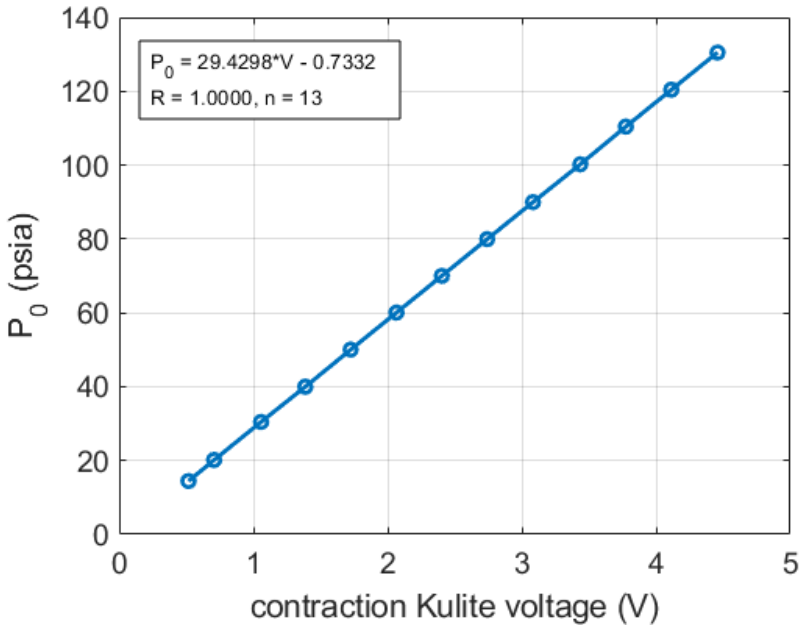

Figure 2.3. Typical contraction Kulite calibration; from Run 0202

Before a run begins, the current stagnation pressure (from the Paroscientific pressure gauge) and stagnation temperature (from a thermocouple located at the upstream edge of the driver tube) in the tunnel are recorded. These values, along with the calibrated contraction Kulite voltages, are used to determine the unit Reynolds number at each point during the run. The isentropic flow relations are used to find the stagnation temperature from the initial stagnation pressure and temperature (equation 2.1) as well as the static pressure (equation 2.2) and temperature (equation 2.3) at the desired time.

$$T_{02} = T_{01}\left(\frac{p_{02}}{p_{01}}\right)^{\frac{\gamma-1}{\gamma}} \tag{2.1}$$

$$p = p_0\left(1+\frac{\gamma-1}{2}M^2\right)^{-\frac{\gamma}{\gamma-1}} \tag{2.2}$$

$$T = T_0\left(1+\frac{\gamma-1}{2}M^2\right)^{-1} \tag{2.3}$$

With the static temperatures and pressures known, the dynamic viscosity of the air can be computed with Sutherland's Law (equation 2.4).

$$\mu = 0.00001716 \frac{\text{kg}}{\text{ms}} \left(\frac{T}{273\text{K}} \right)^{3/2} \left(\frac{384\text{K}}{T + 111\text{K}} \right) \tag{2.4}$$

Finally, the freestream unit Reynolds number can be computed for the flow:

$$Re = \frac{pM}{\mu} \sqrt{\frac{\gamma}{RT}} \tag{2.5}$$

Due to the rapid pressure change at startup and the cantilevered sting configuration for model mounting, models tend to oscillate during a run. This oscillation can cause some repeatability issues for FLDI measurements (see Section 3.2.8). There is also some uncertainty in the stagnation temperature, such as variations in the temperature of the air and the efficiency of the insulation along the driver tube. For a detailed description of the uncertainties in stagnation temperature with the BAM6QT, see Turbeville's dissertation [42].

2.2 Purdue 3-Inch Shock Tube

The Purdue 3-inch shock tube is primarily used for PCB sensor calibration. It is based on the design of the 6-inch shock tube of the Graduate Aerospace Laboratories at Caltech (GALCIT). The shock tube usually generates low amplitude shock waves in a low pressure environment. Both the driver and driven pressures are controlled, with the driver section designed to contain pressures up to 6,895 kPa and the driven section capable of pressures as low as 100 Pa. The shock tube usually uses an electrical burst system in which wires that are attached across the tube are heated to break the Mylar® diaphragms at the desired pressure ratio. Two small Plexiglas™ windows located on opposite sides of the tube were used for optical access for the FLDI. [43], [44]

2.3 Models

Three models were used in this work. A 7° half-angle sharp cone was selected for initial FLDI testing to provide a canonical geometry that is well-understood. Two cone-cylinder-flare geometries were then selected to study the instabilities associated with an axisymmetric separation bubble in hypersonic flow. One model had a 3.5° flare angle and was designed to compress but not separate the boundary layer. The second had a 10° flare angle and was designed to produce an axisymmetric separation bubble based on computations. The cone-cylinder-flare analyses were performed by Dr. Sebastien Esquieu, a researcher from the French Alternative Energies and Atomic Energy Commission (CEA), using DPLR and STABL.

2.3.1 7° Sharp Cone

An aluminum 7° half-angle straight cone model with a sharp stainless steel nosetip was used to do initial testing on the FLDI apparatus. This simple shape was chosen because the flowfield around it is relatively well studied and therefore the density fluctuations measured with the FLDI can be checked against computationally-predicted disturbance frequencies. The model is described in Edelman's Master's thesis [45]. A sketch of this model can be seen in Figure 2.4.

The nosetip had a radius of 76 μm. Roughness inserts were not used during these tests, so a smooth insert was placed near the nosetip. Additionally, no heat transfer measurements were made during the FLDI testing entries, so the position marked for the Schmidt-Boelter heat transfer gauge ("SB Position") instead held another PCB. This position is located 11.09 inches downstream of the nose and 1.34° offset in the azimuthal direction. PCBs 1 through 5 are located 12.33, 13.32, 14.31, 14.81, and 15.30 inches downstream, and -7.54°, -4.73°, -2.24°, -1.09°, and 0° off-axis, respectively. Locations for PCBs 6 through 14 did not contain sensors, and were instead filled with dental plaster.

For complete dimensioned drawings of this model, see Edelman's thesis [45].

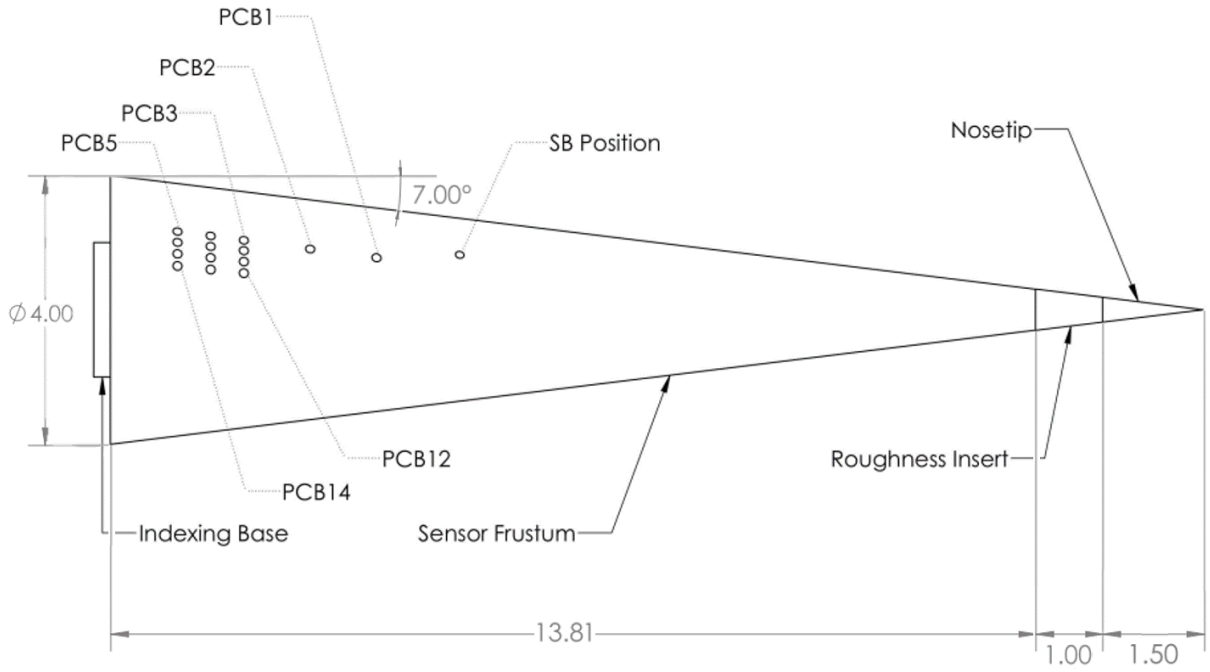

Figure 2.4. 7° half-angle straight cone model [45]. Dimensions in inches.

2.3.2 Cone-Cylinder with 3.5° Flare

The non-separating model consists of an aluminum and PEEK cone-cylinder-flare. The 5° half-angle sharp cone is 0.399-m long, followed by a 0.127-m long cylinder which leads to a 0.239-m-long 3.5° straight conical flare. The model is in three parts; the sharp stainless steel nosetip, the aluminum 5° cone and first part of the cylinder, and the PEEK remainder of the cylinder and 3.5° flare. The nosetip was measured to have a radius of curvature of 0.1 mm.

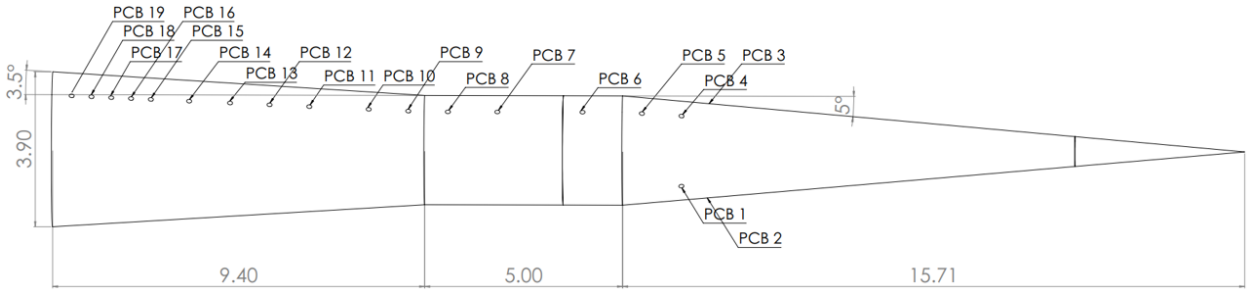

Figure 2.5. Cone-cylinder-flare with 3.5° flare. Dimensions in inches.

Figure 2.5 shows an illustration of this model. There are ports for up to 19 PCB sensors. Table 2.1 lists the axial and azimuthal locations of each of the sensor ports, in meters downstream of the nosetip and degrees around the azimuth, respectively. The main PCB ray is located at 180°.

Table 2.1. 3.5° cone-cylinder-flare model. Sensor port locations.

PCB #	Axial Location	Azimuthal Location	Model Section
1	0.361	90°	cone
2	0.361	0°	cone
3	0.361	270°	cone
4	0.361	180°	cone
5	0.387	180°	cone
6	0.425	180°	cylinder
7	0.479	180°	cylinder
8	0.511	180°	cylinder
9	0.536	180°	flare
10	0.562	180°	flare
11	0.600	180°	flare
12	0.925	180°	flare
13	0.651	180°	flare
14	0.677	180°	flare
15	0.701	180°	flare
16	0.714	180°	flare
17	0.727	180°	flare
18	0.740	180°	flare
19	0.752	180°	flare

For complete dimensioned drawings of the 3.5° cone-cylinder-flare, see Appendix D.1.

2.3.3 Cone-Cylinder with 10° Flare

The separating axisymmetric compression-corner model consists of an aluminum and PEEK cone-cylinder-flare. It is also in 3 components. The sharp (0.1 mm radius) stainless-steel nosetip and aluminum 5° cone-cylinder are the same parts as those used with the 3.5° cone-cylinder-flare. The downstream half of the cylinder and the 10° straight conical flare are the third component, made out of PEEK to obtain IR heat transfer measurements.

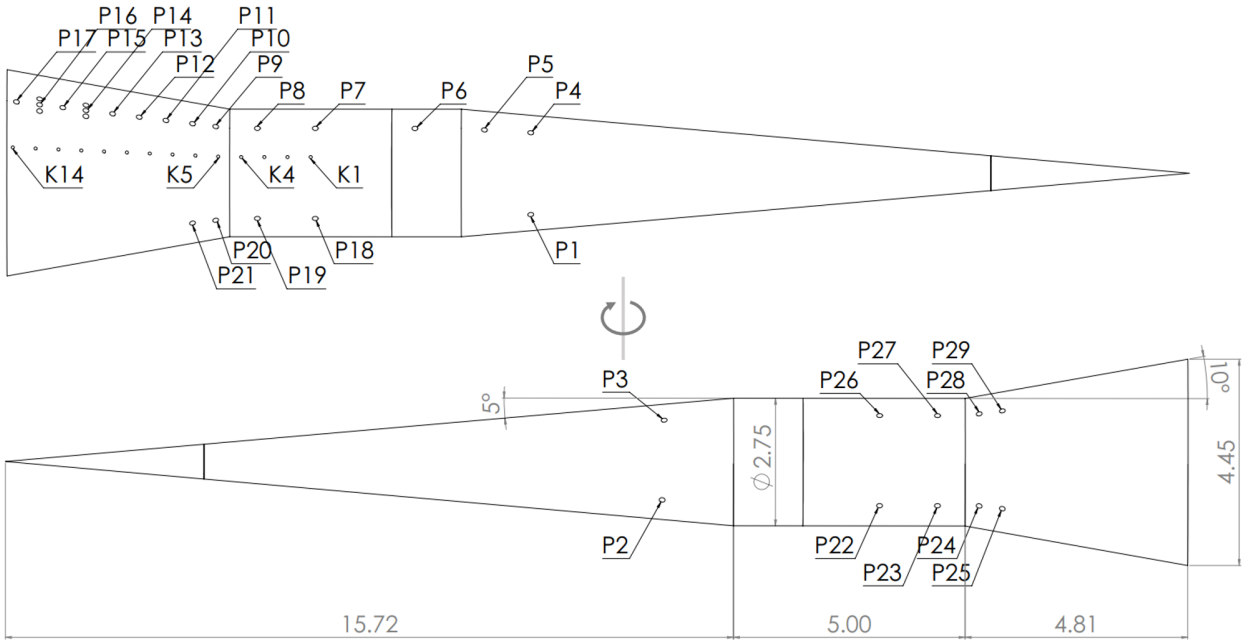

Figure 2.6. Cone-cylinder-flare with 10° flare. Dimensions in inches.

Figure 2.6 shows a drawing of this model. There are ports for up to 33 PCB sensors, with 17 along the central sensor path, four 5° off the main ray (at the same axial positions as PCBs 14 and 16), and the remaining 15 in three groups of five located 90° apart azimuthally around the model. Additionally, there are ports for 14 Kulite sensors located 30° off the main ray (numbered sequentially moving downstream). Tables 2.2 and 2.3 list the axial and azimuthal locations of each of the sensor ports for the 10° model, in meters downstream of the nosetip and degrees along the azimuth, respectively. The main PCB ray is at 180°.

Table 2.2. 10° cone-cylinder-flare model. PCB port locations.

PCB #	Axial Location	Azimuthal Location	Model Section
1	0.361	90°	cone
2	0.361	0°	cone
3	0.361	270°	cone
4	0.361	180°	cone
5	0.387	180°	cone
6	0.425	180°	cylinder
7	0.479	180°	cylinder
8	0.511	180°	cylinder
9	0.536	180°	flare
10	0.548	180°	flare
11	0.561	180°	flare
12	0.577	180°	flare
13	0.590	180°	flare
14	0.606	180°	flare
14R	0.606	175°	flare
14L	0.606	185°	flare
15	0.619	180°	flare
16	0.631	180°	flare
16R	0.631	175°	flare
16L	0.631	185°	flare
17	0.643	180°	flare
18	0.479	90°	cylinder
19	0.511	90°	cylinder
20	0.536	90°	flare
21	0.548	90°	flare
22	0.479	0°	cylinder

Table 2.2. (continued)

23	0.511	0°	cylinder
24	0.536	0°	flare
25	0.548	0°	flare
26	0.479	270°	cylinder
27	0.511	270°	cylinder
28	0.536	270°	flare
29	0.548	270°	flare

Table 2.3. 10° cone-cylinder-flare model. Kulite port locations.

Kulite #	Axial Location	Azimuthal Location	Model Section
1	0.482	150°	cylinder
2	0.494	150°	cylinder
3	0.507	150°	cylinder
4	0.520	150°	cylinder
5	0.532	150°	flare
6	0.545	150°	flare
7	0.558	150°	flare
8	0.570	150°	flare
9	0.583	150°	flare
10	0.595	150°	flare
11	0.608	150°	flare
12	0.620	150°	flare
13	0.633	150°	flare
14	0.645	150°	flare

For complete dimensioned drawings of the 10° cone-cylinder-flare, see Appendix D.2.

2.4 Focused Laser Differential Interferometry (FLDI)

To measure instabilities in the shear layer and boundary layer off the surface of the model, a focused laser differential interferometer (FLDI) was developed for use with the Boeing/AFOSR Mach-6 Quiet Tunnel. Initial work for this dissertation involved designing, testing, and validating the FLDI prior to using it for shear layer measurements (see Chapter 3).

2.4.1 Benefits of FLDI

Focused laser differential interferometry involves a common-path interferometer and offers a number of advantages that make it useful for studying hypersonic shear-layer instabilities. It is highly sensitive and is able to measure density fluctuations due to acoustic waves. From bench testing, the FLDI has a minimum optical path length detection of $\lambda/14,000$, which is approximately 0.0452 nm for the HeNe laser used in this study. This corresponds to a density-fluctuation sensitivity of 3.08×10^{-6} kg/m^3. FLDI is also high speed, with the bandwidth of the system limited only by the photoreceiver chosen (7.3 MHz for the photoreceiver used in the present work). The focusing aspect of the FLDI makes it spatially resolved; the FLDI designed for the BAM6QT has a measured beamwidth of just hundreds of micrometers at the focus and a sensitivity region of 65 mm along the optical axis (see Section 3.1.2.4). FLDI is not limited to making measurements along the surface, and can also probe the flow around the model. Finally, as an optical technique, it is non-intrusive, allowing measurements to be made without altering the flow by the presence of a physical device.

2.4.2 FLDI Theory

The focused laser differential interferometer at its most basic consists of a laser, two polarizers, two birefringent prisms to split the beam, one concave lens, and three convex lenses. Figure 2.7 displays an illustration of this most basic FLDI configuration.

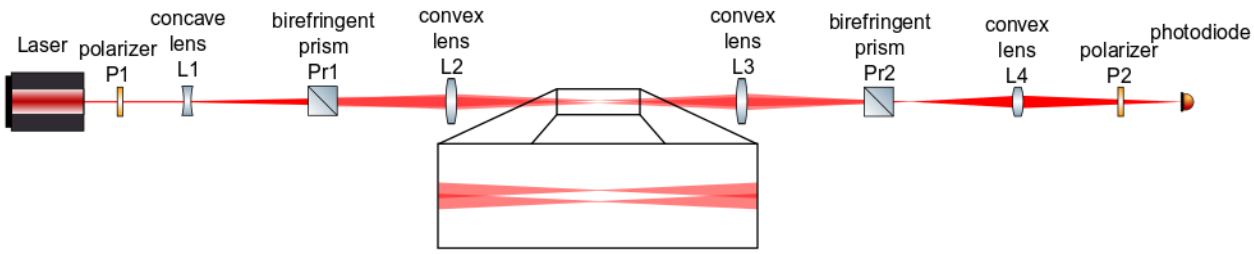

Figure 2.7. Basic FLDI optical setup, beam separation is exaggerated for clarity

The beam is sent through the first polarizer (P1) to polarize the light and then passes through the concave lens (L1) to expand. The order of these two optical components is not fixed; the laser light can go through the beam expanding lens followed by the polarizer if desired. Next, the light passes through the birefringent prism (Pr1) and is split into two closely-spaced, orthogonally-polarized beams. This prism can split at a fixed angle, such as a Wollaston prism (as used by Parziale in [46]–[48]), or can vary the angle, such as a Sanderson prism (as used by Fulghum in [49]). These two beam are both parallelized at a constant beam separation distance and also focused by the first convex lens (L2). The most sensitive part of the device is the region along the beams immediately around the focal point; this is the area where the fluid disturbances to be measured should be located.

After passing through the focal point, the beams go through the second convex lens (L3), which focuses them in the region of the second birefringent prism (Pr2). This prism collocates the beams so that they travel along the same space. However, they cannot yet interfere with each other as they are still orthogonally-polarized. The final convex lens (L4) focuses the beam on the photodiode, but not before it passes through the last polarizer (P2). This polarizer is what allows the beams to interfere and produce the desired signal on the photodiode.

When setting up an FLDI, it is important to observe the interference fringe at the photodetector. To do this, L4 can be moved such that the beam at the photodiode is large. By placing a detector card at the photodiode, interference fringes should be visible. If the beams are separated horizontally, the stripes should be vertical, and if they are separated vertically the stripes should be horizontal. By moving Pr2 along the axis of beam separation, the fringe should traverse along that same axis. To obtain a quantitative measurement with the

FLDI, the fringe must be expanded until infinite fringe diameter is achieved (in other words, the stripes become so wide that only a single shade can be seen in the beam). The fringe can be expanded by changing the distances between L3 and Pr2. This step is important, as it is assumed that the intensity of the beams at the detector is related linearly to the phase shift when processing the data. This assumption is made to prevent aliasing, which occurs when signals collected via sampling are indistinguishable. As can be seen in Figure 2.8, this linear region is most accurate in the range of $-\pi/10$ to $\pi/10$, with a less than 1% difference between $\sin(\theta)$ and θ (where θ is the phase shift between the beams) [49]; however, the signal can be used as far off as $-\pi/6$ to $\pi/6$ with less than 5% error. Salyer, when developing the LDI at Purdue, used the definition of $\lambda/10$ as the restriction for the linear region, which corresponds to a phase shift of $\pi/5$ [50].

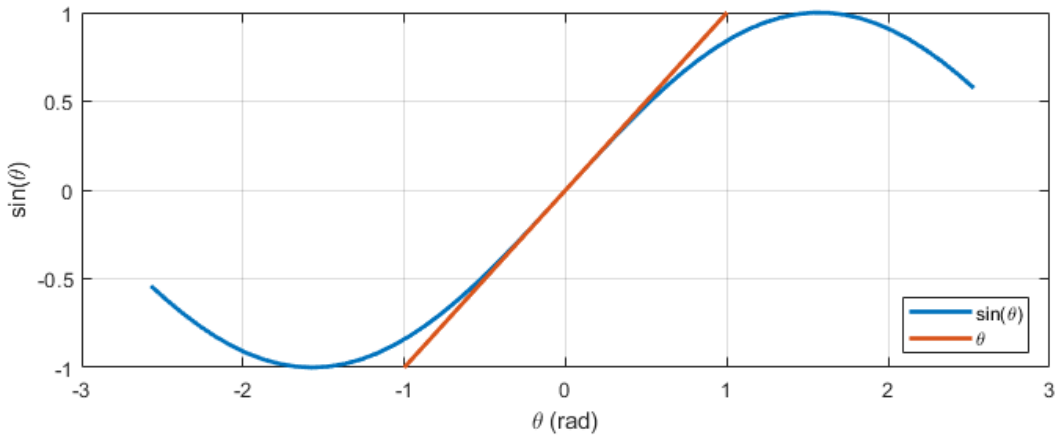

Figure 2.8. Sinusoidal function highlighting linear region about $\theta = 0$

FLDI is a common-path interferometer, which means both beams pass through the test chamber rather than one being redirected as a reference. Common-path interferometry, as opposed to double-path interferometry, benefits from a reduction in vibration sensitivity and measures the finite difference in phase between the two beams $\Delta\phi/\Delta x$, rather than the phase directly as the double-path interferometer does. Shrinking the distance between the two beams (Δx) causes the measurement to more accurately approximate the derivative of the phase, but it also lowers the signal amplitude. [49]

FLDI is unique in that, in addition to passing through the test area together, both beams actually share the same physical position for a majority of their path. This overlap allows signals generated in the shared regions to be rejected, as there would be minimal difference in phase between the two beams [49]. Additionally, the FLDI focuses the beams to small (generally 20-100 μm) points, with much wider beamwidths further from the focus. This variation in beam diameter also helps spatially filter the signal, giving a more "point-like" measurement near the focus [49]. Analysis of a simulated FLDI showed that the spatial averaging was the dominant mechanism in signal rejection away from the focus [51].

The FLDI measures density fluctuations in the flow by using constructive and destructive interference to determine the phase shift of the beams, from which the density change necessary to produce that shift may be computed. Since the optical beams are electromagnetic radiation, their electric fields $\vec{E_1}$ and $\vec{E_2}$ can be defined by Equations 2.6 and 2.7, where $\vec{E_{0\mathrm{i}}}$ is the field amplitude, k is the wavenumber, ω is the angular frequency, and $\phi_{0\mathrm{i}}$ is the phase at the reference plane [52].

$$\vec{E_1} = \vec{E_{01}} \cos\left(ks_1 - \omega t + \phi_{01}\right) \tag{2.6}$$

$$\vec{E_2} = \vec{E_{02}} \cos\left(ks_2 - \omega t + \phi_{02}\right) \tag{2.7}$$

The wavenumber, k, is related to the laser wavelength, λ_0 by $k = \frac{2\pi}{\lambda_0}$

The irradiance I_d of these beams at the photodetector is due to their superposition, $\vec{E_d} = \vec{E_1} + \vec{E_2}$ [52]:

$$I_d = \epsilon_0 c \langle \vec{E_d} \cdot \vec{E_d} \rangle = \langle (\vec{E_1} + \vec{E_2}) \cdot (\vec{E_1} + \vec{E_2}) \rangle \tag{2.8}$$

$$= \epsilon_0 c \langle \vec{E_1} \cdot \vec{E_1} + \vec{E_2} \cdot \vec{E_2} + 2\vec{E_1} \cdot \vec{E_2} \rangle \tag{2.9}$$

$$= I_1 + I_2 + I_{12} \tag{2.10}$$

Here, ϵ_0 is vacuum permittivity and c is the speed of light.

Since the FLDI is set up such that the energy in the two beams is equal, the irradiance of each beam should be equal as well ($I_1 = I_2 = I_0$). This assumption leaves us with the irradiance at the photodetector being described by Equation 2.11:

$$I_d = 2I_0 + I_{12} \tag{2.11}$$

with the irradiance due to interference, I_{12} defined by:

$$I_{12} = 2\epsilon_0 c\langle \vec{E_1} \cdot \vec{E_2} \rangle \tag{2.12}$$

$$= 2\epsilon_0 c\langle \vec{E_{01}} \cdot \vec{E_{02}} [\cos(ks_1 - \omega t + \phi_{01}) \cos(ks_2 - \omega t + \phi_{02})] \rangle \tag{2.13}$$

$$= \epsilon_0 c(\vec{E_{01}} \cdot \vec{E_{02}}) \{ \langle \cos[k(s_1 + s_2) + \phi_{01} + \phi_{02} - 2\omega t] \rangle + \langle \cos[k(s_2 - s_1) + \phi_{02} - \phi_{01}] \rangle \} \tag{2.14}$$

$$= \epsilon_0 c(\vec{E_{01}} \cdot \vec{E_{02}}) \{ \langle \cos[k(s_1 + s_2) + \phi_{01} + \phi_{02} - 2\omega t] \rangle + \langle \cos(k\Delta s + \Delta\phi_0) \rangle \} \tag{2.15}$$

The first cosine term has a time average of 0 (since $k(s_1 + s_2) + \phi_{01} + \phi_{02} = 2\omega t$), making $\langle \cos[k(s_1 + s_2) + \phi_{01} + \phi_{02} - 2\omega t] \rangle = 0$. Additionally, as the beams are collocated at the reference plane, the fields and the phases at the reference plane should also be equal. This means $\vec{E_{01}} = \vec{E_{02}} = \vec{E_0}$, so $\vec{E_{01}} \cdot \vec{E_{02}} = E_0^2$. For the same reason, $\Delta\phi_0 = 0$. Plugging these in, the irradiance due to interference is now:

$$I_{12} = \epsilon_0 c E_0^2 \langle \cos(k\Delta s) \rangle \tag{2.16}$$

The phase shift at the photodetector, $\Delta\phi$ is equal to the value in the cosine term of Equation 2.16. This means that $\Delta\phi$ is only affected by the change in optical path length between the two beams:

$$\Delta\phi = k\Delta s \approx \frac{2\pi}{\lambda_0} L\Delta n \tag{2.17}$$

where Δs is the change in optical path length, L is the integration length, and Δn is the change in index of refraction.

The photodetector obtains a voltage (V) based on the irradiance of the beam hitting it, its receptivity $\mathcal{R}$, and load resistance R_L [47]:

$$V = I\mathcal{R}R_L \tag{2.18}$$

Combining equations 2.11, 2.16, 2.17, and 2.18, a relationship between the photodetector voltage and signal phase change is obtained:

$$\Delta\phi = \sin^{-1}\left(\frac{V}{V_0} - 1\right) \tag{2.19}$$

where V is the voltage measured from the single photodiode and V_0 is the baseline voltage magnitude (when the photodiode is active but no signal is present). Note that the change from inverse cosine to inverse sine is due to the phase shift introduced when the interferometer is aligned in the linear portion of the fringe, which is centered at $\pi/2$.

Equation 2.19 assumes the baseline voltage is perfectly in the center of the fringe, and also assumes that the interference is perfect (in which case a single photodiode would register 0 voltage at total deconstructive interference and $2V_0$ at total constructive interference). This is almost never the case, so a modified version of Equation 2.19 is used instead (originally proposed by Lawson et al. [53]):

$$V = V_{\text{i1}}\cos(\Delta\phi - \Delta\phi_0) + V_{\text{i2}} \tag{2.20}$$

$V_{\text{i1}} = (V_{max} - V_{min})/2$ and $V_{\text{i2}} = (V_{max} + V_{min})/2$ are determined by cycling through a full interference curve (obtained by shifting the second Wollaston prism in the y-direction). The actual baseline voltage (V_0) is set somewhere close to the ideal baseline, V_c (which is equal to V_{i2}), and is used to determine $\Delta\phi_0$, the baseline phase shift. Equations 2.19 and 2.20 are equivalent when $V_0 = V_{\text{i1}} = V_{\text{i2}} = V_c$ (a perfect interference curve exists), which implies $\Delta\phi_0 = \pi/2$ (the baseline voltage is perfectly centered on that curve). This more generalized form represented by Equation 2.20 is useful due to the difficulty in achieving a perfect interference fringe pattern, as well as compensating for any small changes in baseline voltage during the run (as long as the baseline stays within the linear region of the fringe).

If a balanced photoreceiver is used in place of a single photodiode, as in this research, the signal voltage V is instead defined by Equation 2.21:

$$V = \frac{V_{pr}}{2} + V_c \tag{2.21}$$

where V_{pr} is the voltage from the photoreceiver. For this case, since the photoreceiver has no voltage with no signal, the ideal baseline voltage V_c is found by blocking either one of the two photodiodes. Note that V_c is not necessarily equal to V_{i2} for the balanced photoreceiver, so the two quantities must be determined separately; for this work, V_c was found by blocking each photodiode independently and measuring the voltage amplitude of the peaks while V_{i1} and V_{i2} were found by traversing a full interference curve, converting the voltages to a single photodiode equivalent using Equation 2.21, and then computing the phase shift as described above.

Gladstone and Dale determined the relationship between the density of a fluid and its refractive index in 1863 [54]. This relationship is shown in Equation 2.22:

$$n - 1 = K\rho \tag{2.22}$$

with n being the refractive index, K being the Gladstone-Dale constant (here defined as $2.257 \times 10^{-4} \mathrm{m}^3/\mathrm{kg}$), and ρ being the density of the fluid.

From equations 2.17 and 2.22, a relationship between density and phase change can be determined:

$$\Delta\rho = \frac{\lambda_0}{2\pi K L}\Delta\phi \tag{2.23}$$

Note that this assumes a constant density across integration length L. This equation combined with equation 2.19 can be used to relate the voltages from the photodetector to the density changes of the fluid:

$$\Delta\rho = \frac{\lambda_0}{2\pi K L}\cos^{-1}\left(\frac{V - V_{i2}}{V_{i1}}\right) + \Delta\phi_0 \tag{2.24}$$

2.4.3 Coordinate System

To simplify the descriptions in this dissertation, a coordinate system is defined in Figure 2.9. Both the laser beam and the flow are mostly in the horizontal plane with the beam traversing along the z-axis (positive moving from the laser to the photoreceiver) and the freestream along y-axis (in the negative direction). Therefore, moving in the positive y-direction is moving upstream. The z-axis is the optical axis of the system. The x-axis is along the vertical, with positive x pointing upward.

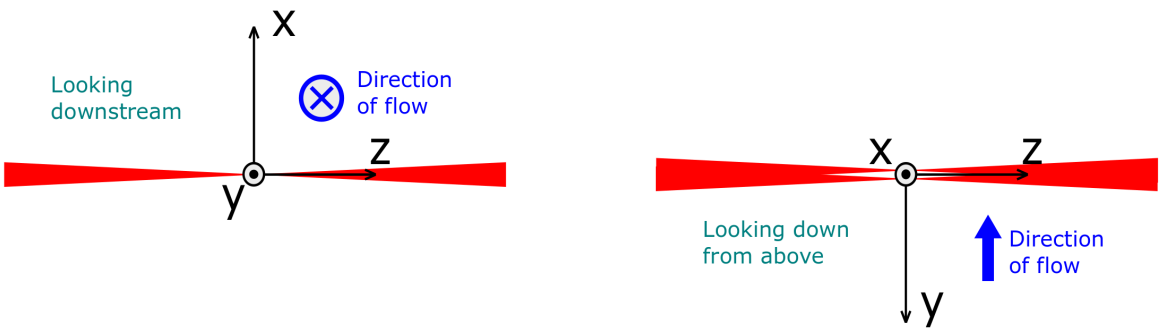

(a) Coordinate system looking downstream; FLDI beams are collocated in this view

(b) Coordinate system looking down from above

Figure 2.9. Coordinate system from two different orientations

2.4.4 Optical Configurations

Four different FLDI optical configurations are defined to be used for the different tests, displayed in Figure 2.10 as simplified illustrations. Individual optical component illustrations were used from Franzen's ComponentLibrary [55]. More comprehensive drawings including all components and instructions on how to align and use the FLDI with the contoured tunnel windows can be found in Appendices A and B. All configurations utilize a Research Electro-Optics (REO), Inc., 1.5 mW linearly polarized, frequency-stabilized 633 nm laser system (part number 32734). Two different balanced photoreceivers were used for the various tests: a ThorLabs PDB210A Large-Area Balanced Photodetector with a 1 MHz 3 dB bandwidth

was used for the sensitivity bench tests and an Ultrafast Sensors & Applications SDX318 Balanced Photodetector with an 8-15 MHz 3 dB bandwidth (depending on the amplification) was used for everything else. The optimal distances between optical components were determined with ZEMAX, a ray-tracing optical analysis software. The criteria used for finding these values were minimizing beamwidth at the focal point, centering the focal point inside the shock tube/BAM6QT, and parallelizing the two beams inside the shock tube/BAM6QT.

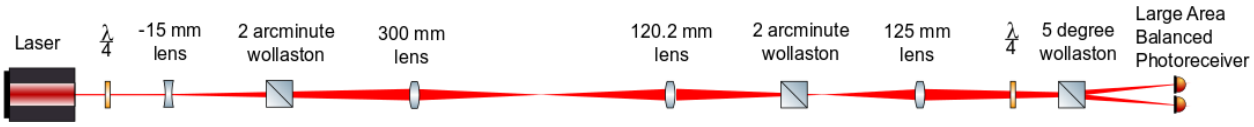

(a) FLDI optical configuration for bench testing (configuration A)

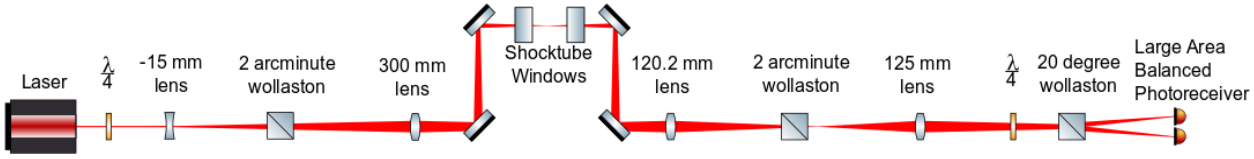

(b) FLDI configuration used with shock tube (configuration B)

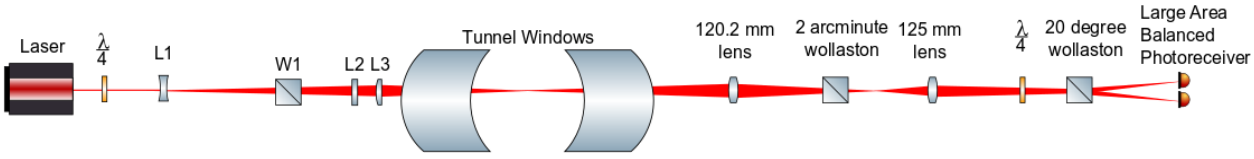

(c) FLDI configuration for window testing (configuration C)

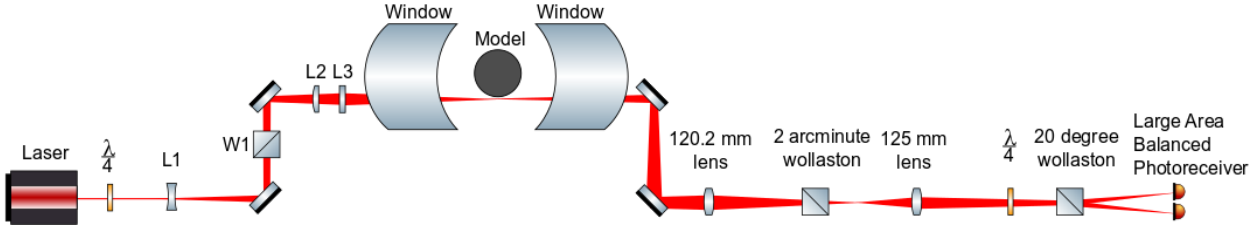

(d) FLDI configuration used with BAM6QT (configuration D)

Figure 2.10. Various FLDI optical configurations used

Figure 2.10a displays configuration A, the simplest iteration of the FLDI that was primarily used for bench testing of the system. This configuration is based on the FLDI used by Parziale in his dissertation [47]. The linearly polarized HeNe laser beam first encounters a quarter-wave plate, adjusting the polarization from linear to circular. This circularly-polarized beam then is expanded through a -15 mm singlet lens. Next comes the first Wollaston prism, which splits the single beam into two orthogonally-polarized beams sepa-

rated by 2 arcminutes. The prism is oriented such the the two beams are located in the y-z plane and are parallel to the z-axis. These beams get parallelized and focused by the 300 mm singlet lens. The focal point, which is the area of highest signal sensitivity, is located 480 mm from the center of this lens; at this point, the beam spacing was measured at 168 μm and the RMS beam radius at 26 μm. Next, the 120.2 mm singlet lens refocuses the beam towards the second 2 arcminute Wollaston prism, which recombines the two beams in space. However, the beams are still orthogonally polarized at this point, so they will not interfere until they pass through the second quarter-wave plate. A 125 mm singlet lens focuses the beams through that quarter-wave plate as well as through a 20° Wollaston prism, which spatially separates the two beams for the two photodiodes on the balanced photoreceiver.

Configuration B (shown in Figure 2.10b) adds some complexity to configuration A. This configuration was used with the shock tube. To elevate the laser light to the height of the tube, a pair of mirrors is used to reflect the two beams up and through the Plexiglas™ windows on either side of the shock tube. The distances between the -15 mm lens, the first 2 arcminute Wollason prism, and the 300 mm lens are adjusted such that the focal point of the beams is in the center of the windows. After passing back out of the shock tube, two more mirrors are used to reflect the light back to the 120.2 mm lens, after which the system is the same as configuration A.

Configuration C (Figure 2.10c) is the FLDI version used to perform bench tests assessing how the BAM6QT windows affect the system. The primary change between this version and configuration B is the decoupling of the focusing axes. In configuration C, the 300 mm lens is replaced by two cylindrical lenses; one (L2, focal length 250 mm) is oriented to parallelize the beams and focus them in the y-direction, while the other (L3, focal length 300 mm) is perpendicular to the first and focuses the beams in the x-direction. The decoupling of the focusing axes allows the beams to compensate for the curvature of the tunnel windows, creating a focal point halfway through the test section that is approximately circular in shape. In addition to this alteration, the -15 mm lens is changed to a -25 mm one (denoted by L1). This change in focal length was necessary to center the focal points of the beams in the tunnel.

Finally, configuration D (Figure 2.10d) is the FLDI actually used with the BAM6QT to acquire the data reported in Chapters 3, 5, and 6. It utilizes the same optical components as configuration C, but differs in the physical location of those components. Due to the height of the tunnel test section relative to the optical table, the first Wollaston (W1) and two cylindrical lenses (L2 and L3) are elevated in order to maintain the correct relative distances between them. The mirrors used in configuration B are once again introduced to reflect the beams upward, and W1, L2, and L3 along with the mirrors themselves, are mounted on 24-inch high rods. See Appendix A for a complete list of all components used in, as well as a scale drawing of, the BAM6QT setup of the FLDI (setup D). Comprehensive instructions for working with this FLDI can be found in Appendix B.

Flat, optical-grade sapphire windows were purchased towards the end of data collection, and were used for entries made after they were pressure-certified (Entry 12 and later). The two cylindrical lenses from configuration D were replaced with a single spherical lens with a focal length of 250 mm when using the FLDI with those windows, as the new windows did not require curvature compensation.

Key features shared by these FLDI configurations include the use of quarter-wave plates for polarization and a balanced photoreceiver for detection. The quarter-wave plates turn the linearly-polarized laser light to circularly-polarized light. When adjusted properly, this polarization allows for independent beam rotation at the Wollaston prisms by rotating those prisms only, without requiring any further optical adjustments. This simplifies the process of aligning the beams with the model surface. The balanced photoreceiver also provides the benefit of increasing the signal-to-noise ratio by summing the signal and subtracting noise present in both beams. Additionally, it makes calibrating the system easier as the linear portion of the infinite fringe location can be found by simply translating the second Wollaston until the signal is zero, indicating that the energy received by each balanced photodiode is equal. During the tunnel filling process, the signal diverges from zero; however, after startup it usually returns to the linear range, providing quantitative measurements. Runs in which the FLDI signals do not return to the linear range are excluded from analysis.

2.4.5 Photoreceiver

An Ultrafast Sensors SDX318 balanced photoreceiver was used to capture the FLDI measurements for all but the sensitivity tests. Balanced photoreceivers have dual photodiodes, one as a reference and one as a signal. The output this instrument produces is a voltage defined by the difference in energy received at each of the photodiodes. This photoreceiver was customized to have 3 mm photodiode diameters, and is specified to have an 8 MHz 3 dB bandwidth. It is designed for IR through UV radiation (350 - 1000 nm) with a peak responsivity of 0.6 A/W at 850 nm.

To test the frequency response of the photoreceiver, a circuit with an LED was created by John Phillips of the Purdue School of Aeronautics and Astronautics Electronics Shop (see Figure 2.11a) to be driven by an HP33120A Function Generator and powered by an Agilent E3620A DC Power Supply. The photoreceiver voltage output, signal generator ouput, and transducer voltage output from the circuit were all measured by a Tektronix MDO3014 100 MHz oscilloscope. The LED was directed at one of the two photodiodes, with the other covered by electrical tape to prevent the signal from leaking into it (see Figure 2.11b).

To investigate the high frequency limit of this photoreceiver, a methodology taken from Fulghum's dissertation [49] was applied. This method uses square waves as an LED input to the photoreceiver at a variety of frequencies; in this case, 1 kHz to 1 MHz square waves were used. A termination resistance of 1 MΩ in the scopes was used for all voltages. Some testing was done to compare frequency response at different termination resistances, but no noticeable effect was observed.

The Fourier transformation of a square wave is an impulse train with delta functions at the signal frequency as well as its odd harmonics. Figure 2.12 demonstrates this with a 5 Hz example sampled at 10 MHz. The photoreceiver, however, has a limited frequency response, which causes the output signal to have rounded leading edges. This rounding-off of the signal decreases the amplitude of the higher harmonics, since the leading edge is no longer sharp and therefore does not require the infinite impulse train to be defined. By comparing the harmonic amplitudes of the normalized input and output signals, the high frequency limit of the photoreceiver can be determined.

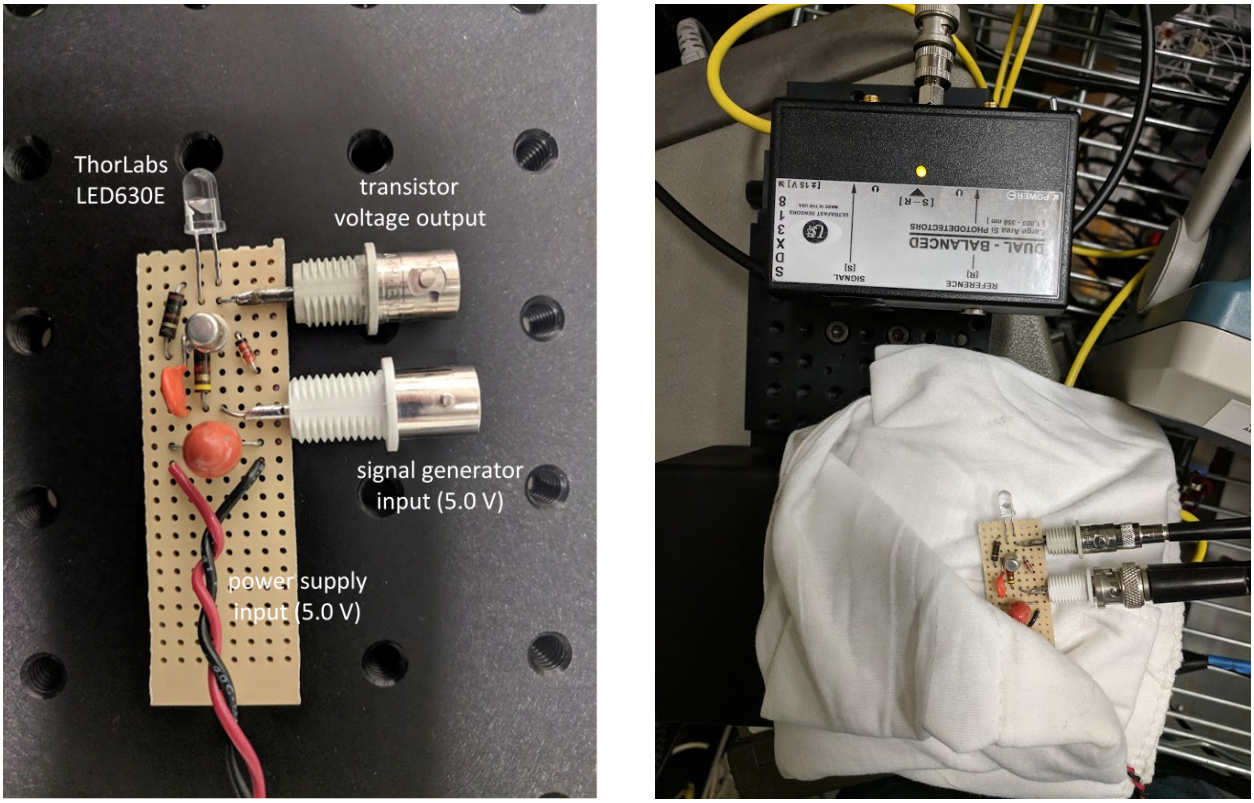

(a) Circuit used to drive LED blinking

(b) Setup of LED test with photoreceiver and circuit

Figure 2.11. Photographs of LED testing of photoreceiver

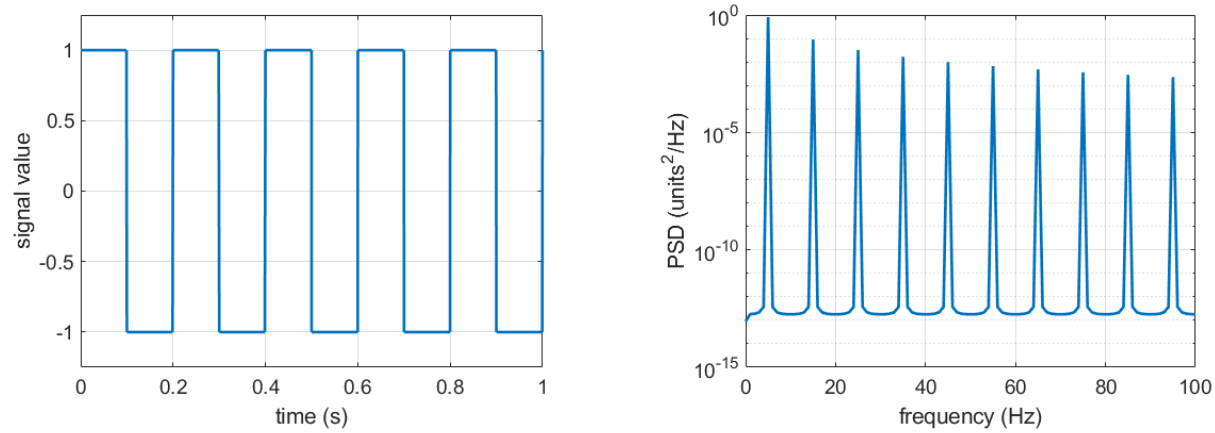

(a) 5 Hz square wave signal with 10 MHz sampling frequency

(b) Power spectral density of 5 Hz square wave signal

Figure 2.12. Square wave and associated power spectral density, highlighting spikes at odd-numbered harmonics

To test the photoreceiver with this method, the voltages at the LED transducer and the output of the photoreceiver were recorded for a generated square wave input. The frequencies selected were all less than the stated bandwidth of 8 MHz and were confirmed with an oscilloscope to have clean square wave signals, so the amplitude at the fundamental frequency of the output should be equal to that at the input. The Fourier transforms of these voltages were computed and used to determine the power spectral densities (PSDs) of the signals. The PSDs were then normalized to account for the different voltage scales. Figure 2.13 shows the normalized input and output power spectra for a 1 kHz example; the initial drop-off in photoreceiver signal can be seen beginning around 3 MHz. The input voltage plotted is the LED transistor voltage, which more accurately depicts the input received by the photoreceiver than the function generator output voltage which drives the LED. This characterization assumes the LED is instantaneously on at full power for all frequencies, so the function generator was limited to 1 MHz, at which the transistor voltages appear to support this assumption. The values at the frequency peaks were extracted and the ratio of their amplitudes was found by dividing the output value by the input value. The ratios were then plotted as a function of frequency.

As Fulghum noted, these ratios describe the transfer function of the system [49]. If the photoreceiver is modeled as a first order low-pass filter, the data measured can be fitted to Equation 2.25:

$$|H(f)|^2 = \left| \frac{1}{\sqrt{1 + (f/f_c)^2}} \right|^2 \tag{2.25}$$

where f is the frequency in Hz, f_c is the crossing frequency (where the value drops below -3 dB) in Hz, and $|H(f)|^2$ is the power transfer function of the photoreceiver.

Figures 2.14a and 2.14b show the resulting frequency responses when the LED is used as an input to the reference (R) and the signal (S) sides, respectively. The power transfer function is found by fitting the low-pass filter equation to the data across all the input frequencies tested. The computed crossing frequency then can be used to define the 3 dB

bandwidth of the photoreceiver, which was determined to be about 7.3 MHz. This bandwidth is slightly less than the specified value of 8 MHz, but is more than sufficient for this research.

2.5 Schlieren

Once large, flat, optical-grade windows were available for use with the BAM6QT, a schlieren system was created to better visualize the flowfield being studied. Two different configurations were used across two entries to image the separation bubble for the 10° cone-cylinder-flare model, illustrated in Figure 2.15. Both configurations used a Photron SA-Z camera with a Nikon 105 mm lens. Additionally, both used a vertical knife edge. Due to space limitations on the optical bench, a triangle configuration was used rather than the traditional Z-type. This setup involves positioning the light source and camera on the same side of the mirrors, which does introduce a coma aberration limiting the quality of the schlieren images. However, despite the aberration, useful results can be achieved when using an incoherent light source.

The first configuration (Figure 2.15a) used 4-inch parabolic mirrors with a focal length of 24 inches for collimating the light and a Newport Xenon 150 W arc lamp as the light source. Images were generally captured at 20,000 frames per second, with a shutter period of 1/4,032,000 seconds. Due to the small size of the mirrors compared to the model, several runs were required at the same conditions to create a composite image of the overall bubble. Between runs, the optical bench with the schlieren system was shifted, and the model was moved to obtain results farther downstream than initially visible through the window.

The second configuration (Figure 2.15b) utilized 8-inch parabolic mirrors with a focal length of 40 inches. Due to the limited size of the optical bench and the longer focal length of the mirrors, a pair of 4-inch flat mirrors was necessary to reflect the light back away from the windows. A simple LED flashlight was used as the light source for this configuration, as that was the only available source at the time. Images were captured at 10,000 frames per second with a shutter period of 1/10,526 seconds. The longer shutter was needed to compensate for the lower brightness of the light source.

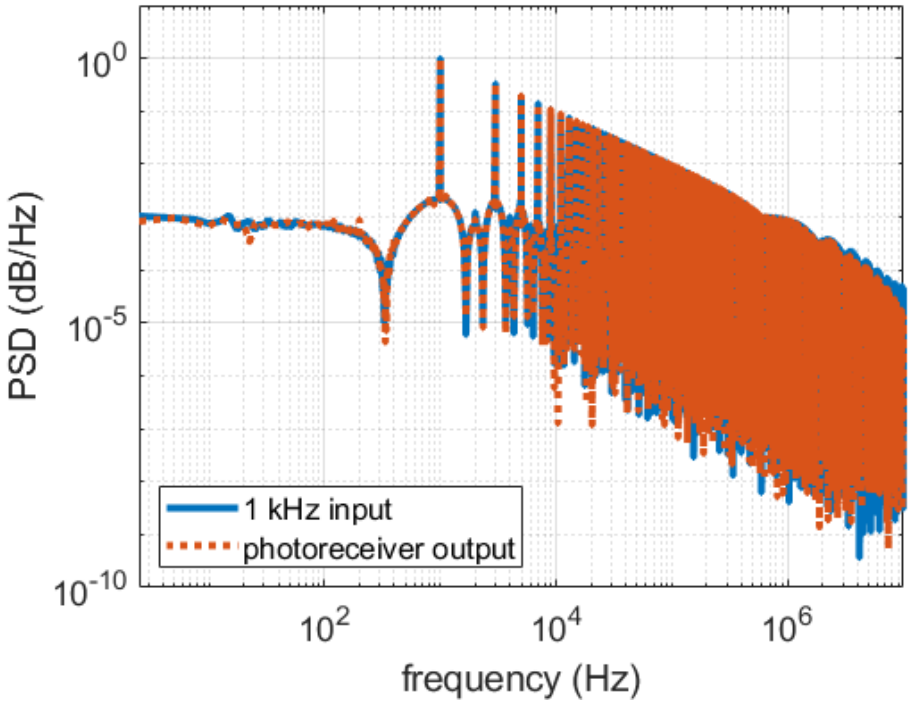

(a) Overall power spectral densities of the input and output voltages from 1 Hz to 10 MHz.

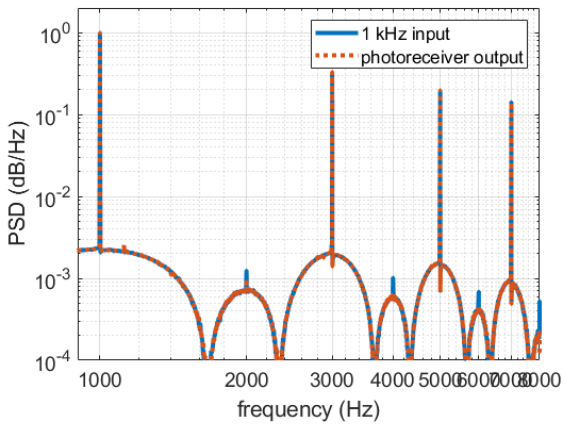

(b) Detail of fundamental frequency peak and harmonics. Note that the normalized input and photoreceiver peaks reach the same values at all these initial harmonics.

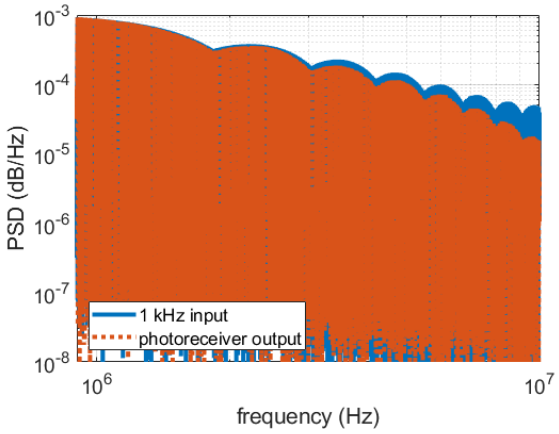

(c) Detail of higher frequency harmonics. Note that the photoreceiver peaks first begin to dip below the input at around 3 MHz.

Figure 2.13. Power spectral densities of transistor and photoreceiver, with regions of interest detailed. Normalized voltages for a 1 kHz square wave input signal.

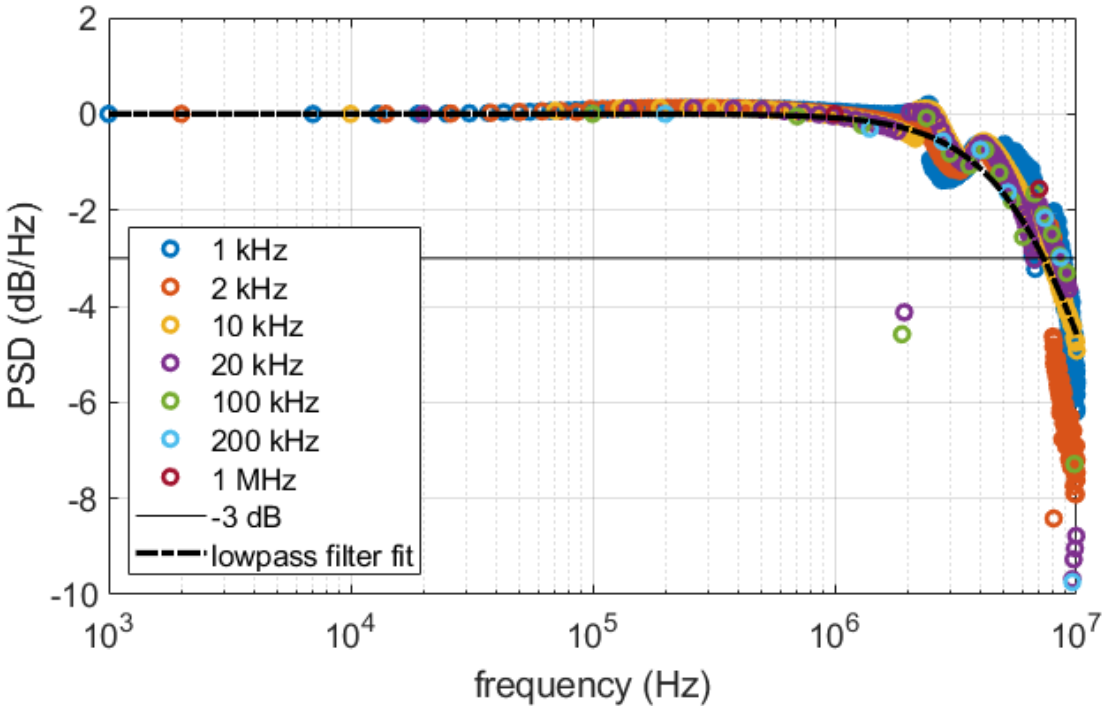

(a) LED input at reference side, $f_c = 7.31$ MHz

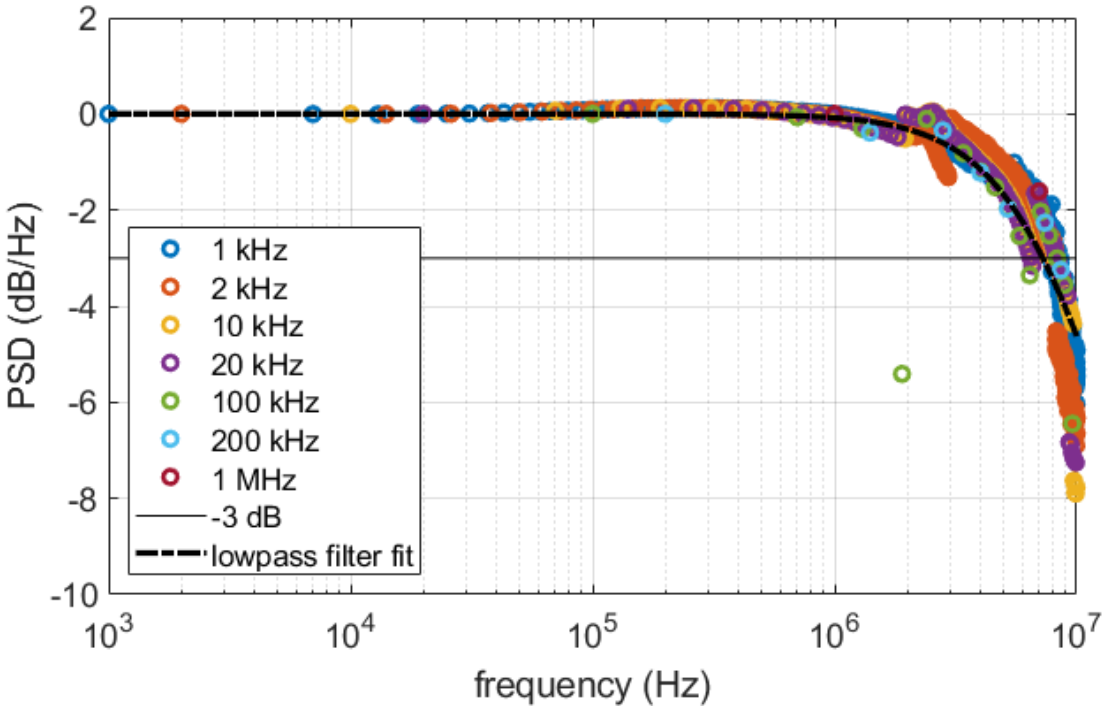

(b) LED input at signal side, $f_c = 7.26$ MHz

Figure 2.14. Power spectra with low-pass filter fit to data

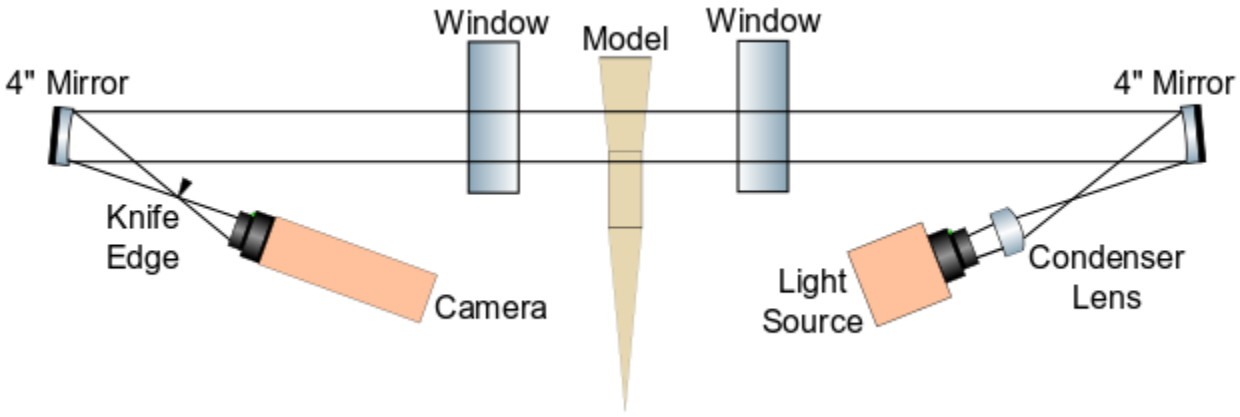

(a) With 4” parabolic mirrors

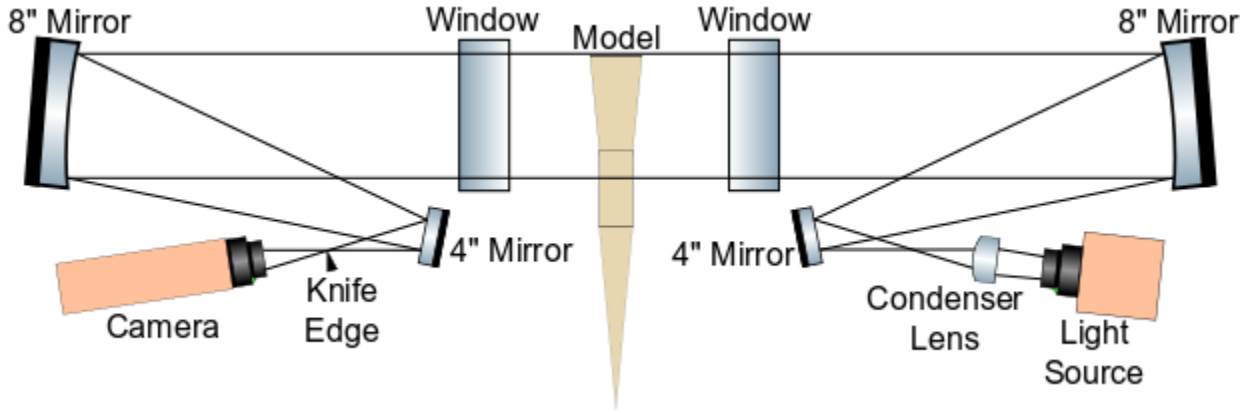

(b) With 8” parabolic mirrors

Figure 2.15. Schlieren configurations used

2.6 PCB Piezotronics Pressure Sensors

To get surface pressure-fluctuation measurements, PCB132A31 and PCB132B38 sensors manufactured by PCB Piezotronics were utilized. These sensors are high-pass filtered above 11 kHz and have a nominal high-frequency response of 1 MHz. Therefore, their output was sampled with a frequency of at least 2 MHz to satisfy the Nyquist criterion. The PCB sensors have a stated resolution of 0.001 psi with a rise time of less than 3 μs. The sensor diameter is 3.175 mm including the housing. The PCB factory calibrations provide a single number to convert voltages to pressure fluctuations; this value was used to scale the voltages to pressure measurements. Recalibration efforts by Mark Wason were undertaken at the Purdue 3-Inch Shock Tube to obtain a more accurate frequency response for the sensors [44], although factory calibration values were used for this dissertation.

2.7 Kulite Pressure Transducers

For additional surface pressure measurements, Kulite XCE-062-15A sensors were used. These transducers can capture lower-frequency disturbances, and offer static pressure measurements as well. They are smaller than PCBs, with a 1.7 mm diameter (including housing), but have a slower response time. This lower response time, coupled with the sensor's large resonance peak around 300 kHz, restrict their usage to below around 270 kHz. The Kulites were calibrated during each entry they were used by letting the tunnel empty to low pressure and simultaneously recording the sensor voltages and tunnel stagnation pressures (from the contraction Kulite that was previously calibrated) averaged over 1 second intervals. The pressures from the Paroscientific pressure gauge were also recorded to compare with the contraction Kulite values at low pressures.

2.8 Infrared Thermography

Heat transfer measurements were conducted using Infrared (IR) thermography techniques developed for the BAM6QT by Zaccara et al. [56] and Edelman [40]. A model made of Poly-Ether Ether Ketone (PEEK), a material with a high-emissivity optimal for IR measurements,

is imaged by an Infratec ImageIR 8300 hp camera prior to and during a run. This camera has a pixel resolution of 640x512 and a temperature resolution of 0.02 K, with an accuracy within 1 K. A Nikon 12 mm f/3.0 wide-angle lens is used to view the maximum model surface area through the 4 inch window. Images are recorded at a 200 Hz rate.

Either prior to installation or after the model is uninstalled, a calibration is performed with the camera in the same position used to image the model. Images of flat plates with a grid of holes at known normal distances off the tunnel centerline are taken for the desired depth-of-field needed for post-processing. This calibration allows for an accurate conversion of pixels to physical space in post-processing. A more detailed description of the calibration process can be found in [56].

IR thermography provides less noisy temperature measurements that are not dependent on the quality of the paint job prior to each entry, as is the case with temperature-sensitive paint (TSP). The InfraTec thermographic software IRBIS 3 is used to control the camera and record the temperature data. The Purdue Infrared Registration ANd Heat transfer App (PIRANHA) developed by Edelman is used to convert these temperature measurements to surface heat transfer values (see Section 2.10.1).

There is some uncertainty in the heat flux measurements made with this technique. Using a similar camera, Yates et al. calculated an uncertainty of approximately 130 W/m^2 [57]. This corresponds to between 3% and 20% of the measurements with the cone-cylinder-flare. Turbeville estimates a minimum heat transfer uncertainty of 10% [42]. For this work, 20% error bars are generally included in the normalized heat transfer plots.

2.9 Data Acquisition

Initial measurements were made on a set of digital oscilloscopes. Specific models used include Tektronix DPO5034B, DPO7054, DPO7104, and MDO3014. Each scope provides four channels for data acquisition. Sampling rates were set such that signals up to at least 1 MHz can be resolved, generally 2 MHz for PCB and Kulite sensors and 10 MHz for FLDI data. An internal Hi-Res mode with 12-bit resolution was used for all acquisitions, which

reduces noise by averaging data sampled at the maximum rate of the scope, effectively acting as a low-pass filter with a 3 dB bandwidth of 0.44 times the set sampling frequency [58].

Once purchased by the lab, later measurements were made with an integrated data acquisition system. An HBM GEN7i with tethered GEN7ta was used with GN815, GN8103B, and GN8102B cards that have 8 channels each. Data acquired on the GN815 cards, which have 18-bit resolution, were sampled unfiltered at the maximum sampling rate of 2 MHz. The GN8103B and GN8102B cards, with 16-bit resolution, have a higher unfiltered noise floor but also support higher sampling rates. Data acquired on these cards were either unfiltered or set to use a real-time Bessel low-pass filter to reduce the noise. More information on the effects of filtering the DAQ data can be found in the BAM6QT DAQ user manual [59].

2.10 Post-Processing

2.10.1 Heat Transfer Data

The Purdue Infrared Registration ANd Heat transfer App (PIRANHA) developed by Edelman [40] was used to reduce the data from temperature measurements to heat transfer. The app includes methods for image stabilization, meshing, and various algorithms for heat transfer computation in a self-contained graphical user interface (GUI). A series of steps takes the user from raw temperatures to processed heat transfer.

Prior to reading in data from a run, the images taken during the calibration procedure are processed. After being read in, the user must select a few points on the grid to define a pair of perpendicular axes. This is repeated for each image, and then PIRANHA utilizes a nonlinear camera pin-hole model to convert 2-dimensional pixel-space to a 3-dimensional physical representation. Output parameters from the model are saved for reference when processing run data.

To process a run, the first step is to generate a mesh along the surface of the model. A cone geometry was used to wrap the flare of the cone-cylinder-flare, with either a 3.5° or 10° half-angle depending on the model used. Figure 2.16 shows an example of a mesh using the 10° flare. This image uses 100 points in the axial and azimuthal directions for clarity, but

when actually processing data, grids with 600 points in each direction were used instead. The mesh can be used to "unroll" the model surface into 2-dimensional space.

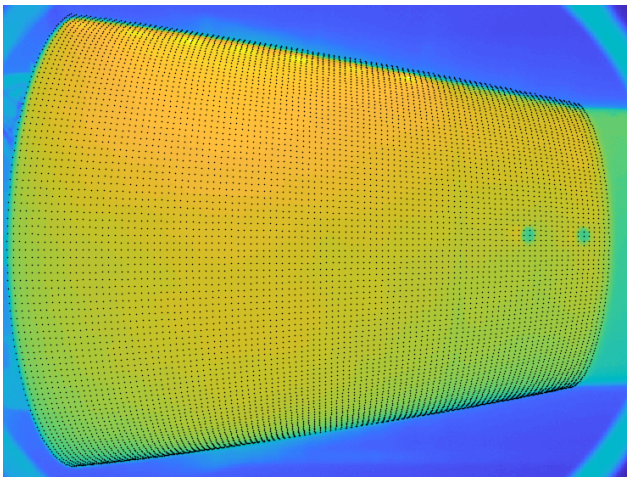

Figure 2.16. Flare mesh example. Points are deliberately sparse for clarity.

Next is the image registration. A small portion of the image is selected with some area of detail like a sensor or edge. This section is used for stabilization, where a 2-dimensional cross-correlation algorithm determines horizontal and vertical shifts between images. The images are adjusted based on these computed displacements for the interpolation steps.

After registration, the temperature values are interpolated onto the computed mesh from the pixel values. At this point, corrections for emissivity and transmissivity are applied, accounting for the properties of the PEEK model and the window, as well as the normal direction of the local surface as determined by the mesh. The PEEK material properties are summarized in Table 2.4. The last step in PIRAHNA is the heat transfer calculation, which is made along the mesh using a 1D FFT algorithm.

Table 2.4. PEEK material properties used in this dissertation.

Property	Value	Units
Density	1300	kg/m^3
Thermal Conductivity	0.29	W/(m*K)
Specific Heat	1026	J/(kg*K)

Once heat transfer is computed, the data are extracted and used along with the computed unit Reynolds number and temperature values to nondimensionalize the heat transfer along the surface. Equation 2.26 shows the computation used to determine the nondimensional Stanton number.

$$St = \frac{q}{\mu Re C_p (T_0 - T_w)} \tag{2.26}$$

In this equation, q is the heat transfer determined by PIRAHNA and μ is the fluid viscosity calculated using Sutherland's Law without the low-temperature correction. Re is the freestream unit Reynolds number and T_0 is the stagnation temperature; both are determined using the method described in Section 2.1.1. T_w is the wall temperature, assumed to be 303 K, and C_p is the specific heat, assumed to be 1.009 kJ/kgK.

Finally, the Stanton number is scaled by $\sqrt{Re}$ (for laminar flow) or $Re^{1/5}$ (for turbulent flow) for the final heat transfer measurements used in this dissertation. This heat transfer representation has units of $m^{-1/2}$ when using the laminar scaling and of $m^{-1/5}$ when using the turbulent scaling. Re is defined in Equation 2.5.

2.10.2 Pressure and Density Fluctuation Data

While heat transfer and schlieren data were used to look at the steady-state features of the flow, measurements obtained by PCB and Kulite pressure sensors or with the FLDI were primarily used to analyze instabilities in frequency space. The pressure fluctuations were normalized by the wall pressure and the density fluctuations were normalized by the edge density. Both the wall pressures and edge densities for the cone-cylinder-flare geometries were computed by Dr. Esquieu with DPLR. The computations were made at one stagnation pressure and then scaled with the stagnation pressure from the relevant time during the run.

The pressure and density time series data were converted to power spectral densities (PSDs) using Welch's method with 50% overlap. The data length was determined by the desired frequency resolution, which was generally taken to be 4 kHz. Root-mean-square (RMS) amplitudes were found by integrating the PSD across a predetermined frequency band, generally from 50 to 270 kHz unless otherwise noted, and then taking the square root.

The frequency band was chosen to encompass the primary instabilities seen in the flow at a variety of unit Reynolds numbers while excluding much of the lower-frequency energy seen in the PCB data generally attributed to vibrations. It also excludes Kulite resonance (around 300 kHz) and captures any broadband effects, allowing for direct comparison between PCBs and Kulites under both quiet and noisy flow. The peak frequency for each relevant instability in the PSD was determined from the PSD by first finding the maximum amplitude in a given frequency range. Then, the two frequencies on either side of that maximum whose amplitudes were a given percentage of the maximum (generally 50%), were found. Finally, the midpoint between those two frequencies was determined, and that was labeled the "peak frequency" for the particular peak. See Section E.3 for an example of this process.

The magnitude-squared coherence was used to determine if a signal likely represented a convective or an absolute instability. A convective instability would travel downstream during a run, while an absolute instability would be a local oscillation in the flow. The coherence estimates a power transfer between the input and output of a linear system, here two sensors with one downstream of the other. It provides a magnitude between 0 and 1 as a function of frequency. For traveling instabilities, the coherence should be high, while for a stationary one it would be low.

The cross-correlation of the signals of two sensors was utilized to estimate the disturbance velocities of various instabilities. The known distance between the two sensors divided by the lag time at the point of maximum cross-correlation gives an estimated group velocity in the direction of the first sensor to the second. For absolute instabilities, the peak cross-correlation should occur at 0.0 s.

To look at first order nonlinearities, the bicoherence was also computed. The bicoherence is a second-order analog of the magnitude-squared coherence, and provides evidence of quadratic nonlinearities in a signal. If a strong enough nonlinearity is present, a peak associated with that nonlinearity's frequency should be present in the PSD. For example, a harmonic of a signal with frequency f_1 should have a peak frequency of $2f_1$, while a nonlinear interaction between two signals f_2 and f_3 would have a peak at $f_2 + f_3$. However, plotting significant bicoherence values can highlight weaker nonlinearities as well, even if the associated peak is not evident in the PSD. This is useful, since weak nonlinearities potentially

intensify moving downstream. The model has a limited streamwise length, so weak nonlinearities could become more significant ones on a vehicle that extended farther downstream. For a more detailed discussion of the bicoherence, see Edelman's PhD dissertation [40].

2.11 Zeroing the Angle of Attack

A zero-degree angle-of-attack adapter was used on the sting in the tunnel to help get the angle of attack of the model as close to zero as possible. The adapter consists of two rods, one that connects to the sting and one that screws into the model. The rod attached to the model screws into the rod that attaches to the sting, which has 4 additional screws located 90° apart from each other. These screws can be independently tightened to move the model-attached rod minutely in two axes. Figure 2.17 displays a photograph of the two parts of the adapter.

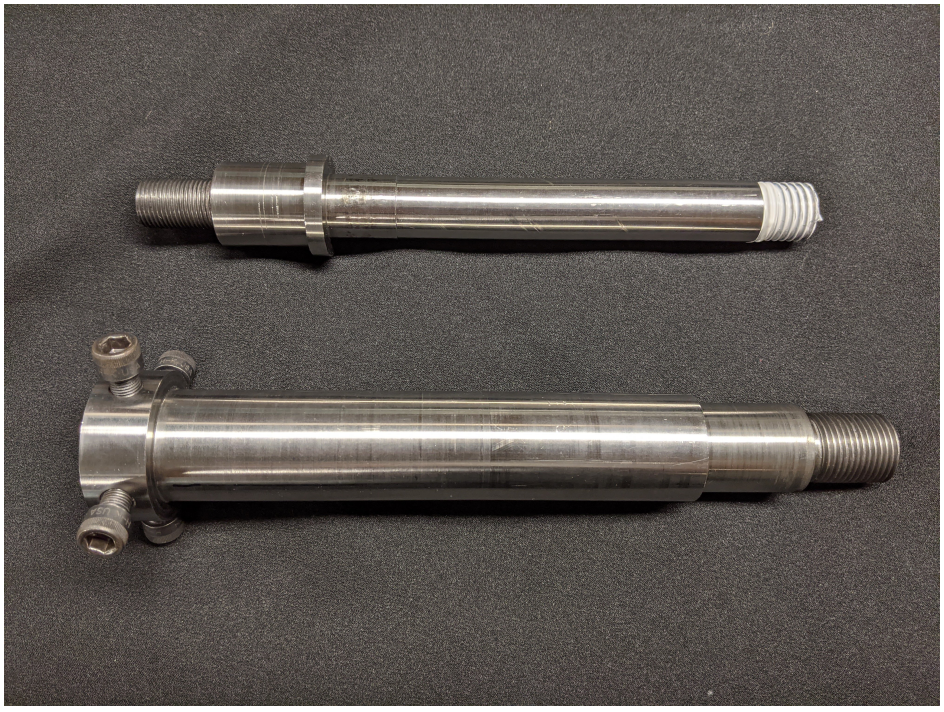

Figure 2.17. Photograph of the zero α adapter.

Second mode pressure fluctuations on the 5° cone section of the model are used to determine whether the angle of attack is close enough to zero and, if not, which direction it

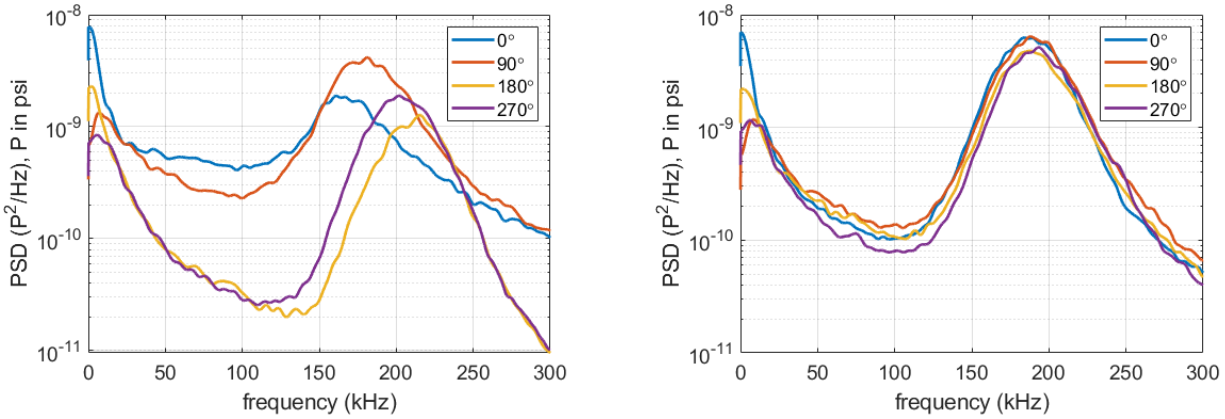

(a) Before zeroing

(b) After zeroing

Figure 2.18. Power spectra of PCBs used to zero the angle of attack, from Runs 0501 and 0503 with the 10° cone-cylinder-flare model. Legend corresponds to azimuthal position of the PCB sensor. Noisy flow, $Re = 7.4 \times 10^6/\text{m}$.

must be shifted to become zero. Four PCB sensor holes are present in the model at one downstream axial location, 0.361 m downstream of the nosetip. They are separated from each other by 90° azimuthally. The second mode fluctuations measured by these PCBs on the sharp cone should peak at the same frequency if the flow is perfectly axisymmetric (in other words, at 0.0° degrees angle of attack). In practice, the model is generally adjusted until the four peaks are within 2% of the mean peak frequency. Based on tests made with the 10° flare model (see Sections 5.2.4 and 5.3.3), that corresponds to an angle of about 0.05°. The runs used to zero the angle of attack are performed at a stagnation pressure selected to maximize the second mode amplitude. Figure 2.18 shows two plots of second mode power spectra. The first figure displays the spectra before the model is adjusted, while the second shows the final result used in that entry. In this particular example, the peaks are initially between 166 and 212 kHz, while after the correction they are just between 188 and 193 kHz.

To see the effect of small, nonzero angles of attack on the separation bubble on the 10° cone-cylinder-flare model, the angle of attack was deliberately altered from its zero location for some runs. The screws that determine the pitch angle were adjusted by half a turn for each run tested. For each pitch adjustment, runs in both quiet and conventional noise flow were made. See Sections 5.2.4 and 5.3.3 for the results of these tests.

3. FLDI DESIGN AND VALIDATION

To make high-speed off-the-surface measurements, a focused laser differential interferometer (FLDI) needed to be designed to work with the unique challenges posed by the Boeing/AFOSR Mach 6 Quiet Tunnel (BAM6QT). This chapter covers the development and testing conducted to validate the FLDI's performance. Some of the results from this chapter were published in Refs. [60] and [61].

3.1 FLDI Design and Sensitivity Testing

This section covers optical-bench testing conducted with the FLDI to determine its sensitivity to applied density gradient signals. Initial tests were conducted with a traditional FLDI apparatus that did not include the thick, contoured tunnel windows (configuration A from Figure 2.10). The apparatus was then modified to account for the window curvature and retested with the windows in place (configuration C from Figure 2.10). The final version used in this dissertation is termed the BAM6QT FLDI, and was designed with optical software modeling prior to purchasing the new components (configuration D from Figure 2.10).

3.1.1 Traditional FLDI Bench Tests

Initial FLDI testing was conducted using configuration A (see Section 2.4.4), here called the "traditional" FLDI. Beam profiles, sensitivity to acoustic waves, and spatial sensitivity were studied.

3.1.1.1 Beam Properties

A ThorLabs CCD Beam Profiler was used to image and measure the beam properties of the FLDI. Figure 3.1 shows a sample of images taken prior to, at, and after the focal points of the beams. The two beams are located along the y-axis. For the traditional FLDI, the beam separation was around 168 μm, and the beams themselves were circular with 26 μm diameters at the focal points. It should be noted that the beam profiler was not purchased

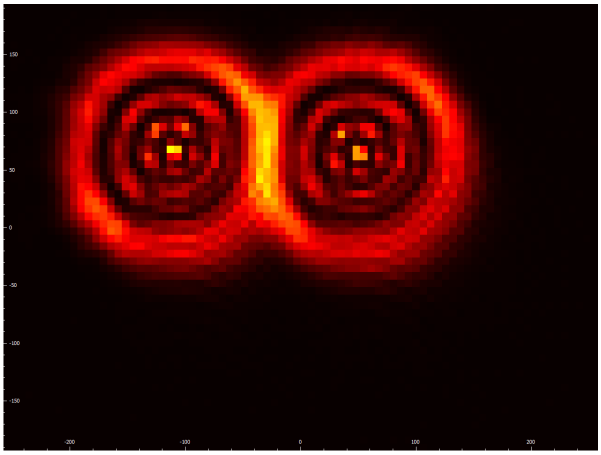

(a) Source side, 6 mm from focus

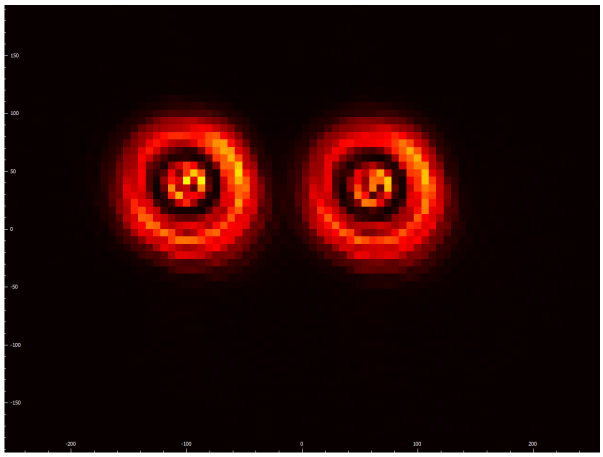

(b) Source side, 4 mm from focus

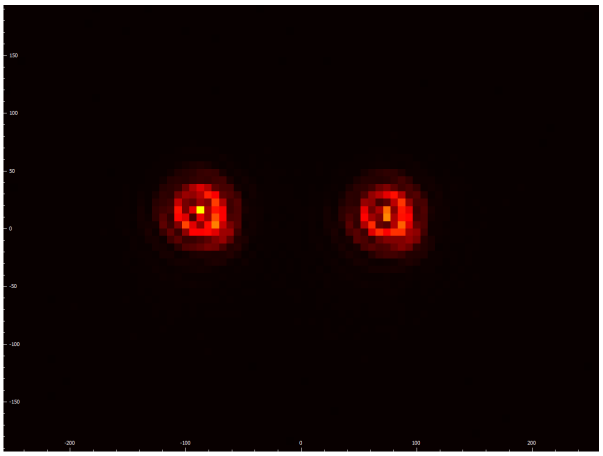

(c) Source side, 2 mm from focus

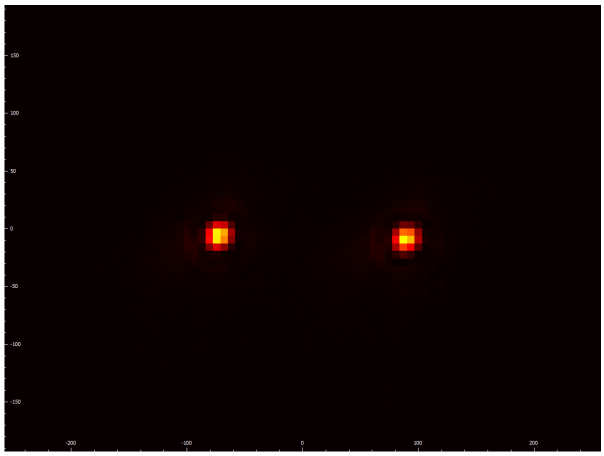

(d) Focal points

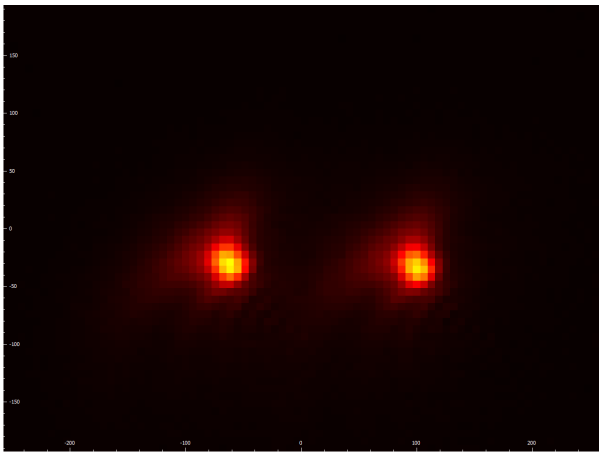

(e) Receiver side, 2 mm from focus

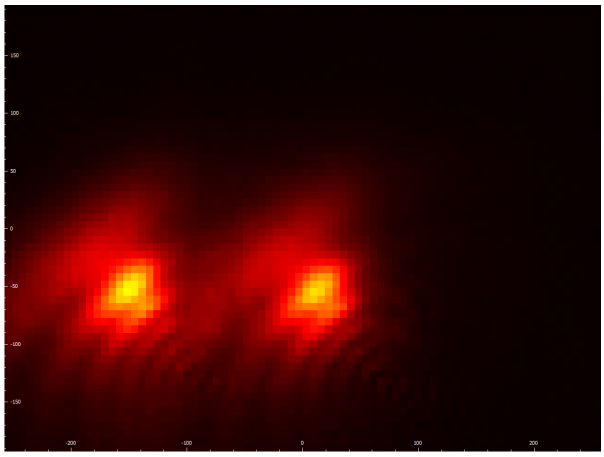

(f) Receiver side, 4 mm from focus

Figure 3.1. FLDI beam profiles moving along z-axis

until after the sensitivity tests were complete. Therefore, these measurements were made at a later time; it is possible that the actual beam shapes during the sensitivity testing differed slightly. The reason for the appearance of concentric rings in the profiles is unknown.

3.1.1.2 Acoustic Sensitivity

The first test performed on the FLDI was to determine whether the interferometer was sensitive enough to pick up acoustic waves. A sine tone generator app on an HTC Pixel XL smartphone was used to play pure sine tones. The speaker of the phone was pointed roughly towards the focus of the beams and tones between 1 and 12 kHz were played. The signal was recorded for 10 seconds at a frequency of 500 kS/s. Figure 3.2 shows the power spectra from 0.1 second selections of each tone. The frequencies of the tones are clearly distinguishable above the noise floor.

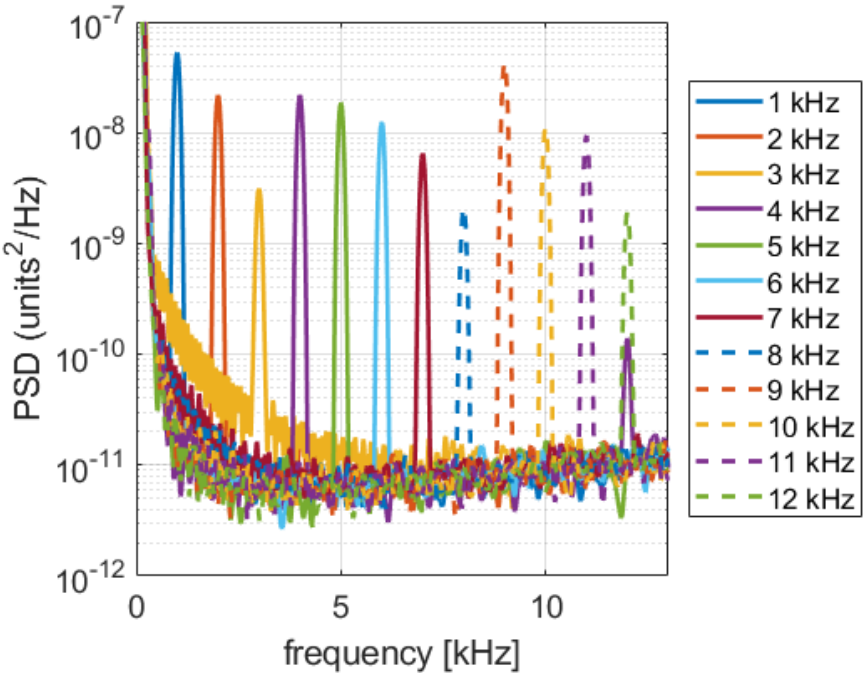

Figure 3.2. PSDs in response to pure sine tones of various frequencies

In addition to pure sine tones, music was also played from the phone while pointed at the FLDI. FLDI voltages were recorded for 20 seconds at a frequency of 250 kS/s. This voltage signal was then played back through Matlab and the recorded song was audibly recognizable.

3.1.1.3 Spatial Sensitivity

A 1 mm diameter needle-nozzle on an air gun was used to produce a jet to test the spatial sensitivity of the FLDI. The air gun was mounted on a Newport ULTRAlign 562-XYZ Steel Linear Stage with 13 mm translation capability, which was itself mounted on a Newport UMR8.51 Double-Row Ball Bearing Linear Stage with 50 mm translation, allowing total translation in the z-direction of 63 mm. The stagnation pressure of the air gun was set to 10 psig for all tests. Figure 3.3 shows a photograph of the setup used for these sensitivity tests. The air gun nozzle is pointed at the foci of the beams. The laser light itself is visible due to condensation in the air from the shock tube pump, which was on at the time, but the individual beams are not distinguishable as they are less than 200 μm apart.

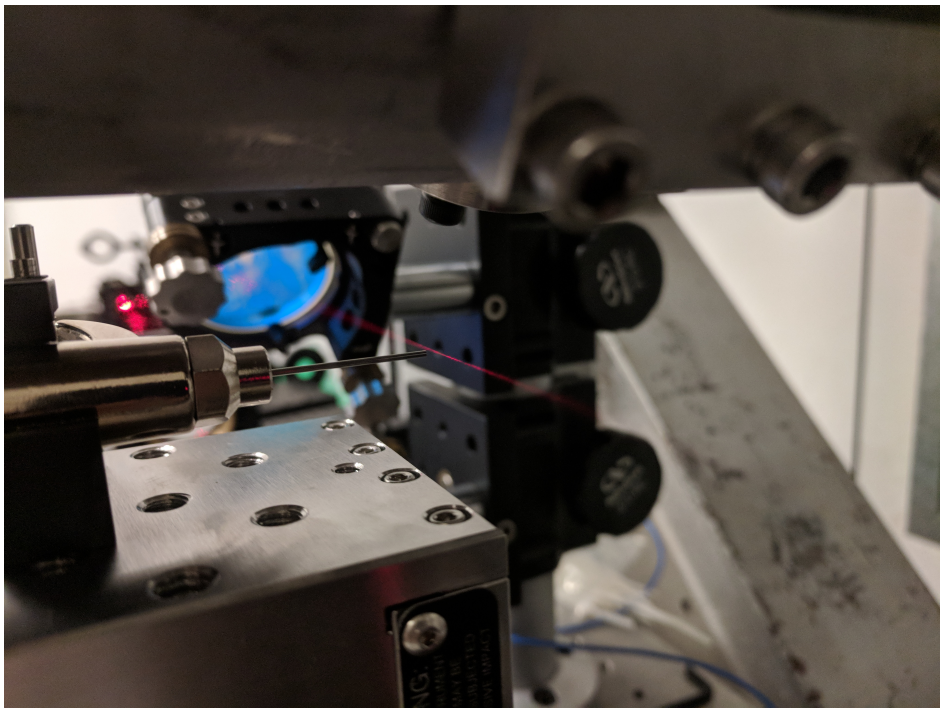

Figure 3.3. Air gun used for spatial sensitivity tests pointed at focus of laser beams

Figure 3.4a shows the normalized phase change root-mean-square (RMS) values measured by the FLDI when the air gun nozzle was 1, 4, and 7 mm away from the beams in the y-direction. The jet was shifted along the x-axis near $z = 0$ until the maximum signal was seen, and then translated along the z-axis to determine the signal falloff with distance from the focus. The FLDI showed the same changes in optical axis sensitivity with distance from the jet nozzle that have been reported by Fulghum [49], [62] and Cerruzzi [63]; as the jet moves away from the beams, the normalized sensitivity region broadens. Fulghum's results for a similar test can be seen in Figure 3.4b. Fulghum's test involved an air jet with a 1 mm nozzle at 30 psia stagnation pressure.

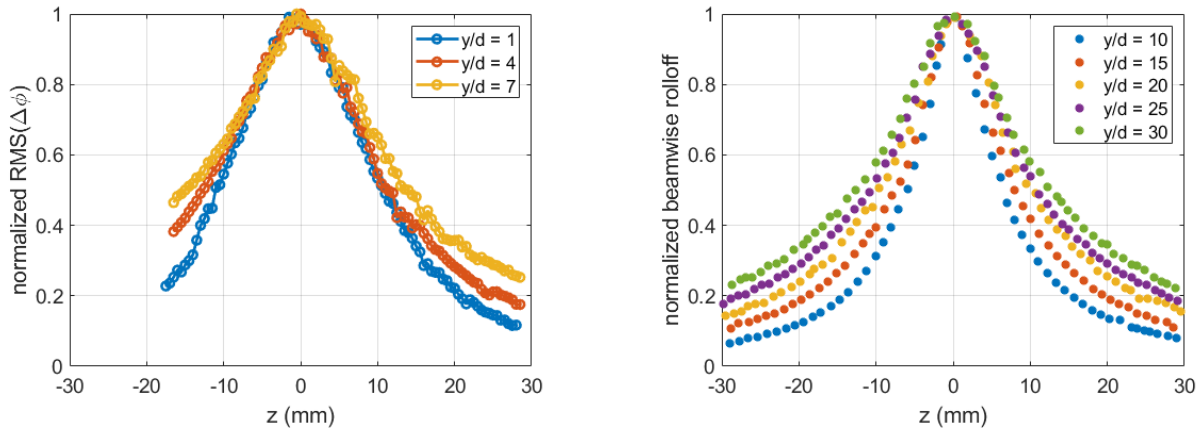

(a) RMS of phase change normalized by maximum value

(b) Normalized RMS found by Fulghum [49], replotted from digitized data

Figure 3.4. Normalized RMS of phase change caused by a small turbulent jet translated along the optical axis.

The spatial sensitivity along the x-axis, perpendicular to the optical axis as well as the plane of beam separation, is shown in Figure 3.5a. Note that the air jet had a nozzle of 1 mm, so the sensitivity could not be measured much smaller than that physical constraint. The actual beam widths, however, were less than 50 μm, so the actual x-axis sensitivity is likely on that scale as no signal should be obtainable by the FLDI where no light is present. As before, the test was repeated for several y values between 1 and 7 mm and the trends found were similar to those seen by Fulghum [49], [62], Ceruzzi [63], and Jewell [64]. Figure 3.5b shows the results Fulghum obtained from a similar test. As before, both tests show

that, with increasing distance from the beams, the normalized RMS of the phase change decreases and widens. Additionally, when the nozzle gets close enough to the beams, there is a dip in signal near $x = 0$ mm due to the FLDI measuring the potential core of the turbulent jet. In this core, the flow is not yet turbulent, and the fluctuations are therefore decreased. However, as the nozzle moves away from the beams, the fluctuation measurements become gaussian.

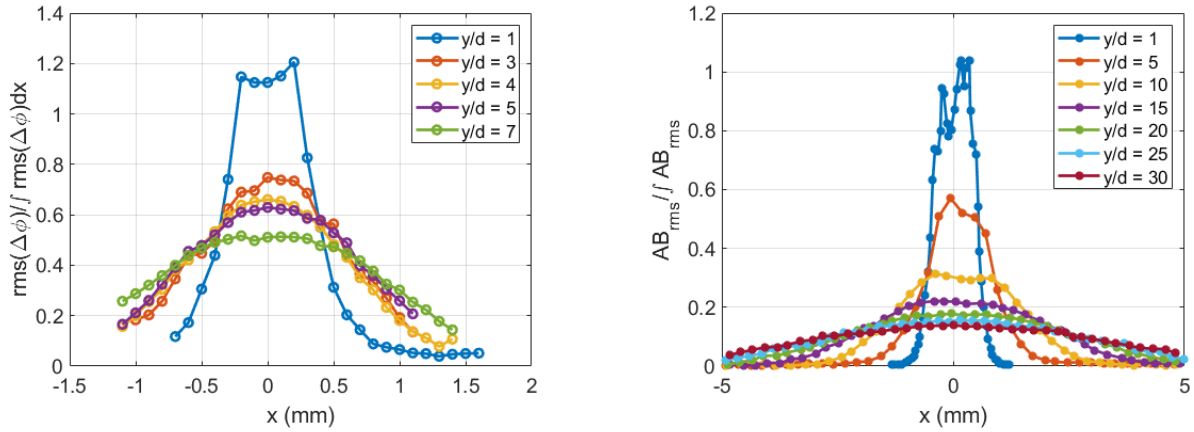

(a) RMS of phase change normalized by area under the curve

(b) Normalized RMS found by Fulghum [49], replotted from digitized data

Figure 3.5. Normalized RMS of phase change caused by a small turbulent jet translated perpendicular to optical axis. Note that Fulghum's y-axis is equivalent to the x-axis in this research.

To get an overall picture of the spatial sensitivity for the simple FLDI, a complete grid was tested with the air jet. Measurements were made at 2 mm intervals across 20 mm along the z-axis, and at 0.1 mm intervals across 2 mm along the x-axis. The air gun nozzle was 4 mm away from the beams in the y-axis. The resulting phase change RMS values are plotted in Figure 3.6. The sensitivity region is defined in Section 3.1.2.4.

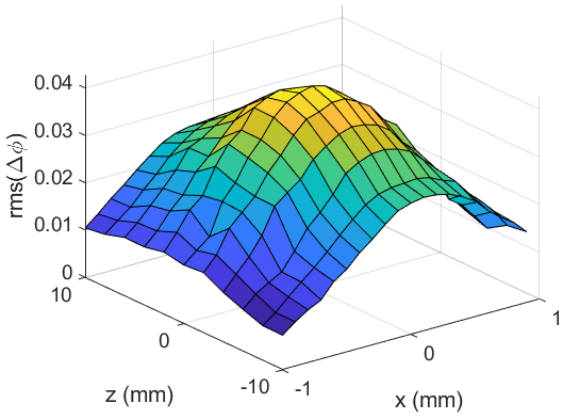

(a) Overall sensitivity in x and z

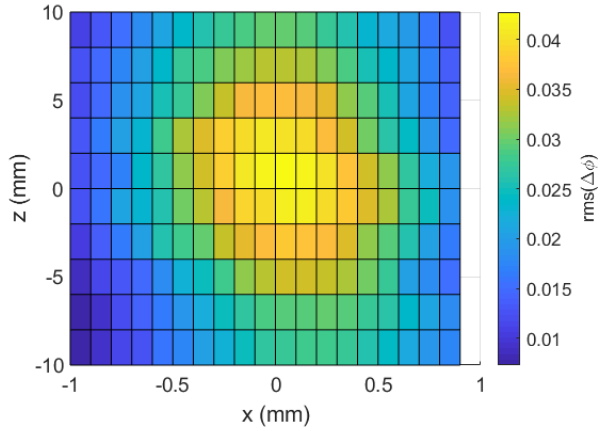

(b) Sensitivity view from above looking down at beams, it can be seen that the beams were slightly off-center in x

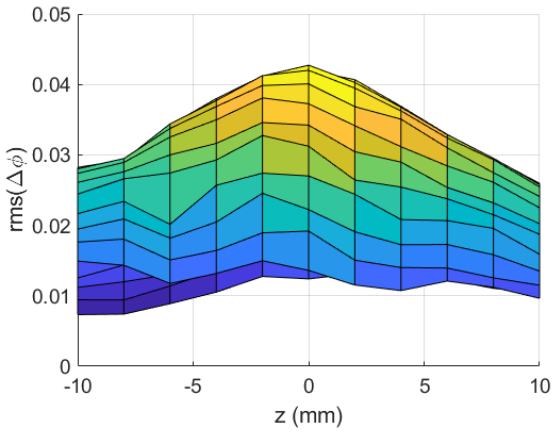

(c) Optical (z) axis sensitivity

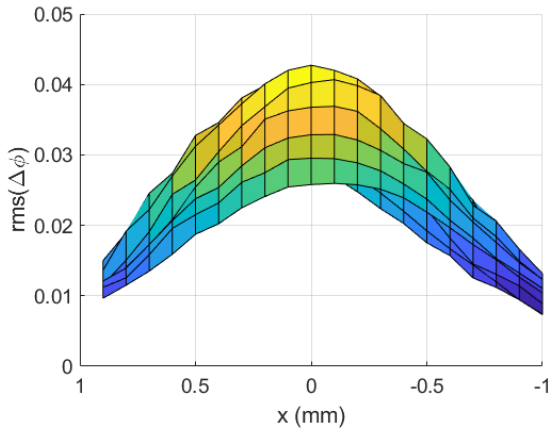

(d) x-axis sensitivity

Figure 3.6. Sensitivity around focal point as a function of x- and z-distance with nozzle located 4 mm away from beam (in y-direction)

3.1.2 FLDI Sensitivity through Contoured Tunnel Windows

Once it was verified that a traditional FLDI could be assembled with sensitivity results similar to previously published studies, a version that was compatible with the contoured tunnel windows was designed. This design was tested with the same optical-bench tests the traditional FLDI underwent to compare the sensitivity of the BAM6QT FLDI with the original apparatus.

3.1.2.1 Zemax Modeling

The BAM6QT FLDI was designed with a combination of ray tracing simulations and bench testing with the physical components. As the tunnel windows are made of thick, contoured Plexiglas, they inevitably act as lenses for the laser and must be taken into account in the FLDI design. The optical analysis software used for the FLDI design was ZEMAX-EE from 2011.

The Plexiglas™ windows are a unique shape, with a cylindrical exterior and an interior curvature that follows the contour of the nozzle. They were simulated by using extended toroidal surfaces in Zemax. Other components of the FLDI are all commercially-available optics with Zemax models. With a computer representation of the FLDI, various lenses could be placed, removed, or shifted to find what would work best with the curved windows.

Figure 3.7 shows a screenshot of the FLDI in Zemax as it was tested on the optical bench. Note that the vertical line between the two windows is a reference plane added to the simulation to view the beam profiles at its location. The final design utilized most of the optics from the traditional FLDI (configurations A and B from Section 2.4.4) with the modification that the focusing lens is no longer a spherical 300 mm lens but two cylindrical lenses with focusing lengths of 300 and 250 mm. The 300 mm lens is set with its curvature about the y-axis such that it focuses the laser in the vertical (x) direction. This is similar to the orientation of the windows, so both the 300 mm lens and the windows work in series to produce the final vertical diameter of the beams at the focus. The 250 mm lens is oriented with its curvature about the x-axis so that is focuses the laser in the horizontal (y) direction. It is the only lens focusing the light along this axis, and it also works to parallelize the beams as well. The 300 mm lens is generally labeled L2, while the 250 mm lens is generally called L3 (as they are the second and third lenses in the FLDI system, located after the biconcave lens, L1).

An added benefit of splitting the function of the spherical focusing lens into two cylindrical lenses is more control over the direction of the beams relative to each axis. While Figure 3.7 shows the beams going through the center of the windows, in reality a model will be located in the center of the test section. As the FLDI will primarily be used to measure

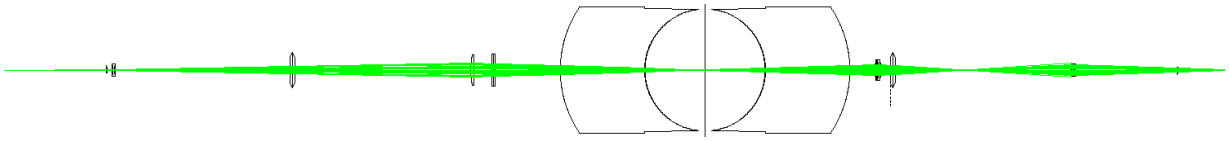

Figure 3.7. FLDI as simulated in Zemax

fluctuations near the surface of the model (for example, in the boundary layer or inside a separation bubble), the beams need to be offset from the centerline. The mirrors used in the full BAM6QT FLDI (configuration D) can be used to shift the beams downward so that they go below the model; however, if the light enters the window at a noncentral location, it will be deflected upward by the curve of the outer surface, and then downward (but not by the same amount) by the inner surface. This causes the beams inside the test chamber to no longer be parallel to the z-axis. However, by offsetting L2 from the optical axis a specified distance, the beams can again be made parallel.

In addition to potentially tilting the direction of the beams, passing the light at an offset from the center changes its x-location inside the test chamber. This interior offset is smaller than offset outside the tunnel due to the curvature of the windows when approaching off-axis. Figure 3.8 shows the different offsets used with the BAM6QT FLDI. The overall offset of the optical axis outside of the tunnel from the center of the tunnel window is denoted as h_1, while the offset of the beams inside the test chamber is marked by h_2. M1 and M2 represent the first two mirrors in the FLDI system used to reflect the beams up to the height of the windows, while W1 is the first Wollaston prism. By offsetting L2 from the optical axis, the beams can be returned to parallel with the z-axis inside the tunnel.

Zemax was used to determine the maximum displacement from the center of the tunnel that the FLDI would be able to reach inside the test chamber. Figure 3.9 plots the results of that analysis. The windows are 175 mm across in the x-direction, making the largest value for h_1 87.5 mm. From the simulation, the maximum displacement inside the test chamber (h_2) achievable is about 55 mm, which requires an L2 offset of -12 mm. In testing the beams have been successfully offset by up to 51 mm from the center of the test chamber. The actual windows are encased in stainless steel frames that begin to clip the beams if they are moved any farther towards the edge. The actual locations of the optics are not

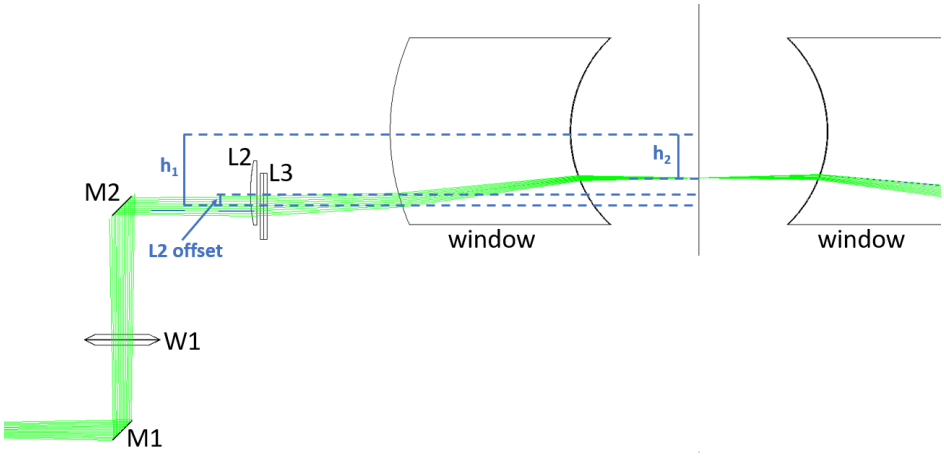

Figure 3.8. Beam offset simulation

as precise in practice as in the simulation; however, the immediate feedback from the beam profiler available while adjusting the locations of the optics allows for good alignment to be achieved. Due to the symmetry about the y-axis, setting the beams above an axisymmetric model theoretically produces the same results as setting them below the model. However, as the optical components are mounted on steel rods, they are more susceptible to vibrations as the displacement along the post increases. Therefore, when the option is available it is recommended that the beams be set to go under the model.

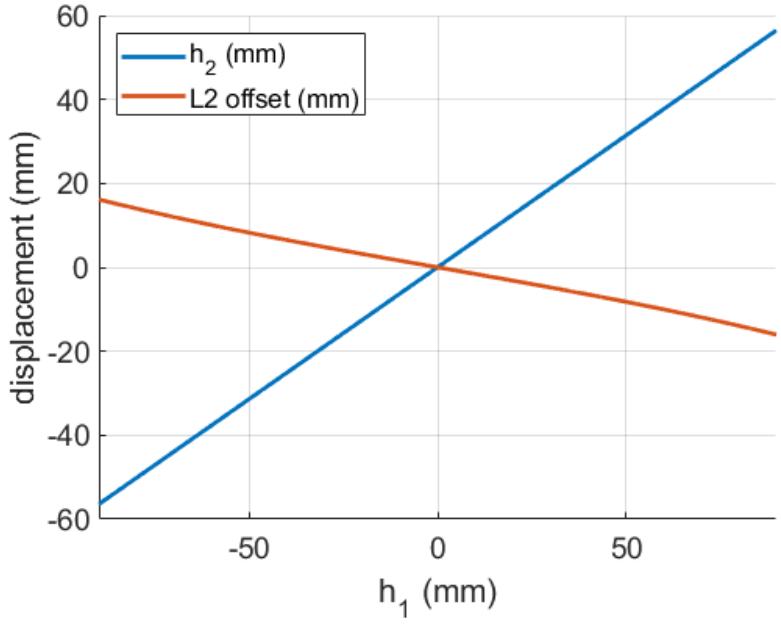

Figure 3.9. Relationship between external beam displacement (h_1), internal beam displacement (h_2), and L2 offset

3.1.2.2 Beam Properties

The Zemax simulation estimated a beam diameter at the focus of between 34 and 81 μm with the beams having a roughly rectangular shape on the source side of the foci and a diamond-like shape on the receiver side (see Figure 3.10). The ThorLabs CCD Beam Profiler was again used to image and measure the beam properties with the tunnel windows to compare the simulated results to what was achieved experimentally. A sample of images taken prior to, at, and beyond the focal points of the beams is presented in Figure 3.11. Interestingly, the beams do appear rectangular prior to the focal points; however, they are highly distorted and have localized hot-spots not present in the Zemax results.

As in Section 3.1.1.1, the two beams are located along the y-axis. For the FLDI in configuration C, the beam separation was measured to be 104 μm. The beam diameters were between 84 and 110 μm, slightly larger than the prediction made with Zemax. Outside of the foci the computed sizes seem to generally agree with the measured ones. Figure 3.12

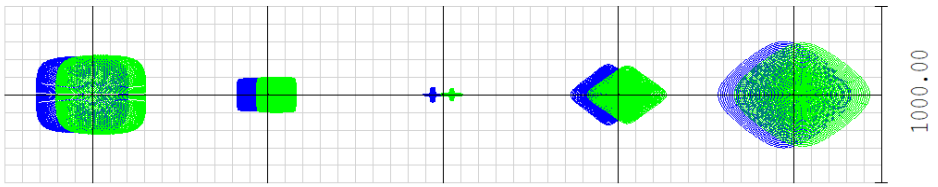

Figure 3.10. Beam profiles at intervals of 4 mm traversing through the focus as simulated in Zemax. The scale on the right is in μm.

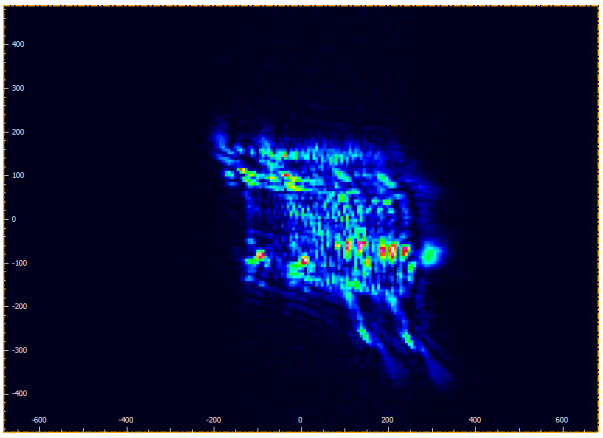

(a) 8 mm from focus on source side

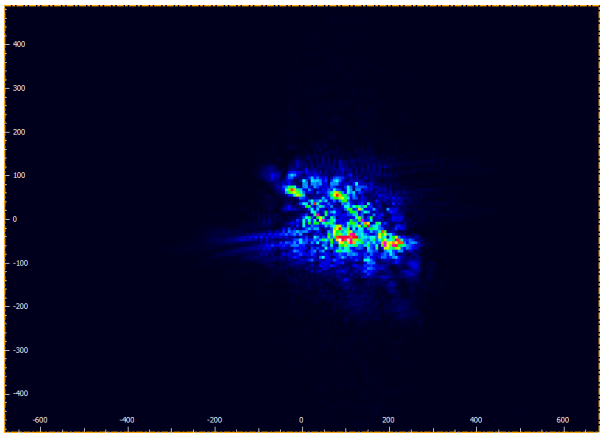

(b) 4 mm from focus on source side

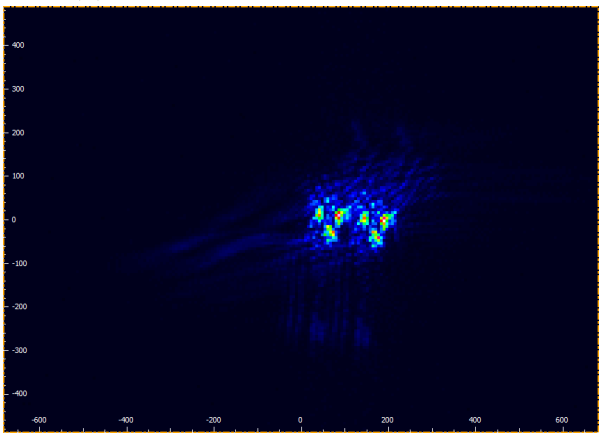

(c) Focus

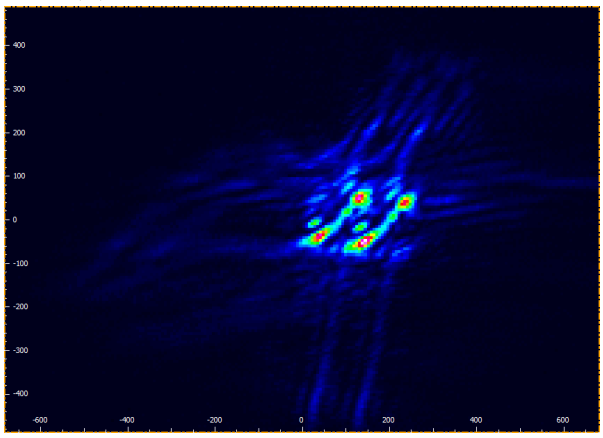

(d) 4 mm from focus on receiver side

Figure 3.11. FLDI beam profiles moving along z-axis. Imaged with the ThorLabs beam profiler.

plots the measured beam profiles (looking at average radius) as compared with the Zemax calculations for the same properties, highlighting this agreement.

The beam profiler was also used to track the source of the beam distortion by placing it at various points along the FLDI beam path as well as placing it near the focus and

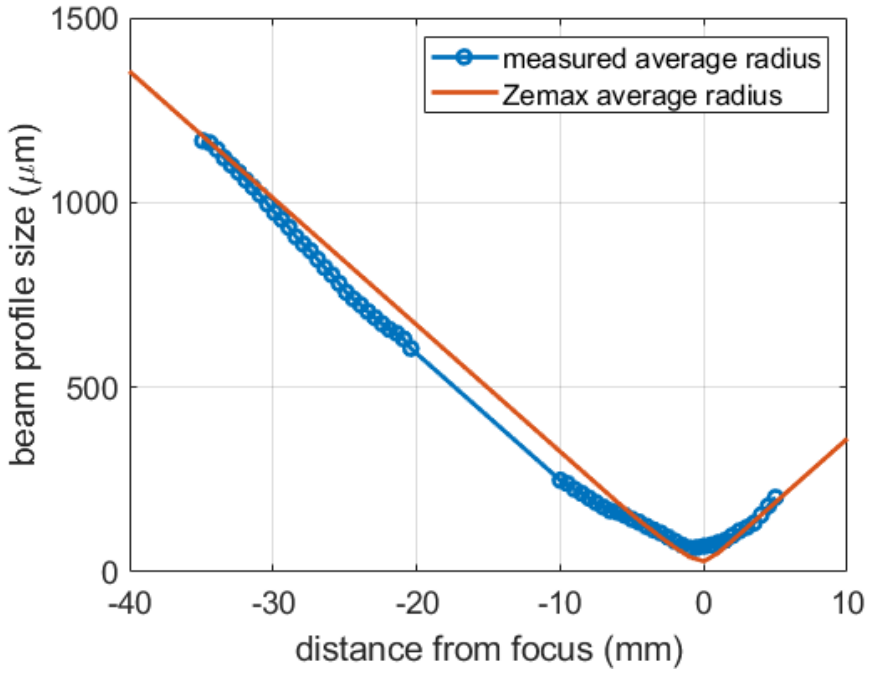

Figure 3.12. Comparison between measured beam profiles and Zemax computations.

removing optical components. Figure 3.13 shows two images from that test; Figure 3.13a is taken near the focus with the expansion lens (L1) removed from the FLDI (making it equivalent to an ordinary laser differential interferometer (LDI)), while Figure 3.13b shows the profile with all the optics in place. The tunnel windows are present in both images; however, after testing each component, the windows were determined to be the cause of the distortion. The reason for the clean Gaussian profiles in Figure 3.13a is due to the small area of the windows the beams traverse when they are not expanded. For an LDI, the beam diameter varies very little in the testing area, so each beam is only about 200 μm across where it passes through the window. However, for an FLDI, the beams are on the order of 20 mm, nearly one hundred times larger, where they traverse the window. Since the windows are made of Plexiglas and are not of optical quality, there are most likely numerous optical impurities that the beams encounter as they pass through. The significantly larger beams of the FLDI will encounter many more impurities, causing distortion. This conclusion was further supported by observing how the beam distortions changed while shifting the optics in

a direction perpendicular to the optical axis. As the windows were shifted, the "hot-spots" in the intensity plots changed depending on where in the window the beams traversed.

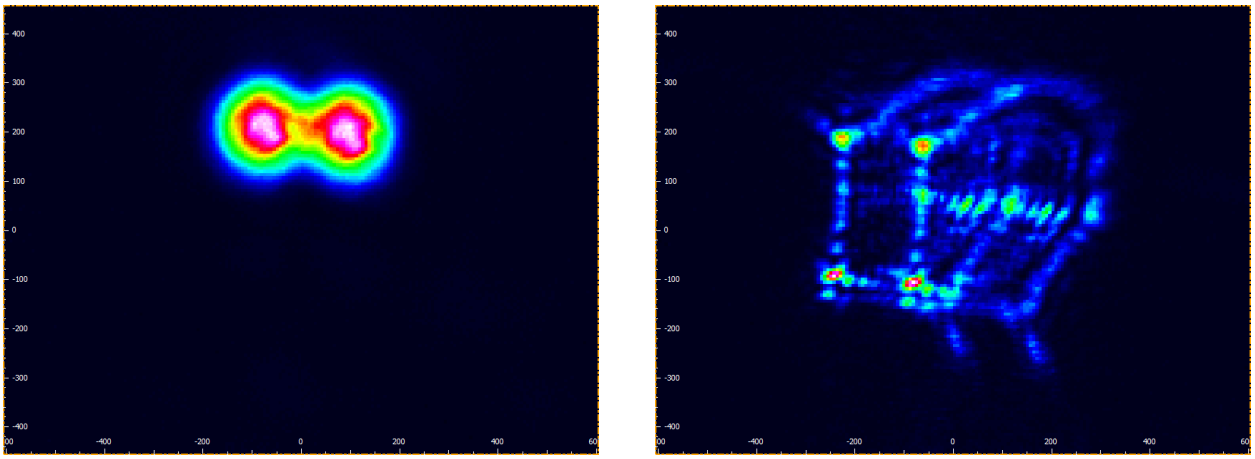

(a) Unexpanded beams near focus

(b) Expanded beams near focus

Figure 3.13. Comparison of unexpanded vs. expanded beams through tunnel windows. Each labeled tick in the horiztonal direction corresponds to 200 μm, while in the vertical direction it is 100 μm.

3.1.2.3 Acoustic Sensitivity

As with the traditional FLDI, the first test performed on the BAM6QT FLDI was to determine whether this version of the interferometer, with its distorted beams, was still sensitive enough to pick up acoustic waves. The same sine tone test was performed as described in Section 3.1.1.2. The results are shown in Figure 3.14, which displays the power spectra from 0.1 second selections of each tone. Once again, the frequency of each tone is clearly distinguishable above the noise floor. However, the results through the Plexiglas™ windows result in a lower overall signal, most likely due to beam distortions (see Fig. 3.13).

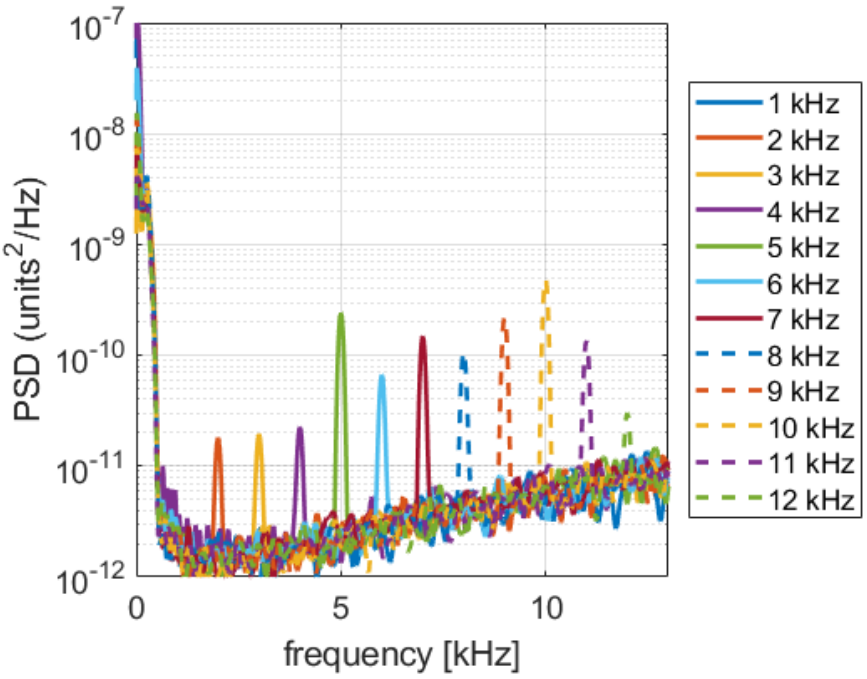

Figure 3.14. PSDs in response to pure sine tones of various frequencies with the window in the FLDI system (configuration B from Section 2.4.4).

3.1.2.4 Spatial Sensitivity

The same small-diameter jet tests were conducted on the BAM6QT FLDI as described in Section 3.1.1.3. The 1 mm diameter needle-nozzle air gun produced a jet with a stagnation pressure of 10 psig, which was pointed at the beams of the FLDI and traversed along and orthogonal to the optical axis. The RMS of the phase change measured by the FLDI at each point was plotted to determine how sensitive the device was to a disturbance at a given location.

Figure 3.15 compares the optical axis sensitivity of the traditional FLDI (configuration A) and the BAM6QT FLDI for bench testing (configuration C). The normalized data is from the $y = 4$ mm air jet test. A Lorentz curve was fitted to the data to allow for extrapolation at farther locations. The "sensitivity region", defined by a 1/e falloff of the signal, was about 35 mm for the traditional FLDI setup, but stretched out to near 65 mm for the BAM6QT version. It is believed that this extension of the sensitivity region is due to the nonuniformity of the beams after they pass through the tunnel windows; the Plexiglas™ material does not

have a uniform index of refraction, and as the beams are expanded before the thick windows they must pass through a not-insignificant volume of the Plexiglas™. This traversal leads to localized hot-spots in the beams' intensities, which remain distinct in the two beams at more distant locations from the focus despite the beams' overlap.

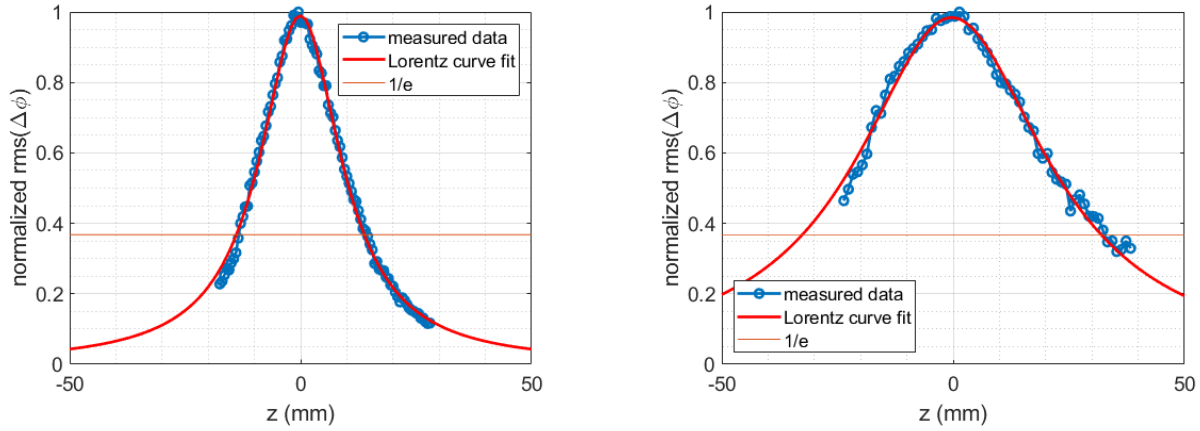

(a) Traditional FLDI configuration sensitivity (configuration A)

(b) BAM6QT FLDI configuration sensitivity (configuration D)

Figure 3.15. FLDI signal response to jet traversing along optical axis

Figure 3.16 displays how the sensitivity for the BAM6QT FLDI varies both along and perpendicular to the optical axis with the jet nozzle placed various distances from the beams. Unlike the simple FLDI, for which the normalized phase change RMS measurements broadened with increasing y-distance, the BAM6QT FLDI did not reveal any obvious trends in sensitivity along the optical (z) axis as the jet was shifted in y (see Figure 3.16a). The reason for this lack of consistency is unknown. The trends in sensitivity perpendicular to the optical axis (along the x-axis), however, are very similar between the simple and BAM6QT versions of the FLDI (shown in Figure 3.16b). As noted before, since the air jet had a nozzle of 1 mm, the sensitivity could not be definitively measured smaller than that value. However, the beams were observed to be less than 100 μm, which would mark the extent of the sensitivity in the x-direction. As the distance in y is increased, the normalized RMS of the phase change widens (note that in this case, the data were normalized by the peak value as opposed to the area under the curve). The dip near $x = 0$ mm for the lower y-values is due to the potential core of the jet, which has fewer fluctuations (similar to the dip in Figure 3.5).

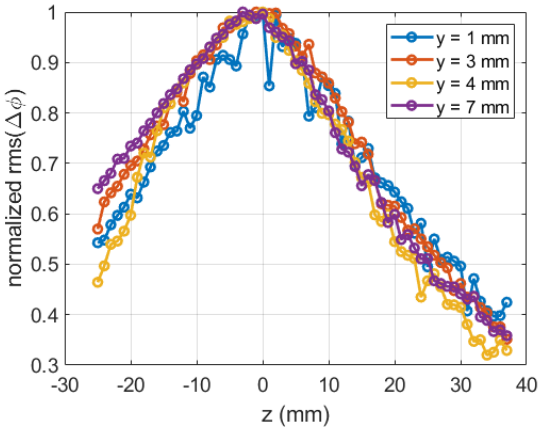

(a) Sensitivity along the optical (z) axis

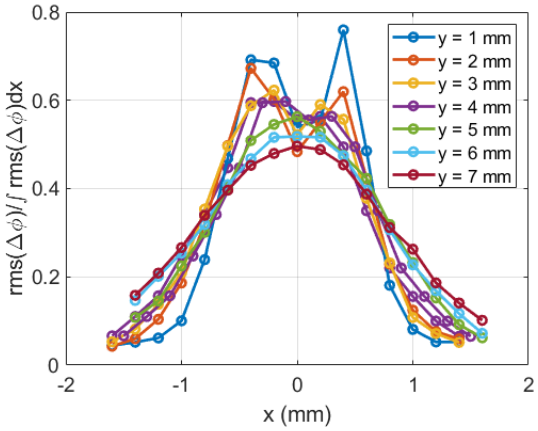

(b) Sensitivity perpendicular to the optical axis (along the x-axis)

Figure 3.16. BAM6QT FLDI configuration for bench testing sensitivity (configuration C)

3.1.3 Summary of FLDI Sensitivity Tests

A traditional FLDI was developed and tested to obtain a baseline sensitivity dataset. The sensitivity to acoustic waves was assessed using a sine tone generator for frequencies between 1 and 12 kHz. The input frequencies were clearly observed as narrow peaks in the FLDI power spectral densities. Spatial sensitivity was probed using a narrow-diameter jet, which was traversed along and perpendicular to the optical (z) axis. The normalized signal RMS followed the same trends previously seen in the literature by Fulghum [49], Ceruzzi [63], and Jewell [64]. Peak sensitivity is achieved at the focal point, dropping rapidly as the jet moves away in x, and less rapidly as it traverses the z-axis.

To work with the contoured windows of the BAM6QT, a new variation of the FLDI was designed using Zemax. The circular focusing lens was replaced with a pair of cylindrical lenses to allow for each axis to be focused independently. Zemax was used to select the lens focal lengths and physical locations, as well as to determine the vertical range of the test section that can be probed. Measured beam diameters and overlap values were compared with the predicted values.

Sensitivity tests conducted with the traditional FLDI were repeated for the BAM6QT version. A decrease in the signal-to-noise ratio was observed with the acoustic test. Ad-

ditionally, the sensitivity region along the optical axis broadened with the inclusion of the tunnel windows. These negative changes are likely be due to the low optical grade of the Plexiglas™ windows. The windows include impurities that alter the beam profiles, creating localized hot-spots in the intensity distribution. However, despite the lower signal amplitude, the BAM6QT FLDI is still sensitive enough, and has a small enough sensitivity region, to obtain measurements in hypersonic quiet flow while suppressing signals from along the nozzle wall.

3.2 FLDI Validation Testing

A 7° sharp cone at 0.0° angle of attack was tested for the purpose of validating the BAM6QT FLDI (configuration D from Section 2.4.4). The FLDI was aligned in the streamwise direction with a surface PCB sensor to compare second-mode peak frequencies between the two sources of measurement. An estimated FLDI signal was computed at different off-surface distances to make further comparison with the FLDI measurements.

3.2.1 Eigenfunction Signal Estimation

The Stability and Transition Analysis for Hypersonic Boundary Layers (STABL) software suite was used to compute the test flowfield. STABL was written by Dr. Heath Johnson at the University of Minnesota [65]. It includes Data-Parallel Line Relaxation (DPLR), an axisymmetric Navier-Stokes flow solver [66], and can solve for disturbances with linear stability theory (LST) or the parabolized stability equations (PSE). The STABL computations made for this study utilized the LST method. They were made to estimate the expected FLDI signal at various distances above the model surface, and the measured FLDI data were then compared to the computed results. The quiet flow case was also used to estimate a disturbance speed for the second mode fluctuations, and to compare measurements taken with a balanced photoreceiver to those from a single photodiode.

3.2.1.1 LST Results

STABL was used to estimate the stability characteristics of the flow and compute the density eigenfunctions that should be measured normal to the model wall. Four cases were run to compare to experiments, with run conditions describe by Table 3.1. Note that STABL cannot replicate the effects of tunnel noise. The grid used a 7° half-angle sharp cone with 752 points parallel to and perpendicular to the model surface (565,504 points total).

Table 3.1. Run conditions used in STABL to compute flow eigenfunctions

Flow	Mach	P_0 (psia)	T_{wall} (K)	T (K)	ρ (kg/m^3)	Re
Noisy	5.8	80	303	53.42	2.80e-2	6.74×10^6/m
Quiet	6.0	130	303	49.84	3.97e-2	11.3×10^6/m
Quiet	6.0	135	303	50.38	4.08e-2	11.5×10^6/m
Quiet	6.0	140	303	50.90	4.18e-2	11.8×10^6/m

The frequencies of the second (Mack) mode oscillations are highly dependent on the thickness of the boundary layer (δ), as their wavelength is approximately 2δ [67]. The boundary layer thicknesses computed for the experimental conditions are plotted in Figure 3.17a. These thicknesses were determined using the return from enthalpy overshoot option in DPLR, which detects the peak enthalpy and then continues moving away from the wall until the enthalpy is near the freestream value [34] (here defined as 100.5% of the freestream value). The results show a boundary layer that thins as the stagnation pressure increases and grows moving downstream, as expected. At the location of the FLDI beams, 0.376 m downstream of the nosetip, the boundary-layer thickness is around 1.99 mm for the conventional noise case, and 1.68 mm, 1.65 mm, and 1.63 mm for the quiet flow cases, respectively.

From the overall instability results from STABL, at 0.376 m downstream (at the location of FLDI and PCB to compare it with), the most amplified frequency occurs at 205 kHz for $Re = 6.74 \times 10^6$/m, 240 kHz for $Re = 11.3 \times 10^6$/m, 245 kHz for $Re = 11.5 \times 10^6$/m, and 250 kHz for $Re = 11.8 \times 10^6$/m with N-factors of 5.4, 7.8, 7.9, and 7.9, respectively. STABL can be run at these particular frequencies to extract the eigenfunction information. Figure 3.17b plots the eigenfunctions at the location of the PCB of interest (PCB 4) for each of the four cases. Note that, since the initial disturbance amplitude cannot be measured, the linear

stability analysis assumes a value. The final results can then be scaled to the measurements for comparison; it is not expected that the computed amplitudes will match the measured amplitudes without scaling.

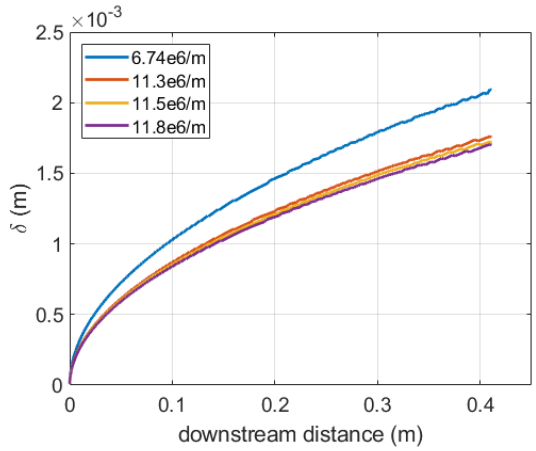

(a) Boundary layer thicknesses from DPLR for STABL-computed cases.

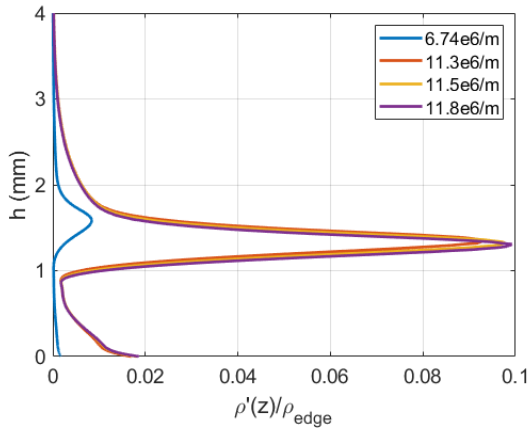

(b) Computed density eigenfunctions 0.376 m downstream of the nosetip (where the FLDI will be located).

Figure 3.17. Computed boundary-layer thicknesses and density eigenfunctions for the 7° sharp cone. The legend describes the flow unit Reynolds number used for the computations.

3.2.1.2 FLDI Estimation

Once the eigenfunctions have been obtained from STABL, they can be used to estimate the relative phase change signal that the FLDI would measure in the BAM6QT. While the FLDI does reduce the signal away from the focal points, it does not completely remove it. Therefore, the measurements made by the FLDI are not directly identical to the computed eigenfunctions, but instead are equivalent to the averaged eigenfunctions over the curvature of the model, across the beam profiles, and through the sensitivity region of the FLDI, scaled by that sensitivity region's profile and the spatial averaging that occurs due to the broadening of the laser beams. The physical representation being probed by the FLDI is illustrated in Figure 3.18. The model surface location, boundary layer thickness, eigenfunction peak locations, and beam diameters are all to scale for beams located 0.376 m downstream of the nosetip. In the image, r is the model radius at the given downstream location, x is the

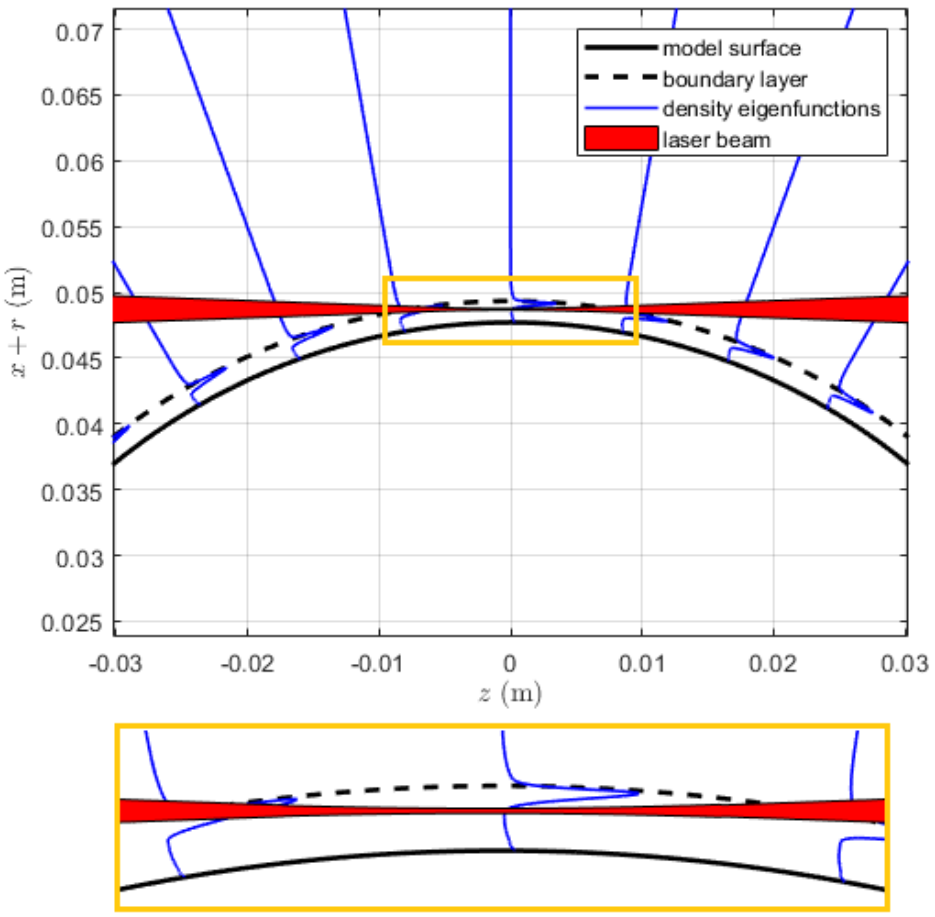

Figure 3.18. Density eigenfunctions along the 7° cone model surface. Beam vertical diameters are taken from measured data, while eigenfunction values and boundary layer thicknesses are from STABL computations.

distance normal to the optical axis of the FLDI, and z is the distance along the optical axis, with all lengths in meters. An enhanced view of the focal area is shown below the plot to get an idea of the size of the focus as compared to the boundary layer.

As can be seen in Figure 3.18, both the curvature of the model and the varying beam diameters cause the FLDI beams to intersect the density eigenfunctions at different points along the model depending on the x and z locations of the beams and their widths. To accurately estimate the relative FLDI signal at a given location above the model surface, the density fluctuations must be averaged along the optical axis. Figure 3.19a shows the computed density eigenfunction for $Re = 11.3 \times 10^6$/m 0.376 m downstream (at PCB 4), with h being the distance normal to the model surface in millimeters and ρ' being the density fluctuations in kg/m^3. Figure 3.19b shows the spatially-averaged density eigenfunction ($\bar{\rho'}$) both over the optical axis and across the beam profile for various distances h of the FLDI beams off-the-surface of the model as a function of distance from the focal point along the optical axis, z. This process assumes that the azimuthal coherence length for the waves is at least as long as the integration length, which may not necessarily be true. However, taking the spanwise effects into account provided better agreement with the experimental measurements than simply comparison the scaled eigenfunction at the focal point. This likely indicates that there is azimuthal coherence along some of the integration path.

Once the signal had been spatially averaged, it was scaled by the sensitivity function determined from the FLDI small-diameter jet bench tests. A Lorentz curve, $g(z)$, was fitted to the normalized sensitivity results obtained with the tunnel windows; this curve is shown in Figure 3.20a. The density fluctuations scaled by $g(z)$ for a variety of distances h off the model surface are plotted in Figure 3.20b.

This process, which is similar to that undertaken by Parziale in his dissertation [47], can be repeated for heights h within the boundary layer of the model at various locations downstream. The scaled and averaged density fluctuation data is then converted to phase change values, and the area under the curve is integrated to obtain the estimated FLDI signal at the given downstream and h distance. The results for each of the PCB locations in the model were computed, and are plotted in Figures 3.21a through 3.21d.

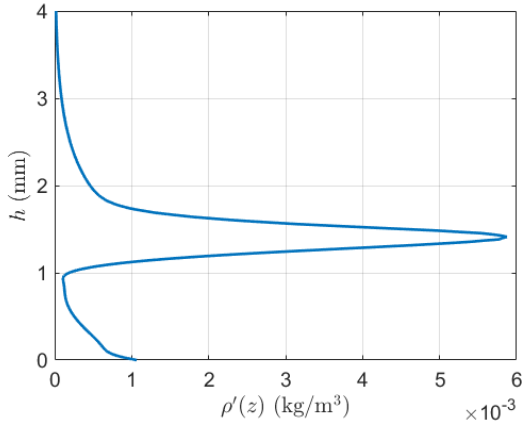

(a) Computed density fluctuation eigenfunction

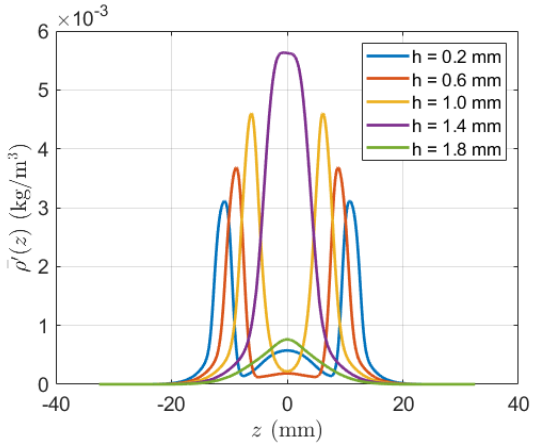

(b) Spatially-averaged density fluctuation eigenfunctions for a variety of FLDI distances off-surface

Figure 3.19. Computed and spatially-averaged density eigenfunctions for $Re = 11.3 \times 10^6$/m at Mach 6

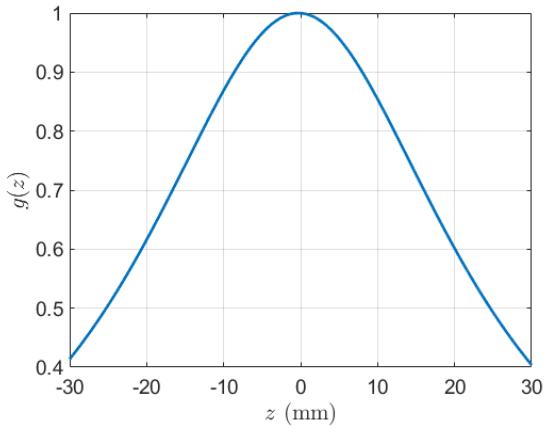

(a) Lorentz function fitted to FLDI sensitivity results

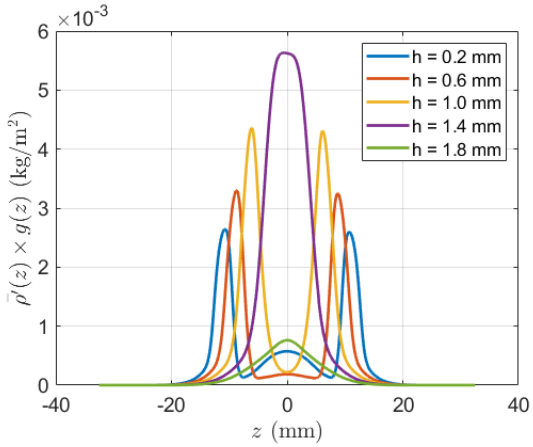

(b) Density fluctuations scaled by $g(z)$ for a variety of FLDI distances off-surface

Figure 3.20. Scaling function and scaled density eigenfunctions for $Re = 11.3 \times 10^6$/m at Mach 6

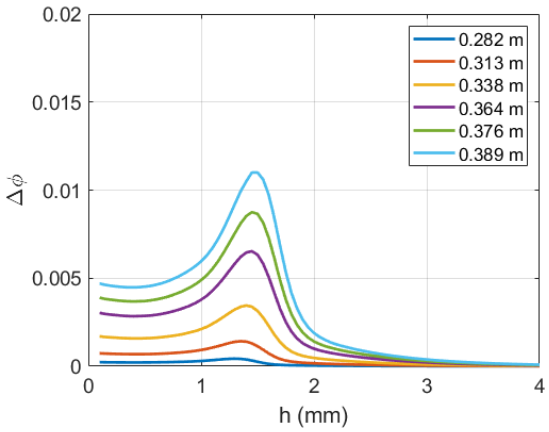

(a) $Re = 6.74 \times 10^6$/m at 205 kHz. Note the vertical axis is one orders of magnitude smaller than the plots of the other conditions.

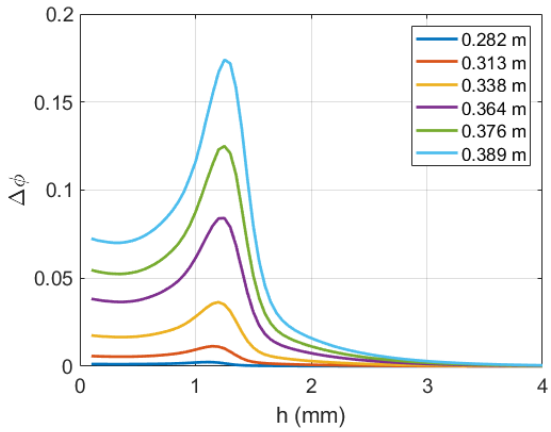

(b) $Re = 11.3 \times 10^6$/m at 240 kHz.

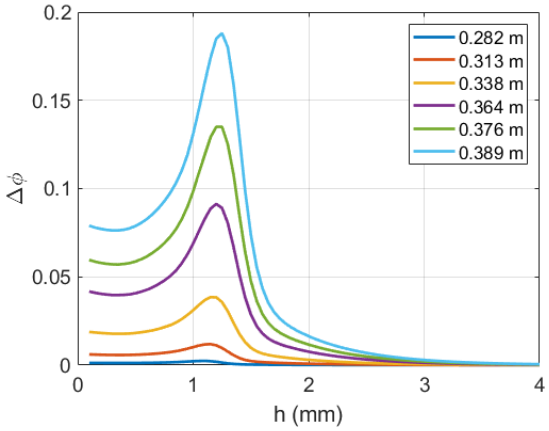

(c) $Re = 11.5 \times 10^6$/m at 245 kHz.

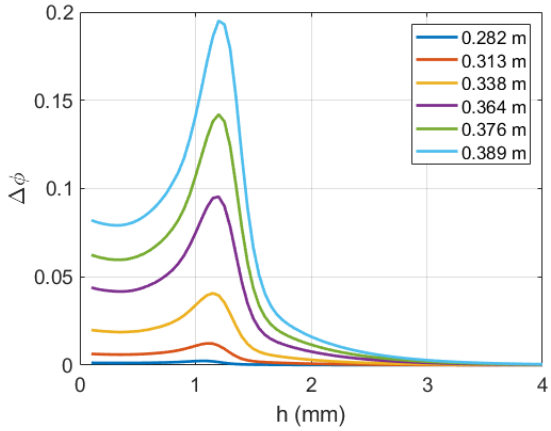

(d) $Re = 11.8 \times 10^6$/m at 250 kHz.

Figure 3.21. Computed FLDI beam phase changes (in radians) as a function of height off the model surface, at various downstream locations. In the experiment, the beams were located 0.376 m downstream of the nosetip.

3.2.2 7° Sharp Cone Apparatus

The Mark II 7° straight cone model was used for this test (see Section 2.3.1). The model was installed in the BAM6QT using the zero-degree angle-of-attack adapter which allows for small adjustments to model angle to more accurately zero the angle of attack (see Section 2.11).

Nine PCB sensors were installed to obtain pressure fluctuation measurements. PCBs 0 through 5 were near the bottom centerline at different downstream axial locations, while PCBs 6 through 8 were located in the same downstream location as PCB 5, but were offset from each other 90° azimuthally. Figure 3.22 displays these PCBs in the model. The FLDI beams were aligned at the same streamwise location as PCB 4, 0.376 m downstream of the nosetip.

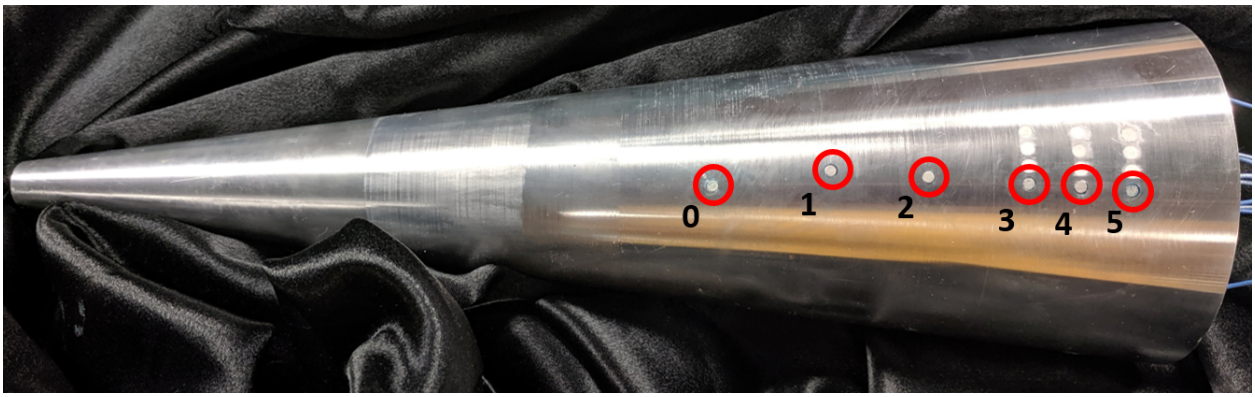

Figure 3.22. PCB sensors mounted in cone, nosetip removed

3.2.3 FLDI Apparatus

FLDI configuration D (see Section 2.4.4) was utilized for these tests. Figure 3.23 shows an illustration of where the FLDI beams were located relative to the model, with the distances between the beams and between the model and the beams being exaggerated. The two FLDI beams were located perpendicular to the flow and parallel to the floor (split in the y-z plane). The absolute offset from the model surface was determined by moving the beams towards the surface until they clipped on the model, and then shifting them slightly away. This absolute

distance is the largest source of uncertainty in the beam location measurement; the relative locations of the beams between runs is calibrated with the beam profiler and were measured to vary by less than 15 μm. Overall, the uncertainty in distance from the model surface, h, can be estimated to be the vertical length of the focal point, which is generally measured to be between 0.1 and 0.3 mm.

Figure 3.23. Illustration of FLDI beam placement relative to model, showing height off the surface, h. Not to scale.

Due to being split in the horizontal plane rather than parallel to the model surface, the upstream beam is slightly farther from the model than the downstream one. With an average streamwise width from upstream edge to downstream edge of about 200 μm, this difference in height from the model is approximately 25 μm, which is about an order of magnitude less than the uncertainty in absolute displacement. The streamwise beam alignment was made by drawing a line at the PCB downstream location on the model with a marker and moving the optical table until the laser hit that line. Once on the line, the optical bench was locked in position and the beams were shifted off of the model by adjusting the micrometers attached to M2 (the upper mirror on the laser side) and L2 (the cylindrical lens for vertical focusing).

3.2.4 Pressure Fluctuation Measurements

PCB sensors were installed at five different downstream positions as described in Sections 2.3.1 and 3.2.2. Power spectral densities of the pressure fluctuations from these sensors can be used to find the peak frequency of the second mode at the surface, as well as compute amplification rates. Figure 3.24 shows some sample PCB power spectral densities from a quiet run at $Re = 11.5 \times 10^6/\text{m}$. Moving downstream, the PCB fluctuations increased in amplitude and decreased in frequency, with the exception of 0.376 m, which decreased in

amplitude. The frequency peak for 0.282 m had an abnormal shape with lower-frequency hump in addition to its second mode peak. The cause of these abnormalities is unknown. As the purpose of this experiment (validating the FLDI) can be satisfied even with the irregularities, they were not investigated further.

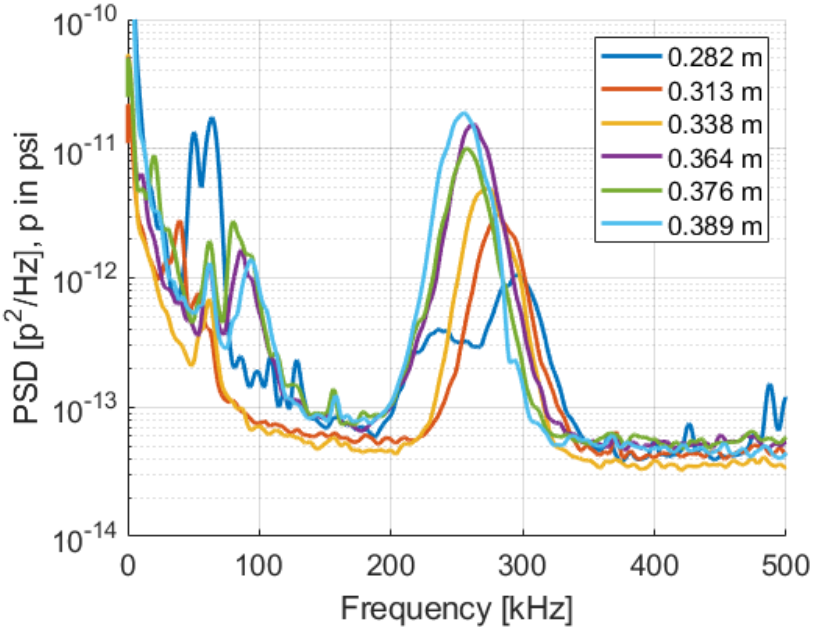

Figure 3.24. PCB power spectral densities for Run 0427, at $Re = 11.5 \times 10^6$/m.

From the pressure PSDs, the peak fluctuation frequency for each sensor can be extracted, as well as the amplitude of the pressure fluctuations. Figure 3.25 plots the STABL computed peak fluctuation frequencies along with the measured values for each of the four cases analyzed, obtained from the peak in computed N-factors. Note that multiple runs are plotted in each figure, with peak frequencies similar enough that they overlap. The STABL results show a stair-step pattern due to the finite number of frequencies analyzed. The noisy case at $Re = 6.74 \times 10^6$/m has excellent agreement between the measured and computed frequencies. The quiet cases have good agreement, with the measured frequencies being about 10 kHz above the computed ones. The reason for this discrepancy is unknown, although there are several possible causes. For example, there Mach number or angle of attack uncertainties. While the second-mode peak frequencies under conventional noise were within 1.5% of the mean, under quiet flow they increased to nearly 7%. Additionally, the physical model

has a finite-radius nosetip that was not modeled in the STABL computations. Despite this discrepancy, PCB most amplified frequencies for all cases were within 5% of the computed values and were consistent across runs.

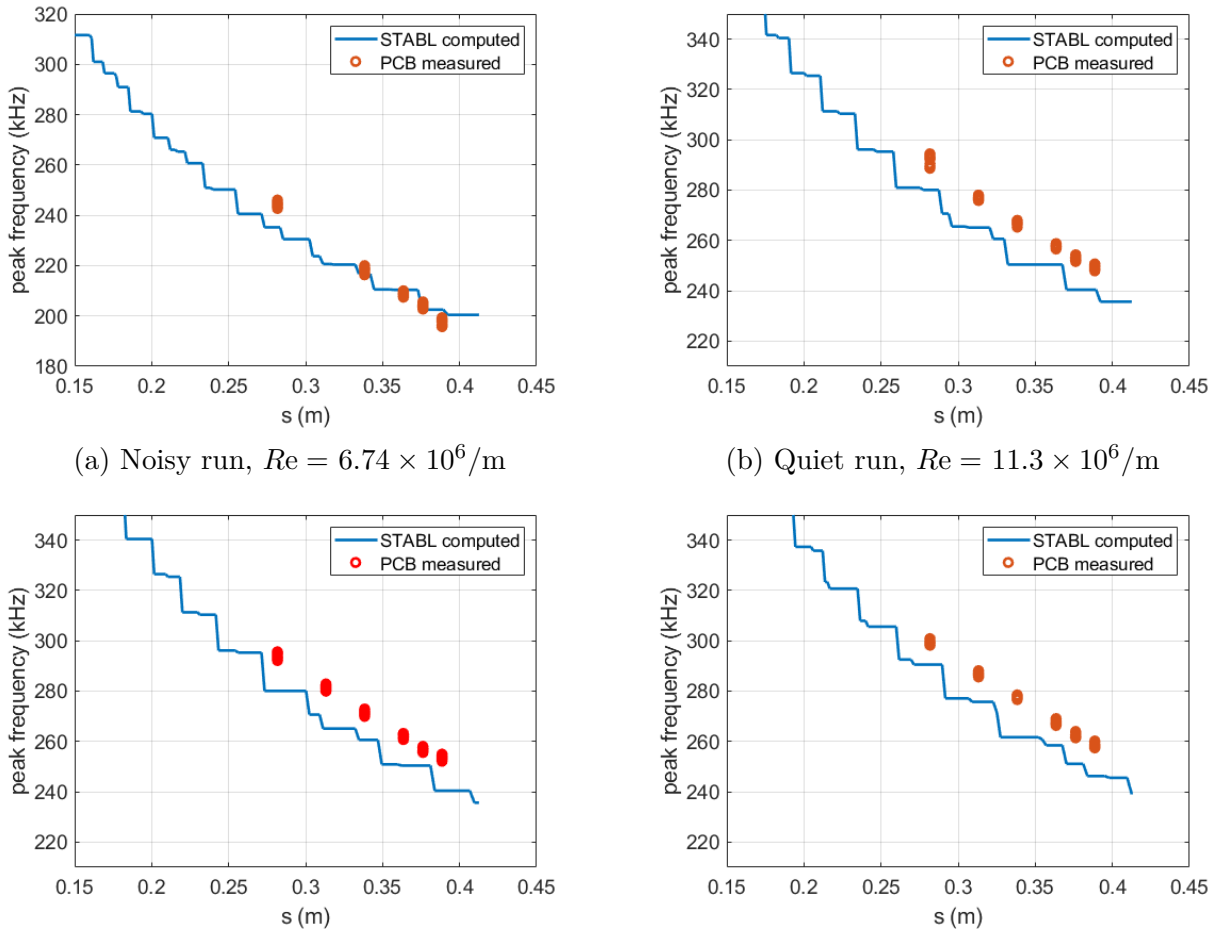

(a) Noisy run, $Re = 6.74 \times 10^6/\text{m}$

(b) Quiet run, $Re = 11.3 \times 10^6/\text{m}$

(c) Quiet run, $Re = 11.5 \times 10^6/\text{m}$

(d) Quiet run, $Re = 11.8 \times 10^6/\text{m}$

Figure 3.25. Computed and measured second mode peak frequencies

Figure 3.26 plots the logarithm of the ratio between measured pressure fluctuations and computed static surface pressures as well as the computed N-factors for each case. The computed linear analysis was offset to align with the measured values 0.376 m downstream of the nosetip, but has the same scaling as the pressure ratios. The wall pressure was computed from STABL. The noisy case at $Re = 6.74 \times 10^6/\text{m}$ appears to have a similar slope between the measured ratio and the computed N-factors. However, the quiet cases all have lower slopes than computed values, indicating a slower amplification from the measurements.

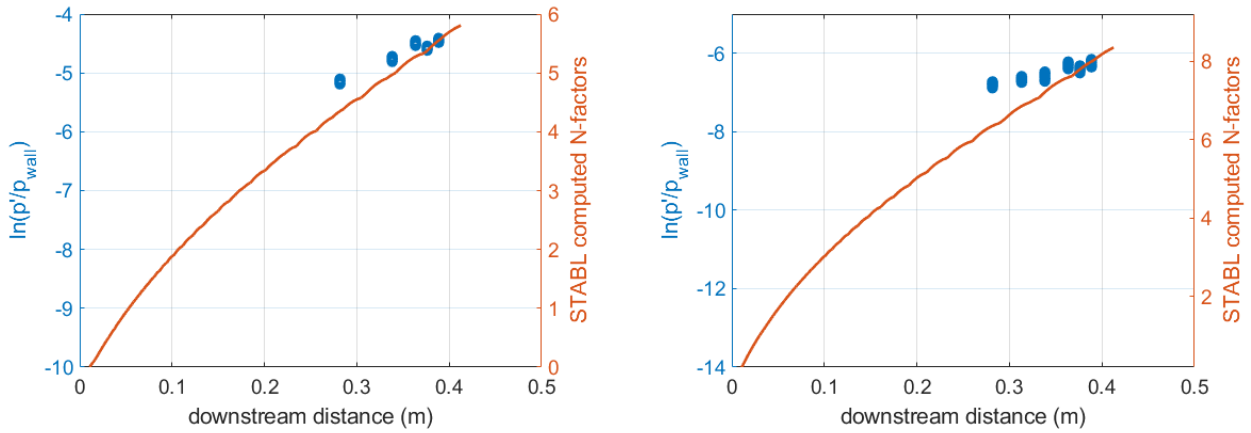

(a) Noisy run, $Re = 6.74 \times 10^6/\text{m}$

(b) Quiet run,$Re = 11.3 \times 10^6/\text{m}$

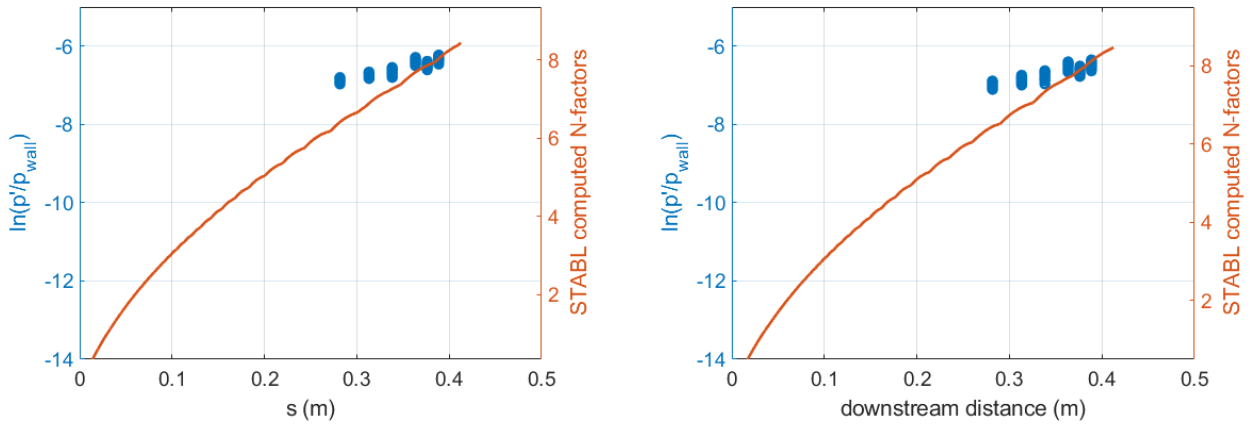

(c) Quiet run, $Re = 11.5 \times 10^6/\text{m}$

(d) Quiet run, $Re = 11.8 \times 10^6/\text{m}$

Figure 3.26. Computed second mode N-factors compared to measured amplitude ratios

3.2.5 FLDI Fluctuation Measurements

FLDI measurements were made in both quiet flow and under conventional noise. The results were compared to PCB fluctuation measurements at the same downstream distance, as well as to the computed estimates.

3.2.5.1 Measurements under Conventional Noise

Measurements under conventional noise were taken in the BAM6QT with the bleed slots closed, so that the turbulence level in the tunnel is similar to that found in conventional (not quiet) hypersonic tunnels. These measurements were made at a stagnation pressure of

80 psia (corresponding to a unit Reynolds number of 6.74×10^6/m). The FLDI beams were positioned between 0.00 mm and 2.60 mm off the surface of the model at a downstream distance of 0.376 m from the nosetip at their midpoint.

Initial validation of the FLDI involved checking that the peak frequency measured in the density fluctuations matched that measured by the PCB at the same downstream location. Figure 3.27 plots the PCB and FLDI data from one of these runs, clearly showing the agreement in peak frequencies between the two signals.

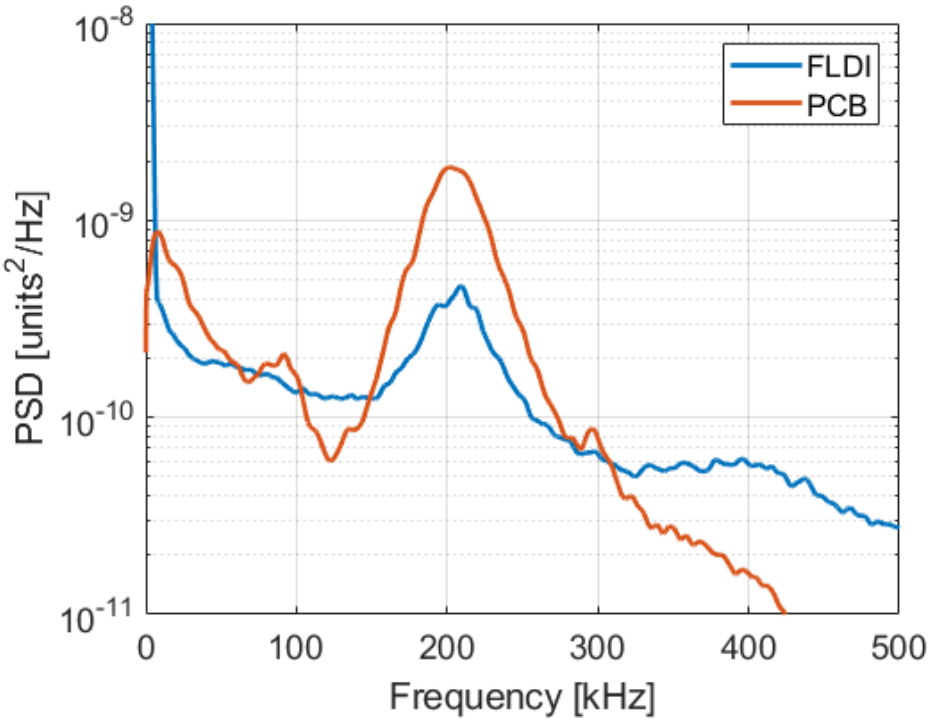

Figure 3.27. PCB fluctuations plotted with FLDI fluctuations showing second mode peak at the same frequency, from Run 0412. Units for the PCB pressures are psi, while for the FLDI phase shifts are radians.

The PCB and FLDI power spectral densities from a small range of unit Reynolds numbers within a single run are shown in Figure 3.28. The FLDI beams were located 1.39 mm off-surface and 0.376 m downstream for these plots. This location is where the frequency peaks from the FLDI were near the maximum amplitude. For both the PCB and the FLDI results, an increase in unit Reynolds number generally corresponded to an increase in both peak

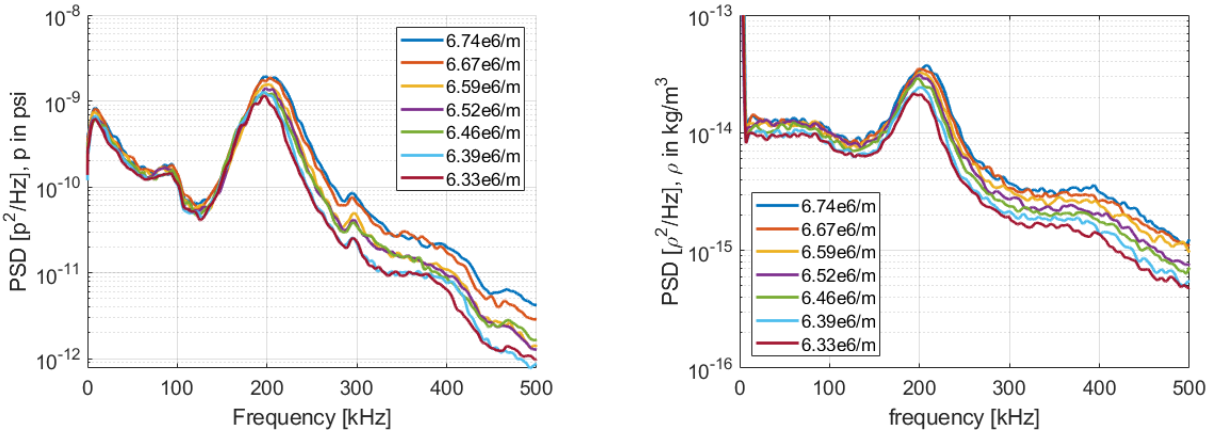

(a) PCB PSDs

(b) FLDI PSDs (1.39 mm off the surface)

Figure 3.28. Noisy PSDs from Run 0416 at Re between 6.33×10^6 and 6.73×10^6/m

frequency and amplitude. The peak frequencies of the PCB and FLDI were within 3 kHz of each other for a given Re.

The similarity in peak frequencies for the PCB and FLDI is highlighted in Figure 3.29a. The peak frequencies increase with increasing Reynolds number for both sets of measurements. Figure 3.29b plots the integrated peak amplitudes normalized by the computed wall pressure (for PCB data) or edge density (for FLDI data, here shown 1.39 mm off the surface). The peaks were integrated from 125 to 300 kHz, and the fluctuations increase in magnitude relative to the computed mean values as the Reynolds number increases.

Next, the change in fluctuation amplitude with distance from the model surface was measured with the FLDI, and compared to the STABL computations. Figure 3.30a displays the FLDI power spectral densities plotted on the same axes, while Figure 3.30b plots them as a function of distance from the model, h. The peak frequency of 205 kHz can be seen in each PSD until about 2.25 mm off the surface. Figure 3.31 plots the integrated peak amplitudes from the FLDI data (integrated between 150 and 250 kHz) against the computed STABL values, with the computed values scaled by the maximum measured value. This scaling was required because the actual initial disturbance amplitude (A_0) cannot be measured (as it is below the noise floor of the sensors), so the linear STABL calculations must assume a value for A_0. Scaling the STABL amplitudes therefore compensates for this input uncertainty.

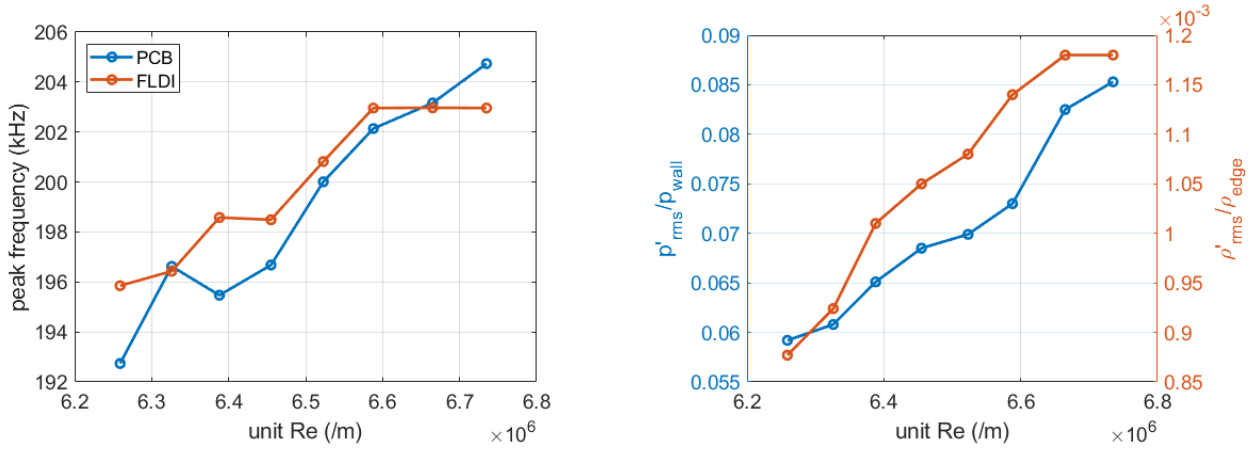

(a) Peak frequencies as a function of unit Reynolds number.

(b) Normalized peak amplitudes as a function of unit Reynolds number.

Figure 3.29. Peak frequencies and amplitudes as a function of unit Reynolds number in conventional noise for PCB and FLDI measurements. Note that the density fluctuation measurements from the FLDI assumes constant density along the integration length, and were taken 1.39 mm off the surface.

While the general shape and location of the peak FLDI phase change coincided between the measurements and the computed estimate, the agreement is not as close as with the quiet results (Section 3.2.5.2). This discrepancy may be due to a shorter azimuthal coherence length for the second mode waves under this conventional noise flow, particularly if the measurements are outside of the second-mode linear growth region.

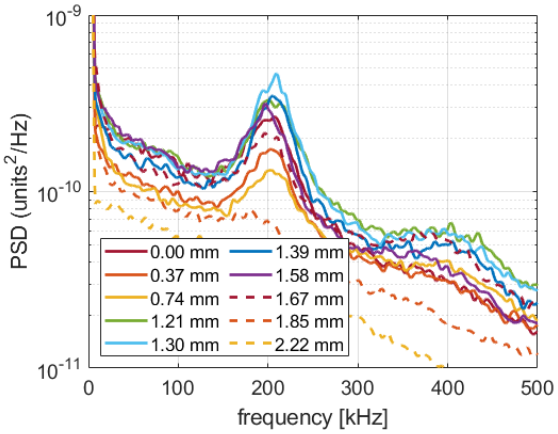

(a) PSDs plotted on the same axes to highlight consistent peak frequencies with varying peak amplitudes.

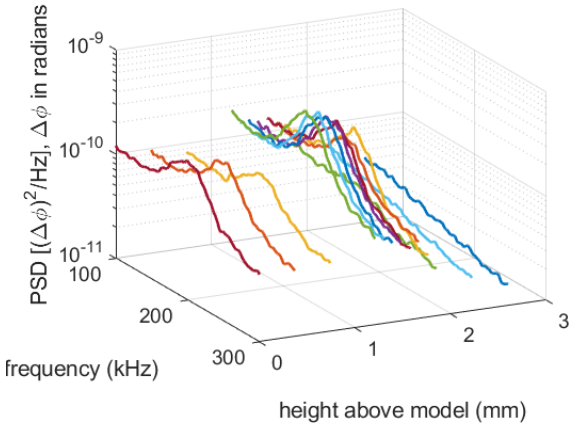

(b) PSDs plotted as a function of distance from the model surface.

Figure 3.30. FLDI phase change power spectral densities from noisy flow with $Re = 6.7 \times 10^6$/m ($P_0 = 80$ psia). From Runs 0404-0407, 0410-0417.

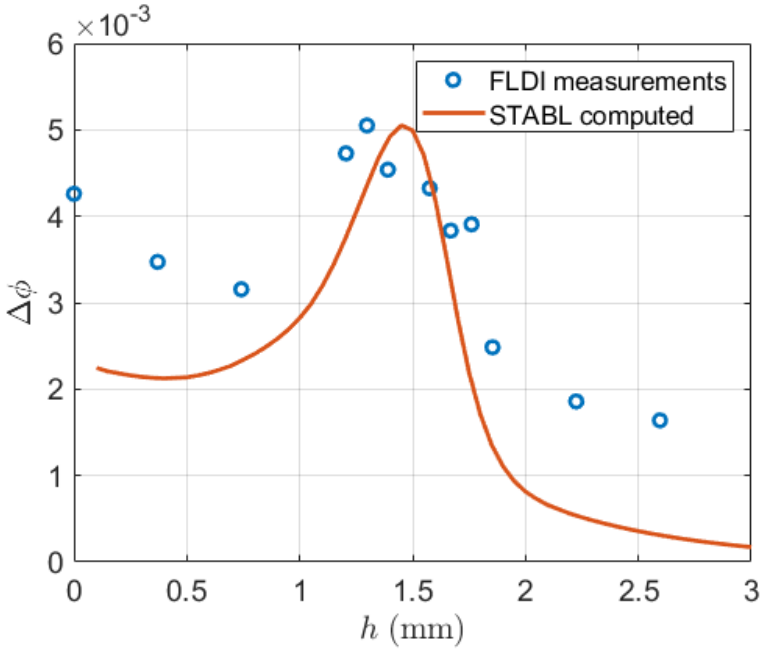

Figure 3.31. Measured FLDI phase change, from peak amplitude integrated between 150 and 250 kHz, at each height above the model plotted with scaled computed FLDI phase change. $\delta = 1.99$ mm.

3.2.5.2 Measurements under Quiet Flow

The FLDI measurements were repeated for a set of quiet runs, at stagnation pressures of 130, 135, and 140 psia (Reynolds numbers of 11.3×10^6, 11.5×10^6, and 11.8×10^6/m, respectively). The FLDI beams were positioned between 0.00 and 2.22 mm off the surface. The thinner boundary layer at these higher stagnation pressures causes the second mode peak frequency to be higher, which can be seen in the PCB and FLDI results. The three selected unit Reynolds numbers were obtained from the same set of runs, by extracting data from different times during each run as the stagnation pressure dropped. Prior to this set of runs, the optical table was shifted slightly. Unfortunately, this shift moved the beams slightly upstream of the PCB location, which resulted in the FLDI signal having a higher frequency at the peak than the associated PCB. Figure 3.32 displays a sample of each PSD from the FLDI and the PCB, showing close but not identical frequency peaks. The FLDI peak is not as aligned with the PCB peak in the quiet cases which may be due to uncertainty introduced by a shift of the optical table before the quiet runs but after the noisy ones. The beams were located 1.25 mm off the model surface.

Figure 3.33 plots the PCB and FLDI signals at various unit Reynolds numbers during a single run. As with the noisy case, both the PCB and FLDI data follow the same trends with Reynolds number. However, unlike the noisy cases, in the quiet runs an increase in Reynolds number corresponded to an increase in peak frequency but a decrease in peak amplitude. The reason for this change is unknown, as the spectra do not appear transitional.

The peak frequencies are plotted in Figure 3.34a. A constant offset of about 10 kHz can be seen between the PCB and FLDI frequencies, likely due to the optical bench shift previously mentioned. As in the conventional noise case, the peak frequencies increase with increasing unit Reynolds number. However, for the quiet runs, the peak amplitudes decrease with increasing unit Reynolds number. This decrease in amplitude was observed for all quiet runs in both the PCB and FLDI data, and is potentially an indication that the sensor location might be downstream of the maximum second mode magnitude [68]. Figure 3.34b plots the integrated peak amplitudes from Figure 3.33 as a function of unit Reynolds number.

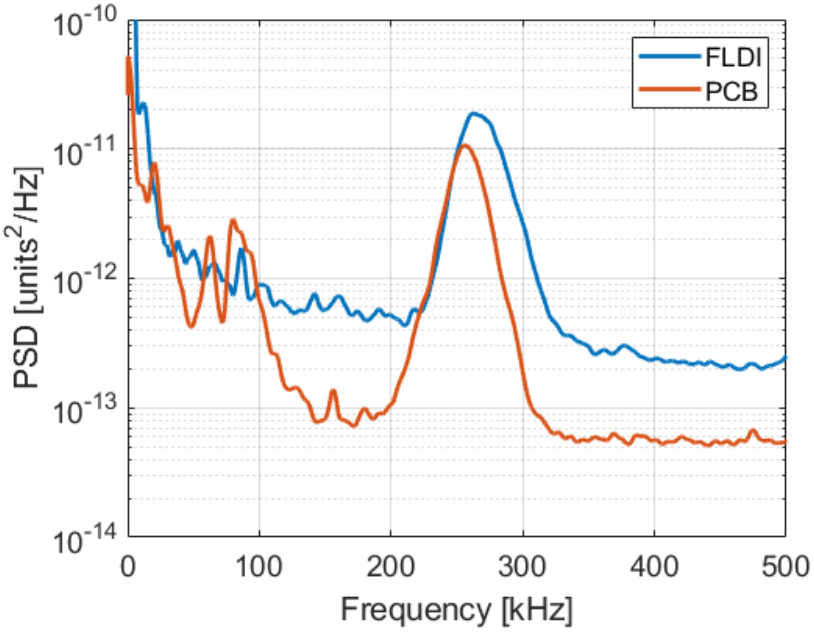

Figure 3.32. PCB fluctuations plotted with FLDI fluctuations showing second mode peak at similar frequencies 0.376 m downstream of the nosetip. From Run 0427.

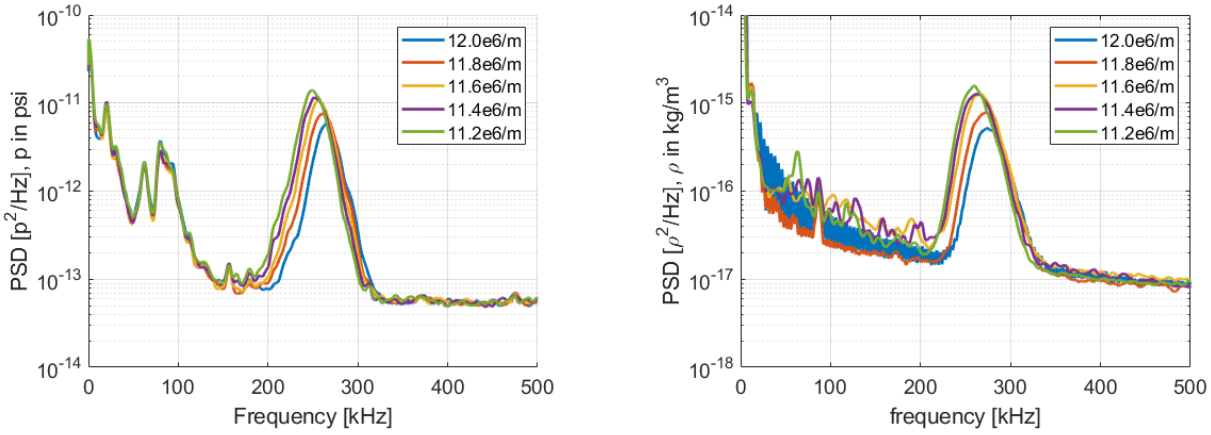

(a) PCB PSDs

(b) FLDI PSDs (1.25 mm off the model surface)

Figure 3.33. Quiet PSDs from Run 0427 for Re between 11.2×10^6 and 12.0×10^6/m

Figures 3.35 through 3.37 show the FLDI and PCB PSDs as they vary with height above the surface of the model, h. A clear increase followed by a sharp decrease in peak amplitude is observed as h increases. The PSDs are plotted in a 2-dimensional view in Figure 3.38

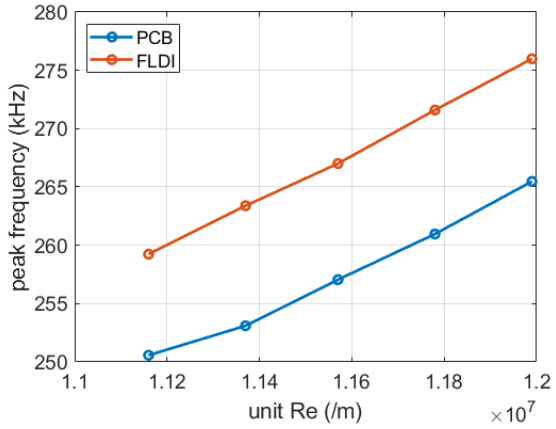

(a) Peak frequencies as a function of unit Reynolds number.

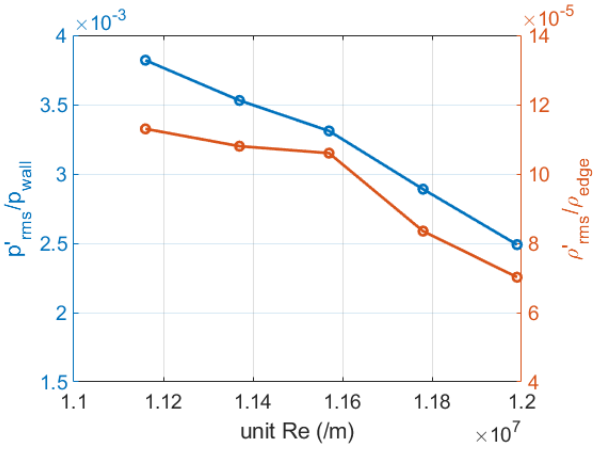

(b) Normalized peak amplitudes as a function of unit Reynolds number (1.25 mm above the wall).

Figure 3.34. Peak frequencies and amplitudes as a function of unit Reynolds number in quiet flow for PCB and FLDI measurements. Note that the density fluctuation estimation from the FLDI assumes constant density across the integration length.

to highlight the constant peak frequency for each unit Reynolds number for various heights above the model. At $Re = 11.3 \times 10^6$/m, the peak is centered at 260 kHz, while at $Re = 11.5 \times 10^6$/m it is at 265 kHz and at $Re = 11.8 \times 10^6$/m it is at 270 kHz. The PCB peak frequency near the downstream location of the FLDI was at 253, 257, and 262 kHz, respectively, for the three Re values. The PCB PSDs for a stagnation pressure of $Re = 11.5 \times 10^6$/m are shown in Figure 3.38d, demonstrating that the instabilities observed in the flow at the surface remained the same throughout each of the runs. A similar result was observed in the PCB data for the other two unit Reynolds numbers studied. Since the PCB spectra for surface pressure fluctuations at the same downstream location did not vary during the same runs, the variation in FLDI peak amplitude was most likely due to changing amplitudes at different distances from the model surface, as opposed to any aerodynamic change of the flow between runs. Overall, the FLDI integrated RMS values varied by up to 97% from the mean, while the PCB values remained within 18%.

The RMS amplitudes of the frequency peaks (integrated between 220 and 320 kHz) are plotted against the computed estimates for each unit Reynolds number in Figures 3.39a

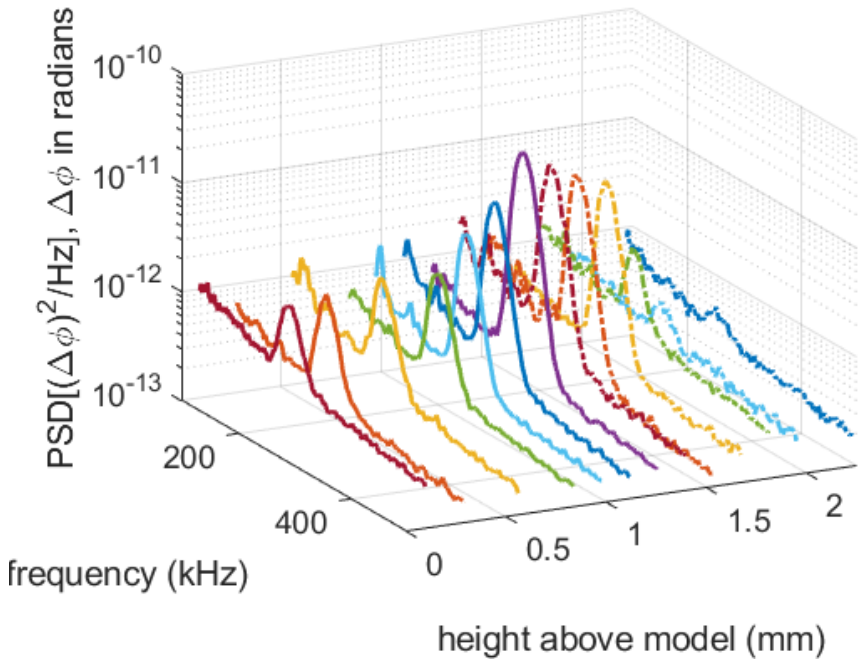

Figure 3.35. FLDI phase change PSDs from quiet flow 0.376 m downstream. $Re = 11.3 \times 10^6/\text{m}$ and $\delta = 1.68$ mm.

through 3.39c. As with the conventional noise case, the computed data was scaled so that the peak was at the same total phase change value as the measured peak. Again, this scaling helps account for the unknown value of the initial disturbance, which cannot be measured but will have an effect on the downstream amplitudes. The measured data agrees well with the computed estimates both in terms of peak location off the surface and general shape of the function. Measured peaks (found by fitting a parabola to the data) occurred at 1.34 mm for $Re = 11.3 \times 10^6/\text{m}$, 1.30 mm for $Re = 11.5 \times 10^6/\text{m}$, and at 1.28 mm for $Re = 11.8 \times 10^6$. Computed peaks were estimated at 1.30 mm for $Re = 11.3 \times 10^6/\text{m}$, 1.25 mm for $Re = 11.5 \times 10^6/\text{m}$, and 1.20 mm for $Re = 11.8 \times 10^6/\text{m}$. The differences correspond to percent errors for peak location of 6.7%, 4.0%, and 3.1%, respectively. The measured data did not reach zero as the computed data did because the noise floor was reached for measurements above 2.22 mm off the surface. As in the noisy case, discrepancies may be due to second-mode waves that are shorter than the FLDI integration length. Additionally,

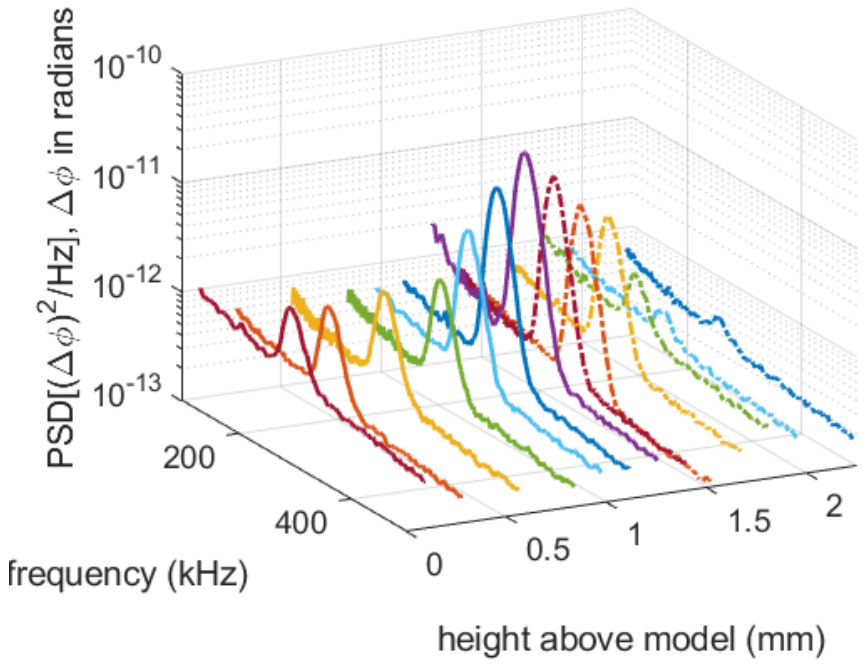

Figure 3.36. FLDI phase change PSDs from quiet flow 0.376 m downstream. $Re = 11.5 \times 10^6$/m and $\delta = 1.65$ mm.

these computations were done using LST, different results may be obtained if PSE was used instead.

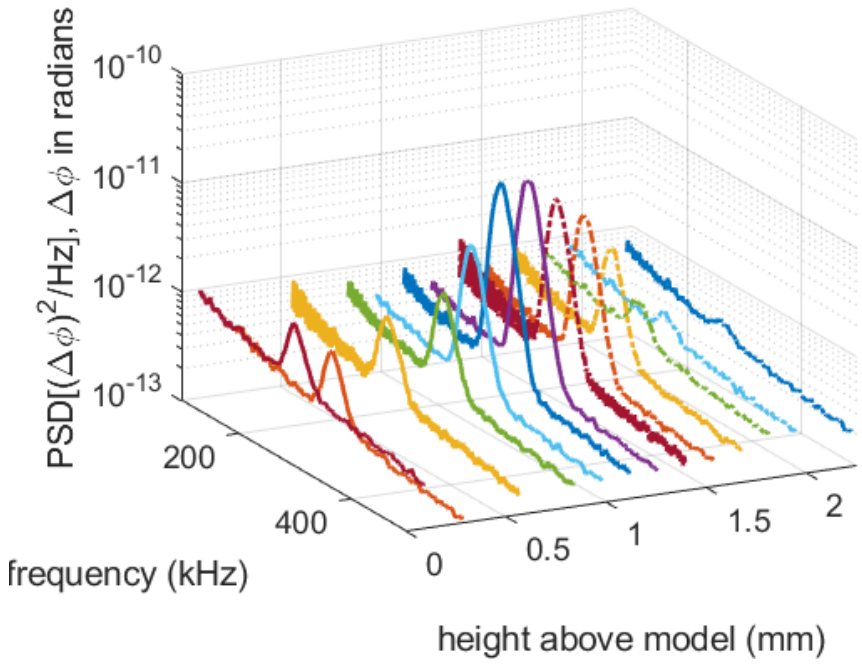

Figure 3.37. FLDI phase change PSDs from quiet flow 0.376 m downstream. $Re = 11.8 \times 10^6/\text{m}$ and $\delta = 1.63$ mm.

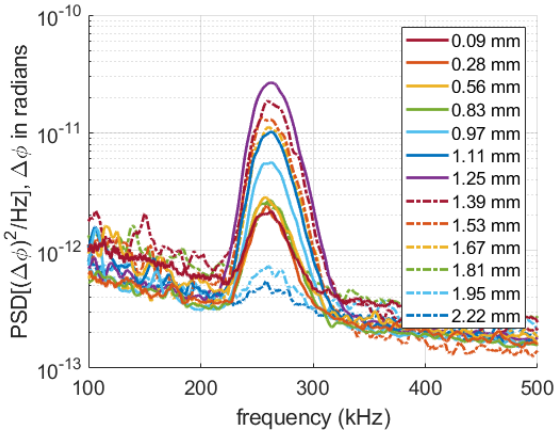

(a) $Re = 11.3 \times 10^6/\text{m}$

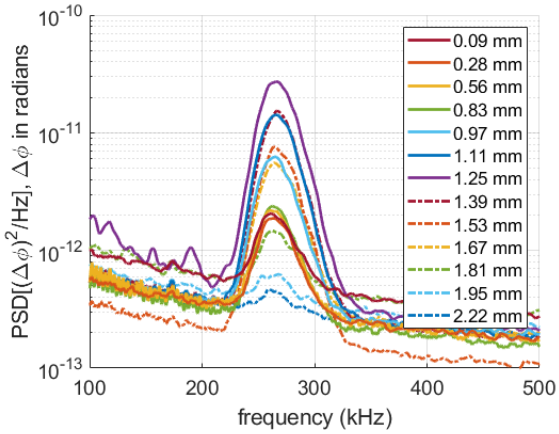

(b) $Re = 11.5 \times 10^6/\text{m}$

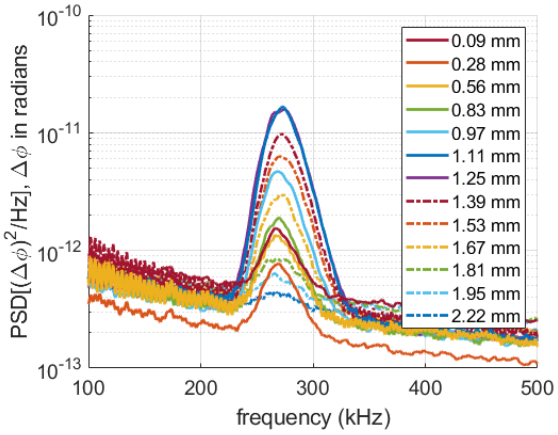

(c) $Re = 11.8 \times 10^6/\text{m}$

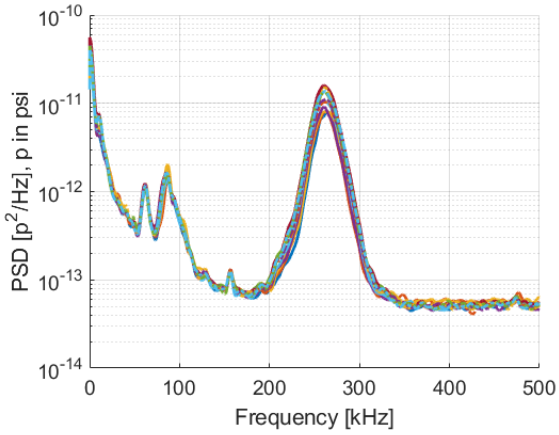

(d) PCB PSDs at $Re = 11.5 \times 10^6/\text{m}$

Figure 3.38. Quiet PSDs showing varying peak amplitude (for the FLDI cases) but constant peak frequency at a given unit Reynolds number.

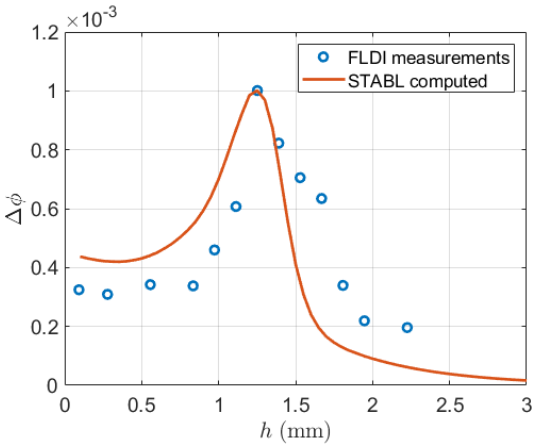

(a) $Re = 11.3 \times 10^6/\text{m}$

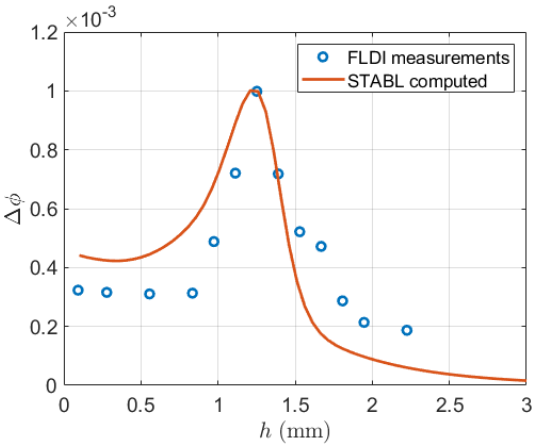

(b) $Re = 11.5 \times 10^6/\text{ma}$

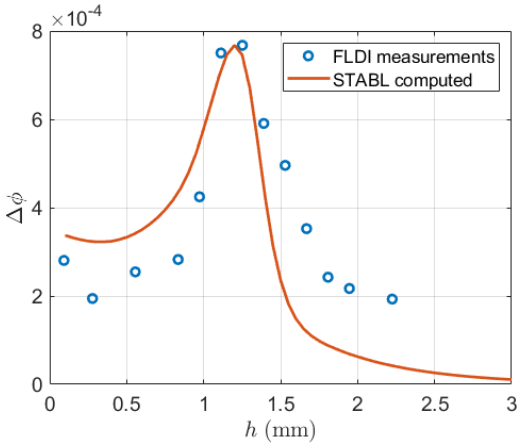

(c) $Re = 11.8 \times 10^6/\text{m}$

Figure 3.39. FLDI phase change amplitudes from quiet flow with comparison to scaled computed values. Integrated between 220 and 320 kHz.

3.2.6 FLDI Harmonic Peaks

The FLDI has a higher frequency response than the PCB sensors, allowing it to measure high-frequency broadband signals as well as their first harmonics. Figure 3.40 shows a noisy and quiet example, with both PCB and FLDI signals from before (to establish the noise floor) and during a run. In the noisy case (Figure 3.40a), clear peaks at 205 kHz are observed in both the PCB and FLDI results. However, the PCB signal drops down to the prerun noise levels by around 800 kHz, while the FLDI signal remains above that level until over 2 MHz. The rapid decline in signal with frequency for the PCB measurements also hides the small harmonic peak seen near 410 kHz in the FLDI data. For the quiet case (Figure 3.40b), outside of the second mode peak at 255 kHz, the PCB signal remains at the prerun noise floor. The FLDI signal, however, is above the prerun noise for the second mode frequency peak at 265 kHz as well as for its first harmonic at 530 kHz.

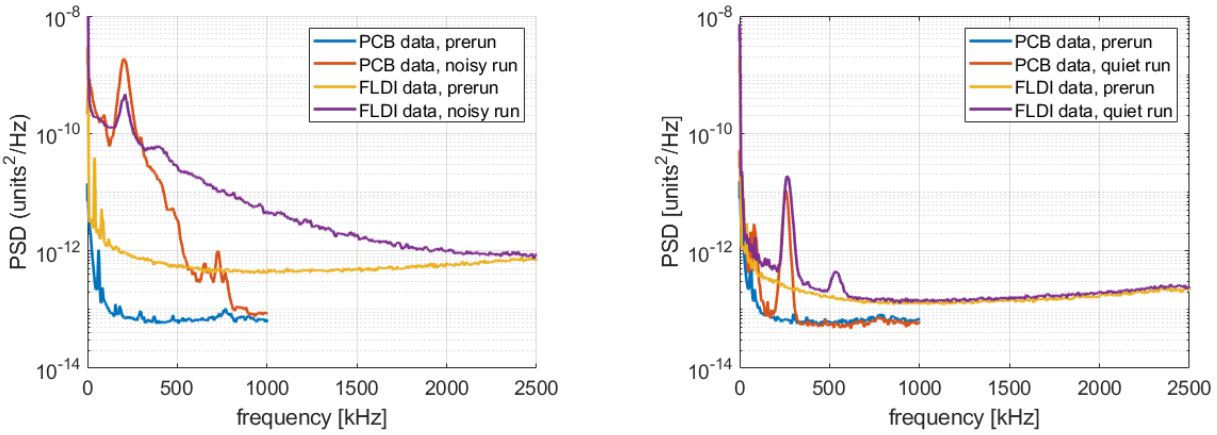

(a) Noisy run, $Re = 6.74 \times 10^6/\text{m}$ (Run 0412) (b) Quiet run, $Re = 11.5 \times 10^6/\text{m}$ (Run 0427)

Figure 3.40. High-frequency comparison of PCB and FLDI measurements

3.2.7 Disturbance Velocity and Phase

The PCBs and the FLDI are measuring the same sinusoidal instabilities, with the PCBs measuring the pressure fluctuations and the FLDI measuring the optical phase change between the interferometer's beams (which is related to the density fluctuations). Thus, their signals can be cross-correlated to measure the lag time between them. Figure 3.41 plots

these cross-correlations between each individual PCB and the FLDI. The FLDI signal was first high-pass filtered at 11 kHz (the same filtering that the PCB signals have) prior to computing the cross-correlation.

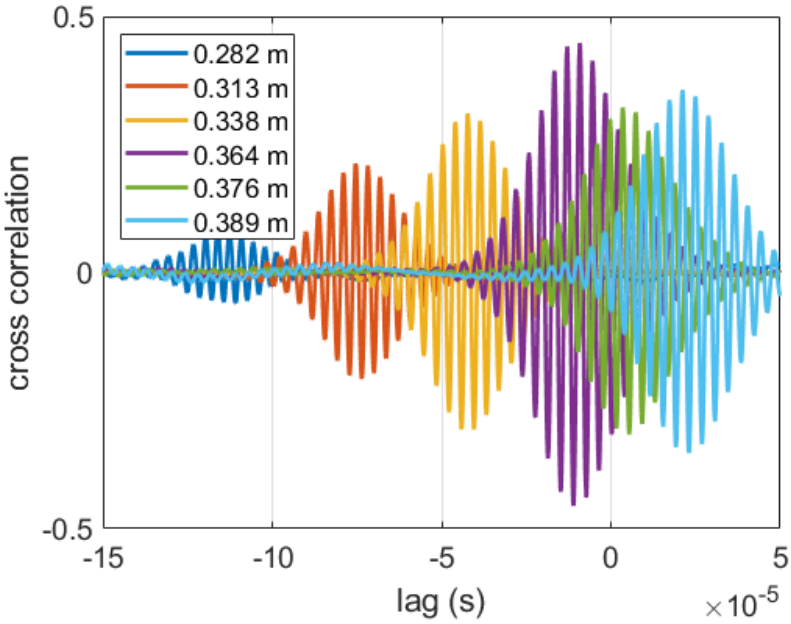

Figure 3.41. Cross-correlation between measurements from PCBs and the FLDI around $Re = 11.5 \times 10^6$/m, from Run 0427. The FLDI was aligned with PCB 4, 0.376 m downstream.

The lag time at the point of maximum cross-correlation increases moving downstream. The PCB 0.376 mm downstream, with which the FLDI was notionally aligned, has the lag closest to 0 seconds. The relationship between lag time and PCB location downstream was highly linear, as can be seen in Figure 3.42. This relationship can be used to estimate the disturbance velocity of the flow. A linear fit of the data results in a slope of 1.28×10^{-3} s/m, which corresponds to a disturbance velocity of 781 m/s in the downstream direction. This value is 89% of the freestream velocity, and 93% of the computed edge velocity, which is typically of the second mode on a sharp cone. Repeating this analysis by cross-correlating the PCB sensors to the PCB located 0.376 m downstream, a disturbance velocity of 777 m/s was computed. This is within 0.5% of the value found by cross-correlating the PCBs with the FLDI.

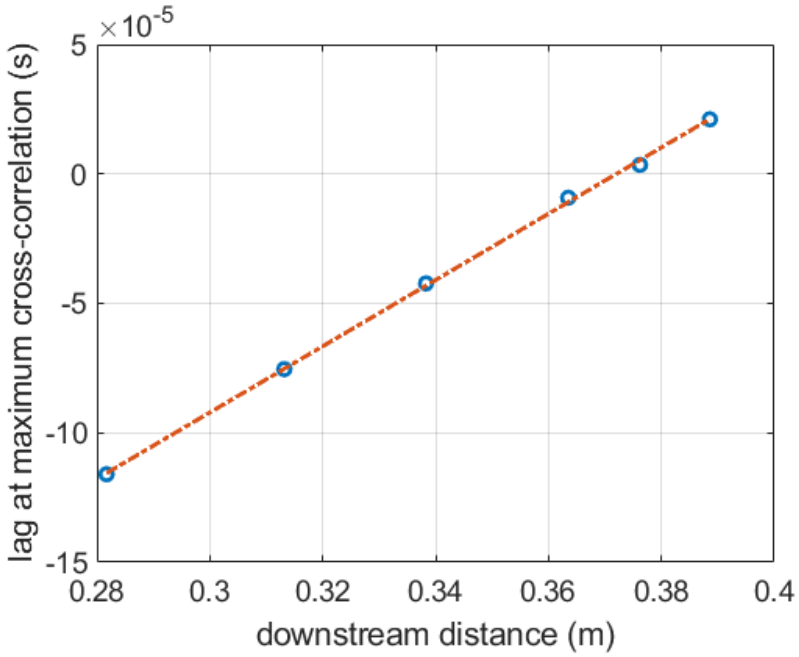

Figure 3.42. Lag times at maximum cross-correlation between measurements from PCBs and the FLDI as a function of PCB downstream distance at $Re = 11.5 \times 10^6/\text{m}$, from Run 0427.

Since the FLDI allows for measurements away from the model surface at the same downstream position as a PCB sensor, a disturbance phase shift as a function of the distance from the model can also be computed. This computation is made by cross-correlating the FLDI signal with the PCB one and looking at the lag time at maximum cross-correlation. Figure 3.43 plots the maximum cross-correlation values and the disturbance phase shift at those points for the quiet flow case at $Re = 11.5 \times 10^6/\text{m}$. In both plots, data points corresponding to cross-correlation values greater than 0.1 are highlighted in red; these were the points that best matched the computed disturbance phase shift. Figure 3.43a shows the peak cross-correlation amplitude as a function of distance from the model, while Figure 3.43b plots the phase shift of the aerodynamic disturbance. The disturbance phase shifts between the PCB and FLDI signals can be computed from these lag times by scaling them by 360° times the frequency of the instability (here 260 kHz) and modulating the results to be between -180° and 180°. When the cross-correlation is high enough to have confidence in

the lag time, there is excellent agreement between the measured and computed phase shift of the second-mode instability.

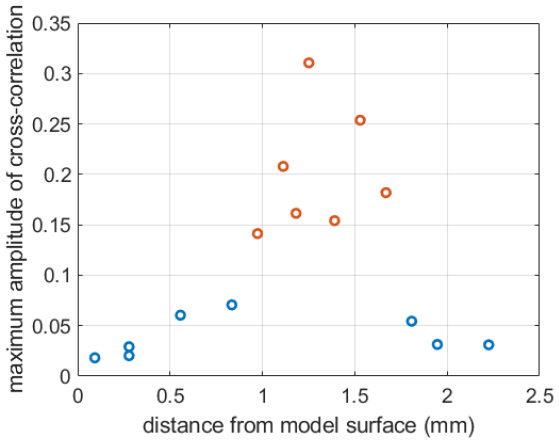

(a) Cross-correlation between measurements from PCB and FLDI measurements around $Re = 11.5 \times 10^6/\text{m}$ at the same downstream position

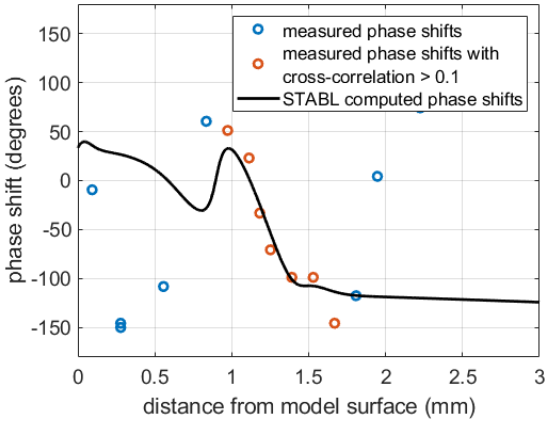

(b) Phase shift of the aerodynamic instability, from PCB and FLDI measurements as a function of FLDI distance from the model surface

Figure 3.43. Cross-correlation and phase shift of the second mode in quiet flow.

The analysis was repeated with the conventional noise data. Good agreement was again found between the measured and computed disturbance phase shift when the peak cross-correlation was sufficiently high.

The excellent agreement between the computed phase shifts with the measured values provides further support for the validity of the BAM6QT FLDI. Additional evidence to support this apparatus was seen with the similar peak frequencies between the FLDI and PCB sensor and the agreement in location of peak fluctuations between the FLDI measurements and the STABL computations. Finally, the disturbance speed computed with the FLDI that is nearly identical to that computed with just the PCBs, and which fits with the expected second-mode group velocity, also offers strong support for the use of this FLDI to obtain hypersonic density-fluctuation measurements in the BAM6QT.

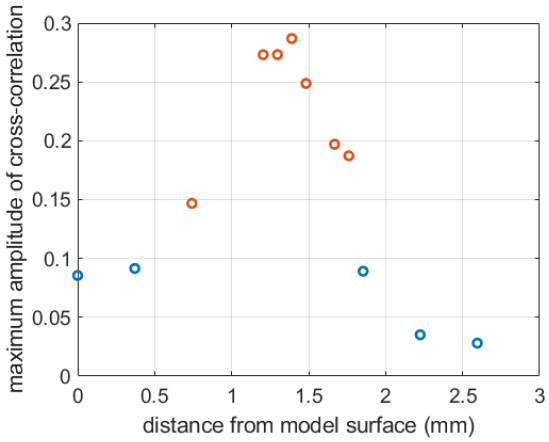

(a) Cross-correlation between measurements from PCB and FLDI measurements around $Re = 6.74 \times 10^6$/m at the same downstream position

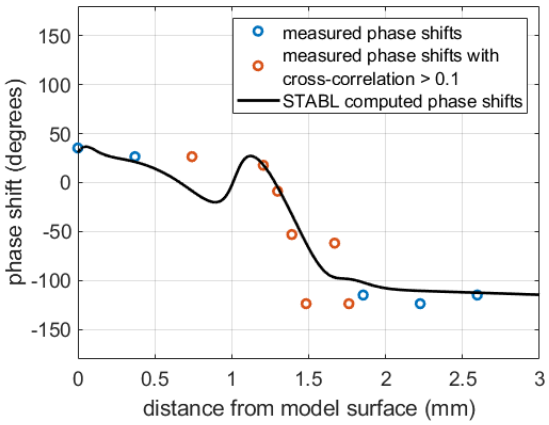

(b) Phase shift of the aerodynamic instability, from PCB and FLDI measurements as a function of FLDI distance from the model surface

Figure 3.44. Cross-correlation and phase shift of the second mode in conventional noise.

3.2.8 FLDI Measurement Repeatability

Establishing the repeatability of measurements is important to instill confidence in a new measurement method. For the FLDI, a couple of cases were run at the same tunnel conditions with the FLDI in the same position relative to the model to check if the computed phase change would be the same. Figure 3.45 shows these results taken during quiet runs at a unit Reynolds number of 11.5×10^6/m.

For each of these locations off the model surface, two runs were made on two separate days. The model remained at the same position between the runs. The peak frequencies for each of these runs were very repeatable, and generally found to be within 2 kHz of each other. The amplitude repeatability was fair, with the RMS values integrated between 200 and 350 kHz having differences of 11.7% and 7.8% for the 0.28 mm and 1.39 mm cases, respectively, with respect to the mean amplitude. For comparison, the difference for the PCB integrated amplitudes between runs 0418 and 0429 was 8.3%.

Part of the variability in repeatability may be due to model vibration. Models are not entirely stationary throughout a run, but tend to oscillate during and after startup. This vibration can be seen as model translations in IR and schlieren images. As the FLDI signal is

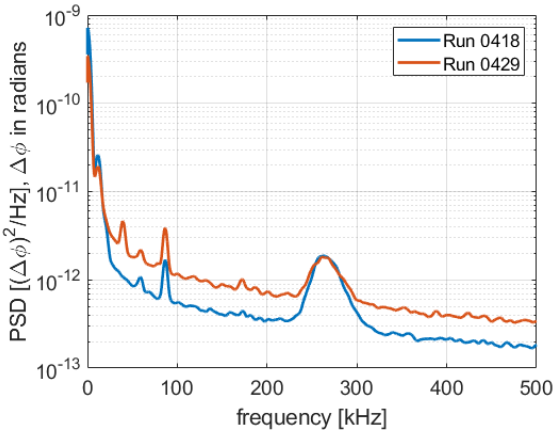

(a) 0.28 mm off the model surface, Runs 0418 and 0429

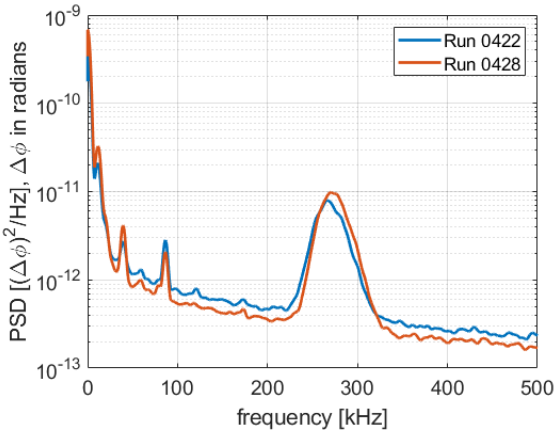

(b) 1.39 mm off the model surface, Runs 0422 and 0428

Figure 3.45. FLDI PSDs from runs at the same conditions to demonstrate repeatability. $Re = 11.5 \times 10^6/\text{m}$

dependent on the distance from the model surface, if the surface moves relative to the beams the signal magnitude will also change. However, since vibrations are generally fast enough to include several cycles than the 0.1 seconds of data analyzed at a time, these variations should average out. See Section 5.2.1.1 for more information.

Another issue in repeatability is the validity of the FLDI calibration voltages during the course of the run. The calibration voltages are measured immediately prior to filling the tunnel and then used to convert the FLDI data to phase change or density fluctuation values. Prior to pressurization, the second Wollaston prism is shifted such that the photoreceiver voltage is at 0. While the tunnel fills, it was observed that this voltages gradually increases or decreases, leaving the linear range of the interference curve, until pressurization is complete. It is believed that the minute changes in window shape that occur as the tunnel pressure increases causes this shift in voltage. However, once the run is initiated, the average voltage generally returns to 0, placing it back in the linear region of the fringe, as the window shape is generally restored.

3.2.9 Summary of 7° Cone Results

To validate the performance of the BAM6QT FLDI with the tunnel, a well-understood canonical geometry was selected for initial testing. A 7° sharp cone at 0.0° angle of attack at Mach 6 creates a flow that is well studied. DPLR was used to compute the flow and STABL was used to compute the stability properties at four different unit Reynolds numbers. The computed eigenfunctions were extracted and used to estimate the relative FLDI beam phase shifts. The model was also instrumented with PCB sensors. The FLDI beams were adjusted to be 0.376 m downstream of the nosetip, near the streamwise position of PCB 4.

The model was run in both quiet flow and under conventional noise, with the FLDI beams at different distances from the surface. The peak frequency observed in the FLDI agreed well with the peak frequency measured by PCB 4. Variation in peak amplitude was observed as the FLDI beams were moved away from the surface. In quiet flow, the resulting FLDI power spectral densities contained a distinct peak between 1.11 and 1.39 mm depending on the unit Reynolds number, which agrees well with the computed estimates. For the same runs, the PCB peak amplitudes remained constant. Cross-correlating the PCB and FLDI signals provided an estimated disturbance velocity of around 89% of the freestream velocity for quiet flow at $Re = 11.5 \times 10^6/\text{m}$. Disturbance phase shifts measured by taking the lag at maximum cross-correlation between the FLDI and PCB 4 also agreed well with computed values for both noisy and quiet flow.

Excellent repeatability in terms of peak frequency was achieved with the FLDI, while peak amplitude repeatability was fair. Overall, the FLDI has been demonstrated to provide measurements of the off-the-surface density fluctuations that have good agreement with computed values for a well-documented flow.

4. CONE-CYLINDER-FLARE MEASUREMENTS WITH THE 3.5° FLARE

The 3.5° cone-cylinder-flare model was used to study how an axisymmetric compression corner without separation affects the flow. This chapter discusses measurements made with this non-separating model. It should be noted that all quiet runs for this analysis provided primarily laminar flow with transition only potentially occurring at the very end of the model. Even up to the maximum quiet unit Reynolds number (around 12×10^6/m), clear second-mode peaks were observed amplifying downstream without broadening in frequency. Conventional noise measurements provide an example of transitional and turbulent flow along the flare. Both quiet and conventional-noise results are dominated by the second-mode instability.

4.1 Cone-Cylinder-Flare Apparatus

As described in Section 2.3.2, this model consists of a 5° half-angle sharp cone leading to a cylinder, followed by a 3.5° half-angle straight conical flare. The model is divided into three sections: a steel nosetip, an aluminum mid-body containing the initial 5° cone and the upstream part of the cylinder, and a PEEK base including the downstream part of the cylinder and the 3.5° conical flare. The intersection of the cylinder with the 3.5° cone presents a compression corner to the oncoming flow. There are 16 sensor ports located along the centerline of the model, with 3 additional holes located azimuthally around the first cone for zeroing the angle of attack (see Section 2.11). Figure 4.1 displays the model (without its nosetip).

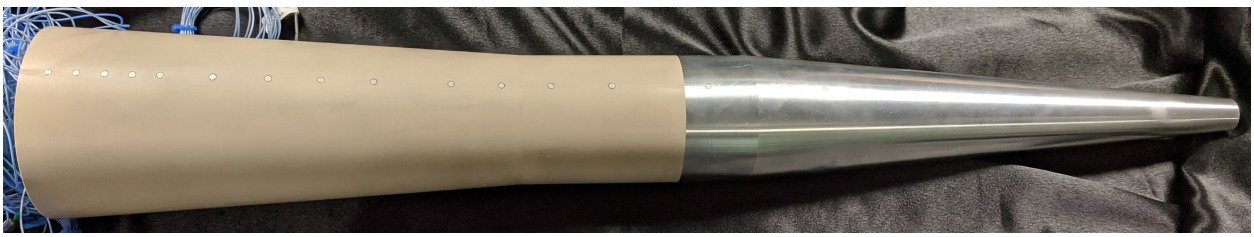

Figure 4.1. Photograph of model with sensors installed (excluding the nosetip).

4.2 Measurements under Quiet Flow

Measurements were primarily made in quiet flow at the BAM6QT. Surface heat transfer and pressure fluctuations were measured. The flow remained laminar to the downstream edge of the model for all quiet cases based on the pressure fluctuation spectra. However, transition onset might be occurring towards the downstream end as the heat transfer begins to rise in that region.

4.2.1 Heat Transfer Measurements

Due to the length of the model with the 3.5° flare relative to the available window, IR measurements of the flare needed to be made in two runs for each unit Reynolds number of interest. A sample of the laminar-scaled quiet-flow heat-transfer results for three different unit Reynolds numbers can be seen in Figure 4.2. The left column shows heat transfer images for the upstream portion of the flare, located immediately downstream of the compression corner at 526 mm. The right column has results for the downstream portion of the flare. PCB 13, located 651 mm downstream of the nosetip, can be seen in both sets of images.

Qualitatively, the quiet flow results all look roughly identical, with no locations of increasing heat transfer. Figure 4.3 provides a more quantitative comparison by plotting the normalized heat transfer averaged from slices taken between 80° and 100° in the azimuthal direction. The upstream portion of the flare can be seen in Figure 4.3a, while the downstream portion is in Figure 4.3b. In the quiet flow runs, the heat transfer is relatively constant across the surface of the flare, with only slight increases seen towards the downstream edge. With the exception of the $Re = 11.5 \times 10^6$/m case, heat transfer values for all of these runs collapse on top of each other. It is unknown why the highest Reynolds case has higher heat transfer, but the results were consistent across the two runs made to capture the upstream and downstream portions of the flare. No unexpected disturbances were seen in the PCB spectra for the $Re = 11.5 \times 10^6$/m case as compared to the other unit Reynolds number cases.

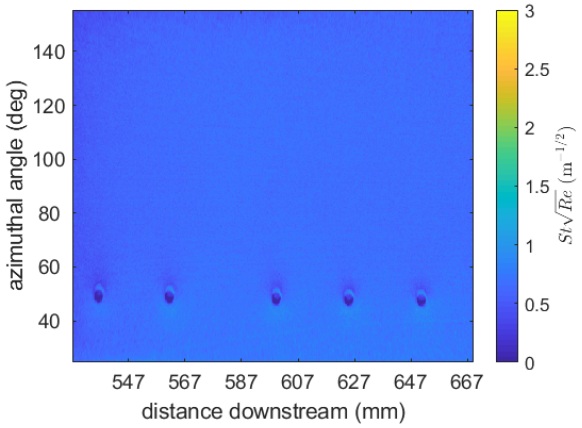

(a) $Re = 11.5 \times 10^6$/m, upstream

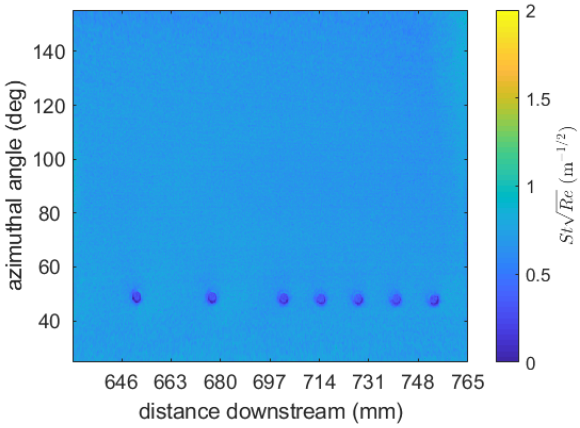

(b) $Re = 11.5 \times 10^6$/m, downstream

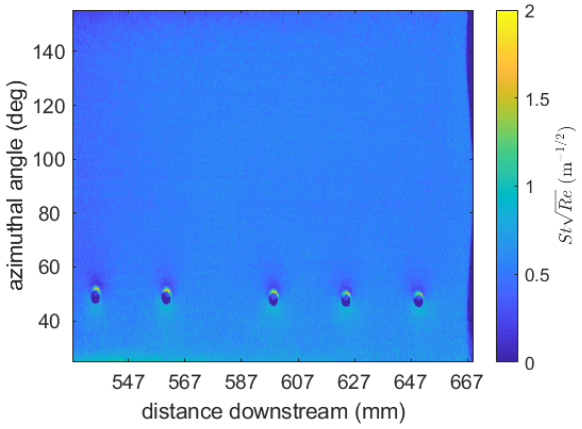

(c) $Re = 8.82 \times 10^6$/m, upstream

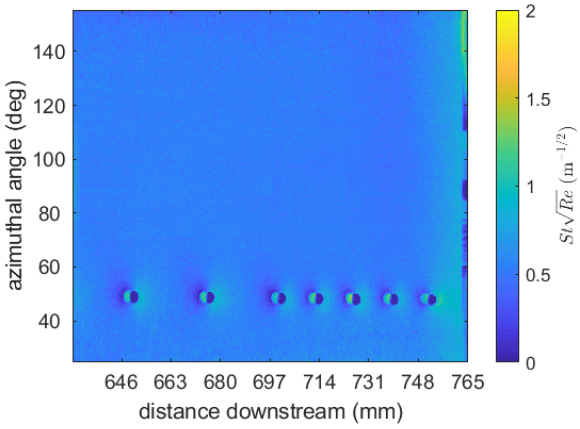

(d) $Re = 8.82 \times 10^6$/m, downstream

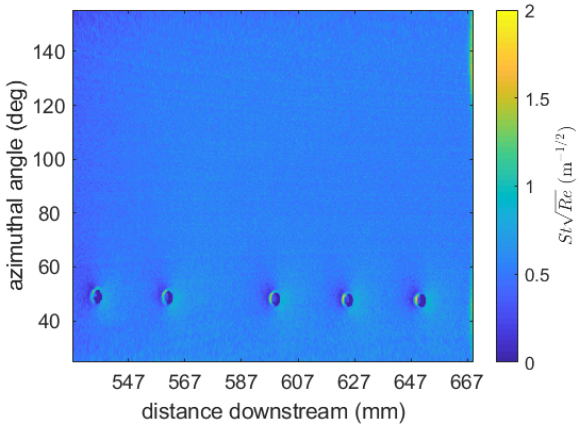

(e) $Re = 6.09 \times 10^6$/m, upstream

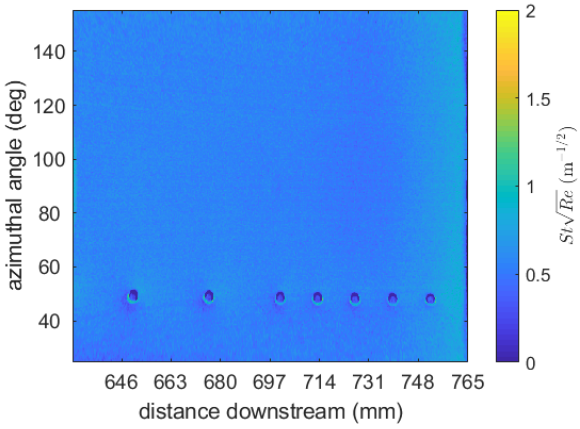

(f) $Re = 6.09 \times 10^6$/m, downstream

Figure 4.2. Laminar-scaled heat transfer images on the unrolled 3.5° flare in quiet flow. Flow is from left to right, with distance measurements being relative to the nosetip. The compression corner is located at 526 mm, just to the left of the first vertical axis, while the downstream edge of the model is at 765 mm.

Heat transfer values computed in STABL by Dr. Esquieu from the French Alternative Energies and Atomic Energy Commission (CEA), are included for two stagnation pressures, 75 psia and 150 psia (corresponding to unit Reynolds numbers of 5.57×10^6/m and 11.15×10^6/m, respectively). The computed values agree very well with measurements. The computational results are described in more detail in Ref. [69].

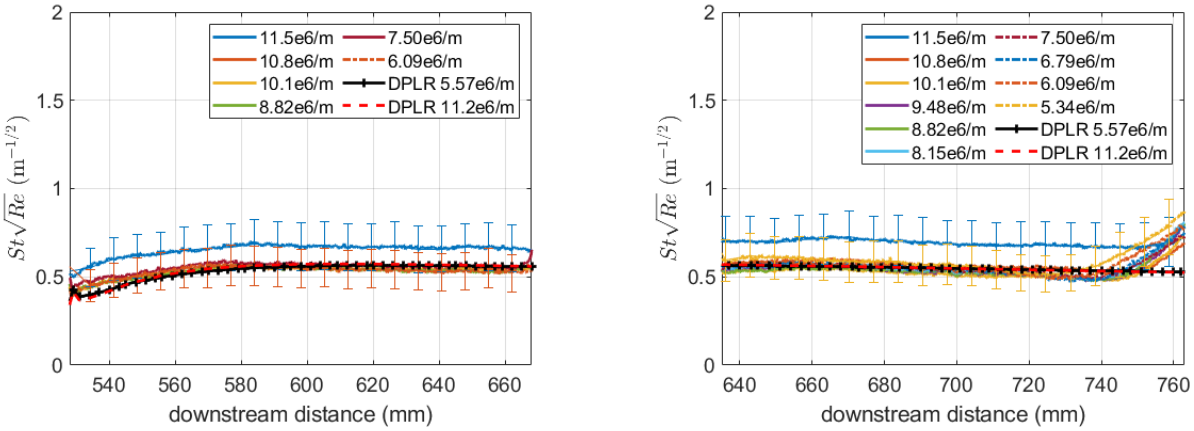

(a) Upstream portion of flare

(b) Downstream portion of flare

Figure 4.3. Laminar-scaled heat transfer along 3.5° flare under quiet flow at various unit Reynolds numbers. The compression corner is located at 526 mm, just to the left of the first vertical axis, while the downstream edge of the model is at 765 mm. 20% error bars are included for the largest and smallest unit Reynolds number cases.

Around 740 mm downstream of the nosetip, the heat transfer values begin to rise for all cases (except the highest unit Reynolds number case, which begins rising around 750 mm). This rise could potentially mark the onset of transition, although it does not seem to be influenced by unit Reynolds number in terms of location or magnitude. Pressure fluctuation power spectral densities in that region do not show any peak broadening that is indicative of transition (see Figure 4.5f), and the peak amplitude of the downstream-most PCB sensor is only slightly above the linear trend of the sensors further upstream (see Figure 4.7b). Due to its downstream location, the heat transfer increase could potentially be due to end-of-model conduction effects as well.

Table 4.1. Wall pressures along the 3.5° cone-cylinder-flare for $P_0 = 135$ psia (9.308×10^5 Pa), computed in STABL. Values were scaled by stagnation pressure to normalize surface pressure fluctuations.

Downstream position (mm)	Wall Pressure (Pa)
361	921.85
387	916.76
479	489.64
511	523.43
562	738.05
600	780.42
651	790.39
701	790.02
727	789.02
752	787.88

4.2.2 Pressure-Fluctuation Measurements

Figure 4.4 displays some of the PCB pressure power spectral densities (PSDs) at various unit Reynolds numbers and downstream positions along the cone and cylinder. The results were normalized by the computed surface pressure, with values listed in Table 4.1. These wall pressure values were scaled by the stagnation pressure during the run, resulting in noise levels that vary by unit Reynolds number. The spectra were also high-pass filtered at 500 Hz to reduce some ringing in the spectra. Second mode fluctuations are apparent on the cone section between 200 and 270 kHz at unit Reynolds numbers 9.48×10^6/m and above. The second mode is damped as it goes through the expansion along the cylinder. As the unit Reynolds number increases, so does the instability amplitude and peak frequency, as expected for the second mode. The sharper peaks at various frequencies are also present in the prerun voltages, and are therefore due to electronic noise (for example, around 60 kHz in Figure 4.4a).

Figure 4.5 shows PSDs of pressure fluctuations along the flare. The second mode can be seen amplifying as it moves downstream between 70 and 150 kHz. STABL computations by Dr. Esquieu show second-mode waves in the same frequency band. Additionally, the instability peaks increase in amplitude and peak frequency with increasing unit Reynolds number. As before, sharper spikes present in the prerun data are due to electrical noise. The

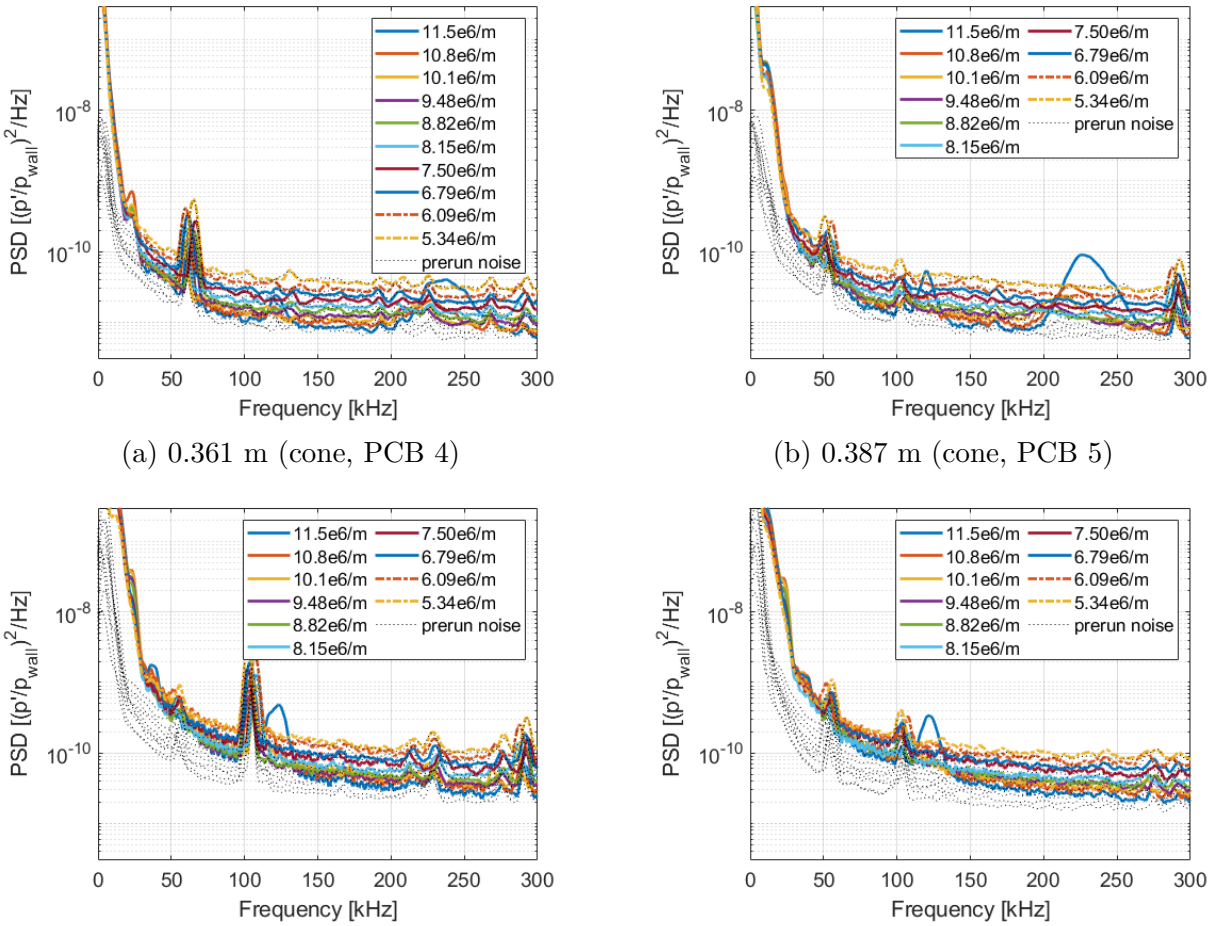

(a) 0.361 m (cone, PCB 4)

(b) 0.387 m (cone, PCB 5)

(c) 0.479 m (cylinder, PCB 7)

(d) 0.511 m (cylinder, PCB 8)

Figure 4.4. PCB PSDs along the 5° cone and the cylinder at Re between 5.34×10^6 and 11.5×10^6/m in quiet flow.

frequencies of these noise spikes vary between the channels, and similar results have been observed in other cases with the GN815 cards used to acquire these data.

It appears that the fluctuations along the flare at the highest unit Reynolds numbers (found between 100 and 150 kHz) seem to be transmitting their signal upstream to the cone and cylinder segments, potentially through model vibration. These spectra are not seen in the pre-run noise. The reason for this is uncertain, as the same cone-cylinder model segment is used in the separating experiments where only the expected second mode peaks are seen (between 200 and 300 kHz, see Figure 5.10). The 3.5° flare model is significantly longer than the 10° one, so if the fluctuations along the flare are inducing vibrations, they would have a

larger effect on the longer model. Model vibrations have been seen at such high frequency on long models in other cases as well [70]. However, more testing is needed to conclusively determine the source of these 100-150 kHz peaks along the cone.

In general along the flare, other than a second-mode harmonic seen at the highest unit Reynolds number 0.752 m downstream, only one frequency peak is seen at each PCB station (excluding electronic noise spikes). There is a rise in lower-frequency fluctuations, but this is generally broadband as any peaks seem to coincide with the PCB high-pass filtering at 11 kHz. High amplitude, low frequency fluctuations are common in PCB spectra, and are most likely due to model vibration. Tests with a vibrometer should be used with this model in the future.

The second mode peaks amplify moving downstream without broadening, implying that the flow remains laminar through the end of the model for all unit Reynolds numbers tested in quiet flow. Figure 4.6 plots the integrated RMS amplitudes between 50 and 270 kHz along the flare as a function of sensor Reynolds number. The runs with lower freestream unit Reynolds numbers are not amplified above the noise floor, so their amplitudes remain constant with sensor Reynolds number. However, the higher unit Reynolds number runs begin amplifying exponentially moving downstream along the flare.

Figure 4.7 compares the measured pressure spectra to the peak second-mode N-factors predicted with STABL as a function of frequency. The frequencies at the peak N-factor for each location agrees well with the peak frequencies seen in the experiments. The second-mode peaks along the flare (downstream of 526 mm) occur around 125 kHz for both, while the peaks along the cone (upstream of 437 mm) occur between 200 and 250 kHz.

The experimental pressure fluctuation amplitudes are compared with computed N-factors in Figure 4.8. The natural logarithm of the peak pressure fluctuation measurements from Run 1107 divided by the computed static wall pressures are plotted on the left axis. The PCB power spectral density peaks were integrated between 100 and 150 kHz to obtain the fluctuation amplitudes. The N-factors from STABL are on the right axis. The scale for each data set is the same; since the N-factors are amplification values based on powers of e they can compare with the natural logarithm of the measured pressure ratios. All data were taken with a stagnation pressure of 130 psia ($Re = 10.13 \times 10^6/\text{m}$). The N-factors were

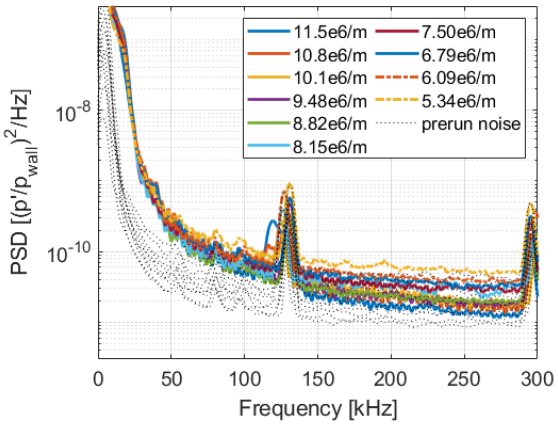

(a) 0.562 m (PCB 10)

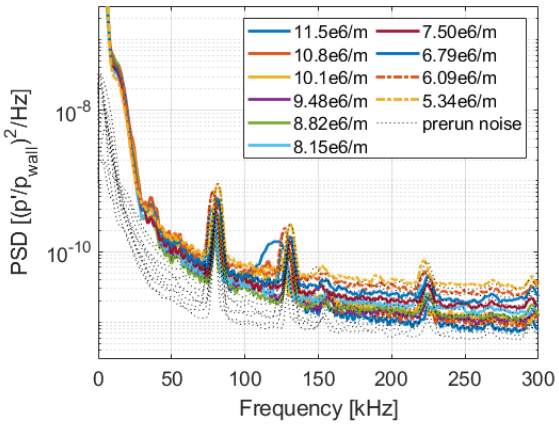

(b) 0.600 m (PCB 11)

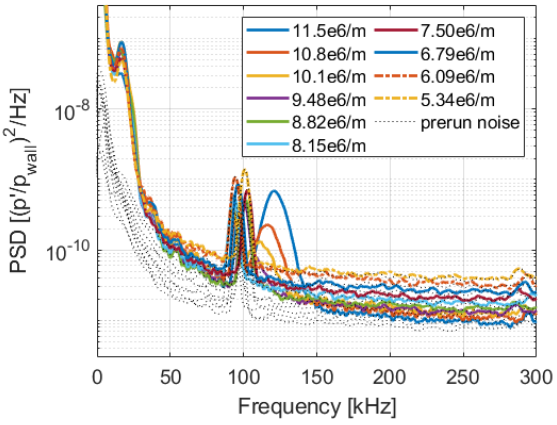

(c) 0.651 m (PCB 13)

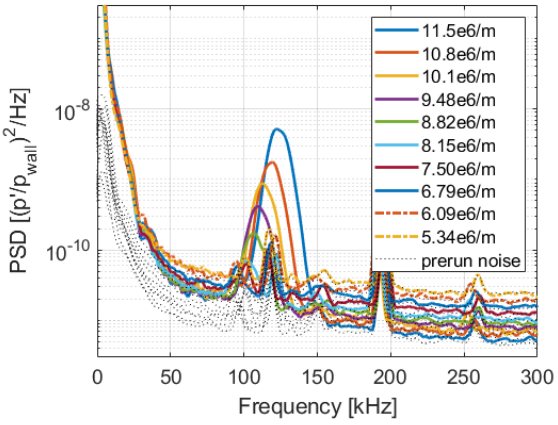

(d) 0.701 m (PCB 15)

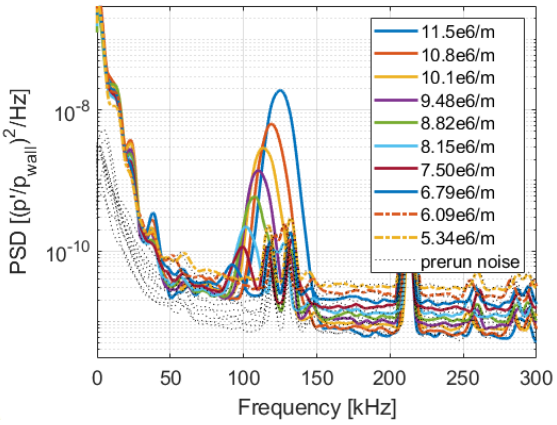

(e) 0.727 m (PCB 17)

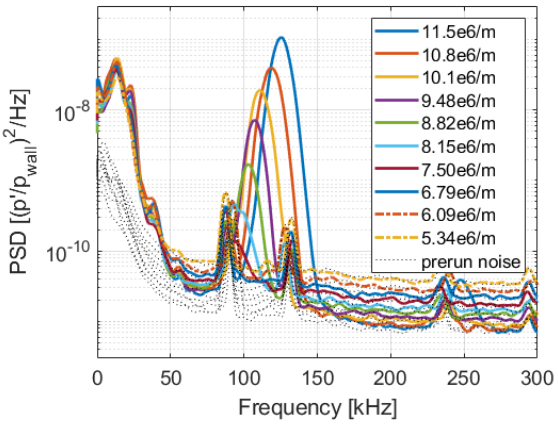

(f) 0.752 m (PCB 19)

Figure 4.5. PCB PSDs along the 3.5° flare at unit Reynolds numbers between 5.34×10^6 and 11.5×10^6/m in quiet flow.

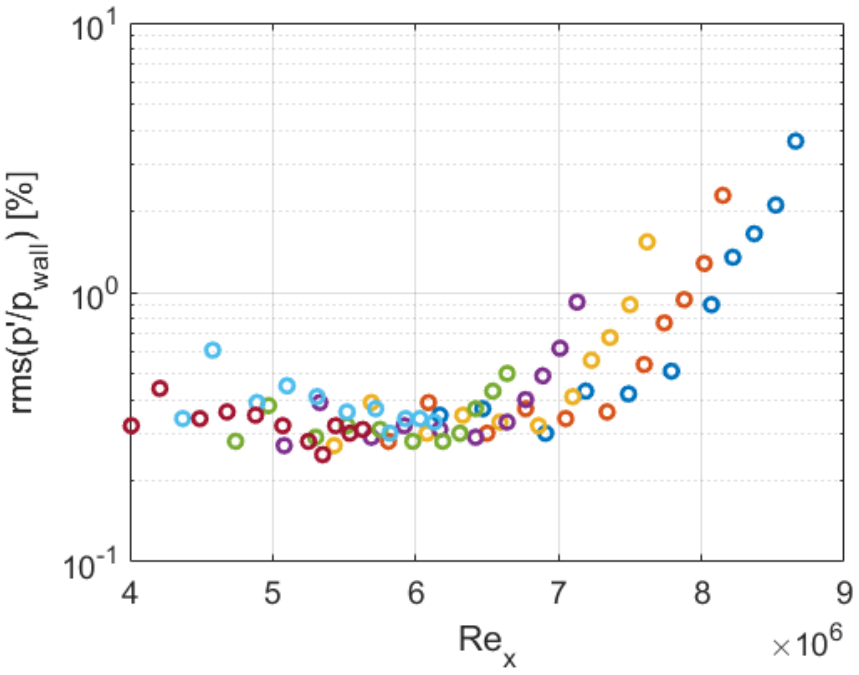

Figure 4.6. Normalized RMS amplitudes integrated between 50 and 270 kHz under quiet flow. Each color represents a single run.

computed with a pressure fluctuation frequency of 120 kHz, which was comparable to the peak frequencies along the downstream end of the flare. Along the cone and cylinder, any signal present at 120 kHz is below the noise floor. By 650 mm downstream of the nosetip, when the fluctuations are 0.2% of the computed wall pressure, second-mode frequency peaks start to rise above the noise floor. From that point onward the experimental amplitudes agree well with the computed N-factors.

The second mode consists of a traveling wave in the boundary layer. Finding the coherence between two adjacent sensors can determine if an instability at a given frequency is convective. Figure 4.9 shows the power spectral densities and coherences for the PCBs on the downstream portion of the flare at $Re = 11.5 \times 10^6$/m. The signal for the coherence was high-pass filtered at 25 kHz. The second mode can be seen in the PSDs for each sensor around 125 kHz, with the downstream-most PCBs also showing the first harmonic at 250 kHz (Figure 4.9a). Narrow peaks present in the prerun spectra are due to electronic noise. The coherence plot (Figure 4.9b) shows values near unity in the same band as the second

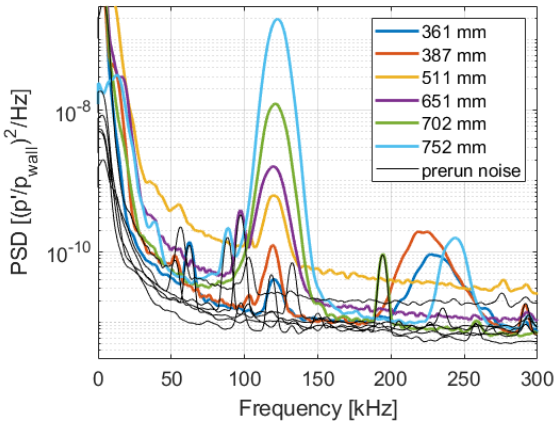

(a) Power spectral densities at along the model from Run 1104.

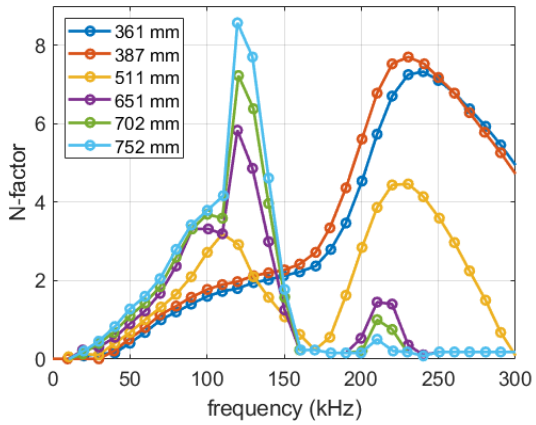

(b) Largest N-factors along model as a function of frequency, computed with STABL.

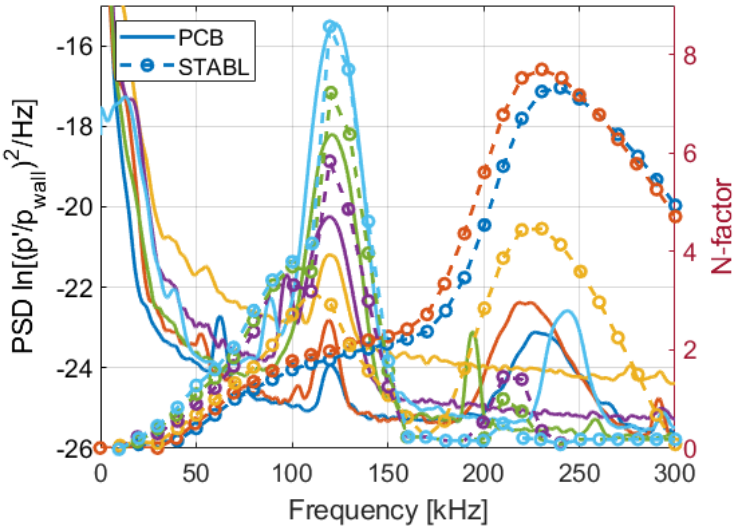

(c) PCB measurements and STABL computed N-factors on the same axis for comparison.

Figure 4.7. Power spectra comparison with frequencies of computed N-factors. The cone-cylinder junction is 437 mm downstream, while the cylinder-flare junction is at 526 m. $Re = 11.15 \times 10^6/\text{m}$.

mode, as well as moderately high coherence for the first harmonic. Due to the high coherence values, the instability is convective, as expected for the second mode instability.

Figure 4.10 plots time series data from consecutive PCB sensors, highlighting wave packets of the second mode as they amplify and convect downstream. Several second-mode wave packets can be seen with very low amplitude at 0.677 m from the nosetip. These packets

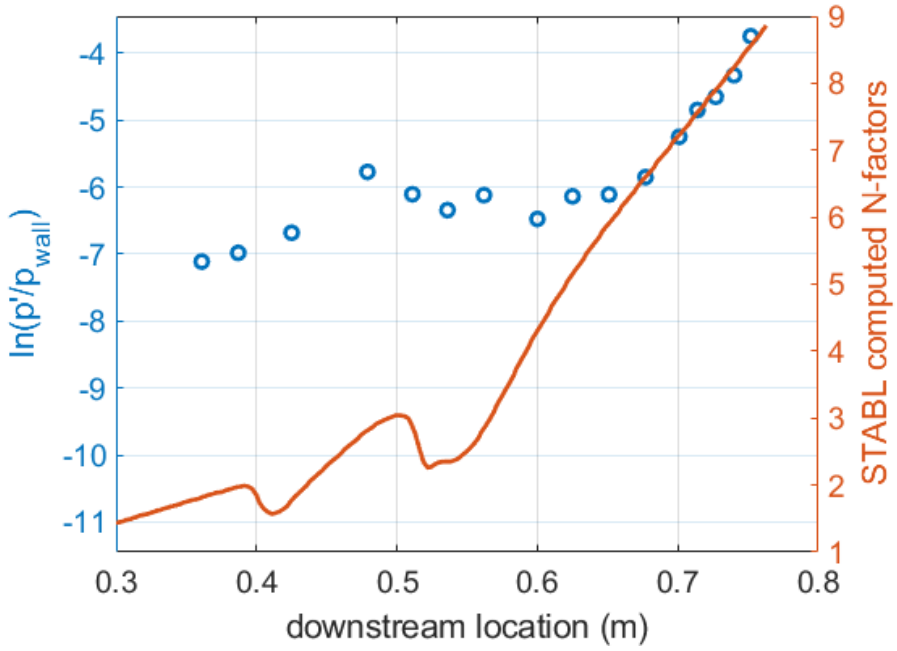

Figure 4.8. Comparison of measured pressure fluctuation amplitudes with STABL computed N-factors around 120 kHz at a stagnation pressure of 130 psia ($Re = 10.13 \times 10^6$/m).

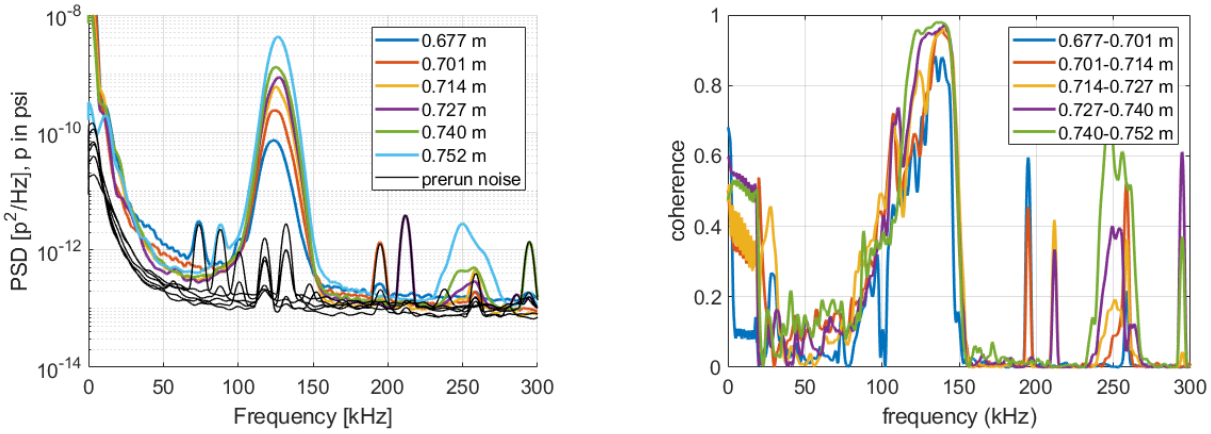

(a) PCB PSDs

(b) Coherence of PCB pairs

Figure 4.9. Power spectral densities and coherence between PCB sensors, $Re = 11.5 \times 10^6$/m. From Run 1132.

shift later in time as they move downstream, increasing in amplitude at each successive sensor. By cross-correlating the signals, a disturbance velocity of the wave packets can be determined (see Figure 4.11a). The velocity is found by fitting a line to the plot of lag at

maximum cross-correlation versus downstream distance (Figure 4.11b). The second-mode waves convect with a speed of approximately 711 m/s (about 83% of U_∞). This speed is slightly lower than the computed disturbance velocity of approximately 790 m/s, or 92% of U_∞. The second-mode disturbance speed is very close to the phase velocity of a slow acoustic wave, $c = (1 - 1/M)U_\infty$, where $c = 0.83U_\infty$ for $M = 6$ [71]. The waves have a frequency of around 125 kHz, which is the same frequency of the peak in the power spectra for this unit Reynolds number (11.5×10^6/m).

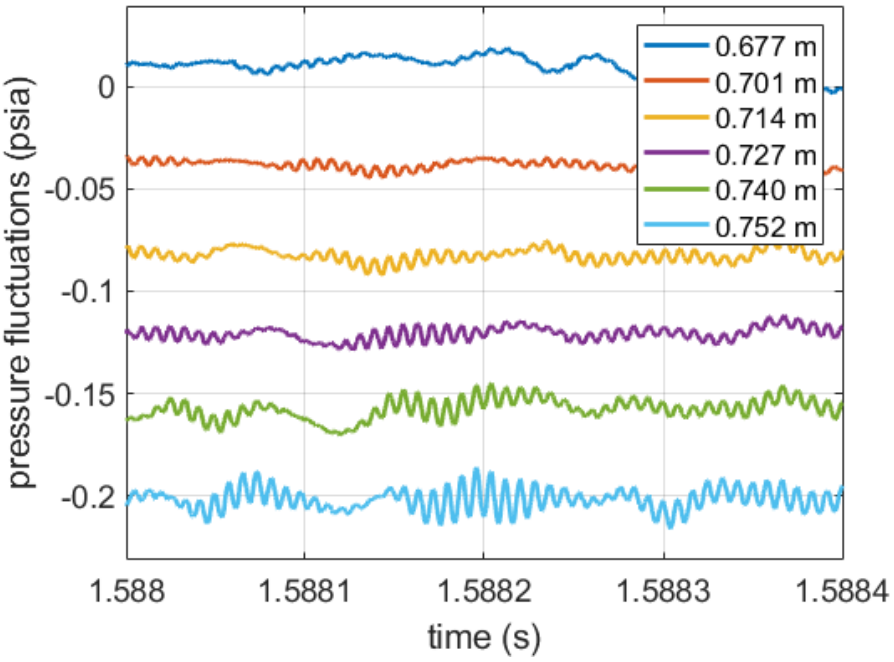

Figure 4.10. Waterfall plot showing the amplification of second-mode wave packets as they convect downstream. The PCB pressures are offset at a value proportional to the distance between the sensors. $Re = 11.5 \times 10^6$/m, from Run 1104.

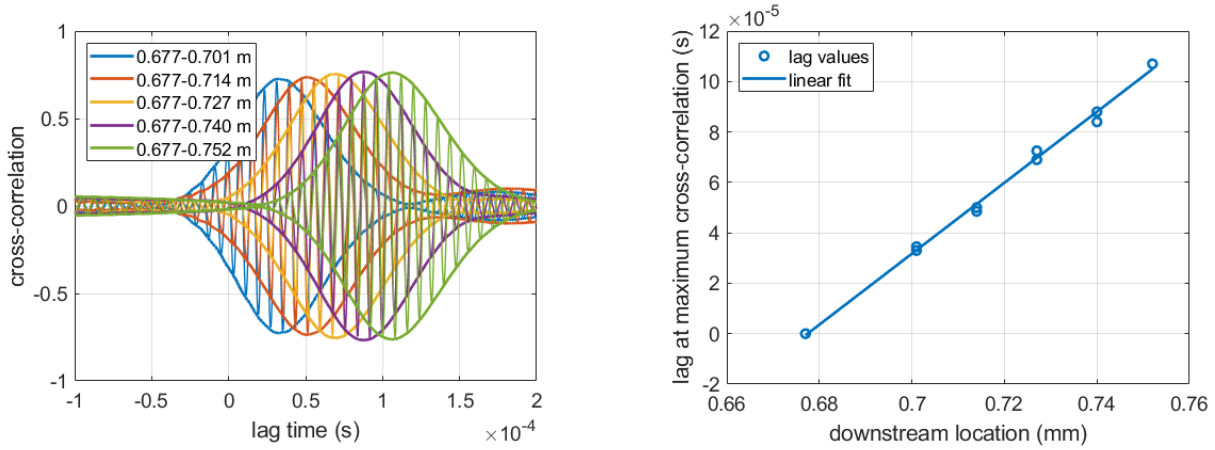

(a) PCB cross-correlation

(b) Lag time at maximum cross-correlation

Figure 4.11. Cross-correlation values between adjacent PCB sensors and their lag time at maximum cross-correlation, $Re = 11.5 \times 10^6$/m. From Run 1132.

4.3 Conventional-Noise Measurements

Since the quiet flow results were all laminar, additional measurements were made under conventional noise in the BAM6QT. Surface-pressure fluctuations and heat transfer were again measured. The flow spanned the laminar, transitional, and turbulent regimes as the unit Reynolds number increased, based on surface pressure spectra.

4.3.1 Heat Transfer Measurements

As with the quiet cases, IR measurements of the flare needed to be made across two runs for each unit Reynolds number of interest, due to the small window size relative to the model length. Figure 4.12 displays a sample of the normalized heat transfer results at three different unit Reynolds numbers. Much more variation can be seen for the conventional noise runs than in the quiet results. The different Re values no longer have similar values, as in the quiet cases, but have varying levels of heat transfer at different downstream locations. At the highest unit Reynolds number, the flow is entirely turbulent on the flare, and the heat transfer is relatively constant at an elevated level (Figures 4.12a and 4.12b). For the lower Re, the flow is transitional on the flare. At $Re = 5.22 \times 10^6$/m (Figures 4.12c and

4.12d), the surface pressure spectra reveal fully turbulent flow by 0.651 m downstream (see Section 4.3.2). In the heat transfer images, a broad peak seems to appear around the locations corresponding with transition. At $Re = 3.70 \times 10^6/\text{m}$ (Figures 4.12e and 4.12f), the surface pressure spectra begin broadening around 0.651 m downstream, and the flow is still transitional by the last PCB sensor. The heat transfer image shows a relatively constant low value that begins to have a larger rise around 0.62 m.

Figure 4.13 plots the same information more quantitatively, showing the average heat transfer between azimuthal angles of 80° and 100° as a function of downstream distance. Despite using a laminar formula for normalization (multiplying the Stanton number, St, by the square root of the unit Reynolds number, $\sqrt{Re}$), the turbulent cases seem to collapse on each other, at a heat transfer level above what was seen for the laminar results in quiet flow. The same data is showed with turbulent scaling in Figure 4.14 (computed by multiplying the Stanton number, St, by the fifth root of the unit Reynolds number, $Re^{1/5}$). One run, made at $Re = 2.16 \times 10^6/\text{m}$ with heat transfer measurements only for the downstream portion, has a relatively constant heat transfer around the same level as the quiet results (one example quiet run with $Re = 10.8 \times 10^6/\text{m}$ is plotted as well). The heat transfer values, coupled with surface pressure spectra that never broaden by the downstream edge of the model, suggest that particular run had laminar flow for the entirety of the flare.

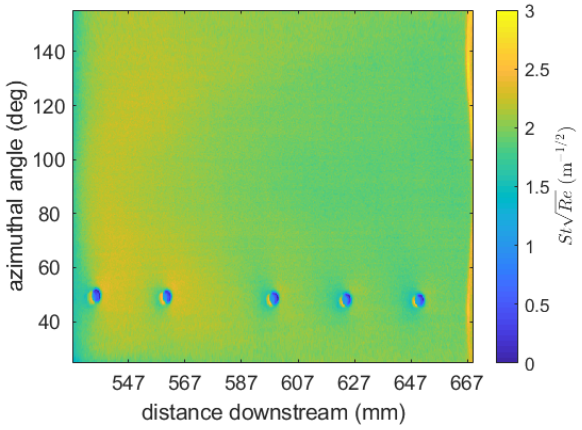

(a) $Re = 9.71 \times 10^6$/m, upstream

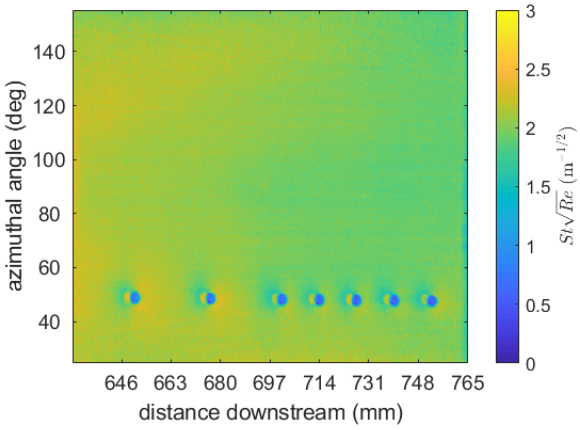

(b) $Re = 9.71 \times 10^6$/m, downstream

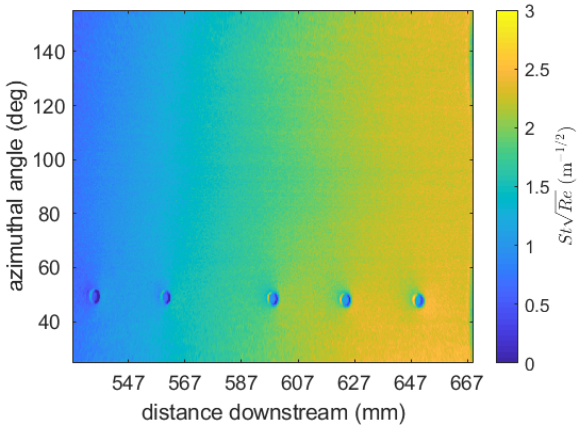

(c) $Re = 5.22 \times 10^6$/m, upstream

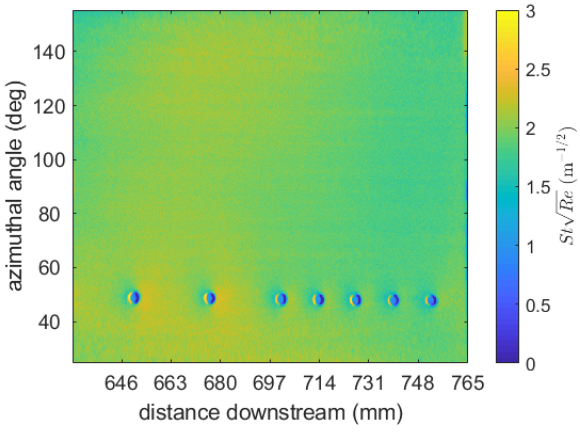

(d) $Re = 5.22 \times 10^6$/m, downstream

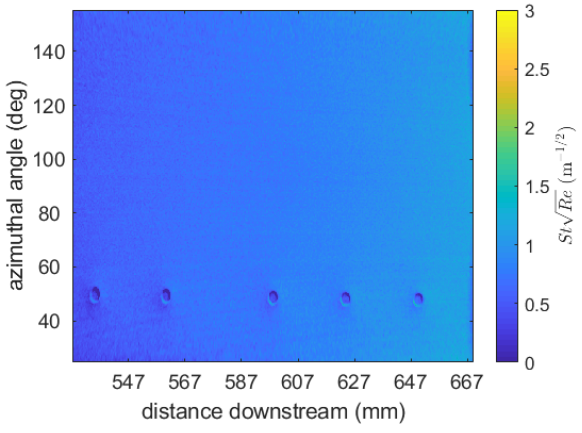

(e) $Re = 3.70 \times 10^6$/m, upstream

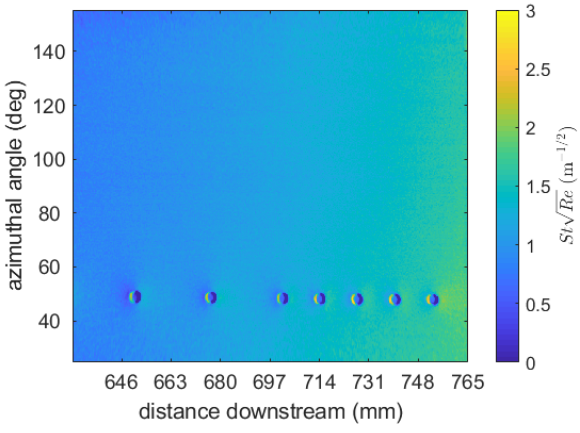

(f) $Re = 3.70 \times 10^6$/m, downstream

Figure 4.12. Laminar-scaled heat transfer images on the unrolled 3.5° flare in conventional noise. Flow is from left to right.

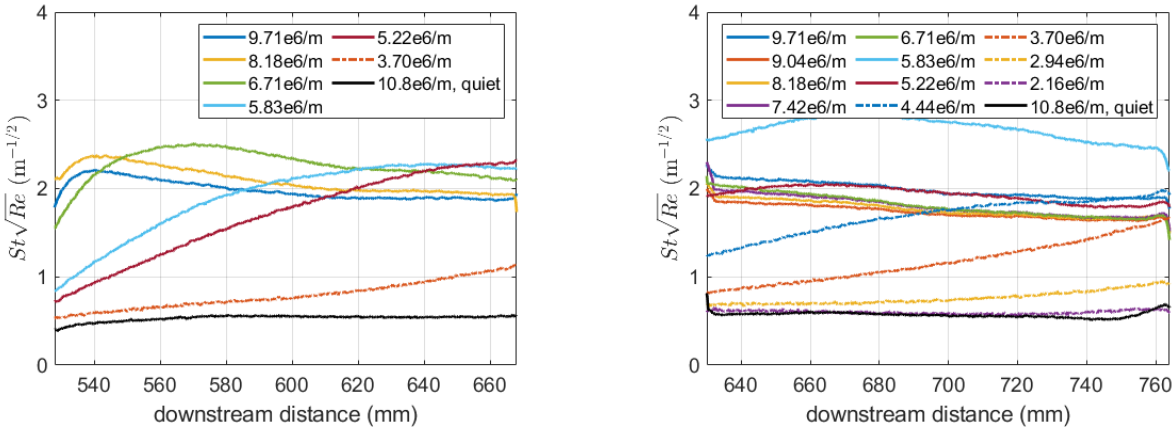

(a) Upstream portion of flare (b) Downstream portion of flare

Figure 4.13. Laminar-scaled heat transfer along 3.5° flare under conventional noise at various Reynolds numbers.

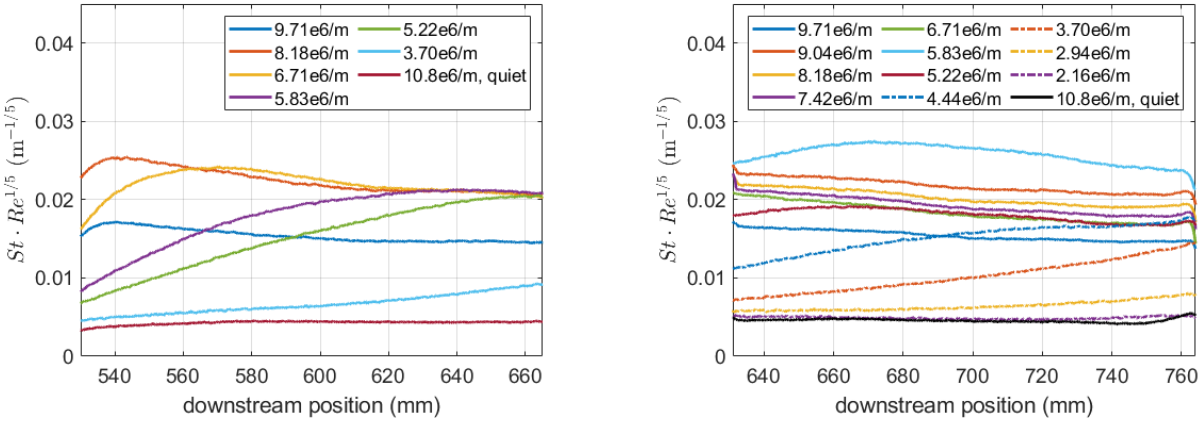

(a) Upstream portion of flare (b) Downstream portion of flare

Figure 4.14. Turbulent-scaled heat transfer along 3.5° flare under conventional noise at various Reynolds numbers.

4.3.2 Pressure-Fluctuation Measurements

Surface pressure fluctuation measurements were again taken with PCB pressure transducers. Figure 4.15 plots the resulting power spectral densities for the sensors located on the cone and cylinder portions of the model. As in the quiet cases, the spectra were normalized by wall pressure, resulting in noise floors that vary with unit Reynolds number. Frequency peaks associated with the second mode, as well as their first harmonics (which have peaks

at twice the frequency of the primary peak) can be seen on the cone. On the cylinder, the second-mode amplitudes decrease as the flow moves through the expansion. For both sections, the peak frequencies and amplitudes increase with increasing unit Reynolds number. The trend continues until transition begins, when the peaks broaden and begin to decrease in amplitude. Once fully turbulent, the spectra are generally broadband, with no peaks other than a slight increase near 300 kHz that may be associated with the PCB sensor resonance. The range of unit Reynolds numbers tested was selected to include laminar flow for the entire model through entirely turbulent flow. As in the quiet cases, the sharp peaks that are also present in the pre-run spectra are due to electronic noise, rather than an aerodynamic effect.

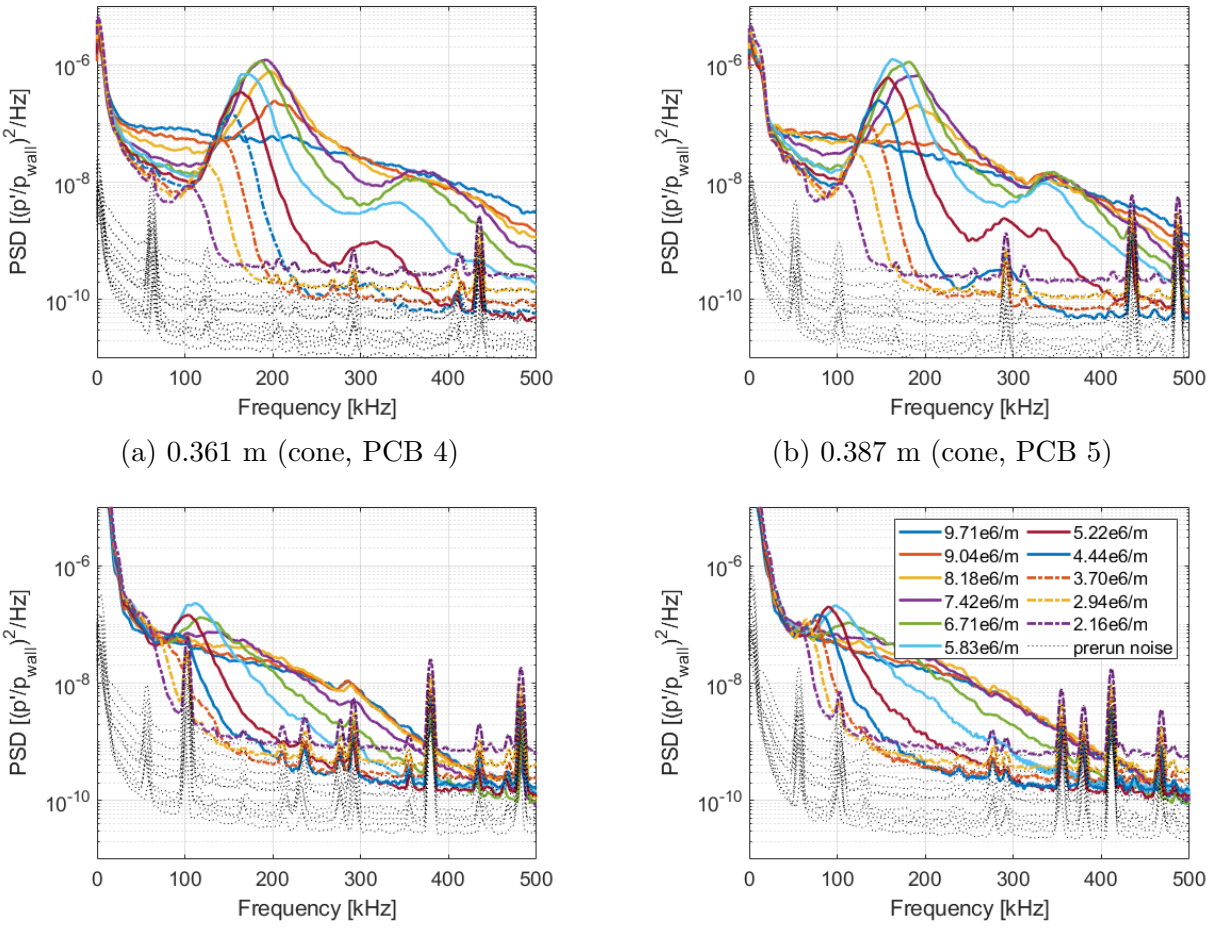

(a) 0.361 m (cone, PCB 4)

(b) 0.387 m (cone, PCB 5)

(c) 0.479 m (cylinder, PCB 7)

(d) 0.511 m (cylinder, PCB 8)

Figure 4.15. PCB PSDs along the 5° cone and the cylinder at unit Reynolds numbers between 2.16×10^6 and 9.71×10^6/m in conventional noise. The legend is the same for all sub-plots, but is removed from some for clarity.

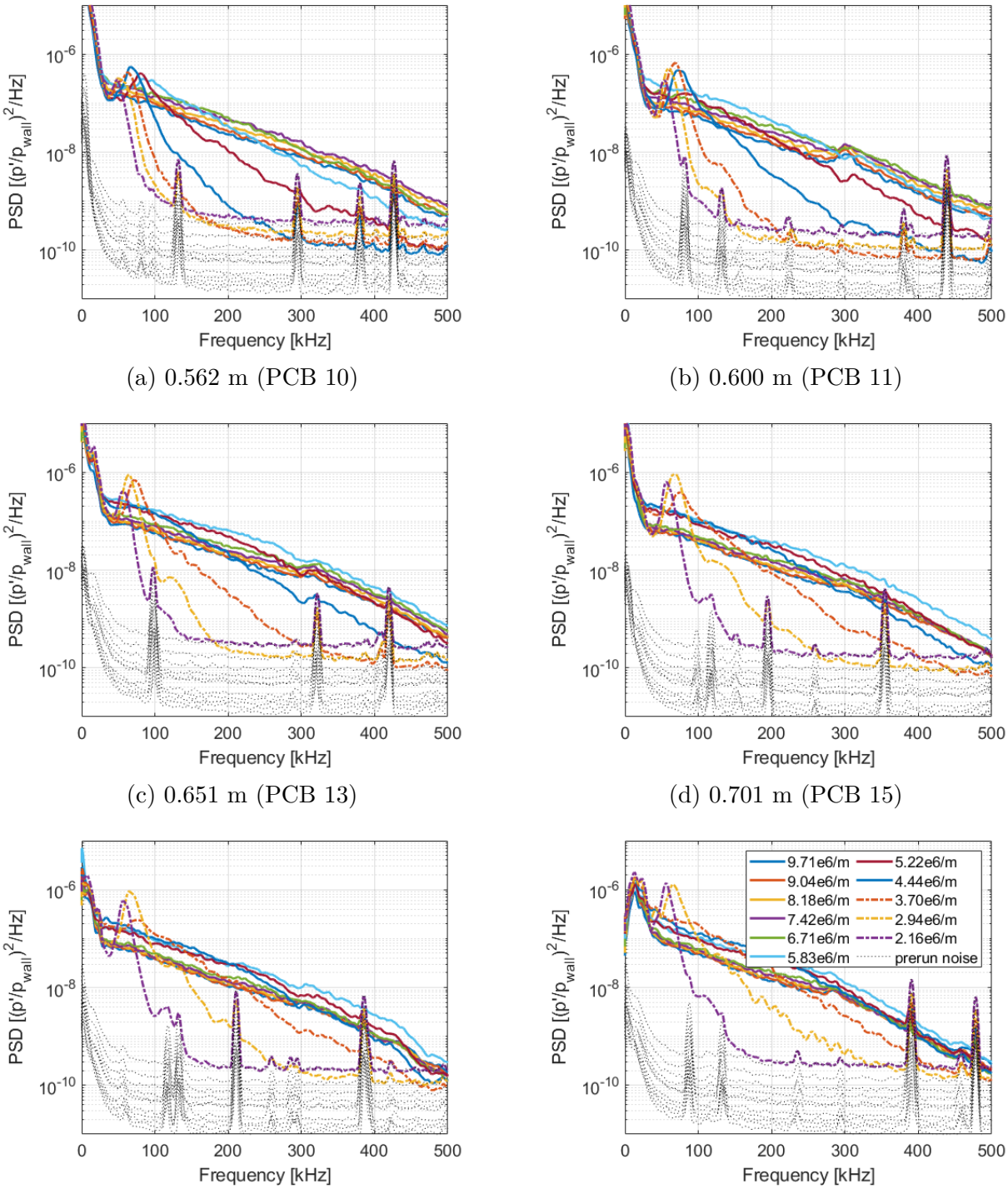

(a) 0.562 m (PCB 10)

(b) 0.600 m (PCB 11)

(c) 0.651 m (PCB 13)

(d) 0.701 m (PCB 15)

(e) 0.727 m (PCB 17)

(f) 0.752 m (PCB 19)

Figure 4.16. PCB PSDs along the 3.5° flare at unit Reynolds numbers between 2.16×10^6 and 9.71×10^6/m in conventional noise. The legend is the same for all sub-plots, but is removed from some for clarity.

The pressure fluctuation spectra along the flare are plotted in Figure 4.16. As along the cone and cylinder sections, only peaks believed to be associated with the second mode (between 50 and 100 kHz) can be seen (the peak around 11 kHz at 0.752 m is most likely due to the high-pass filtering of the sensor). Again, the peak frequencies and amplitudes increase with unit Reynolds number until transition begins, where they decrease and broaden. As the unit Reynolds number increases, transition moves upstream on the flare.

The integrated RMS amplitudes along the flare for the conventional noise runs are displayed with linear fits in Figure 4.17. Each color represents data from a single run. The amplitudes are plotted as a function of sensor Reynolds number. The intersection of the two lines corresponds to the Reynolds number of 2.5×10^6. This Reynolds number corresponds to the axial position where the heat transfer begins to increase along the flare (see Figure 4.12).

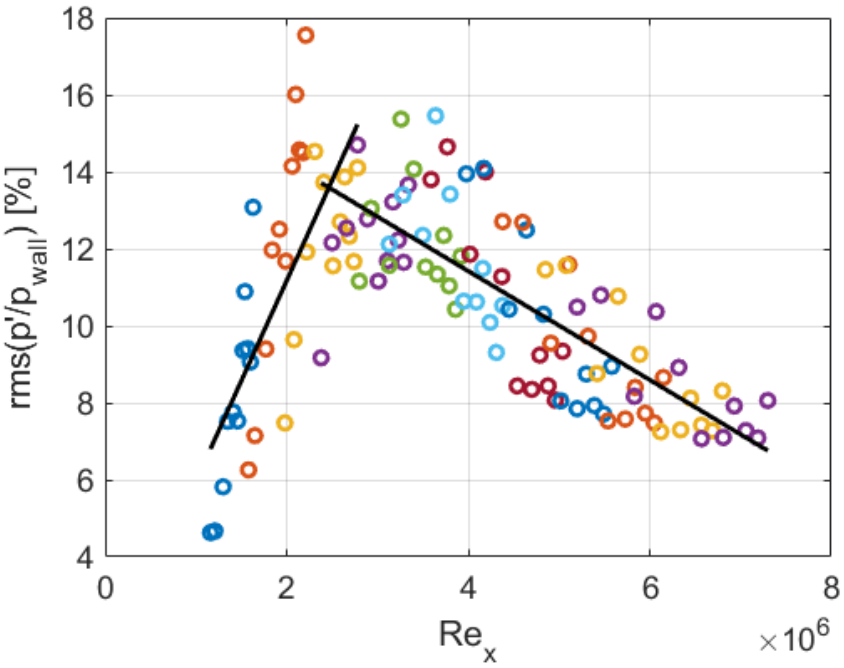

Figure 4.17. Normalized RMS amplitudes integrated between 50 and 270 kHz under conventional noise. The black lines represent linear fits to the data.

Figure 4.18 shows an example of a wave packet transitioning as it convects downstream along the flare. Pressure fluctuation time series data are offset at the different PCB stations

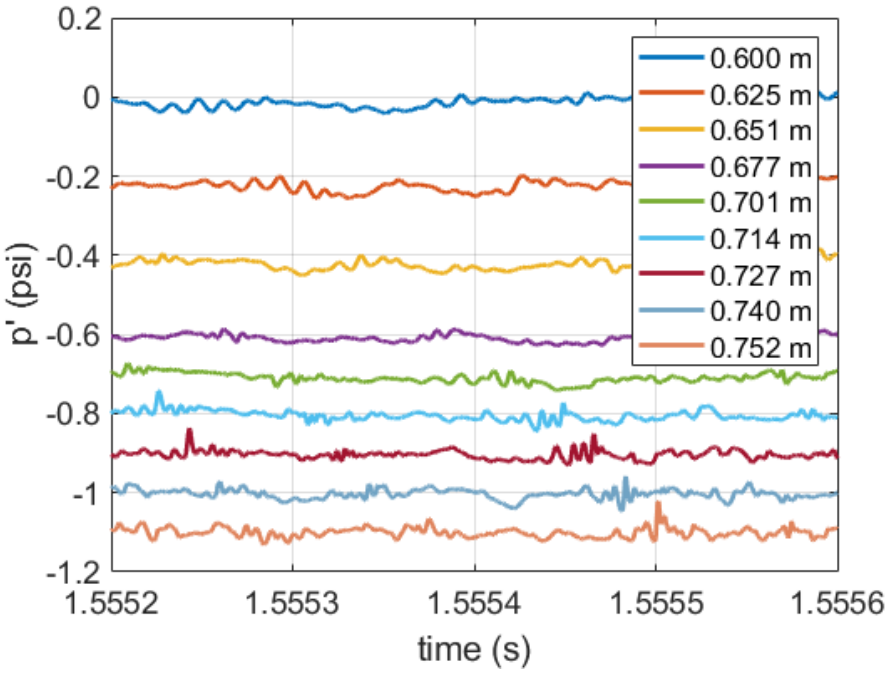

Figure 4.18. Waterfall plot displaying second-mode wave packets transitioning to turbulent spots as they convect downstream. The PCB pressures are offset at a value proportional to the distance between the sensors. $Re = 4.44 \times 10^6$/m, from Run 1124.

for clarity, with the spacing between the curves proportional to the distance between the sensors. The second-mode wave packet at 0.600 m has a frequency of about 75 kHz and a sinusoidal shape. As it moves to 0.625 m, it maintains its sinusoidal appearance and has a slightly higher amplitude. Moving towards 0.651 to 0.677 m, the shape of the wave packet is starting to become distorted. By 0.701 m and farther downstream, the disturbance contains high-frequency components that are characteristic of a turbulent spot. This location corresponds to $Re_x = 3.1 \times 10^6$.

4.4 Summary of Results without Separation Bubble

Heat transfer and surface pressure fluctuation measurements were made on a sharp cone-cylinder-flare model with the compression angle of 3.5°, which is sufficiently small to prevent

the boundary layer from separating. Tests were made at a variety of unit Reynolds numbers in both quiet and conventional noise flow at 0° angle of attack.

In quiet flow, the boundary layer most likely remains laminar for the entirety of the model. Normalized heat transfer measurements show a relatively constant value over the course of the flare for all unit Reynolds numbers. Pressure fluctuations on the cone show frequency peaks for the second mode and its first harmonic, which are damped along the cylinder. On the flare, pressure fluctuations reveal only one peak. This peak amplifies moving downstream, but stays at a constant frequency due to the thickness of the boundary layer remaining constant along the flare. Therefore, this instability is consistent with the second mode. Peak frequencies across the model agree well with computations conducted using STABL by Dr. Sebastien Esquieu. Nondimensionalized amplitudes along the downstream portion of the flare also agree with N-factor predictions from the computations. Second-mode wave packets can be observed in the pressure time traces amplifying as they convect downstream. Since transition was not observed, the quiet flow transition Reynolds number must be greater than 8.7×10^6.

Under conventional noise, flow spanning laminar, transitional, and turbulent regimes is observed. Heat transfer measurements generally agree with the quiet values for the laminar case, but are higher for turbulent runs. Transitional runs resulted in a broad peak in heating along the flare. As in the quiet runs, pressure spectra along the cone show peaks associated with the second mode and its first harmonic, which are again damped along the cylinder. Pressure fluctuations along the flare only show peaks associated with the second mode. These peaks increase in frequency and amplitude with unit Reynolds number until transition, where they broaden and decrease in amplitude. The location of transition moves upstream with increasing unit Reynolds number. Second-mode wave packets transitioning to turbulent spots can be seen in the pressure fluctuation time series. The conventional noise transition Reynolds number is about 2.5×10^6. This is less than one-third of the minimum value under quiet flow.

These results provide a baseline for comparison with results for an axisymmetric separation bubble (described in Chapter 5).

5. CONE-CYLINDER-FLARE MEASUREMENTS WITH THE 10° FLARE

The 10° cone-cylinder-flare model provided an axisymmetric separation bubble that had sufficient distance post-reattachment to study convective instabilities generated or amplified in the shear layer through the reattached boundary layer. This chapter discusses measurements made with this flow-separating model. As in the non-separating case, all quiet runs for this analysis provided primarily laminar flow. Even up to the maximum quiet stagnation pressure, clear second-mode peaks were observed amplifying downstream without broadening in frequency. Conventional noise measurements provide an example of transitional and turbulent flow along the flare. Some of these results were published in Refs. [72] and [73].

5.1 Cone-Cylinder-Flare Model Apparatus

As described in Section 2.3.2, the model used for the separation bubble tests consists of a 5.0° half-angle sharp cone leading to a cylinder, with a 10.0° half-angle straight conical flare downstream. The model is divided into three sections: a steel nosetip, an aluminum mid-body containing the initial 5° cone and the first part of the cylinder, and an PEEK base including the latter part of the cylinder and the 10° conical flare. The intersection of the cylinder with the 10° cone creates an axisymmetric compression corner to the oncoming flow, which was designed to create an adverse pressure gradient sufficiently large enough to cause the boundary layer to separate. The model was designed by Dr. Sebastien Esquieu from CEA. 14 sensor holes are located along the centerline of the model, with 3 additional holes located azimuthally around the first cone and 3 additional sets of 4 holes located near the compression corner at 90°, 180°, and 270° around the model. Additionally, 2 pairs of holes are located on either side of the 0.606-m and 0.631-m ports to look at spanwise variations. Analysis of these off-axis fluctuations and further spanwise studies are left for future work. For heat transfer measurements, the PEEK 10° flare was imaged with an IR camera. The recorded temperature information was then used to compute the surface heat transfer as described in Section 2.8. A Zygo ZeGage optical profiler was used to measure the radius of

curvature at the compression corner, which was found to be approximately 0.45 mm. Figure 5.1 displays the model as instrumented.

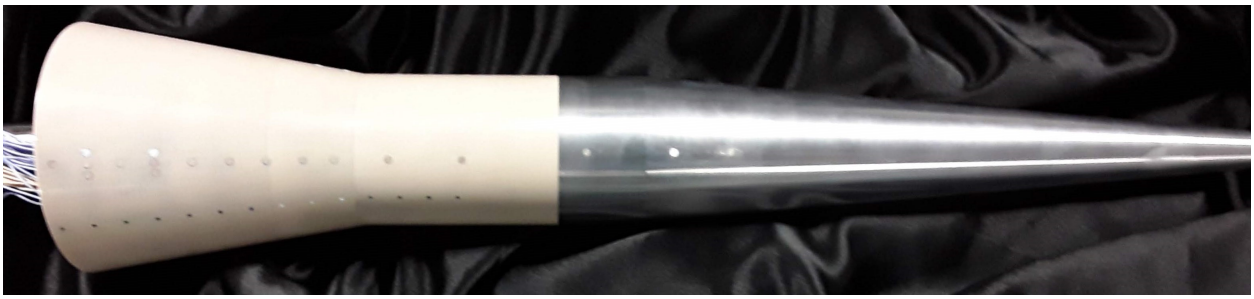

Figure 5.1. 10° cone-cylinder-flare model instrumented with PCB and Kulite pressure sensors, nosetip removed.

5.2 Quiet Flow

Surface pressure fluctuation, heat transfer, and off-the-surface density fluctuation measurements were made at several unit Reynolds numbers in quiet flow. PCB and Kulite power spectra show that the quiet runs resulted in entirely laminar flow.

5.2.1 Mean Measurements

5.2.1.1 Schlieren

Schlieren images were taken of the cylinder-flare section of the model to understand the geometry of the bubble and where reattachment occurs. Two entries were conducted with differing setups and conditions due to what was available at the time of testing. All runs use a frame rate of either 10,000 or 20,000 frames per second, with a shutter period of 1/10,526 or 1/4,032,000 seconds, respectively. Runs were made near maximum quiet (around 12×10^6/m for Entry 13 and 10×10^6/m for Entry 14) as well as a couple of lower unit Reynolds numbers to see the effect on bubble size. During Entry 13, four-inch mirrors were used, so several runs were made at max quiet conditions to get an overall image of the flow around the model. By Entry 14, eight-inch mirrors were available, but the maximum quiet stagnation pressure dropped from 155 to 125 psia due to a nozzle change in the BAM6QT.

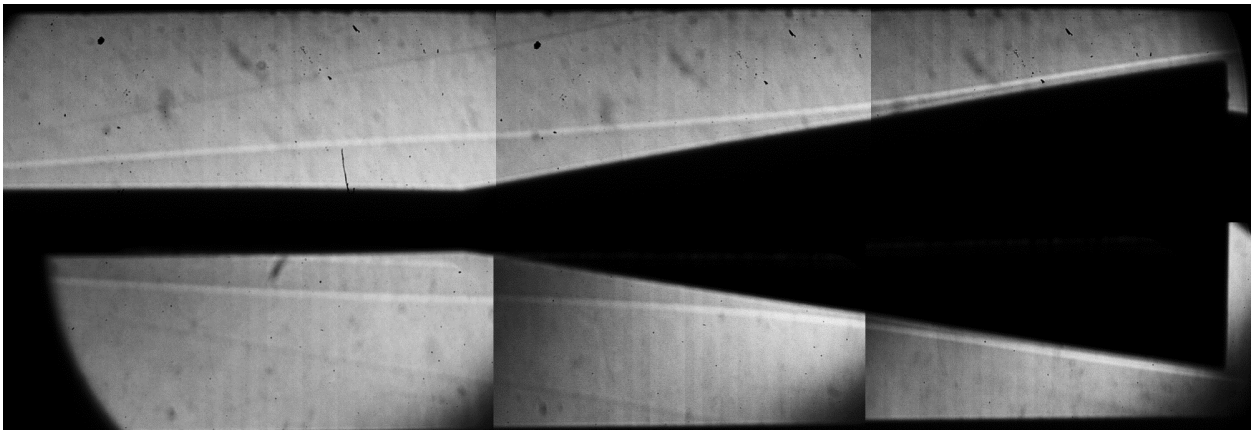

Figure 5.2. Composite schlieren image at $Re = 11.7 \times 10^6$/m. Flow is from left to right. From, in counterclockwise order from the top left corner, Runs 1314, 1308, 1319, 1321, 1323, and 1324.

Figure 5.2 shows a composite image taken from six runs at $Re = 11.7 \times 10^6$/m under quiet flow. In this figure, the shear layer and the reattached boundary layer are seen as white lines off the surface of the model. At the corner, the shear layer is between 7.6 and 8.2 mm away from the wall when looking at the lower or upper surface, respectively (a variation that is less than 8%). Note that the model was shifted upstream before Run 1319 to obtain the appropriate view through the windows. This shift may have very slightly altered the model's angle of attack, causing the difference in shear layer heights at the corners for this composite image. The dark lines seen in the upstream-most images farther from the surface than the shear layer are the separation shocks from the beginning of the bubble, which is located upstream of the figure. Faint smudges can be seen in the downstream-most images; these correspond to the reattachment shocks.

The size of the bubble can only be indirectly approximated from the schlieren. There are several methods for doing this. Schaefer and Ferguson in 1962 used extrapolation of the shear layer to the model surface to determine separation and reattachment [14]. With this method, the bubble at $Re = 11.7 \times 10^6$/m would be 179 mm long, reattaching 0.600 m downstream of the nosetip. Ginoux in 1965 used extrapolation of the separation and reattachment shocks to estimate separation extent [17]. This method results in a 158 mm long bubble that reattaches 0.579 m downstream of the nosetip. Most likely, reattachment is

somewhere between those two values. For both approximations, the boundary layer separates from the model surface about 0.105 m upstream of the corner, which is along the cylinder portion of the model.

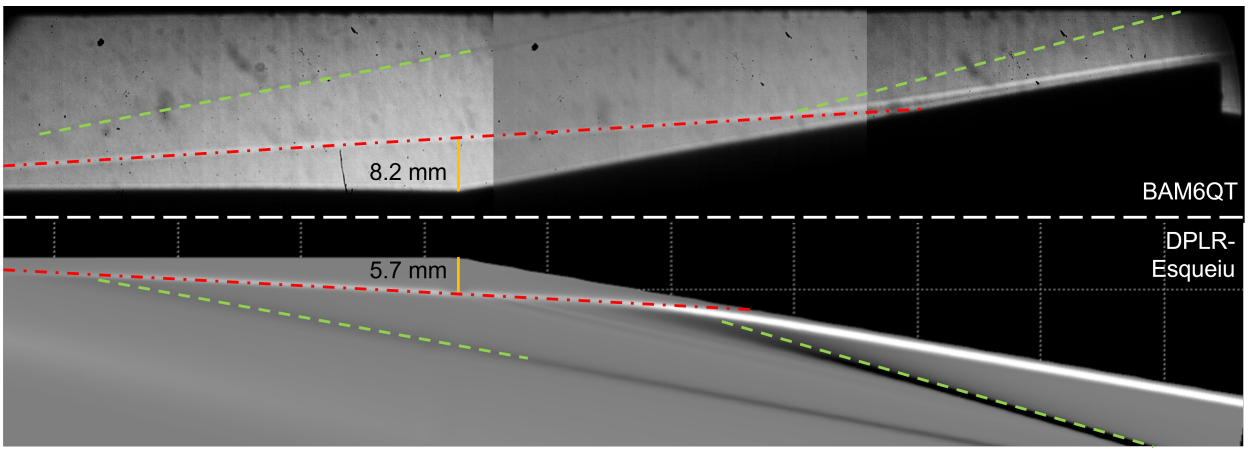

Figure 5.3. Comparison between schlieren and computed pseudoschlieren (computation by Dr. Esquieu). The shear layer in each image is outlined in red, while the separation and reattachment shocks are in green. The yellow lines go from the compression corner to the shear layer.

The estimated reattachment location is downstream of the reattachment point computed by Dr. Esquieu in DPLR. A comparison between the schlieren and computed pseudoschlieren is shown in Figure 5.3. The shear layer and separation and reattachment shocks (represented by red and green dashed lines, respectively) are drawn in both images. In the pseudoschlieren, the shear layer and separation shock are slightly closer to the model surface, and bubble appears to reattach further upstream. If the same estimation technique is applied to the computed case, the shear layer extrapolates to the model surface 0.573 m downstream of the nosetip, while the reattachment shock reaches the shear layer about 0.568 m downstream.

Two different unit Reynolds numbers are displayed in Figure 5.4. At the corner, the shear layer is 8.2 and 5.8 mm off the surface at the higher and lower unit Reynolds number, respectively. The lower unit Reynolds number case has lower contrast than the higher one due to the lower density gradients in the flow, so the separation and reattachment shocks are not visible. However, since the shear layer height is lower, the bubble is most likely smaller in the 2.55×10^6/m case. Using the shear layer extrapolation estimate of bubble size, the

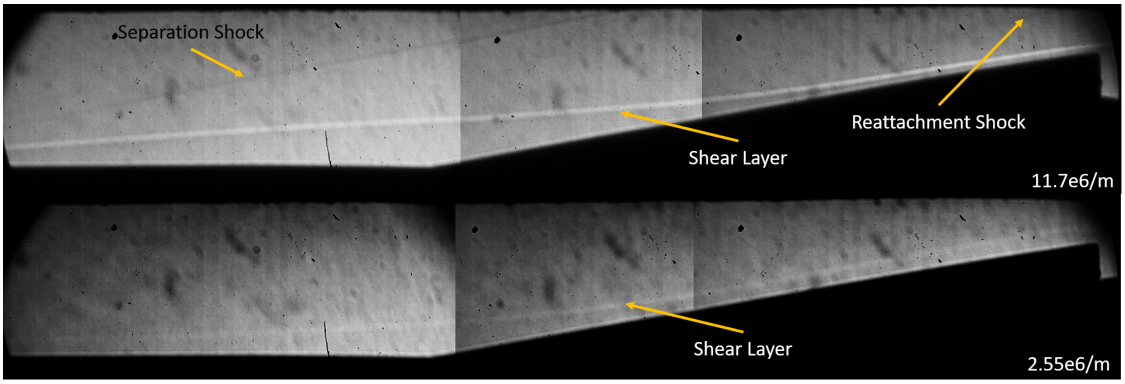

Figure 5.4. Composite schlieren images at $Re = 11.7 \times 10^6$/m and $Re = 2.55 \times 10^6$/m highlighting variation in bubble size at different unit Reynolds numbers. Flow is from left to right. From Runs 1314, 1308, 1319, 1316, 1318, and 1320.

separation bubble is approximately 136 mm long, reattaching around 0.585 m downstream of the nosetip. This trend of increasing bubble size with increasing unit Reynolds number is a laminar trend that has been observed in previous experiments with supersonic and hypersonic laminar bubbles [12], [15].

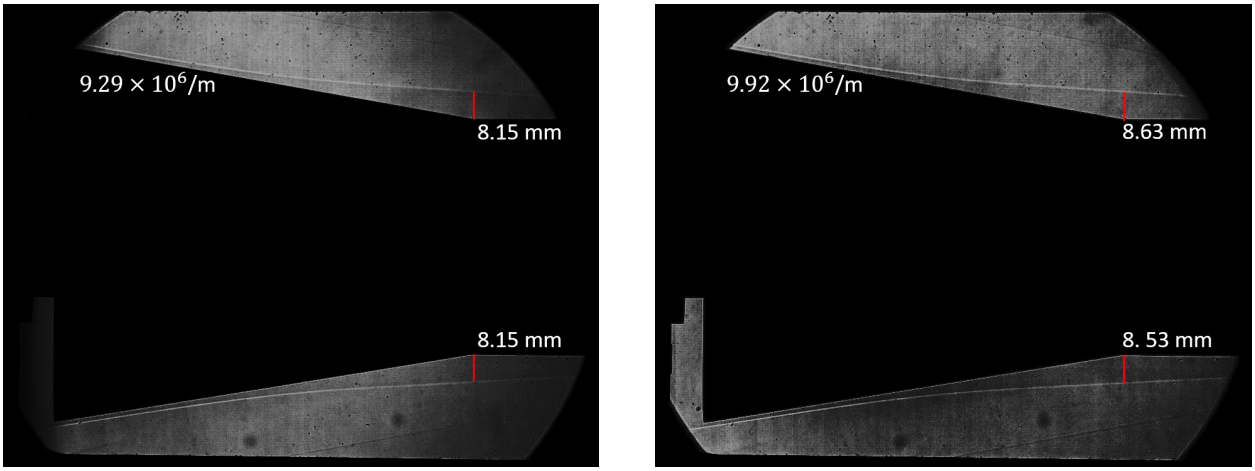

(a) Run 1413 (b) Run 1416

Figure 5.5. Schlieren images highlighting bubble symmetry at 0.0° angle of attack for two runs during Entry 14. Single frames are depicted.

To get a better idea of the symmetry of the bubble when the model is at 0.0° angle of attack, larger eight-inch mirrors were used for Entry 14 to image the bubble on both

sides of the model simultaneously. Figure 5.5 shows instantaneous images from two runs at and just below the maximum quiet pressure available at the time (125 psia for this entry, around $Re = 9.9 \times 10^6/\text{m}$). The height of the shear layer off the surface of the model at the compression corner was measured in individual frames and found to be within 1.2% of the mean height of the shear layer for the two sides. By averaging 1000 consecutive frames instead of looking at individual ones, the variation increases slightly to just under 3.5%; this increase in variation in shear layer height between the upper and lower surfaces is believed to be due to the smearing of the model edge and shear layer from oscillatory model motion during the run (described at the end of this section). In either case, the bubble appears to be highly symmetric at 0.0° angle of attack. When the angle of attack was deliberately varied by small amounts, the shear layer heights on the top and bottom of the model began to differ more significantly (see Section 5.2.4).

Taking images at 20,000 frames per second allows for measurements of the time it takes to establish the laminar bubble. Figure 5.6 displays five frames captured immediately after the flow was started and quiet around a unit Reynolds number of $11.9 \times 10^6/\text{m}$. Just 0.2 ms after the first frame that contained a laminar boundary layer, a clear separation bubble can be seen right at the corner, with a separation shock and a reattachment shock that merge in the center of the composite image. The bubble initially grows quickly, expanding both upstream and downstream from the corner for the first few milliseconds. It continues growing at a slower pace until it reaches its steady-state size around 10.0 ms after quiet flow initiation.

Once fully developed under quiet flow, the shear layer was remarkably steady. This differs from the conventional noise results, seen in Section 5.3.1.2, where the shear layer appears to move relative to the model surface throughout the run. With 20,000 frames per second, model oscillations of up to 10 kHz can be qualitatively measured. By plotting the relative pixel intensity of a small square of 6x6 pixels at the model corner relative to time, a low-frequency model vibration of about 32 Hz can be detected. This oscillation is believed to be due to model motion as opposed to optical-bench motion as it was not seen in FLDI measurements made on the same bench. The shear layer appears to track this vibration, remaining approximately the same distance from the surface as the surface shifts. Figure

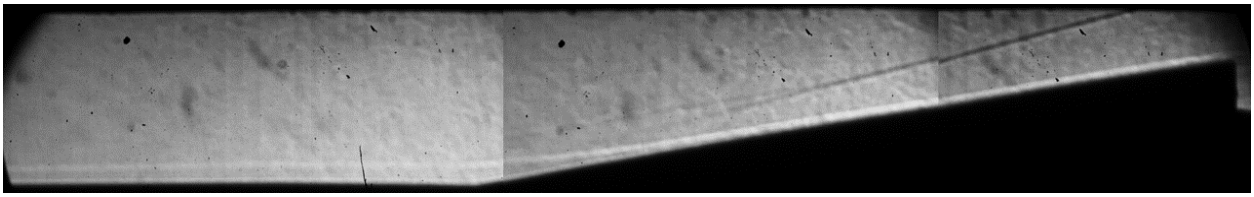

(a) 0.2 ms

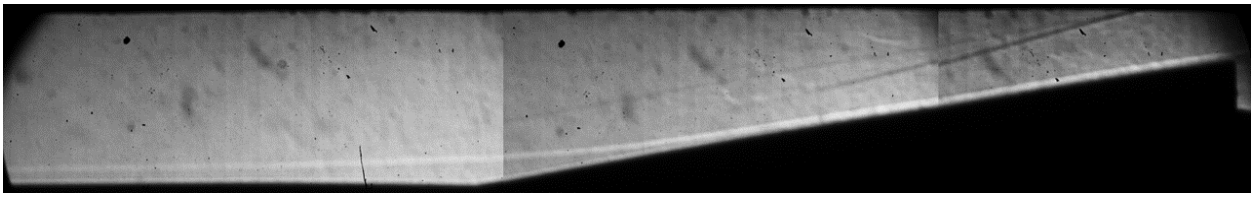

(b) 0.5 ms

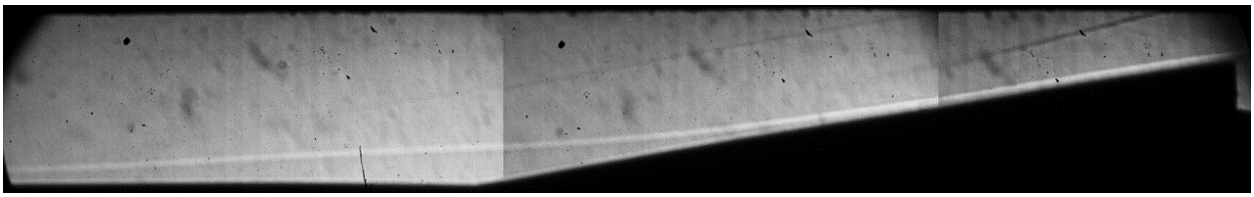

(c) 2.0 ms

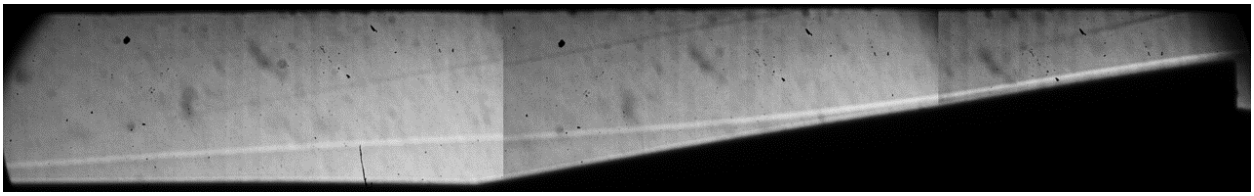

(d) 5.0 ms

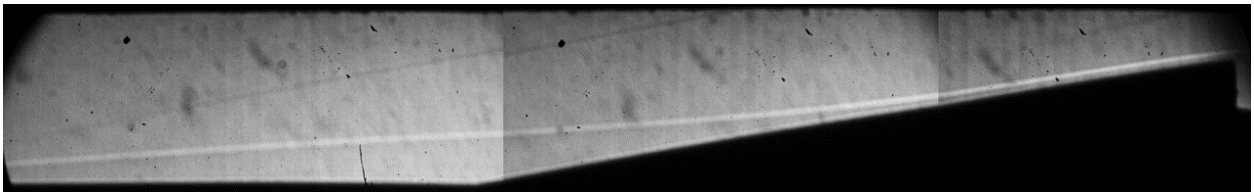

(e) 10.0 ms

Figure 5.6. Bubble formation after quiet flow initiation. Captions list time after first frame that contains a laminar boundary layer. From Runs 1314, 1308, and 1319.

5.7 displays this qualitative vibration measurement. Further testing with a vibrometer is necessary to determine the amplitude of the motion. No waves or other instabilities were directly observed in the shear or boundary layers, perhaps due to smearing from the low shutter speed relative to the instability velocity.

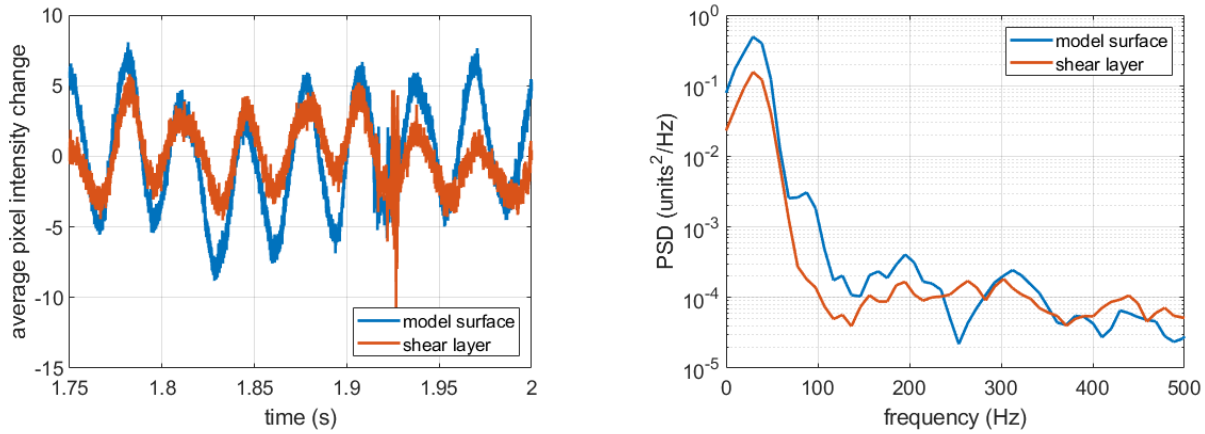

(a) Relative pixel intensities over time for the model surface and shear layer at the corner.

(b) PSDs of relative pixel intensities, with peak around 32 Hz.

Figure 5.7. Sinusoidal variation in pixel intensity at the model surface and of the shear layer 0.526 m downstream of the nosetip highlighting low-frequency model vibration. Average unit Reynolds number of 11.6×10^6/m, from run 1314.

5.2.1.2 Heat Transfer

Heat transfer measurements using IR thermography were made along the flare section for a range of unit Reynolds numbers under quiet flow. A sample of the normalized results can be seen in Figure 5.8. In these images, the flare has been unrolled and stretched to fit a square two-dimensional surface. In general, the heat transfer increases along the duration of the flare, with a location of rapid increase that most likely signifies reattachment. Streamwise streaks, which have been seen in other studies, are not apparent. It was later determined that these runs had a small angle of attack of 0.15° (see Section 5.2.4 for more information on angle of attack effects).

The unit Reynolds number does not appear to have an effect on the laminar-scaled heat transfer. Qualitatively, the results are similar in Figures 5.8a, 5.8b, 5.8c, and 5.8d. All three cases experience an increase in heat transfer at around the same location, which most likely means the reattachment point does not vary significantly with unit Reynolds number. In general, the heat transfer slowly increased moving downstream along the flare until it reached a steady value around 610 mm. The slight (approximately -0.15°) angle of attack

for the quiet flow cases is the cause of the asymmetry in the images. The row of dots around 150° are Kulite sensors.

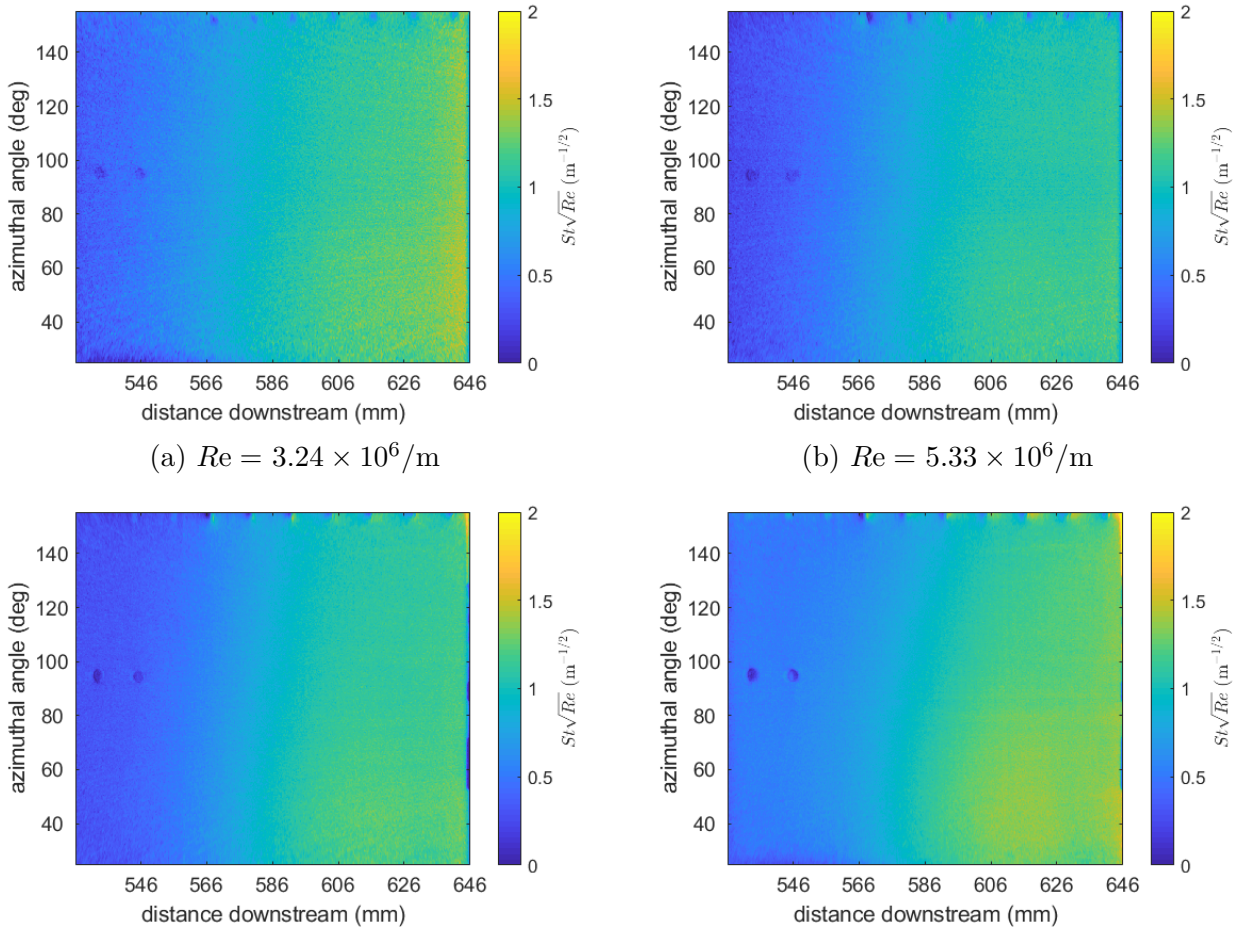

(a) $Re = 3.24 \times 10^6/m$

(b) $Re = 5.33 \times 10^6/m$

(c) $Re = 9.51 \times 10^6/m$

(d) $Re = 11.6 \times 10^6/m$

Figure 5.8. Laminar-scaled heat transfer images on the unrolled 10° flare. Flow is from left to right.

Figure 5.9 plots laminar-scaled heat transfer as a function of the distance downstream, averaged from two slices of the data (located above and below the PCB sensors that can be seen in Figure 5.8 at about 90°). This plot provides a more quantitative view of what is hinted at in the previous figures. The compression corner is at the start of the horizontal axis, 526 mm downstream of the nosetip. The computed heat transfer at two unit Reynolds numbers from DPLR are included [69]. Computations from Dr. Pedro Paredes at NASA Langley made with VULCAN-CFD are also included for comparison [74]. The results are laminar, therefore

the heat transfer profiles collapse with this normalization. DPLR calculations conducted by Dr. Esquieu tended to underestimate the heat transfer along the flare under the separation bubble. Additionally, DPLR computed an increase in the rate of heat transfer rise farther upstream than what was measured, indicating that the computed separation bubble may be smaller than what is physically generated. The schlieren comparison also showed a smaller computed bubble (see Figure 5.3). The VULCAN-CFD results also underestimate the heat transfer under the separation bubble. The reason for the discrepancy between the CFD and the measurements is unknown, but may be due to the experiment reaching the noise floor in the region under the bubble. The measured heat transfer trends are similar to those seen by Schaefer and Ferguson in the 1960s [14]. Note that the heat transfer appears to change from increasing to approximately constant in the 580 to 600 mm range, the same axial location that reattachment is estimated from the schlieren images.

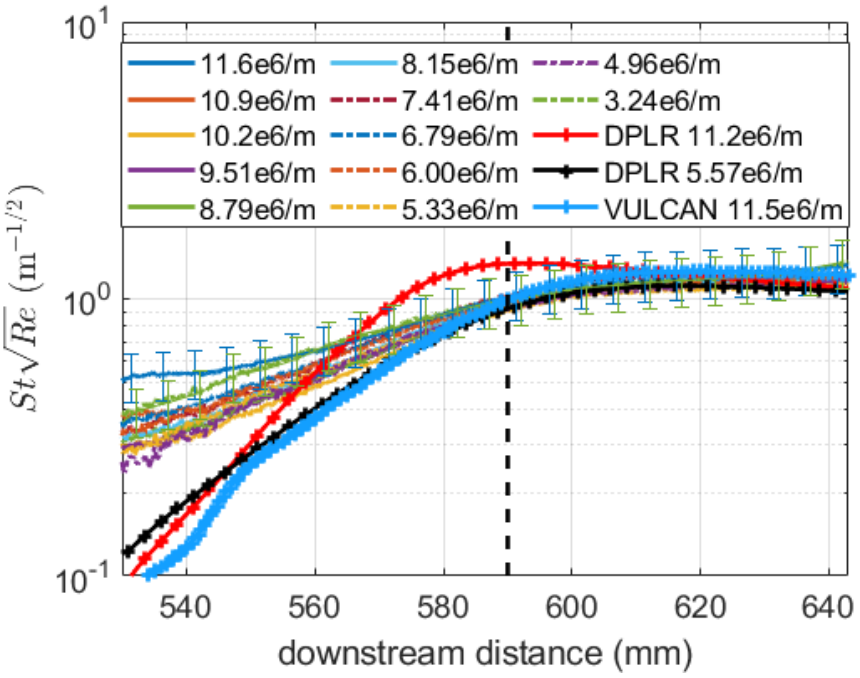

Figure 5.9. Laminar-scaled heat transfer for Re between 3.24×10^6 and 11.6×10^6/m. The compression corner is at the left edge (526 mm downstream). The black dashed line shows the estimated reattachment location.

Table 5.1. Wall pressures along the 10° cone-cylinder-flare for $P_0 = 150$ psia, computed in DPLR. Values were scaled by stagnation pressure to normalize the measured surface pressure fluctuations.

Downstream position (mm)	Wall Pressure (Pa)
361	1023.4
387	1019.8
425	556.05
479	747.30
511	822.63
536	838.00
548	956.65
561	1250.4
577	1654.5
590	1873.3
606	1937.7
619	1950.2
631	1949.7
643	1942.9

5.2.2 Pressure-Fluctuation Measurements

Pressure-fluctuation measurements were made with PCB and Kulite pressure sensors installed in the model surface. Initial analyses use power spectral densities (PSDs) of the pressure signals to determine at what frequencies instabilities exist along the surface, if any are present. Amplitudes have been normalized by the computed surface pressure values given in Table 5.1, which were scaled by the stagnation pressure during the run.

5.2.2.1 Cone and Cylinder

Figure 5.10 shows the PSDs from sensors on the cone and cylinder portions of the model normalized by the wall pressures from Dr. Esquieu's STABL computation, at unit Reynolds numbers between 6.58×10^6/m and 12.0×10^6/m. Figures 5.10a and 5.10b are on the cone, where the second mode instability can be seen clearly between 200 and 300 kHz. As expected with second mode fluctuations, the peak frequency and amplitude of the instability both increase with increasing unit Reynolds number. Once over the cylinder (Figures 5.10c and 5.10d), the second mode amplitudes are smaller as they damp out following the expansion

of the flow. Figure 5.11 plots the RMS integrated amplitudes of these PCBs as a function of the Reynolds number at the sensor.

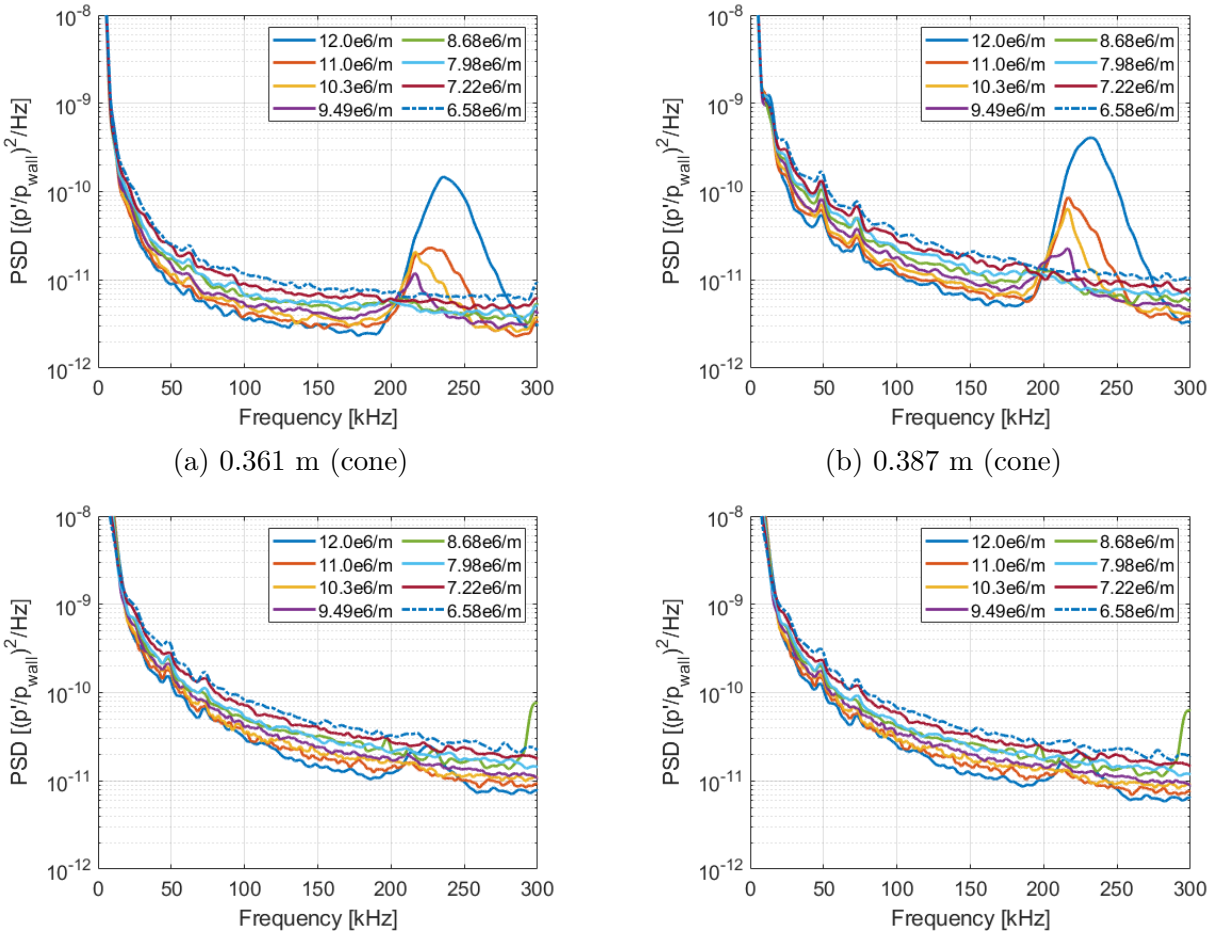

(a) 0.361 m (cone)

(b) 0.387 m (cone)

(c) 0.479 m (cylinder)

(d) 0.511 m (cylinder)

Figure 5.10. PCB PSDs along the 5° cone and the cylinder at unit Reynolds numbers between 6.58×10^6 and 12.0×10^7/m.

AC-coupled Kulites on the cylinder resulted in similar PSDs showing the dampened second mode (Figure 5.12). Note that the usual 300 kHz Kulite resonance generally was not excited in quiet flow except when large instabilities were present (such as on the downstream end of the flare). Unlike in the nearby PCB spectra, the upstream-most Kulite (at 0.482 m) showed a strong signal around 20 kHz. This instability was not visible in the PCB results. The PCBs have a cutoff frequency of 11 kHz and generally contain more noise from vibrations in the lower frequency ranges, obscuring signals below 50 kHz. This frequency

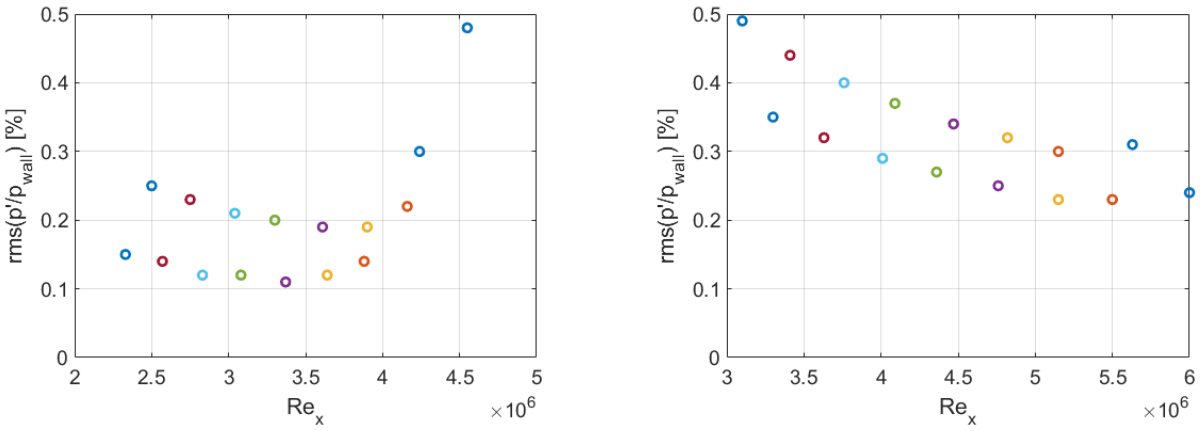

(a) Cone (b) Cylinder

Figure 5.11. Integrated RMS amplitudes of PSDs along the 5° cone and the cylinder at unit Reynolds numbers between 6.58×10^6 and 12.0×10^7/m. Each color corresponds to a single run. Integrated between 50 and 290 kHz.

peak may be a sign of the separation shock oscillating. The frequency corresponds to a Strouhal number of 0.1. Figure 5.13 plots the integrated RMS amplitude of the instability as a function of sensor Reynolds number (integrated between 5 and 50 kHz). The normalized amplitude begins increasing with Reynolds number around 5×10^6. Further work is needed to understand this 20 kHz oscillation.

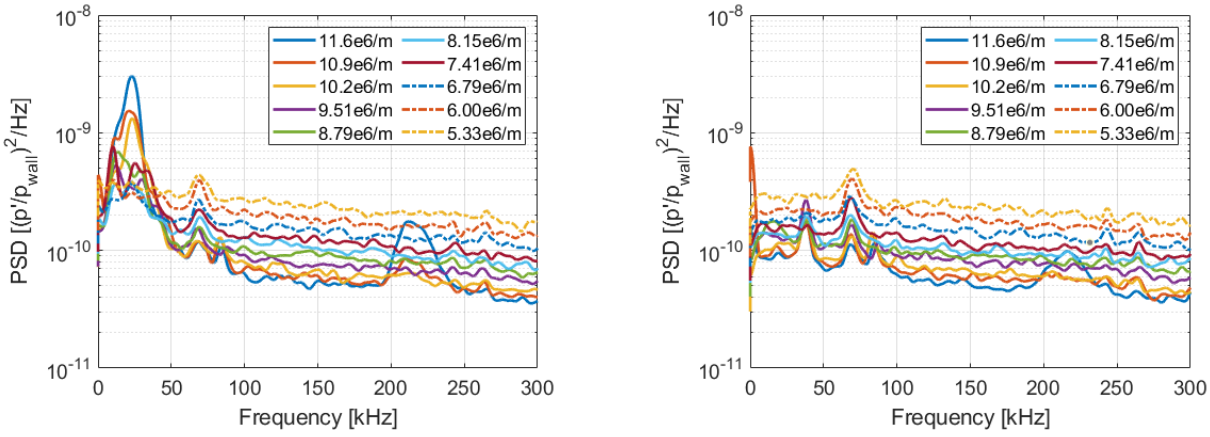

(a) 0.482 m (b) 0.507 m

Figure 5.12. Kulite PSDs along the cylinder at unit Reynolds numbers between 5.31×10^6 and 12.4×10^6/m.

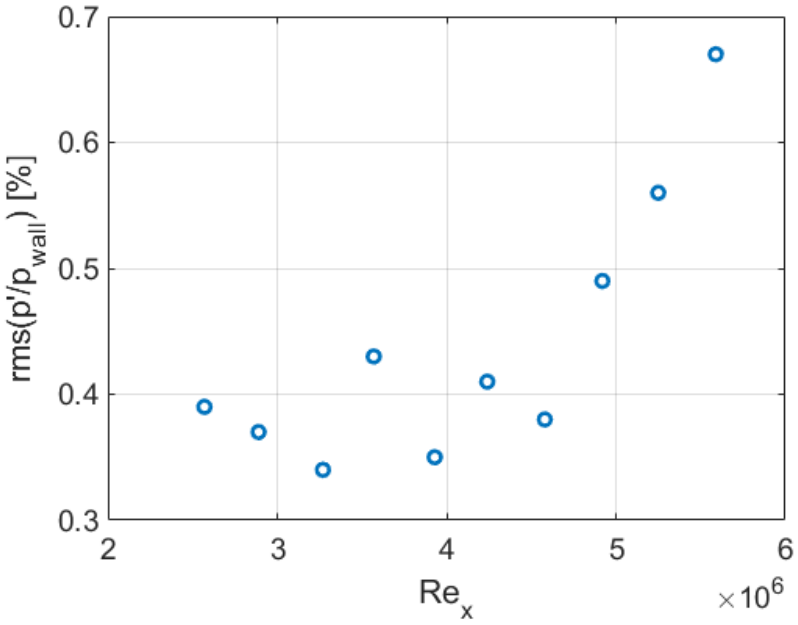

Figure 5.13. RMS amplitude for 20 kHz instability seen in the Kulite located 0.482 m downstream of the nosetip. Plotted as a function of sensor Reynolds number. Integrated between 5 and 50 kHz.

5.2.2.2 Flare

Figure 5.14 plots the PSDs for PCB sensors along the flare moving downstream. On the flare, the second mode instability can be seen amplifying between 170 and 290 kHz. As on the cone, an increase in unit Reynolds number corresponds to an increase in both amplitude and peak frequency for this instability, as expected. In addition, the peak amplitude also generally increases moving downstream. A second frequency peak exists between 50 and 170 kHz. This peak is not seen in the measurements made on the 3.5° flare without separation, and is believed to be due to an instability that is generated or amplified in the shear layer above the separation bubble. This instability also increases in amplitude with unit Reynolds number, but does not change peak frequency. However, moving downstream, the peak frequency tends to increase until the instability breaks down into two distinct peaks at the last PCB sensor. The integrated RMS amplitudes for the instabilities seen along the flare are plotted in Figure 5.15. Data from Entries 5 and 10 are shown to display the repeatability of instabilities. The PCB measurements from Entry 10, however, have slightly higher integrated

amplitudes for the lower sensor Reynolds numbers due to the higher noise floor of the cards used with the data acquisition system, compared to the oscilloscopes used during Entry 5 and the lower-noise cards used with the Kulites.

Figure 5.16 plots PCB and Kulite power spectra for several downstream stations along the flare. Moving downstream, the second mode amplifies but does not change significantly in peak frequency due to the relatively constant thickness of the boundary layer along the flare. The shear-generated instability, however, both amplifies and increases in peak frequency moving downstream between 0.547 m and 0.631 m, although it decreases in amplitude at 0.643 m where it splits into two distinct peaks. The same trends were seen in both the PCB and Kulite sensors, although slightly different amplitudes were obtained most likely due to the different frequency responses of the sensors.

To see whether these fluctuations are local oscillations or traveling waves, the coherence between PCB sensor pairs both upstream and downstream of the reattachment point was computed. The reattachment point was estimated to be between 0.58-0.60 m downstream of the nosetip based on the schlieren described in Section 5.2.1.1. Figure 5.17 displays these coherences, shown with the PCB power spectra from the same run for reference. The signals were high-pass filtered at 25 kHz. Upstream of reattachment, when the sensors are under the bubble, only low levels of coherence are seen (Figure 5.17b) and the associated power spectral densities reveal small frequency peaks for only the downstream-most sensor. The two narrow peaks in the coherence plot at 120 and 160 kHz are due to electronic noise, and can be seen in the prerun spectra in Figure 5.17a. However, downstream of reattachment, peaks can be seen in the sensor PSDs between 50-170 kHz as well as around 220 kHz, as shown in Figure 5.17c. High coherence values are associated with adjacent pairings of the PCBs downstream of reattachment (Figure 5.17d). The distances between paired sensors is 12.7 mm. The coherence is significant for both the second mode fluctuations as well as the 50-170 kHz instability in all pairs, implying that both the second mode and the lower-frequency fluctuations are traveling waves. Due to evidence from FLDI measurements (discussed in Section 5.2.3), as well as their behavior when controlled disturbances are introduced (Chapter 6), these are termed "shear-generated traveling waves." This is the first time naturally-

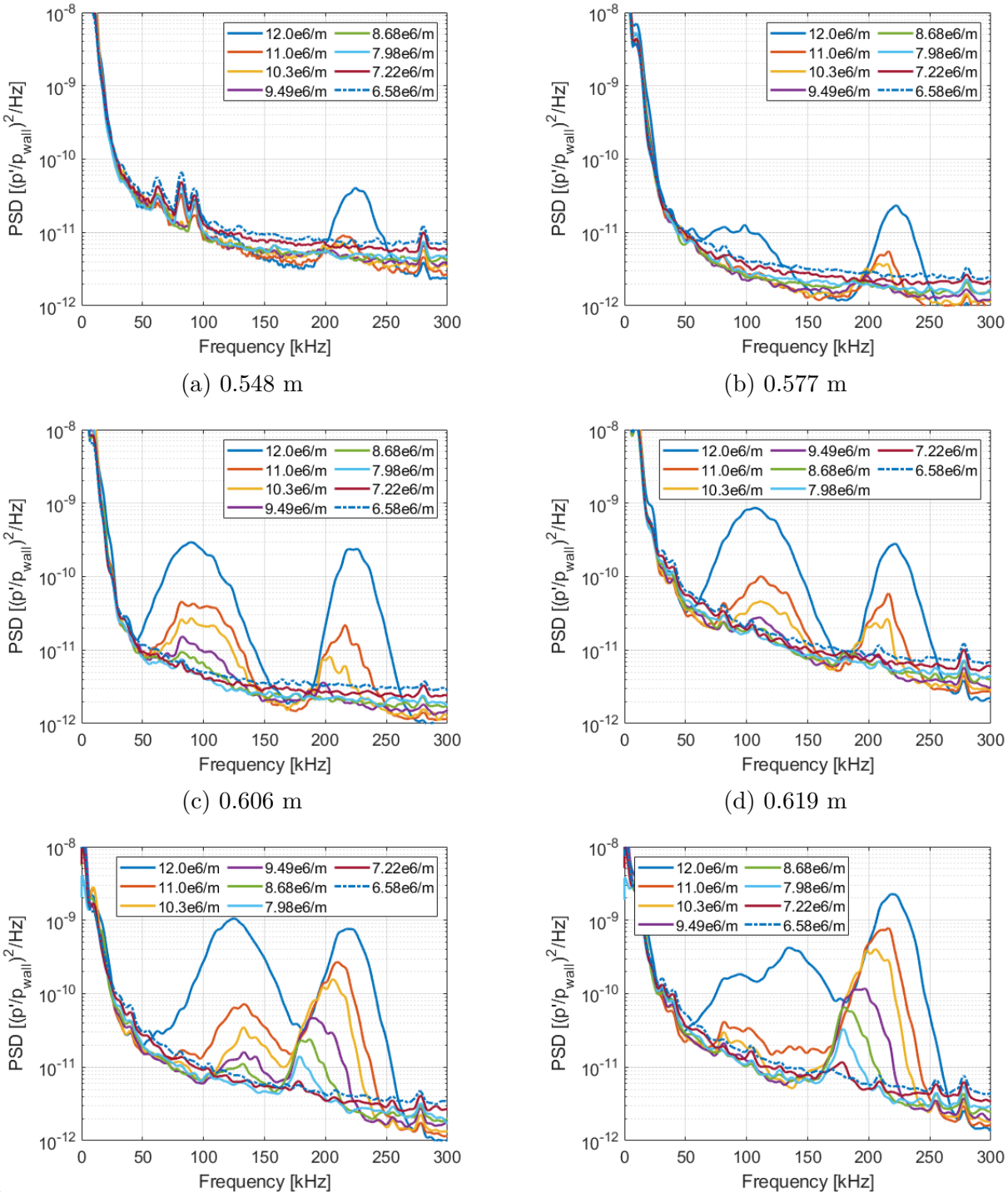

(a) 0.548 m

(b) 0.577 m

(c) 0.606 m

(d) 0.619 m

(e) 0.631 m

(f) 0.643 m

Figure 5.14. PCB PSDs along the 10° flare at unit Reynolds numbers between 6.58×10^6 and 12.0×10^6/m, from Entry 5. Distances are downstream of the nosetip.

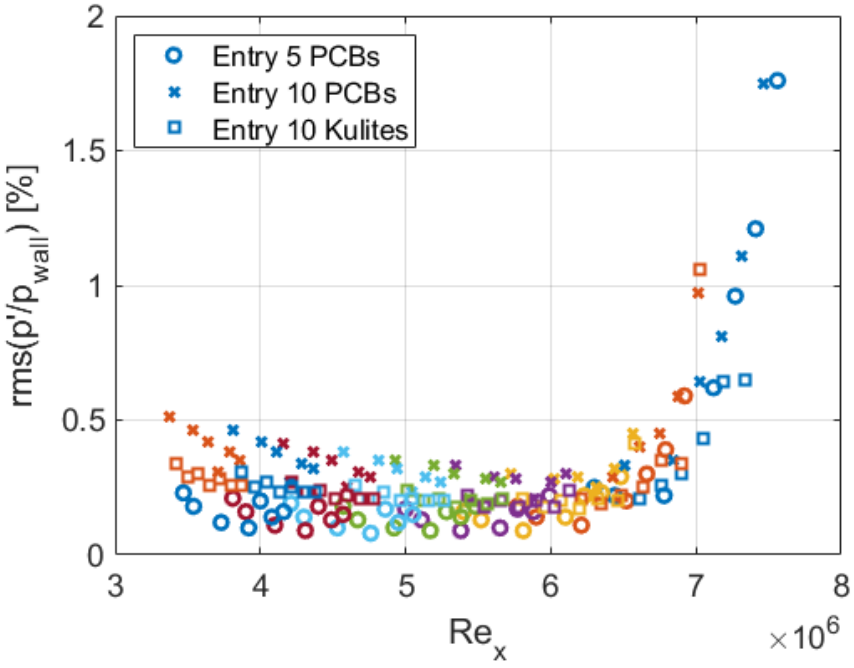

Figure 5.15. Integrated RMS amplitudes of surface pressure fluctuations along the 10° flare under the reattached boundary layer. In quiet flow, integrated between 50 and 270 kHz. Plotted as a function of length Reynolds number based on sensor axial position.

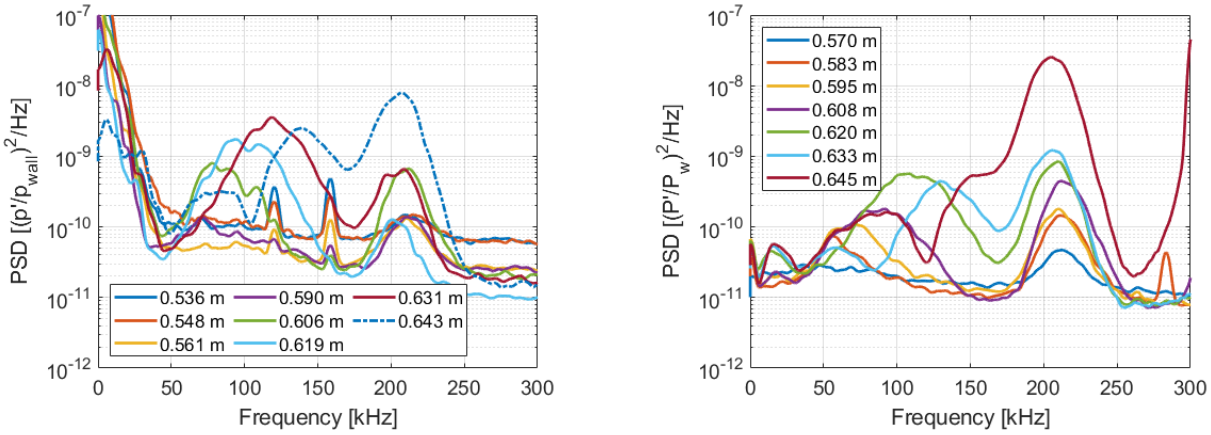

(a) PCB spectra

(b) Kulite spectra

Figure 5.16. Power spectra for $Re = 11.5 \times 10^6/\text{m}$ at several downstream locations along the flare, from Run 1037.

occurring traveling waves associated with a separation bubble have been directly measured in quiet hypersonic flow.

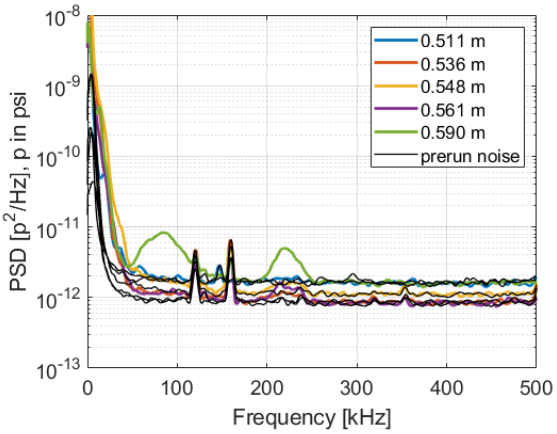

(a) PCB PSDs upstream of reattachment.

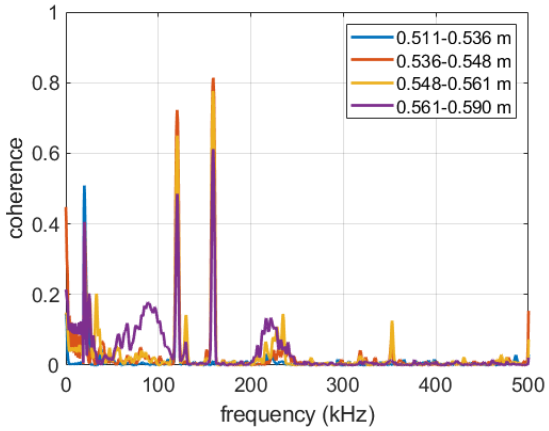

(b) Coherence of PCB pairs upstream of reattachment.

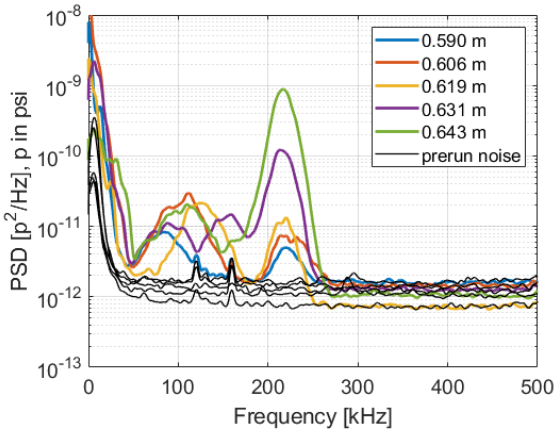

(c) PCB PSDs downstream of reattachment.

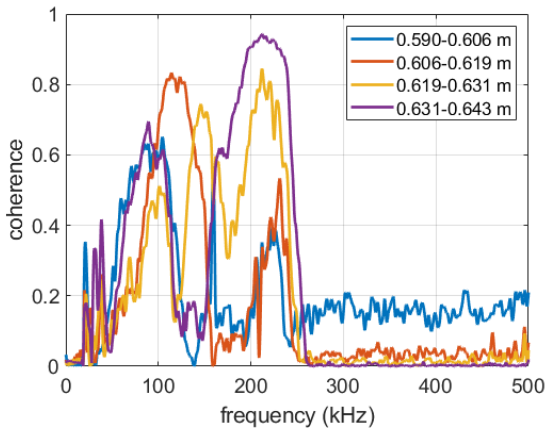

(d) Coherence of PCB pairs downstream of reattachment.

Figure 5.17. Power spectral densities and coherence between PCB sensors upstream and downstream of reattachment along the 10° flare, $Re = 11.4 \times 10^6/\text{m}$. From Run 1040.

Bandpassing the signal (using Matlab's `bandpass` function) to look at the two instabilities separately reveals two different phase speeds. Figure 5.18 highlights this difference. Figures 5.18a and 5.18b plot an example of the cross-correlation as a function of lag time for the shear-generated and second-mode waves, respectively. The lag times at maximum cross-correlation are in Figure 5.18c, taken from 60 runs that span two entries, all at $Re = 11.58 \times 10^6/\text{m}$. Linear fits have been made to the lag plot to estimate the velocities of the two instabilities. The second mode (between 170 and 290 kHz) has a phase speed of around

695 m/s (about 81% of U_∞), while the shear-generated traveling waves (between 50 and 170 kHz) are around 843 m/s (about 98% of U_∞). Note that these speeds assume no waves are located between the sensors, otherwise the velocity needs to be divided by the number of cycles between them. Due to the unusually high velocity relative to the freestream computed for the shear-generated instability, it is likely that there is at least one cycle between each consecutive sensor; future measurement FLDI with closely-space beam pairs could be used to more accurately determine the disturbance velocity. As for the non-separating model, the second mode disturbance speed is very close to the phase velocity of a slow acoustic wave, $c = (1 - 1/M)U_\infty$, where $c = 0.83U_\infty$ for $M = 6$ [71], as was the case with the 3.5° flare (see Section 4.2.2). This contrasts with the shear-generated instability, which convects at a higher velocity.

Figure 5.19 shows a sample of the pressure fluctuation time series from a single run. The unit Reynolds number was 12.0×10^6/m, and all four sensors were under the reattached boundary layer. In the time series, a wave packet with a frequency of about 105 kHz can be seen in the three upstream-most sensors. This frequency corresponds to the shear-generated traveling waves. The amplitude of the oscillations as they convect downstream remains relatively constant. A short time later, a higher frequency wave packet (around 215 kHz) can be seen in the time series; these fluctuations are due to the second mode instability. This wave packet is seen in all four sensors, and amplifies as it convects downstream.

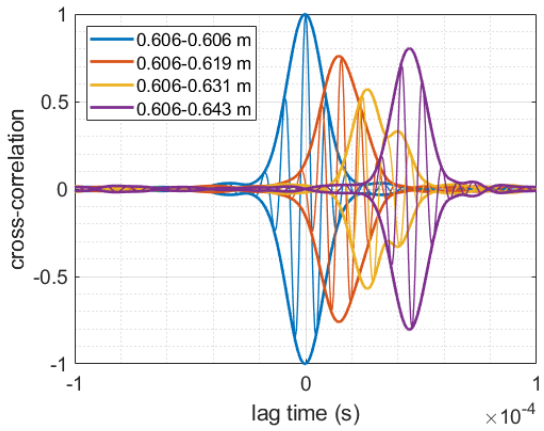

(a) Cross-correlation for the shear-generated traveling waves (bandpassed at 50-170 kHz)

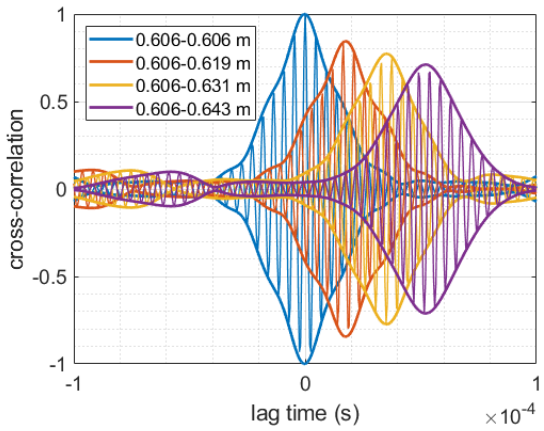

(b) Cross-correlation for the second mode (bandpassed at 170-290 kHz)

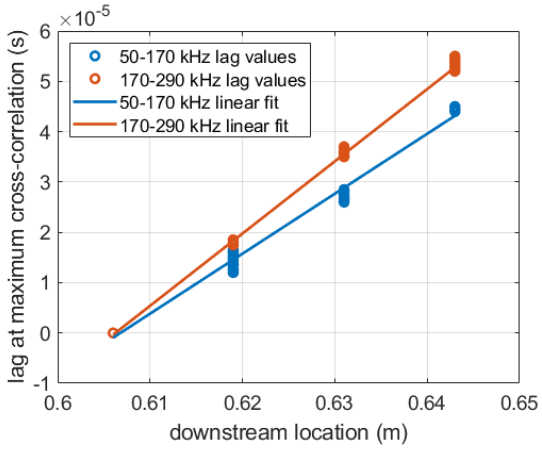

(c) Lag times at maximum cross-correlation

Figure 5.18. Cross-correlation and lag times used to estimate disturbance velocities for the shear-generated and second-mode waves. The cross-correlation plots are from Run 0714, while the lag times are accumulated from 60 runs across Entries 7 and 9. All results are at $Re = 11.58 \times 10^6/\text{m}$.

Computations by Paredes et al. offer a probably explanation of the shear-generated waves. Fig. 5.20 shows an example from their results. Good agreement was found between the shear-generated peak frequencies. From the simulations, the source of the shear-generated instability appears to be the oblique first modes along the cone, although analysis of these results is ongoing. These computations will be discussed in more detail in future papers.

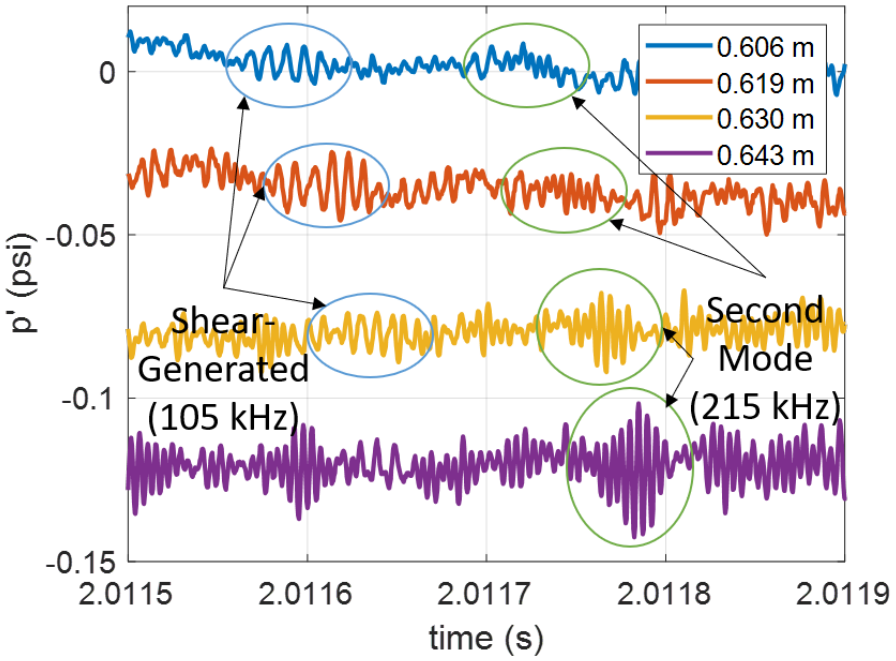

Figure 5.19. Time series showing progression of shear-generated traveling waves as well as the second mode in the reattached boundary layer. Re = 12.0e6/m, from Run 0519.

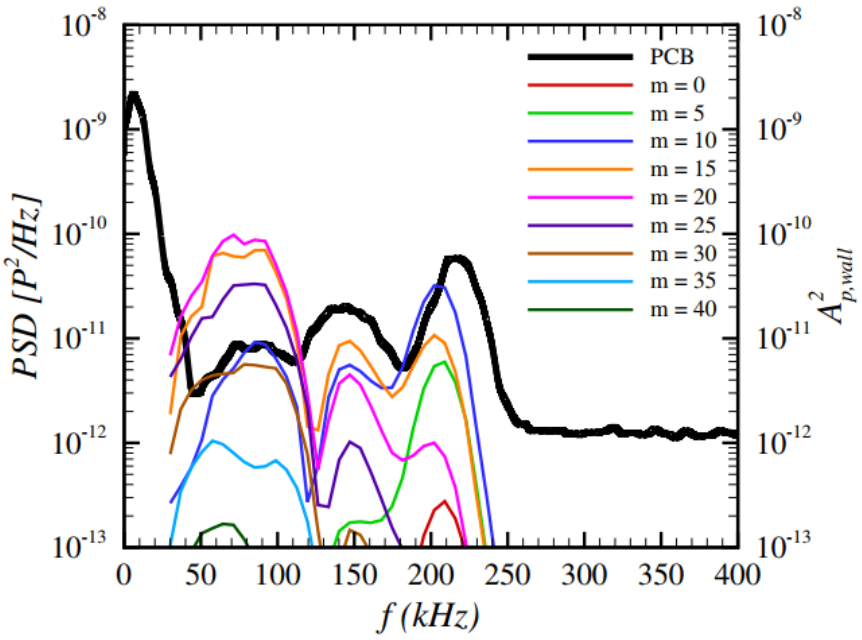

Figure 5.20. Figure from Ref. [74] highlighting agreement between PCB power spectral density and computed wall-pressure disturbance spectra. Re = 11.5×10^6/m, 0.631 m downstream of nosetip.

5.2.2.3 Nonlinear Interactions

The bicoherence of the PCB pressure measurements was used to study quadratic nonlinearities present in the signals. The script used to compute the bicoherence was written by Edelman, and a complete description of the code and the significance of the bicoherence can be found in Appendix F of his dissertation [40]. The bicoherence can reveal the existence of harmonics as well as the nonlinear interaction between fluctuation modes; harmonics are seen when the bicoherence has a peak near $f_1 = f_2$, while a second-order nonlinear interaction is present when the bicoherence peaks where $f_1 \neq f_2$, with f_1 and f_2 being the frequencies of the interacting modes. In either case, if a nonlinearity is present, a third mode, $f_3 = f_1 + f_2$ should exist in the power spectrum (although it may be below the noise floor). See Appendix F of Edelman's dissertation for more information on using the bicoherence to see hidden signals [40].

Figures 5.21 through 5.24 show the power spectra and squared bicoherence, b^2, for a series of PCBs moving downstream along the model. The data are from Run 0732, with $Re = 11.45 \times 10^6/\text{m}$. Progressing downstream along the model from Figure 5.21 through Figure 5.24, nonlinearities appear and amplify. For clarity, the nonlinear interactions will be labeled N_1, N_2, etc in the descriptions. The 95% significance level of the bicoherence for these plots is $b^2_{95} = 0.0075$.

Starting at 0.606 m downstream, a small peak ($b^2 = 0.040$) in the bicoherence can be seen between an f_1 of 200-250 kHz and an f_2 of 60-100 kHz (N_1). This peak represents a nonlinear interaction between the apparent second mode fluctuations and the shear-generated traveling waves, and implies that a peak around 260-350 kHz might exist that would show in the PSD if the fluctuations were strong enough and the noise floor low enough. For PCBs upstream of this location, the two peaks were still seen in the spectra (see Figure 5.16a), but the bicoherence did not reveal any nonlinear interactions between them.

Moving downstream to 0.619 m, the bicoherence has a stronger b^2 value for N_1 (over 50% higher than at the previous location, with $b^2 = 0.063$) in similar frequency ranges. In addition, there are two weaker peaks; one of which represents a harmonic generation at around 215 kHz (N_2), and the other a nonlinear interaction between the 200-250 kHz mode

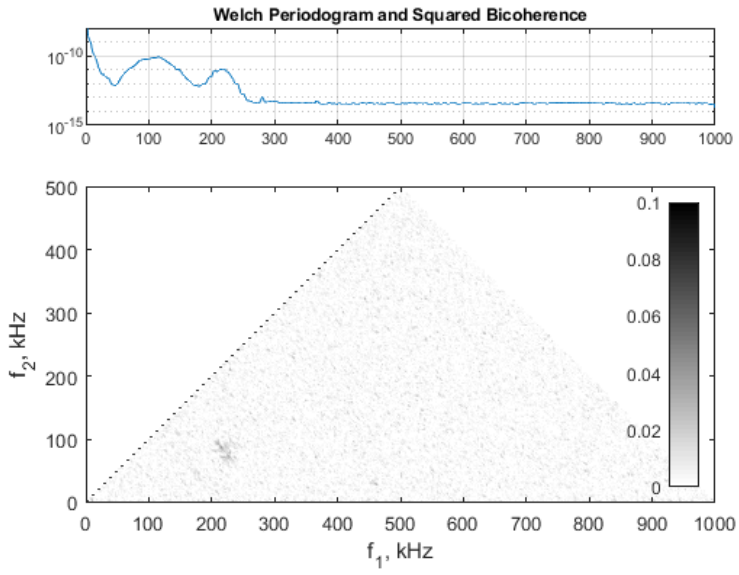

Figure 5.21. PCB bicoherence from Run 0732 at 0.606 m downstream. Maximum $b^2 = 0.040$ at $(f_1, f_2) = (216, 88)$ (significance threshold $b^2_{95} = 0.0075$). This peak corresponds to a nonlinear interaction between the second mode and shear-generated waves, N_1.

and a 100-140 kHz mode (N_3). The power spectral density at this location shows three distinct peaks, at 61, 128, and 216 kHz. The 216 kHz peak corresponds to the second mode, while the 61 and 128 kHz peaks are from the shear-generated traveling instability after is has begun to break down to two peaks. The bicoherence values for N_2 and N_3 are 0.043 and 0.041, respectively.

At 0.631 m downstream, the harmonic generator N_2 has become the dominant nonlinearity with $b^2 = 0.125$. N_1 has also continued amplifying, with $b^2 = 0.084$. N_3 is not as clear in this bicoherence plot, although a local maximum of $b^2 = 0.029$ is present at $(208, 156)$. In the power spectral density, there are now peaks at 89, 156, and 215 kHz.

Finally, 0.643 m downstream has the strongest nonlinear interactions according to the bicoherence. As before, N_2, the harmonic generator, is the strongest nonlinearity with $b^2 = 0.419$ at its peak. N_1 now has a b^2 value of 0.112, while N_3 is at 0.160. With such a large bicoherence, the harmonic of the 218 kHz mode can be seen in the power spectral density, a peak at 435 kHz. A peak at 328 kHz is also visible in the PSD, the result of the

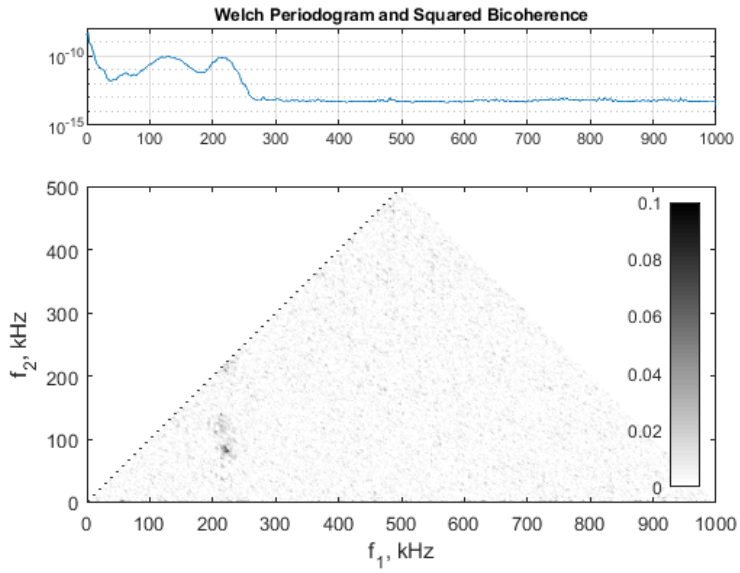

Figure 5.22. PCB bicoherence from Run 0732 at 0.619 m downstream. b^2 has a peak at $(222, 80)$ with a value of 0.063 (N_1), as well as weaker peaks at $(220, 210)$ and $(214, 140)$ with values of 0.043 (N_2) and 0.041 (N_3), respectively (significance threshold $b^2_{95} = 0.0075$).

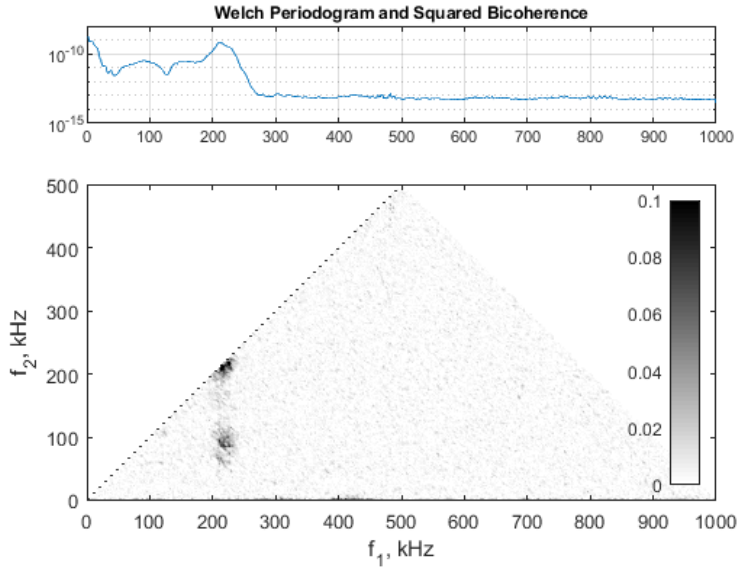

Figure 5.23. PCB bicoherence from Run 0732 at 0.631 m downstream. b^2 has peaks at $(212, 92)$ and $(214, 210)$ with values of 0.084 (N_1) and 0.125 (N_2), respectively (significance threshold $b^2_{95} = 0.0075$).

nonlinear interaction N_3. Similar to previous spectra, the apparent second mode peak is at 218 kHz, as well as the shear-generated peak at 110 kHz. In addition, a new nonlinearity, N_4, exists for f_1 between 400-460 kHz and f_2 between 190-240 kHz. This nonlinearity represents the first harmonic interacting with the 218 kHz mode.

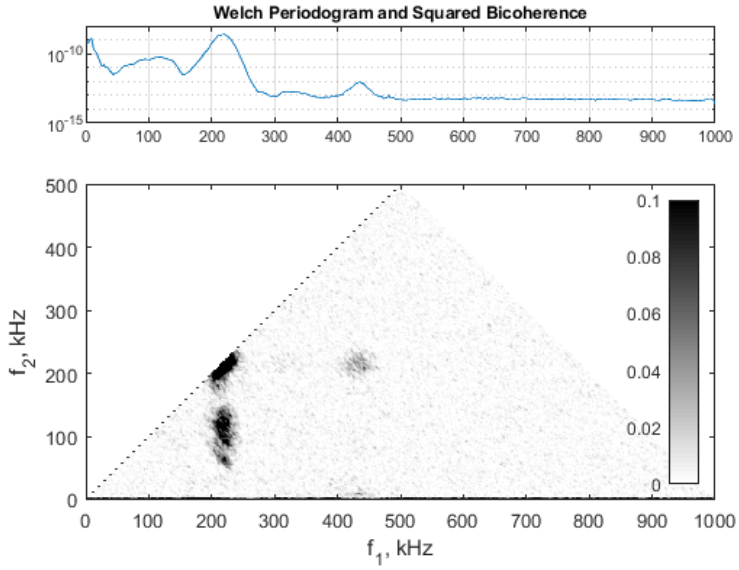

Figure 5.24. PCB bicoherence from Run 0732 at 0.643 m downstream. b^2 has peaks at $(220, 64)$, $(224, 218)$, $(214, 100)$, and $(442, 208)$ with values of 0.112 (N_1), 0.419 (N_2), 0.160 (N_3), and 0.060 (N_4), respectively (significance threshold $b^2_{95} = 0.0075$).

Figure 5.25 shows the power spectra and squared bicoherence of the PCB 0.643 m downstream of the nosetip during Run 0716 at the same unit Reynolds number as Figures 5.21 through 5.24. This plot provides an example of the repeatability of the bicoherence; both Runs 0714 and 0732 have four primary peaks in b^2, approximately around $(f_1, f_2) = (220, 60)$, $(220, 115)$, $(225, 215)$, and $(440, 215)$.

This bicoherence analysis highlights the interactions between the shear-generated and second-mode instabilities. This is significant because it shows that the two instabilities are not isolated, but form additional, higher-frequency disturbances as they convect downstream. It is possible that this interaction can lead to transition if the disturbances had more space to convect. In general, boundary-layer transition tends to include a region of linear amplification

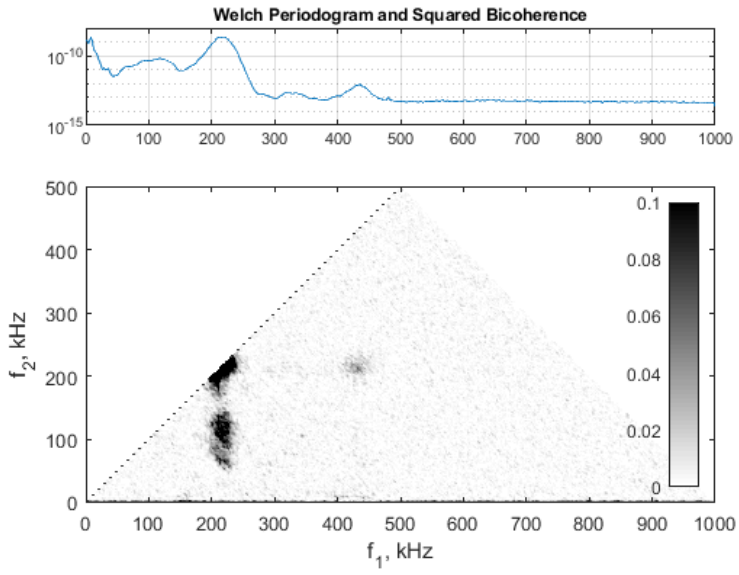

Figure 5.25. PCB bicoherence for Run 0716 at 0.643 m downstream highlighting repeatability of nonlinear interactions. b^2 has peaks at $(214, 68)$, $(228, 222)$, $(218, 110)$, and $(432, 212)$ with values of 0.113 (N_1), 0.409 (N_2), 0.172 (N_3), and 0.063 (N_4), respectively (significance threshold $b^2_{95} = 0.0075$).

followed by a region of nonlinear breakdown. While transition was not observed for this geometry under quiet flow, this analysis provides an example of the potential importance of the shear-generated instability through its nonlinear interaction with the second mode.

5.2.2.4 Mode Switching

For most times during a run started near $Re = 12.0 \times 10^6$/m, the shear-generated fluctuations grow along the flare in the boundary layer downstream of reattachment, but at the PCBs near either 0.631 m or 0.643 m downstream, the peak breaks down from one to two approximately equal-amplitude peaks and remain neutral in overall amplitude towards 0.643 m. However, at certain times during various runs, this breakdown process gets altered, with one larger peak seen at 0.631 m at the same frequency where previously there was a trough between two peaks. This phenomenon, here termed a "mode switch," generally lasts between 0.02 and 0.06 seconds, and does not correspond to a turbulent burst, shock reflection, or other aerodynamic event recorded on the hot film mounted in the tunnel wall. It occurred

during multiple runs across different entries, but no consistent trend was found for when it would happen. Mode switches were observed both during and between expansion wave reflections, so do not appear to be related to those reflection.

Figure 5.26 displays an example of this event. Spectrograms with the same intensity scale are depicted at each downstream station. Changes around times 2.22 and 2.45 seconds can be seen in the spectrograms for 0 and 0.619 m downstream. At 0.619 and 0.631 m downstream, the shear-generated fluctuations become dominant in amplitude over the second mode fluctuations at these two times, while at 0.643 m downstream they become approximately equal in amplitude to the second mode. Figure 5.27 shows two samples from the time series of these PCB sensors during each mode. In Figure 5.27a, the second mode wave packets can be seen amplifying moving downstream. From their PSDs, the wave packets have a relatively constant peak frequency of 210 kHz at each PCB station, while the peak amplitudes (integrated from 190 to 250 kHz) grow moving downstream (Figure 5.28). In Figure 5.27b, the shear-generated traveling wave packets are seen amplifying and convecting downstream. The peak frequencies of these waves increase linearly moving downstream, with a rate of approximately 1.4 kHz per mm. The RMS amplitudes (integrated from 50 to 170 kHz) amplify moving downstream, but appear to approach a limit of about 28 Pa.

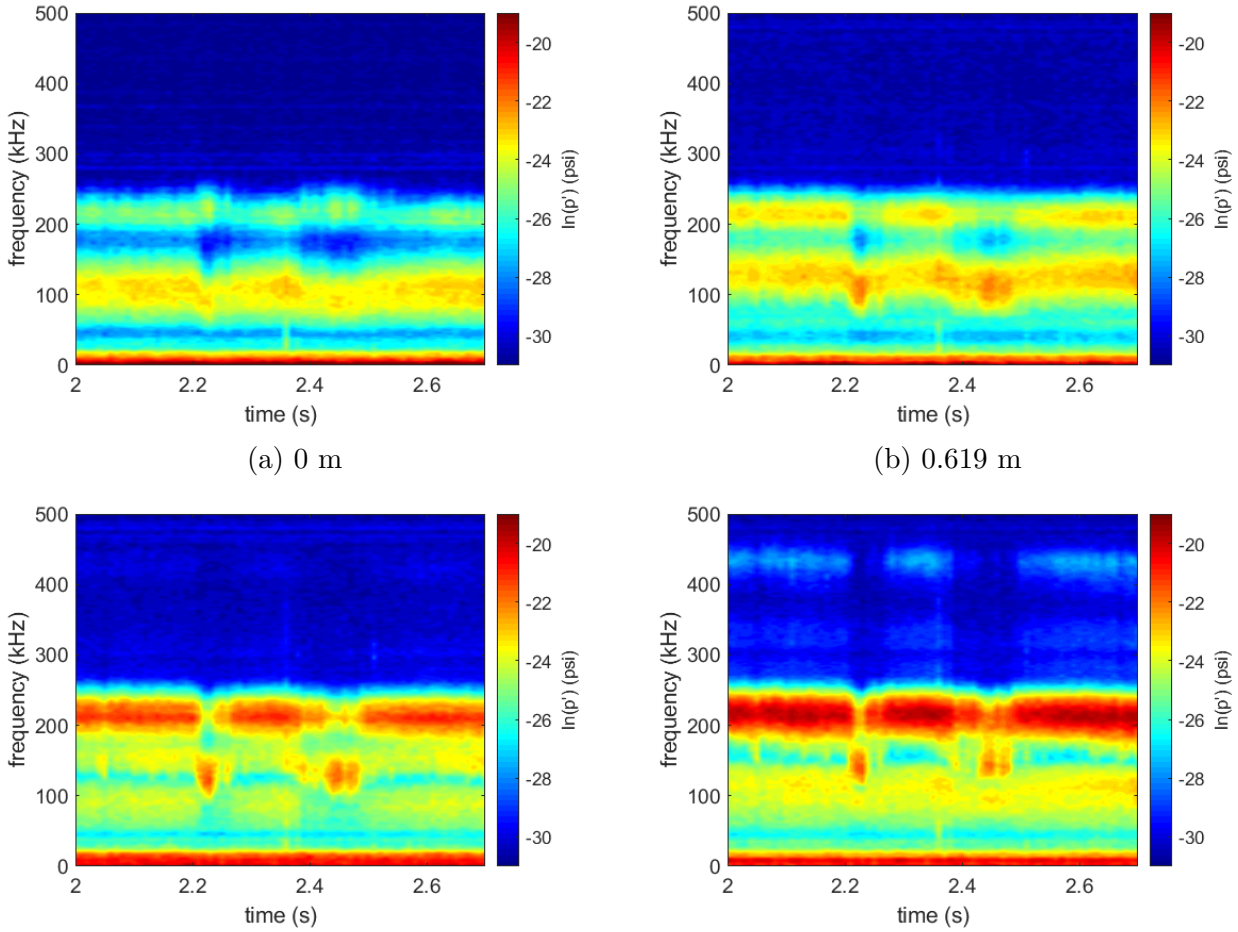

(a) 0 m

(b) 0.619 m

(c) 0.631 m

(d) 0.643 m

Figure 5.26. Spectrograms of PCB data on downstream end of flare, highlighting change in the dominant instability around $t = 2.24$ and $t = 2.45$ seconds under the reattached boundary layer. From Run 0716.

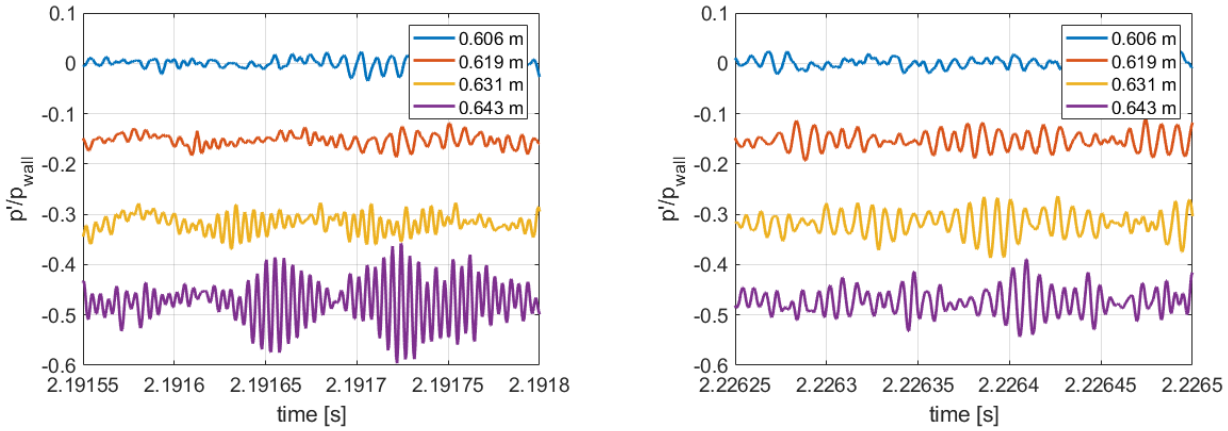

(a) Second-mode waves dominating (b) Shear-generated waves dominating

Figure 5.27. Waterfall plot of PCB time series for the two different modes shown in Figure 5.26. Signals are offset vertically for clarity. From Run 0716, $Re = 11.38 \times 10^6/\text{m}$.

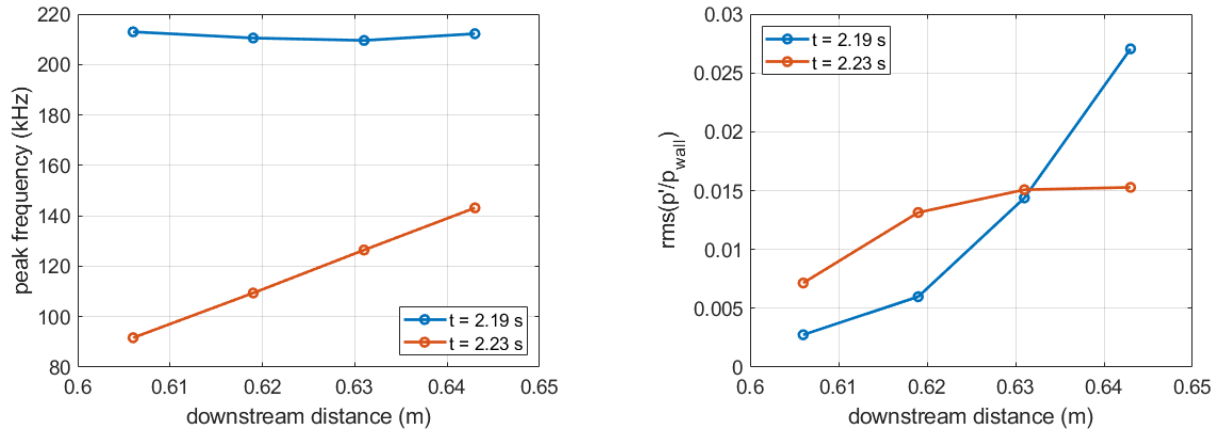

(a) Peak frequencies (b) RMS amplitudes

Figure 5.28. Peak frequencies and amplitudes as a function of downstream distance for the two different modes shown in Figure 5.26. The second mode is dominant at 2.19 s, while the shear-generated instability is dominant at 2.23 s. From Run 0716, around $Re = 11.38 \times 10^6/\text{m}$.

5.2.2.5 Repeatability

It is important to consider the run-to-run and entry-to-entry repeatability of the instabilities that were measured. Instability and transition are known to be sensitive to small changes in experimental conditions. Since each off-surface measurement with the FLDI required its own run, dozens of runs at the maximum quiet stagnation pressure have been completed over several entries. While the FLDI beams were moved between runs to measure different distances from the model surface, the PCB sensors remained in the same position (on the model surface) each time. These runs, which all encompass the same unit Reynolds numbers, can be used to look at the consistency of the spectra measured with the PCB sensors under identical conditions for the 10° cone-cylinder-flare.

Data from 60 runs spread across Entries 7 and 9 for the four downstream-most PCBs were collected into histograms in Figure 5.29. These sensors were all located on the flare under the reattached boundary layer. The spectra used to obtain the values were divided into two parts; a 50-170 kHz section was selected to encompass the shear-generated traveling waves, and a 170-290 kHz section was chosen for the second-mode fluctuations.

Figures 5.29a and 5.29b display the results for the shear-generated traveling waves. For this instability, the peak frequencies tended to have a large spread between sensors. Moving downstream from 0.606 m to 0.619 m, the peak shifts towards higher frequencies. This trend is similar to what McKiernan observed with his artificially induced traveling waves [35], [36]. However, at 0.631 m downstream the peaks become more ambiguous as the waves tend to break into two different frequencies, with either the lower or higher lobe dominating depending on the particular run. In Figure 5.29a, there are actually three groups of peak frequencies, one around 90 kHz, one around 130 kHz, and one around 150 kHz. The 90 kHz group corresponds to the lower of the two peaks that is generated at that location, while the 150 kHz group corresponds to the higher of the two. The 130 kHz group exists due to mode switching (see Figure 5.26c for an example of this). By 0.643 m, the two peaks remerge into a new peak with a frequency somewhere between the two. The amplitudes of the peaks, however, had a much tighter spread than the frequencies. The low-frequency traveling waves tended to have an integrated RMS around 10 Pa, or about 0.5% of the computed wall

pressure, with a standard deviation between 2 and 3 Pa depending on which sensor is of interest. The relatively constant amplitudes potentially indicate that the shear-generated waves may be neutrally stable downstream of reattachment.

The second-mode results can be seen in Figures 5.29c and 5.29d. The second-mode peak frequencies centered around 220 kHz, and in general did not vary moving downstream. This lack of variation is most likely due to the relatively constant thickness of the boundary layer along the flare after reattachment. The peak amplitudes, however, did vary with distance downstream. Near reattachment, at 0.606 m, the second-mode RMS amplitude is between 3 and 4 Pa (about 0.2% of the computed wall pressure). Moving downstream, the amplitude begins to increase until it is over 2.5% of the computed wall pressure, and it also spread in variance between runs. The standard deviation between runs goes from 0.5 Pa (0.02% of P_{wall}) near reattachment to about 10 Pa (0.5% of P_{wall}) by the 0.643 m.

The integrated RMS amplitudes for each instability is plotted as a function of downstream distance in Figure 5.30. Lines are plotted connecting the mean values at each axial position for both instabilities. As seen in the previous histograms, the shear-generated instability maintains a relatively constant amplitude, averaging around 0.5% of the computed wall pressure. The variability from sensor to sensor also remains relatively constant for this instability. The second mode, however, increases in amplitude moving downstream. It also sees an increase in variability at each consecutive sensor.

Figure 5.31 shows a selection of PSDs from the PCB located the farthest downstream. For all cases, $Re = 11.58 \times 10^6$/m. Differing noise floors between the two entries is due to the different data collection methods used. In Entry 7, Tektronix oscilloscopes acquired the data, while in Entry 9 the HBM data acquisition system (DAQ) was used. The DAQ can have higher noise floors when utilizing the high-speed cards without filtering, as was the case for Entry 9 (see Section 2.9). In Figure 5.31a, it can be seen that the pressure fluctuations (both from the second-mode and the shear-generated traveling waves) are repeatable across runs and entries. However, matching unit Reynolds number does not guarantee identical results. Figure 5.31b gives an example of PSDs for the same PCB from a different selection of runs. While the spectra in this case are again similar in peak frequencies and general shape, the amplitudes of the instabilities vary. These differences may be due to the mode

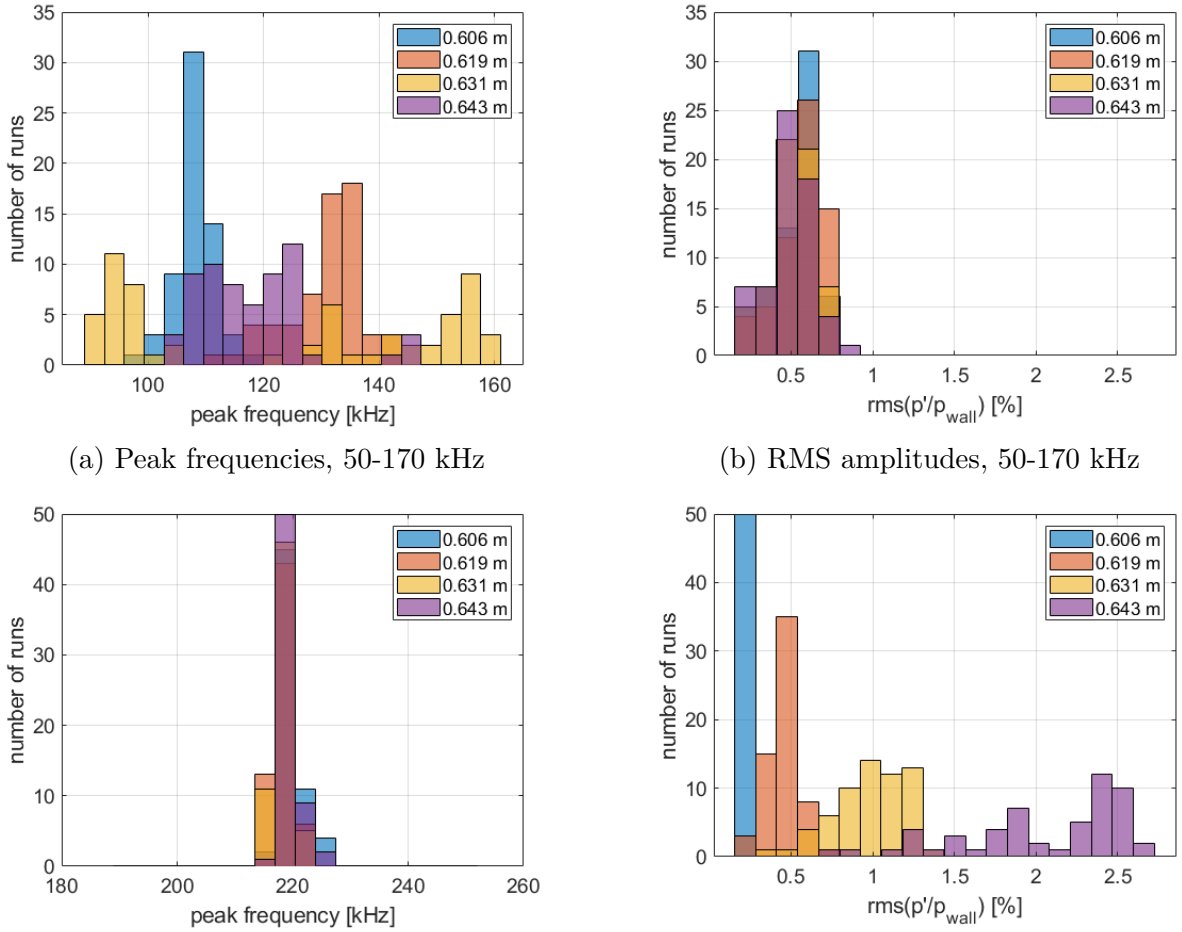

(a) Peak frequencies, 50-170 kHz

(b) RMS amplitudes, 50-170 kHz

(c) Peak frequencies, 170-290 kHz

(d) RMS amplitudes, 170-290 kHz

Figure 5.29. Histograms of PCB peak frequencies and amplitudes. Horizontal axes have the same range for peak frequencies, but are centered around different values.

switching discussed in Section 5.2.2.4. This mode switching sporadically occurs during a run when the dominant instability seems to change from the second mode to the shear-generated instability, sometimes changing the shape of that instability peak in the process. In this example, the shear-generated instability in Runs 0712 and 0933 splits into a double peak, and the second-mode amplitude is reduced. However, the second-mode peak frequency remains unchanged with the mode switch.

The integrated RMS amplitudes normalized by the wall pressure are listed in Table 5.2. They were integrated between 50 and 270 kHz. For the runs from Figure 5.31a, which do not include a mode switch, the mean amplitude was 2.54%, while the standard deviation between

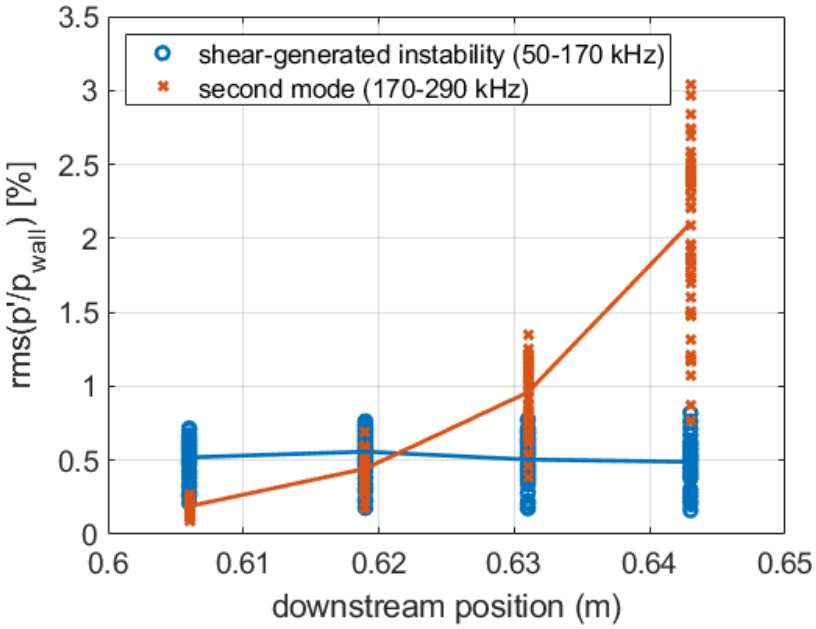

Figure 5.30. Normalized surface pressure fluctuation amplitudes as a function of downstream distance. Lines connect mean values for each instability at the four axial location.

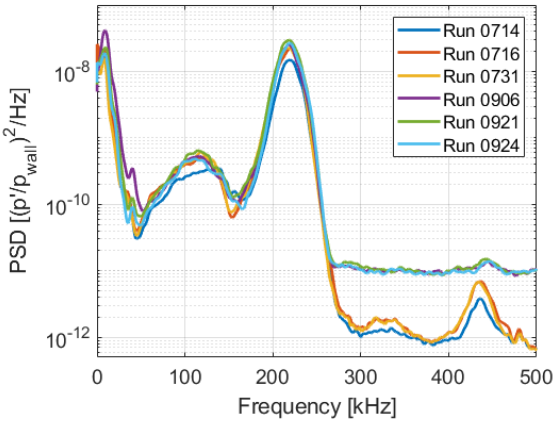

(a) Selection of runs highlighting consistency when no mode switching occurs.

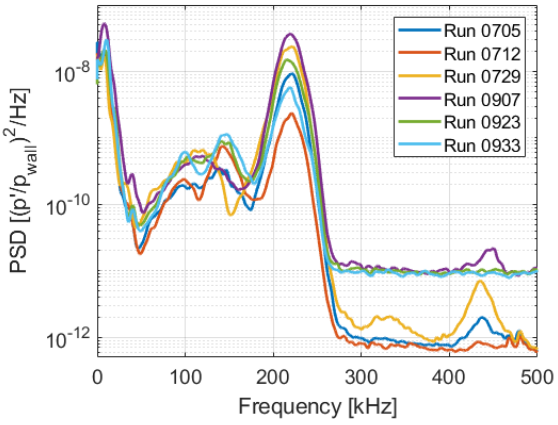

(b) Selection of runs highlighting variation due to mode switching (see Section 5.2.2.4).

Figure 5.31. PCB power spectral densities 0.643 m downstream from a variety of runs showing repeatability of frequency peaks within an entry. Entry 9 runs have a higher noise floor due to data being collected via unfiltered, high-speed cards in the DAQ rather than the set of oscilloscopes. All runs at $Re = 11.58 \times 10^6/\text{m}$.

Table 5.2. Normalized RMS values for runs in Figure 5.31. $Re = 11.58 \times 10^6$/m, integrated between 50 and 270 kHz.

Figure 5.31a (without mode switching)		Figure 5.31b (with mode switching)	
Run	RMS (%)	Run	RMS (%)
0714	2.04	0705	1.59
0716	2.52	0712	0.96
0731	2.53	0729	2.61
0906	2.61	0907	3.13
0921	2.89	0923	2.13
0924	2.65	0933	1.42

runs was only 0.28%. The mean for the runs from Figure 5.31b, which include a mode switch, was 1.97% and the standard deviation was 0.81%, over three times higher than cases without a mode switch. Future analysis of this data will include comparing the bicoherence for runs with and without mode switching. Additionally, wall temperature variations between runs will be compared to see their effect on the RMS amplitudes of each instability.

5.2.3 Off-the-Surface Density Fluctuation Measurements

The FLDI (in configuration D from Figure 2.10) was used to study the density fluctuations off-the-surface of the model, both in and around the separation bubble at the compression corner, downstream along the shear layer, and after reattachment along the flare. These locations can be seen superimposed on a schlieren image of the model with a measured heat transfer overlay in Figure 5.32. Note that, based on schlieren images, reattachment is not believed to have occurred until somewhere between 0.58 and 0.60 m downstream. The first set of runs was made right at the compression corner (0.526 m downstream of the nosetip), looking at fluctuations in the separation bubble and the shear layer above it. The second set was made 0.577-m downstream, also looking at the shear layer above the bubble. The third set of runs was made 0.606-m downstream, just downstream of where the boundary layer likely reattaches. The density fluctuations were computed assuming an integration length of 65 mm (see Section 3.1.2.4). They were normalized by edge densities computed by Dr. Esquieu in DPLR, summarized in Table 5.3.

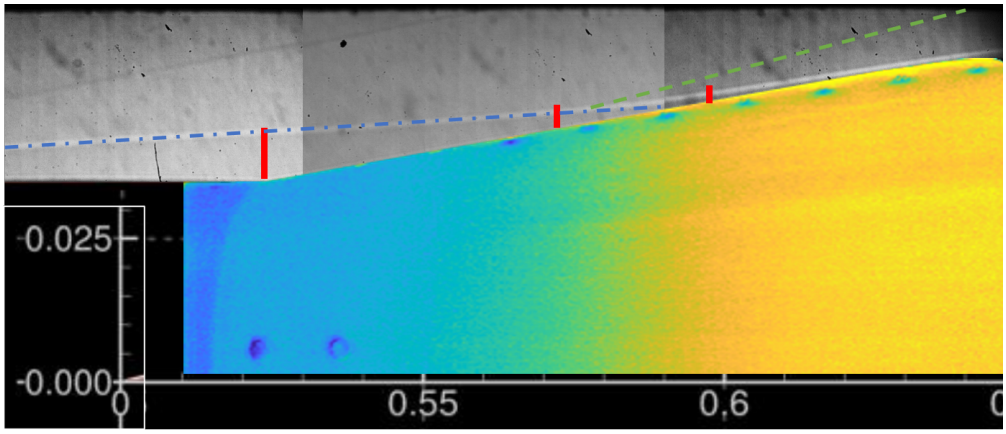

Figure 5.32. FLDI sweep locations (red lines), with schlieren and heat transfer overlays, $Re = 11.5 \times 10^6/\text{m}$. Flow is from left to right. The shear layer is outlined with a blue dotted line, while the reattachment shock is outlined with a green dashed line.

Table 5.3. Edge densities along the 10° cone-cylinder-flare for $P_0 = 150$ psia, computed in STABL. Values were scaled by the stagnation pressure during the run to normalize the density fluctuations.

Downstream position (mm)	Edge Density (kg/m^3)
526	0.04158
577	0.06406
606	0.04727

5.2.3.1 Shear Layer Upstream of Reattachment

PSDs of the FLDI measurements can be seen in Figure 5.33 for the two locations upstream of reattachment. Inside the separation bubble and the shear layer, at the compression corner, only fluctuations associated with the second mode are seen, with peaks around 220 kHz. The fluctuation amplitudes remain relatively constant close to the surface inside the bubble, but increase with the height above the wall, reaching a peak around 7.40 mm off-surface. No fluctuation peaks can be seen once in the freestream above the shear layer. Moving further downstream to 0.577 m, but still along the shear layer, the second-mode peak remains around 220 kHz, with the same maximum peak amplitude (Figure 5.34), here measured at 2.95 mm off the surface. Additionally, the shear-generated traveling waves are now evident, rising above the noise floor beginning 1.68 mm off-surface. These waves appear as a broad peak

between 50 and 170 kHz. The higher noise floor for this set of measurements is due to the unfiltered DAQ used for data acquisition, as opposed to the oscilloscopes used for the other two sets.

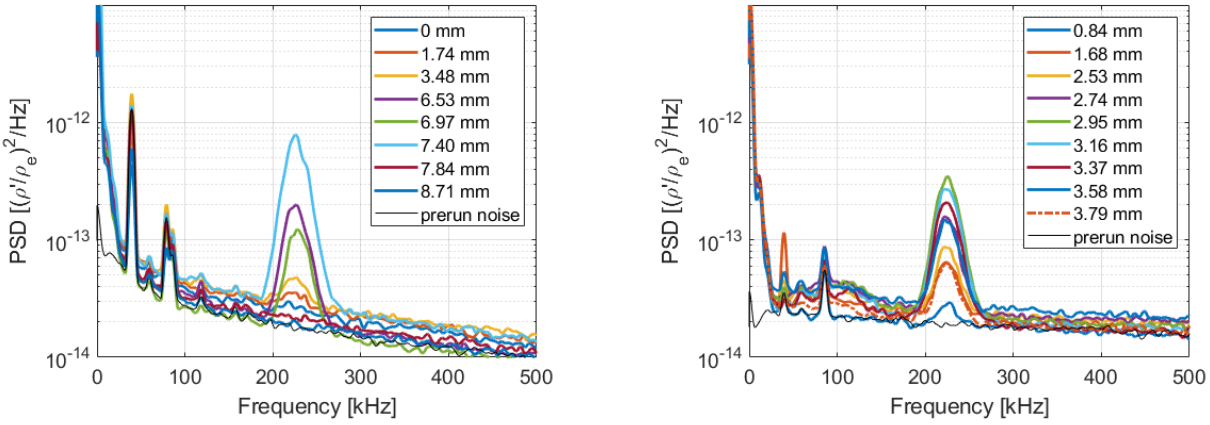

(a) 0.526 m downstream (at compression corner)

(b) 0.577 m downstream (just upstream of reattachment)

Figure 5.33. Normalized FLDI density fluctuation PSDs upstream of reattachment for $Re = 11.5 \times 10^6$/m.

The FLDI measurements of the shear layer at the corner only contain second-mode waves but at 0.577 m they also include the lower-frequency traveling waves. Additionally, these waves are not present in measurements made on the same geometry with a smaller (3.5°) flare angle without a a separation bubble (see Section 4, Figures 4.4 and 4.5). Together, these sets of measurements point to these waves being amplified by the shear layer above the separation bubble.

The role of the second mode in the generation of these shear-layer waves was not considered in this work, but should be a focus of future study. Similar experiments by Butler on an axisymmetric separation bubble found that energy from the second mode was radiated away in the shear layer [38]. This energy shedding could explain the neutral stability of the second mode as it convects downstream through the shear layer, but it is uncertain what relationship this has to the shear-generated instability. It would be informative to observe the effect of damping the second mode upstream of the separation bubble to better determine its role in the amplification of the shear-generated instability.

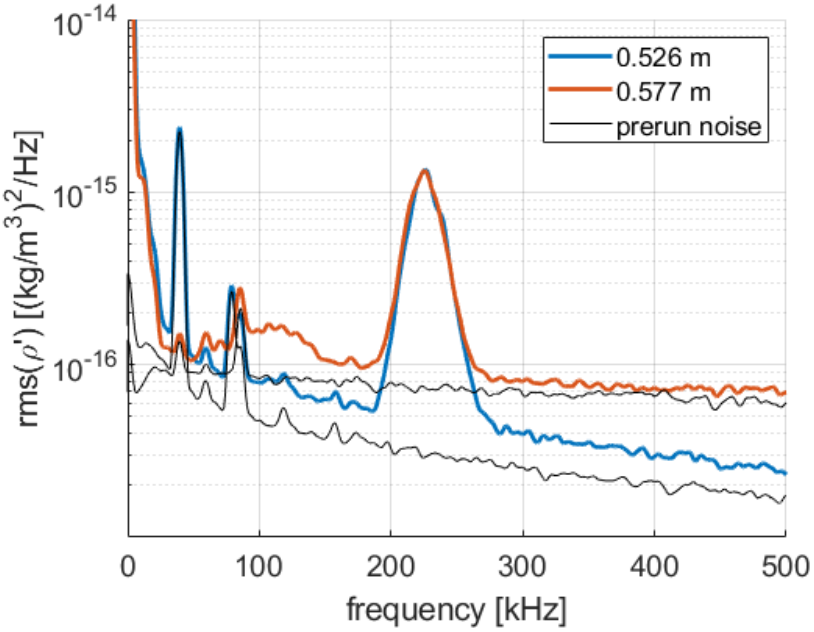

Figure 5.34. Peak FLDI density fluctuation PSDs for two shear-layer locations without normalization. Runs 0732 and 0919, $Re = 11.5 \times 10^6/\text{m}$.

5.2.3.2 Downstream of Reattachment

Additional FLDI measurements were taken just downstream of the estimated point of reattachment, 0.606 m downstream of the nosetip. The beams were at the same axial location as one of the surface PCB sensors, allowing for comparisons between the surface pressure and off-surface density fluctuation measurements at that station.

Figure 5.35 shows the spectral qualities of the FLDI and the PCB located directly below the FLDI beams. The signals are from Run 0732, when the FLDI was at the location off-surface that resulted in the largest peak amplitudes (1.25 mm). In the spectra, the apparent second mode fluctuations around 215 kHz and the shear-generated fluctuations centered on 100 kHz can be seen in both the surface pressure as well as the off-the-surface density measurements. Additionally, both instabilities are highly coherent between the FLDI and PCB signals.

In fact, the high coherence between the FLDI and PCB signals exists for all PCBs both at the same axial location as the FLDI as well as downstream of it. Figure 5.36 plots the

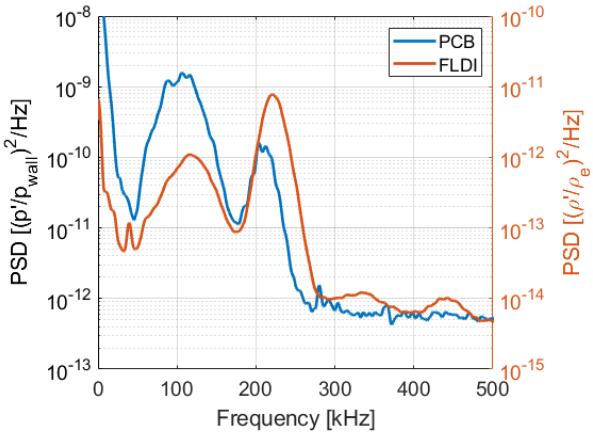

(a) PSDs (normalized by computed wall pressure for the PCB and computed edge density for the FLDI)

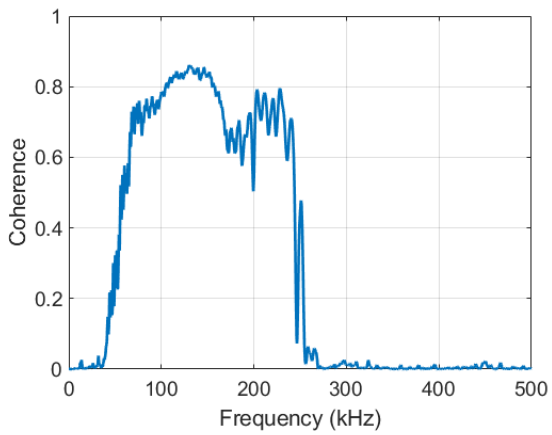

(b) Coherence between the FLDI and PCB

Figure 5.35. FLDI and PCB spectral qualities, 0.606 m downstream of the nosetip. From Run 0732, $Re = 11.45 \times 10^6$/m.

coherence as a function of frequency for the FLDI with each of these PCBs. The coherence between 50 and 250 kHz is nearly entirely above 0.5; for the PCBs at 0.631 and 0.643 m (near the downstream end of the model) there is also non-zero coherence between 300 and 350 kHz, as well as between 400 and 450 kHz. These peaks correspond to a nonlinear interaction between the shear-generated and second-mode instabilities and the first harmonic of the second mode, respectively (see Section 5.2.2.3).

Figure 5.37 displays the variation in peak amplitude as a function of distance from the model surface for $Re = 11.45 \times 10^6$/m. The same information is seen in Figure 5.38a compressed onto the same axis to better differentiate peak amplitudes. The integrated amplitudes are plotted in Figure 5.38b. Both the second mode and the shear-generated traveling waves increase in amplitude farther from the surface until they reach a peak around 1.68 mm away, and then both quickly decrease as the distance from the model surface increases.

The cross-correlation values between the FLDI signal and PCB signals located both upstream and downstream of the FLDI beams can be seen in Figure 5.39. Figure 5.39a shows the cross-correlation plotted as a function of time lag, while Figure 5.39b displays the peak cross-correlation values and lag at those values as a function of downstream distance. From the time lags at maximum cross-correlation, the phase speed in the downstream direction is

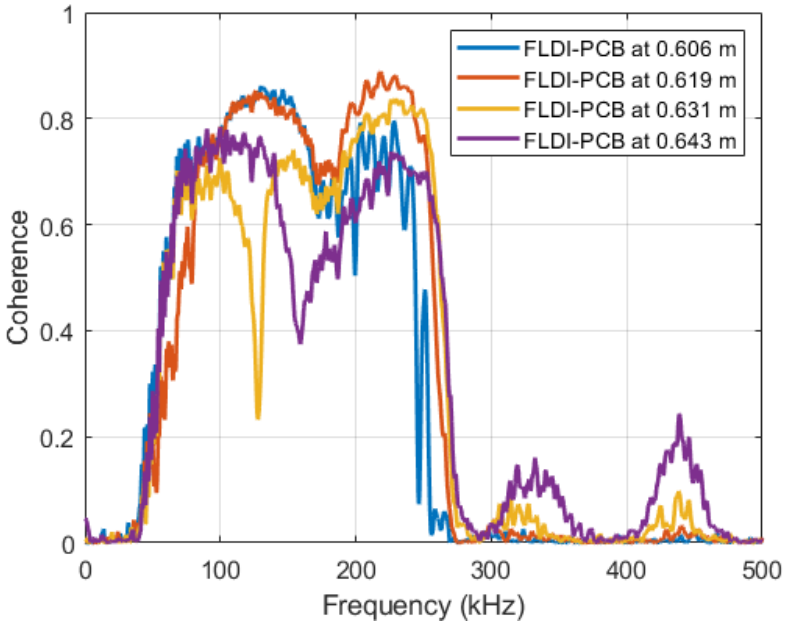

Figure 5.36. Coherence between FLDI signal and PCBs located downstream of FLDI.

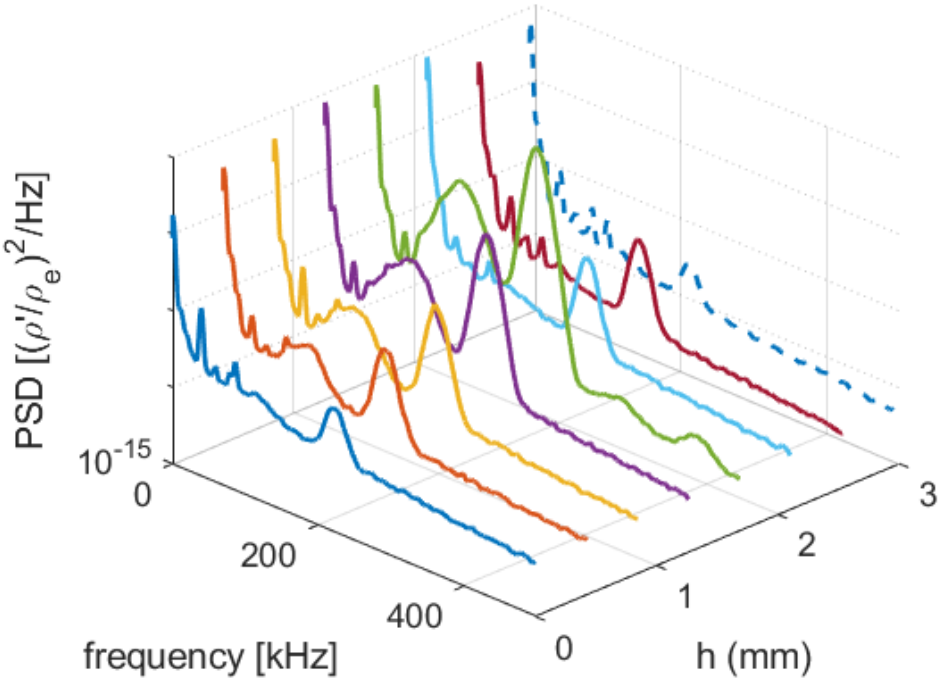

Figure 5.37. Phase change PSDs from quiet flow with $Re = 11.45 \times 10^6/\text{m}$

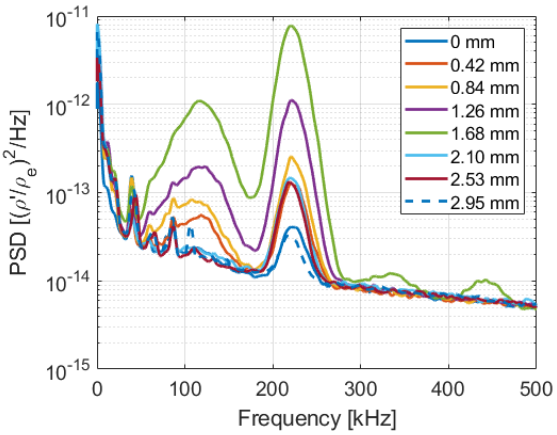

(a) FLDI PSDs at various distances from model wall

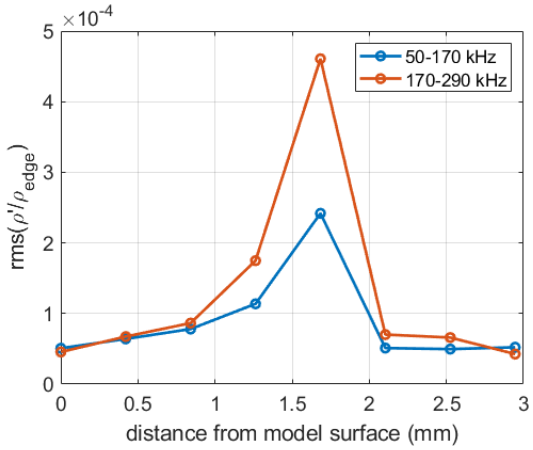

(b) Integrated peak amplitudes (50-170 kHz and 170-290 kHz) as function of distance from model surface

Figure 5.38. FLDI spectra and integrated peak amplitudes, normalized by edge density. $Re = 11.56 \times 10^6/\text{m}$.

computed to be 763 m/s, which is within 1% of the value computed from the PCB cross-correlations. By bandpassing the signals again, phase speeds of 691 m/s (81% of U_∞) and 849 m/s (99% of U_∞) are computed for the second mode and shear-generated traveling waves, respectively, with the same assumptions as those from the PCB calculations. These phase speeds are also within 1% of the PCB values.

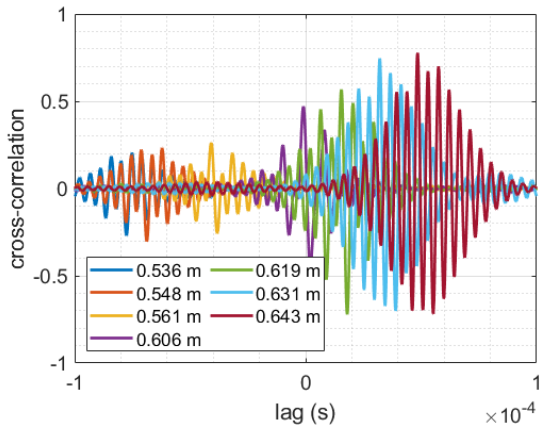

(a) Cross-correlation of FLDI and PCB sensors.

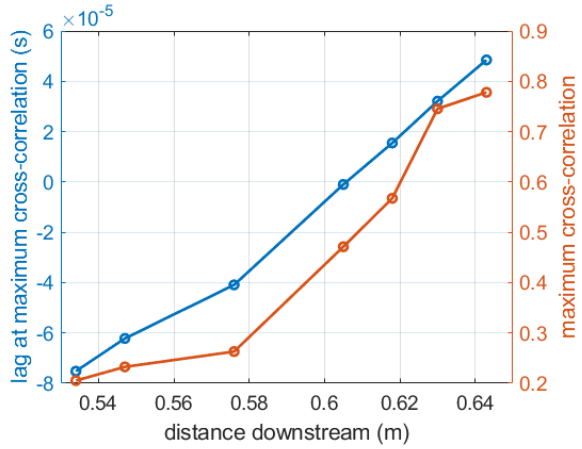

(b) FLDI-PCB cross-correlation peak values and lags.

Figure 5.39. Cross-correlation between FLDI (located 0.606 m downstream) and PCB sensors upstream and downstream of the beams.

Interestingly, the FLDI signal does not have the greatest peak cross-correlation value with the PCB sensor installed at the same axial location (0.606 m); instead, the maximum cross-correlations between the FLDI and the PCB sensors grow monotonically moving downstream. In the surface pressure measurements, peaks near 330 and 440 kHz are not seen until 0.643 m downstream, but they already appear at 0.606 m in the peak FLDI measurements. A possible explanation is that disturbances above the surface in the boundary layer are being convected towards the surface as they move downstream along the flare.

The bicoherence of the FLDI signal 1.68 mm from the surface is shown in Figure 5.40. Despite being located 0.606 m downstream, its bicoherence is more representative of a signal between 0.631 and 0.643 m downstream when compared with the PCB bicoherences, which reinforces the theory inferred from the cross-correlations that the disturbances off-the-surface are convecting towards the surface as the flow moves downstream. There are two peaks seen in the data; one representing a harmonic of the second mode around $(f_1, f_2) = (220, 216)$ kHz and one potentially denoting a nonlinear interaction between the second mode and the shear-generated traveling waves at $(222, 110)$ kHz. Associated peaks for these two nonlinearities can be seen in the PSD at 438 kHz and 332 kHz, respectively.

The run with the FLDI positioned at the height of the peak fluctuations (1.68 mm off-surface) was repeated again to check the repeatability of the FLDI measurements with this more complex flow (compared to the 7° cone). The results for the FLDI, as well as the PCB directly below it during the same two runs, are shown in Figure 5.41. Good agreement was observed between the flow instabilities as shown by the PCB spectra in Figure 5.41b. The FLDI measurements also had good agreement in both peak frequencies as well as peak amplitudes for the two runs.

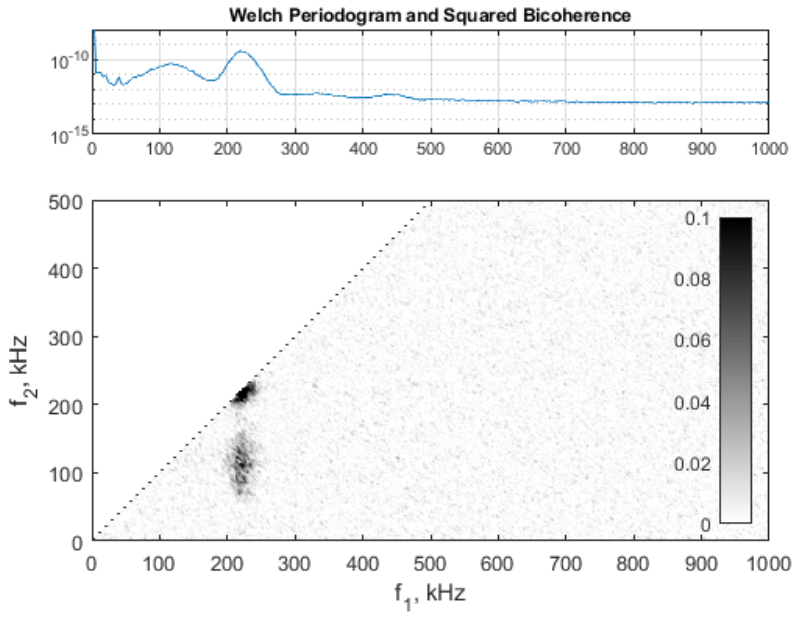

Figure 5.40. FLDI bicoherence at 0 m downstream. b^2 has peaks at $(222, 110)$ and $(220, 216)$ with values of 0.117 and 0.175. From Run 0732.

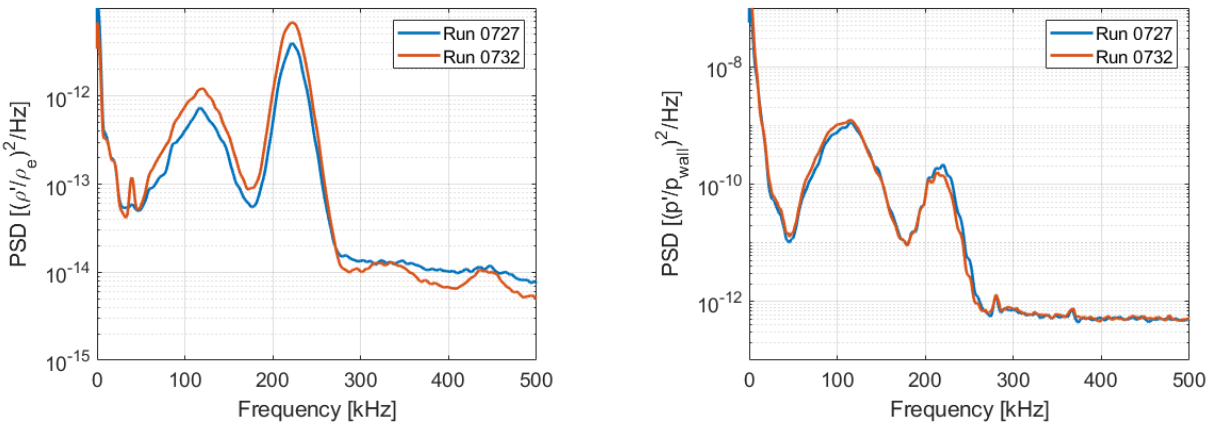

(a) FLDI PSDs at peak fluctuations.

(b) PCB PSDs for the same two runs.

Figure 5.41. FLDI and PCB power spectral densities at the same axial locations, highlighting repeatability. 0.606 m downstream from Runs 0727 and 0732, $Re = 11.45 \times 10^6/\text{m}$.

5.2.4 Effect of Small Angles of Attack

A series of runs were made at $Re = 11.5 \times 10^6/\text{m}$ where the angle of attack (α) was deliberately altered to see the effect of small angles of attack on the surface heating and

pressure fluctuations. To determine the angle of attack, the 0.0° run was first selected as the run that resulted in the closest second-mode peak frequencies for the four azimuthal PCB sensors on the cone in quiet flow at the desired unit Reynolds number, with P_0 =147 psia and T_0 =418 K (see Section 2.11). The angles relative to that position were then estimated by fitting a mesh to the model's heat transfer images and adjusting the angle of that mesh until it was in visual agreement with the image (see Section 2.10.1). These values were checked against angles determined by the geometric relationship between the number of turns of the screws used to set the pitch of the model given the thread size of those screws. The two sets of angles were within 0.02° of each other. Figure 5.42 shows an illustration of the angle of attack definition used in this dissertation.

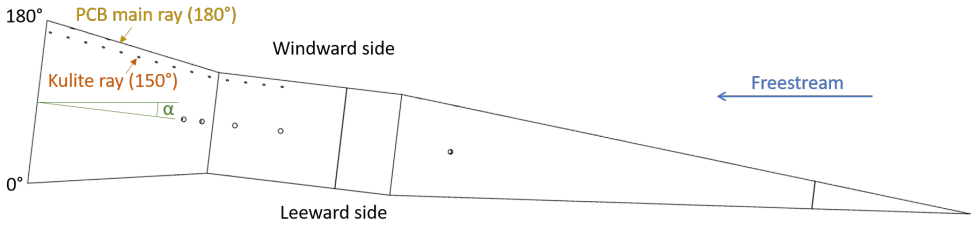

Figure 5.42. Drawing of model at a positive angle of attack as it is defined in this dissertation (angle exaggerated for clarity). The main PCB ray is located at 180°, which is defined as the windward side. The Kulite ray is located at 150°

The variation in second mode peak frequencies along the pitch axis (the "pitch %," β) was then used to better understand the angle of attack. Equation 5.1 defines how β is calculated, with f_{Az} referring to the second-mode peak frequency at azimuthal angle Az. The pitch % was found by dividing the second-mode peak frequency of the PCB at an azimuthal angle of 0° (on the leeward side of the model for positive α) with the average of the peak frequencies from the PCBs at azimuthal angles of 90° and 270° (those along the yaw axis).

$$\beta = \frac{f_{0^\circ}}{0.5(f_{90^\circ} + f_{270^\circ})} \tag{5.1}$$

Table 5.4. Second-mode peak frequencies along the cone at azimuthal angles of 0°, 90°, and 270°. The 0° PCB is along the pitch axis, while the 90° and 270° PCBs are along the yaw axis.

Angle of Attack	0° Az.	90° Az.	270° Az.
-0.15°	242.8 kHz	239.0 kHz	229.2 kHz
0.0°	235.0 kHz	240.3 kHz	231.4 kHz
0.15°	219.3 kHz	235.8 kHz	231.1 kHz
0.3°	208.1 kHz	235.0 kHz	238.8 kHz
0.45°	196.5 kHz	236.2 kHz	242.7 kHz
0.6°	183.6 kHz	235.7 kHz	244.4 kHz

The boundary layer at 90° should be similar to that at at 270° when varying only the angle of attack. Therefore, the PCBs along the yaw axis should have peak frequencies similar to what would be expected at an angle of attack of 0.0°. The model was not adjusted between runs for each quiet and conventional noise pair at a given angle of attack. Table 5.4 lists the second-mode peak frequencies measured for each of the quiet runs. Note that the PCB at 180° had a very low signal, so only registered with the conventional-noise runs (which generally have higher amplitude waves). In general, the PCBs along the yaw axis varied by less than 4% from their value at 0.0° for the quiet runs, and less than 6% for the conventional-noise runs (see Section 5.3.3).

There was some disagreement between the angles of attack under quiet flow and conventional noise. Figure 5.43 plots the pitch % as a function of the estimated angle of attack determined by the mesh fitting process described above. The variation in second-mode peak frequency along the pitch axis does not completely align for the quiet and conventional noise runs. Notably, the estimated 0.0° angle only corresponds to near-0 pitch % for the quiet case. This disagreement can be due to a number of causes. The quiet and noisy runs were made at different unit Reynolds numbers, and the BAM6QT runs at slightly different Mach numbers for the two types of flow (it is lowered to around $M = 5.8$ for conventional noise, from 6.0 for quiet flow). Additionally, it has also been observed that the nozzle flowfield is not perfectly uniform and parallel due to nonuniform nozzle temperature. This non-uniformity will affect the relative boundary layer thicknesses on the tunnel wall at different azimuthal angles [75].

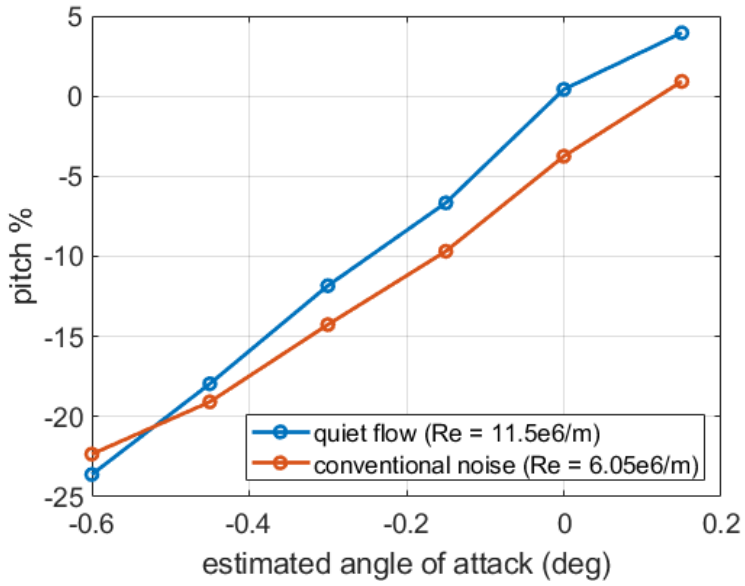

Figure 5.43. Relationship between estimated angle of attack and second mode peak frequency range along the pitch axes (which varies with α) as a percentage of the mean second mode peak frequency along the yaw axis (which does not change significantly with α).

A stability analysis conducted by Mullen at TAMU in 2019 estimated the change in second-mode peak frequency with small angles of attack [76]. This computation was conducted on a 7° half-angle (Θ) cone at Mach 6, 0.387 m downstream of the sharp nosetip at $Re = 11.3 \times 10^6$/m. The analysis resulted in 1.4% change in peak frequency per $\Delta\alpha/\Theta$. The quiet results from the present experiments, taken 0.361 m from the nosetip at $Re = 11.5 \times 10^6$/m, found a 1.7% change in second-mode peak frequency per $\Delta\alpha/\Theta$, which is within 22% of the estimate. The conventional noise experiments resulted in a 1.6% change in peak frequency per $\Delta\alpha/\Theta$, or within 15% of the computed estimate. However, these results also were at a lower Mach number (5.8 as opposed to 6.0 for the computation and quiet runs), and also a much lower unit Reynolds number ($Re = 6.05 \times 10^6$/m). Figure 5.44 plots the measured and computed percent change in peak frequencies as a function $\Delta\alpha/\Theta$.

Figure 5.45 displays the laminar-scaled heat transfer images of the unrolled flare for quiet, laminar flow taken from the yaw side. The magnitude of heat transfer is similar between all the angles, with the exception of 0.0°, which seems to have slightly higher

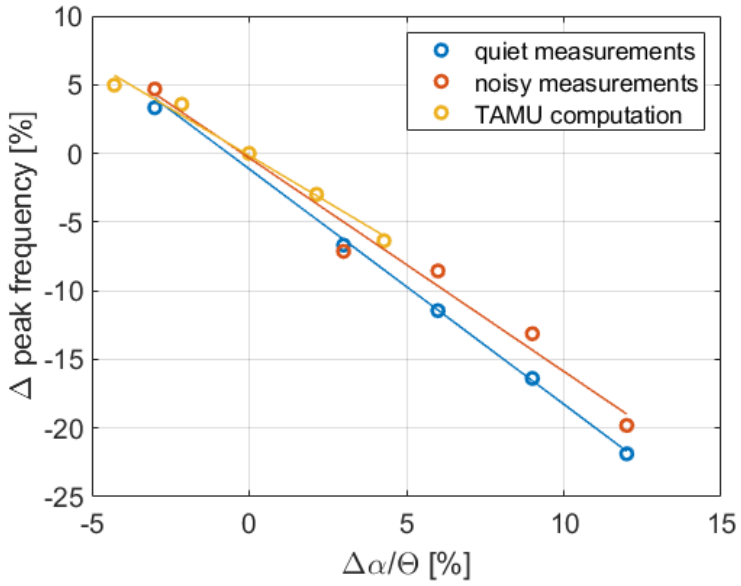

Figure 5.44. Measured and computed percent change in second-mode peak frequencies as a function the percent change in angle of attack (α) per cone half-angle (Θ). The second-mode is from the leeward side for positive angles of attack.

heating after reattachment. The 0.0° heat transfer also seems to contain streamwise vortices in the reattached boundary layer. These vortices are discussed in Section 5.4. Along the flare, an azimuthal angle of 180° is the windward side for positive angles of attack. The heat transfer images display azimuthal angles between 30° and 150°. The main ray of PCB sensors is at 180° (located outside the view of the images), while the row of Kulite sensors are at 150° (and can be seen along the top of the images). The increase in heating seen between 570 and 610 mm is believed to be due to reattachment; the flow remains laminar to the end of the model for all cases based on surface pressure fluctuation measurements.

A more quantitative view of the heat transfer in the streamwise direction can be seen in Figure 5.46. All runs occurred at the same unit Reynolds number. Heat transfer values averaged on the upper surface (near an azimuthal angle of 140°) and lower surface (near 40°) are plotted as a function of downstream distance. Near the windward side, the heat transfer increases with angle of attack. This trend continues up to a point, after which the

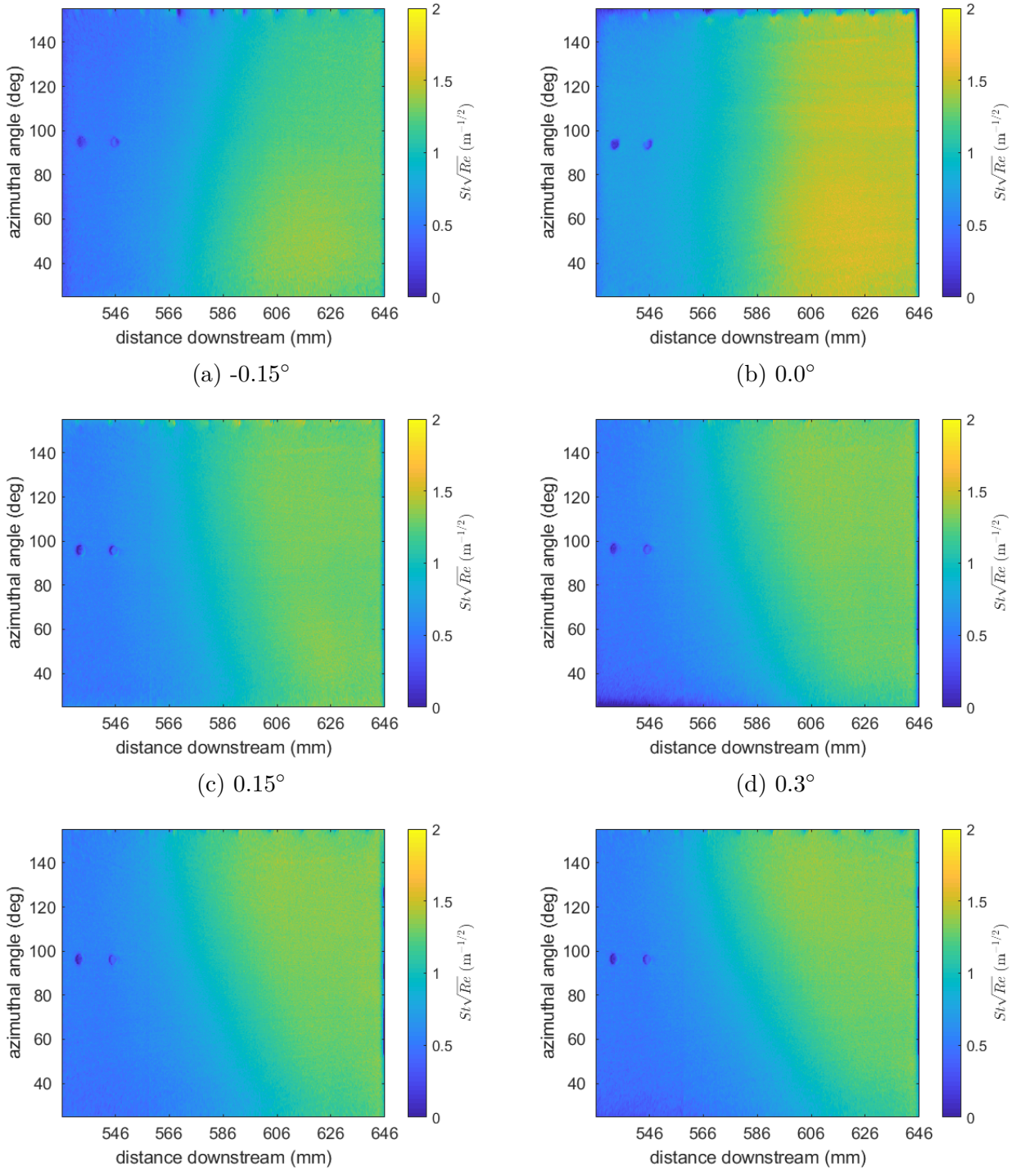

(a) -0.15°

(b) 0.0°

(c) 0.15°

(d) 0.3°

(e) 0.45°

(f) 0.6°

Figure 5.45. Laminar-scaled heat transfer images on the flare (unrolled and stretched into 2-dimensional space) at small angles of attack, $Re = 11.5 \times 10^6$/m. The flow is quiet and moves from left to right, and the images include azimuthal angles between 30° and 150°. The main PCB ray was located at 180° azimuthal angle (the windward side for positive α), while the Kulite ray is at 150° and can be seen along the top of the images.

heat transfer curves begin to collapse. Near the leeward side, heat transfer increases going from -0.15° to 0.0°, and then decreases with increasing α.

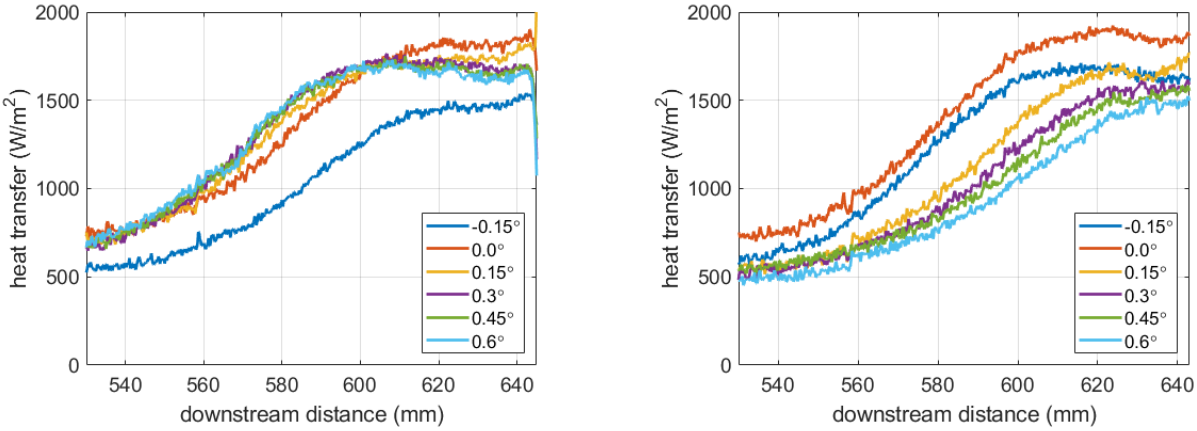

(a) Near-windward side.

(b) Near-leeward side.

Figure 5.46. Heat transfer as a function of downstream distance for the 10° flare under quiet flow.

When the model is closest to 0.0°, the heat transfer seems symmetric in the azimuthal direction. The heat transfer values are roughly constant for all azimuthal angles at a given axial position with this case. When the angle of attack is nonzero, however, the lines of constant heat transfer are sloped such that different azimuthal angles result in different heat transfer values at the same downstream position. Figure 5.47 illustrates this effect. Locations from each run where $St\sqrt{Re} = 1$ ($\pm$ 5 $\times$ 10^{-4}) m$^{-1/2}$ were plotted and lines were fit to the data. A linear-fit angle of 0° would correspond to a perfectly vertical heat transfer front. Plotting the angle of these linear fits as a function of angle of attack, it can be seen that as α increases, the angle of the constant-heat-transfer line decreases. The angle of the linear fit is closest to 0° when the angle of attack is closest to 0.0°, implying azimuthal symmetry.

The streamwise rise in heat transfer (generally seen between 0.57 and 0.61 m in Figure 5.46) is most likely associated with reattachment rather than laminar-turbulent transition. Surface pressure fluctuation spectra measured through the downstream end of the model do not reveal any amplitude broadening that would be associated with transition. Additionally, schlieren measurements taken at 0.0° angle of attack and Re = 11.7 $\times$ 10^6/m reveal that reattachment location appears to occur near the peak heat transfer gradient, between 0.58

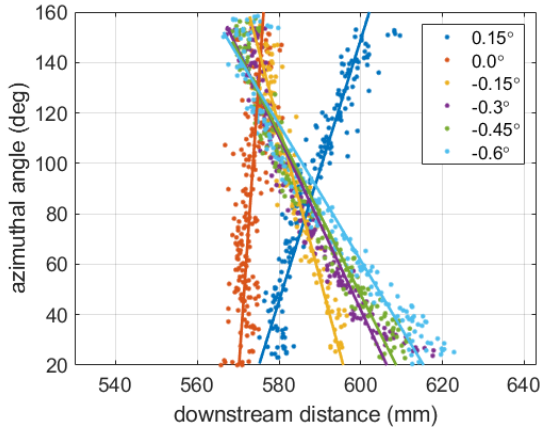

(a) Locations and linear fits for $St\sqrt{Re} = 1$ $m^{-1/2}$.

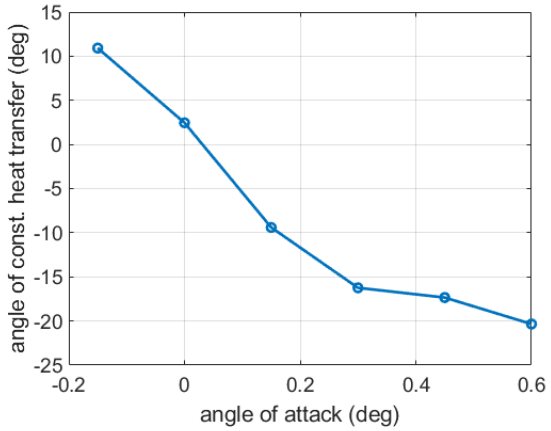

(b) Angles (determined from the slope) of linear fits as a function of angle of attack. 0.0° corresponds to a perfectly vertical line.

Figure 5.47. Linearly fitted data for $St \cdot Re^{1/2} = 1$ $m^{-1/2}$. The angle of the lines of constant heat transfer decrease monotonically with increasing angle of attack. From quiet runs with laminar flow.

and 0.60 m downstream (see Section 5.2.1.1). Therefore, based on the small angle of attack heat transfer results, it appears that the separation bubble reattachment extends farther downstream near the leeward side as the angle of attack increases, while this reattachment moves upstream near the windward side.

Figure 5.48 shows schlieren images taken during a later entry under quiet, laminar flow at $Re = 9.86 \times 10^6$/m (P_0 =122 psia, T_0 = 411 K). This unit Reynolds number was the highest available at the time. The reattachment shock from each image on the windward side (Figure 5.48a) is highlighted with a dashed blue line that is extrapolated to the shear layer to estimate a reattachment location for each angle of attack. As the angle of attack increases, the reattachment point moves upstream, corresponding to a smaller separation bubble. Reattachment moves from around 0.58 m downstream of the nosetip at 0.0° to 0.55 m at 0.6°. This result agrees with the trend seen in the heat transfer results, where the rise in heat transfer associated with reattachment moves upstream with increasing angle of attack near the windward side. The red line at the compression corner is the same length across all images. At 0.0°, the line reaches the shear layer on both the windward and leeward sides; the bubble is symmetric. As the angle of attack increases, the shear layer moves towards

the surface on the windward side and away from the surface on the leeward side. This again agrees with the bubble shrinking on the windward side with increasing angle of attack, and growing on the leeward side.

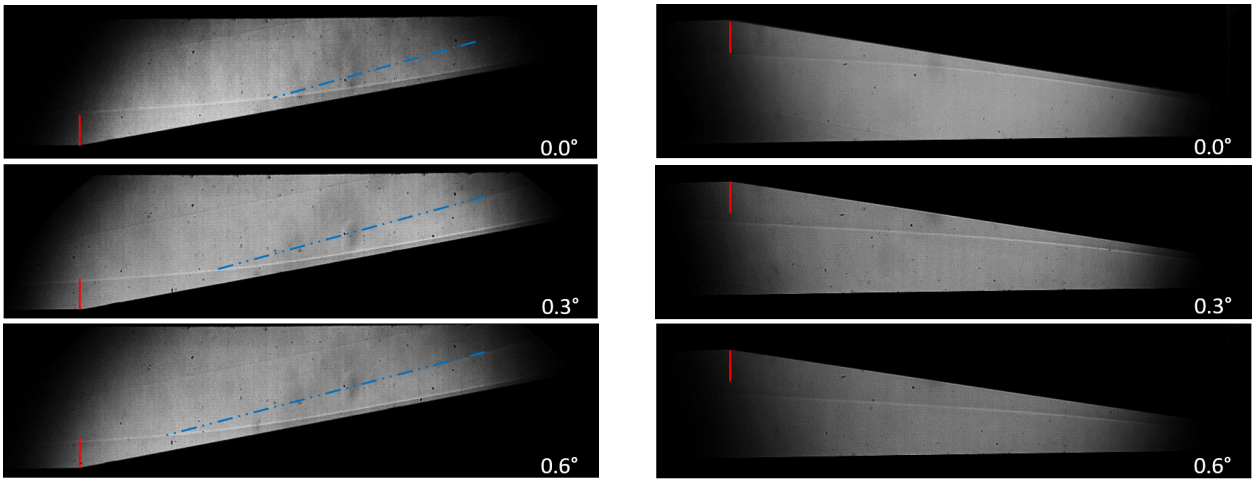

(a) Windward side (b) Leeward side

Figure 5.48. Schlieren images of the bubble in quiet flow at $Re = 9.86 \times 10^6$/m, with flow from left to right. The reattachment shock on the windward side is extrapolated with a blue dashed line to highlight its intersection point with the shear layer. The red lines in each image are the same length.

By altering the angle of attack, the length of the bubble and of the reattached boundary layer can be manipulated. A higher α creates a smaller bubble along the main PCB ray (which is on the windward side), providing a longer reattached boundary layer downstream of it. The sensors installed under the reattached boundary layer can be studied to see the impact of the small angles of attack (and therefore slight changes in the bubble size) on the surface pressure instabilities. Figure 5.49 plots PCB power spectral densities (PSDs) for two locations at each of the α values studied. Figure 5.49a shows the PCB located 0.387 m downstream, on the cone, while Figure 5.49b shows the PCB 0.511 m downstream, on the cylinder. Narrow peaks at 120 and 145 kHz are due to electronic noise and are present in the prerun spectra.

Along the cone, second-mode frequency peaks can be seen between 200 and 300 kHz depending on the angle of attack. With the exception of -0.15°, which is much larger, the

peaks all have similar amplitudes. The amplitude is most likely larger at -0.15° because the sensor ray is on the leeward side, where the second mode is more unstable [77], [78]. As the angle increases, the peak frequency also increases. This trend is logical, since as the α becomes more positive, the boundary layer on the windward side (where the sensor is located) thins. For the second-mode instability, where the frequency is coupled with the boundary layer thickness, a thinner boundary layer corresponds to a higher peak frequency.

On the cylinder, the second mode is damped after going through an expansion. A slight peak can still be seen between 200 and 230 kHz for the -0.15° case, but the others drop below the noise floor. A second frequency peak is visible for the largest positive angles, between 50 and 100 kHz. The coherence of the sensors along the cylinder which display this peak is near zero, implying a local oscillation that is not convecting downstream. The sensors on the cylinder are most likely inside the separation bubble, so this 50-100 kHz peak may just be an absolute instability of the bubble, similar to what was seen by Leinemann et al. in the bubble on the hollow cylinder-flare in 2019 [20]. Two sensors upstream but still on the cylinder had PSDs similar to Figure 5.49b.

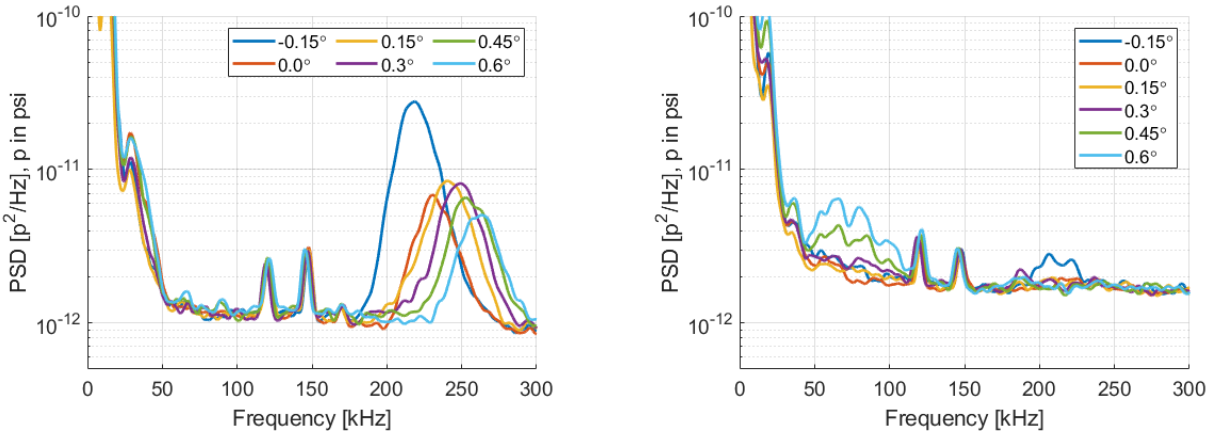

(a) 0.387 m downstream, on the cone.

(b) 0.511 m downstream, on the cylinder.

Figure 5.49. Power spectral densities for PCB sensors located on the cone and cylinder on the windward ray at various small angles of attack in quiet flow. $Re = 11.5 \times 10^6/\text{m}$.

Figure 5.50 shows PSDs for pressure sensors on the flare, near and downstream of reattachment. In these plots, the second mode can be seen between 170 and 290 kHz, while

suspected shear-generated traveling waves are found between 50 and 170 kHz. These waves are similar to those seen in previous experiments conducted at a near-zero angle of attack [72]. The second-mode peak frequencies generally increase as α increases. While larger α values correspond to smaller separation bubbles on the windward side, and therefore a longer reattached boundary layer, the windward boundary layer tends to be thinner with increasing α. As on the cone, a thinner boundary layer would correspond to higher second-mode peak frequencies, as observed.

The shear-generated peaks, found between 50 and 170 kHz, vary much more than the second-mode ones. They are the largest when the local bubble length is the longest and are smaller near 0.0° angle of attack, but are larger again for negative α. At zero α, these peaks were observed to amplify and increase in peak frequency moving downstream in the reattached boundary layer, until they broke down into two peaks near the downstream end of the model [72]. This downstream location at which the single peaks break down into two peaks appears to move upstream as the angle of attack increases. For -0.15°, it occurs at 0.643 m, while at 0.0° it is at 0.631m, and for 0.15° it happens by 0.619 m. When the sensor array is pitched farther forward, the peaks also lose their roughly parabolic shape, and peak frequencies tend towards 50 kHz. Kulite power spectra show similar results to the PCBs.

The second-mode and shear-generated peak amplitudes appear to generally follow opposite trends. Figure 5.51 plots the integrated peak amplitudes for the shear-generated and second-mode waves as a function of angle of attack. The second mode has the greatest peak amplitude for an α of 0.15° for most downstream positions, where the shear-generated instability has the smallest peaks. For higher angles of attack, the second-mode peaks decrease in amplitude, while the shear-generated ones increase.

Overall, the angle of attack study highlights a few key implications. The first is that the symmetry of the separation bubble is highly dependent on the angle of attack. As α increases, the reattachment point moves upstream on the windward side and downstream on the leeward side under quiet, laminar flow. Additionally, both the shear-generated instability and the second mode are present for each angle of attack analyzed. While the bubble symmetry is extremely sensitive to α, these two instabilities persist despite asymmetry, and therefore should be taken into account when designing a hypersonic vehicle. The shear-

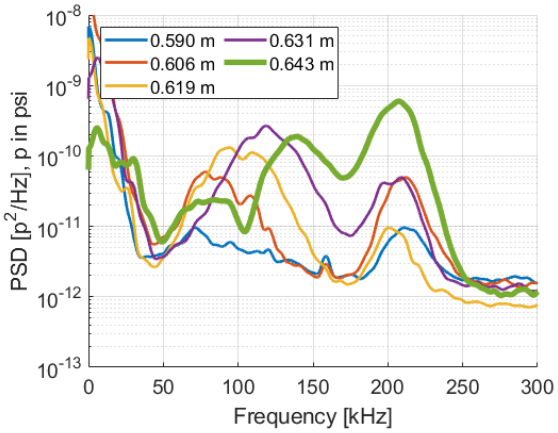

(a) -0.15°

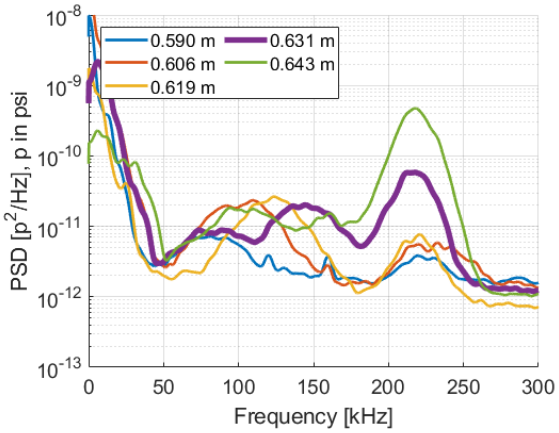

(b) 0.0°

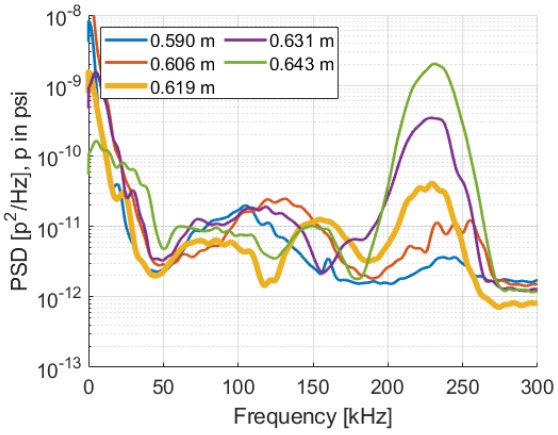

(c) 0.15°

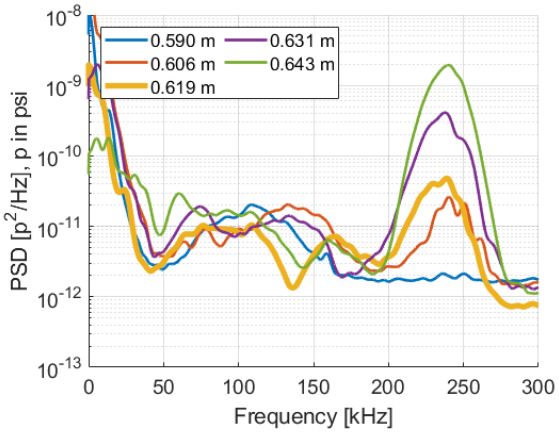

(d) 0.3°

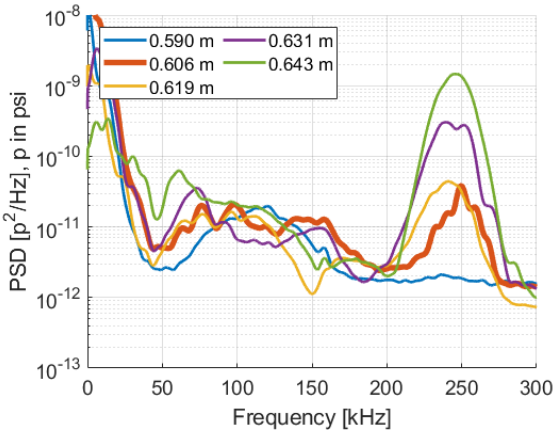

(e) 0.45°

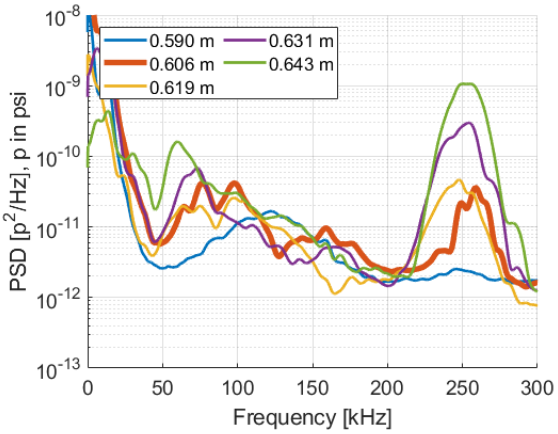

(f) 0.6°

Figure 5.50. PCB PSDs along the 10° flare on the windward ray at different small angles of attack, with $Re = 11.5 \times 10^6/\text{m}$ in quiet flow. The PSD for the sensor at which the shear-generated instability breaks down into two peaks occurs is highlighted by a thicker line.

generated waves also appear to be more amplified on the leeward side of the model, and may play a more significant role in transition when on that side. In flight, a real hypersonic vehicle will frequently be at nonzero angles of attack, so it is important to understand the implications of such configurations on aerodynamic instability and transition.

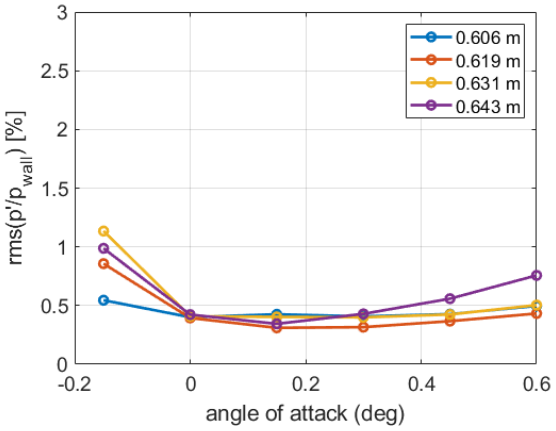

(a) Amplitudes of shear-generated waves (integrated over 50-170 kHz)

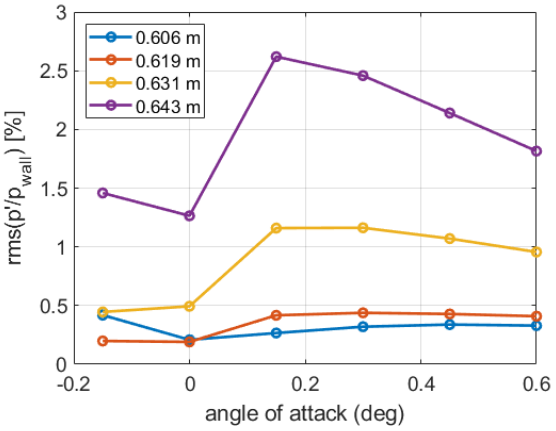

(b) Amplitudes of second-mode waves (integrated over 170-290 kHz)

Figure 5.51. Integrated RMS amplitudes for shear-generated (50-170 kHz) and second-mode (170-290 kHz) waves in quiet flow. Values normalized by computed wall pressures at 0.0° angle of attack. Under quiet flow, $Re = 11.5 \times 10^6$/m. On the windward ray for positive α.

5.3 Conventional-Noise Flow

Based on the PCB power spectra and heat transfer results, quiet flow resulted in laminar boundary layers for all unit Reynolds numbers. To see how a transitional or turbulent boundary layer behaves with this model, a series of runs were made with conventional noise at the BAM6QT.

5.3.1 Mean Measurements

5.3.1.1 Heat Transfer

IR-thermography surface-heat-transfer measurements were again obtained along the flare for a number of unit Reynolds numbers under conventional noise. A sample of the results

can be seen in Figure 5.52. Figure 5.52a shows a laminar run, which results in very similar heating to that seen in the quiet-flow runs. Figures 5.52b and 5.52c are from transitional runs. A peak in heat transfer can be seen along the flare for those runs. This peak occurs farther upstream for the higher unit-Reynolds-number case. Finally, Figure 5.52d shows a turbulent run. The heat transfer rapidly comes to a peak at the corner and then remains level moving downstream.

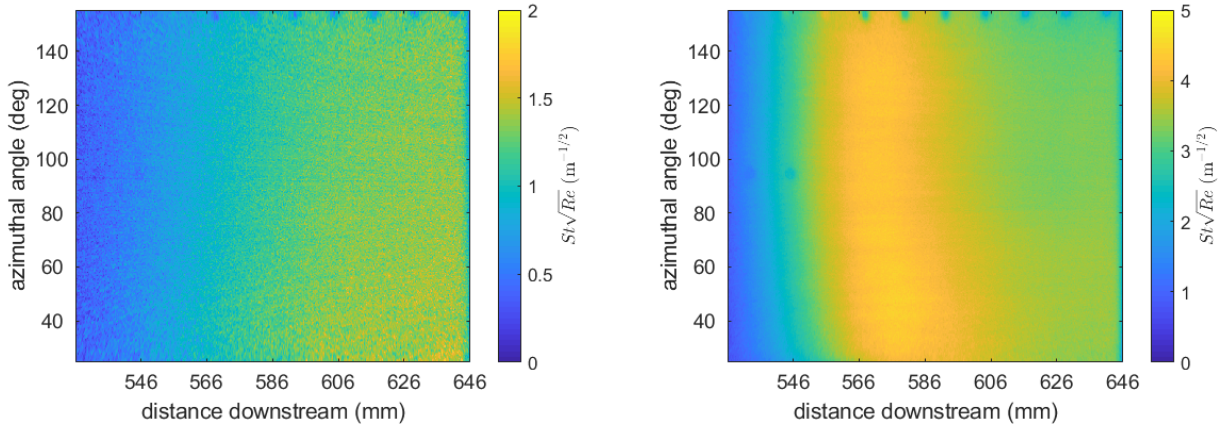

(a) $Re = 1.99 \times 10^6$/m, note the lower color scale for this Reynolds number

(b) $Re = 5.36 \times 10^6$/m

(c) $Re = 6.60 \times 10^6$/m

(d) $Re = 8.89 \times 10^6$/m

Figure 5.52. Heat transfer images on flare in noisy flow. The flow moves from left to right.

Figure 5.53 plots laminar-scaled heat transfer as a function of distance downstream, again averaged from two slices of the data (located above and below the PCB sensors that can be seen in Figure 5.52). The location of the compression corner is again at 526 mm

downstream. As the runs in conventional noise span laminar, transitional, and turbulent flow, distinct trends can be seen in the heat transfer. For runs above $Re = 6.60 \times 10^6$/m, the flow was turbulent along the flare, and the heat transfer results are similar with a peak just downstream of the corner. For Re between (and including) 5.36×10^6/m and 6.60×10^6/m, the flow appears to be transitional along the upstream portion of the flare, and is fully turbulent by 620 mm downstream. For these cases, a broader peak in heat transfer can be seen on the flare (see Figures 5.52b and 5.52c). This peak shifts upstream with increasing Reynolds number, and rises above the turbulent peak heating values. Runs at $Re = 2.80 \times 10^6$/m and $Re = 3.58 \times 10^6$/m also seem to be transitional moving along the flare, but are not fully turbulent by the downstream end of the model. Finally, the lowest Reynolds number cases ($Re = 1.99 \times 10^6$/m and 2.16×10^6/m) appear to be laminar on the flare, with nondimensional heat transfer values generally aligning with those from the quiet runs; one case from the quiet flow results is plotted along with the noisy cases to highlight this (Figure 5.53a). The heat transfer results have also been plotted using turbulent scaling ($Re^{1/5}$ rather than $\sqrt{Re}$) in Figure 5.53b. Bars showing 20% error are plotted for the highest unit Reynolds case, as well as a transitional one. Data collapse within this nominal error everywhere for the turbulent cases, and downstream of 0.610 m for the transitional ones.

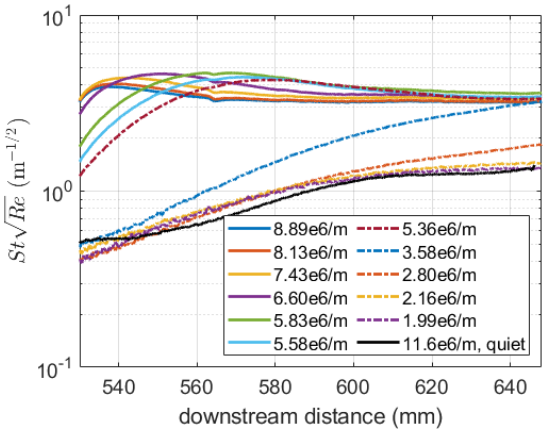

(a) Laminar scaling, with one case under quiet flow for comparison.

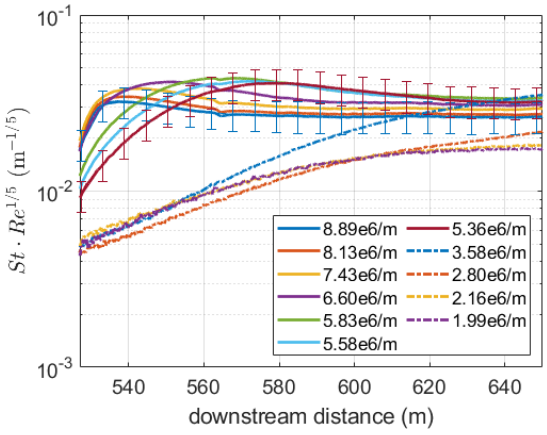

(b) Turbulent scaling, with 20% error bars for $Re = 8.89 \times 10^6$/m and 5.36×10^6/m to show overlap for turbulent heat transfer.

Figure 5.53. Laminar-scaled heat transfer for Re between 1.99×10^6 and 8.89×10^6/m under conventional noise.

5.3.1.2 Schlieren

Schlieren images were again taken of the cone-cylinder section of the model under conventional noise to better understand the geometry of the bubble and where reattachment occurs. As with the quiet cases, two entries were conducted with differing setups and conditions due to what was available at the time of testing. The first entry (Entry 13) utilized four-inch mirrors and recorded runs with a frame rate of 20,000 frames per second and a shutter period of 1/4,032,000 seconds. The second entry (Entry 14) had eight-inch mirrors and recorded images at 10,000 frames per second and a shutter period of 1/10526 seconds.

Under conventional noise, runs were primarily conducted at unit Reynolds numbers that correspond to transitional flow, although the lowest unit Reynolds number appeared laminar. Figure 5.54 shows single frames from three unit Reynolds numbers. Unlike in the quiet cases, as the unit Reynolds number increases, the shear layer height decreases, indicating a smaller bubble. Additionally, more fluctuations can be seen downstream of reattachment for higher unit Reynolds numbers, as the flow transitions to turbulence around reattachment for the noisy, transitional cases. The trend of bubble size decreasing with unit Reynolds number is a transitional trend that has been seen in previous supersonic and hypersonic bubble experiments [12], [15]. Note that the red line in each images is the same length.

As in the quiet cases, the larger eight-inch mirrors were used to look at the bubble symmetry under conventional noise. Figure 5.55 shows an example image of the separation bubble in noisy flow at 0.0° angle of attack and $Re = 5.26 \times 10^6$/m. The bubble again appears symmetric, with the shear layer at the same height off the surface on both the upper and lower sides of the model. Since the reattachment shock was clearly visible on both sides as well, the estimated reattachment point for this unit Reynolds number can be determined based on where the extrapolated shock (yellow dashed line) would intersect the shear layer. This location was determined to be 16.2 and 16.7 mm downstream of the compression corner for the upper and lower surfaces, respectively. This corresponds to just a 3% difference in reattachment location.

A distinct difference noticed between the quiet and noisy schlieren was in the steadiness of the flow. The quiet cases were all laminar, and the shear layer only appeared to move

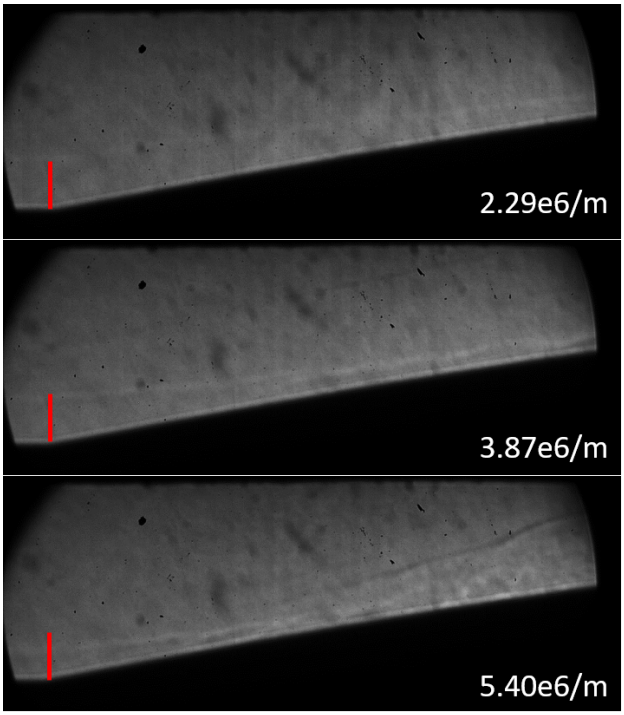

Figure 5.54. Schlieren images at $Re = 2.29 \times 10^6/\text{m}$, $3.87 \times 10^6/\text{m}$, and $5.40 \times 10^6/\text{m}$ with 0.25 μs exposure, highlighting variation in bubble size at different unit Reynolds numbers under conventional noise. The red line at the corner is the same length in all three images. Flow is from left to right. From Runs 1310, 1311, and 1313.

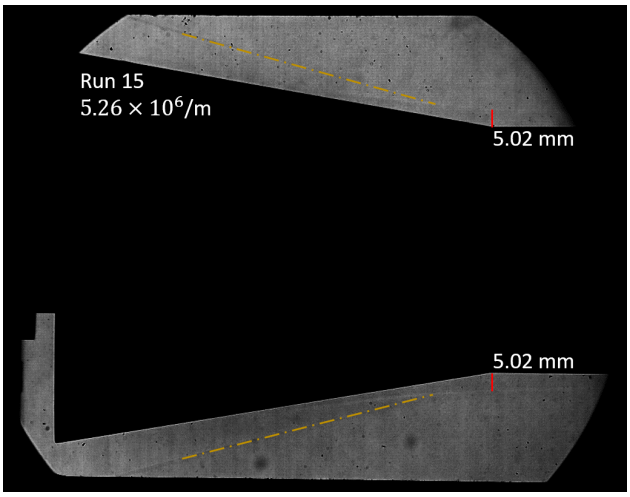

Figure 5.55. Schlieren image of cone-cylinder section under conventional noise at $Re = 5.26 \times 10^6/\text{m}$ highlighting symmetry of bubble at 0.0° angle of attack. From Run 1415.

with the motion of the model, with almost no perceptible variation between frames. The conventional noise cases, however, contain larger fluctuations, where the images from one frame to the next are frequently different, even when the flow was laminar. Figure 5.56 shows an example of this difference. In each column, the upper two images show two consecutive frames from a run with laminar flow. The third frame in the column shows the contrast-enhanced difference between the two. A quiet-flow example is in Figure 5.56a, while a conventional noise case is in Figure 5.56b. For these examples, the images were captured at 20,000 frames per second, so the frames are 50 μs apart. In quiet flow, there is no perceptible difference in the shear layer height or shape between consecutive frames; the flow is steady. Under conventional noise, though, some fluctuations can be seen in the shear layer, and even in the separation shock above it. This variation between quiet and noisy flow steadiness was apparent in every schlieren run. It appears that the tunnel noise is generating oscillations, as expected.

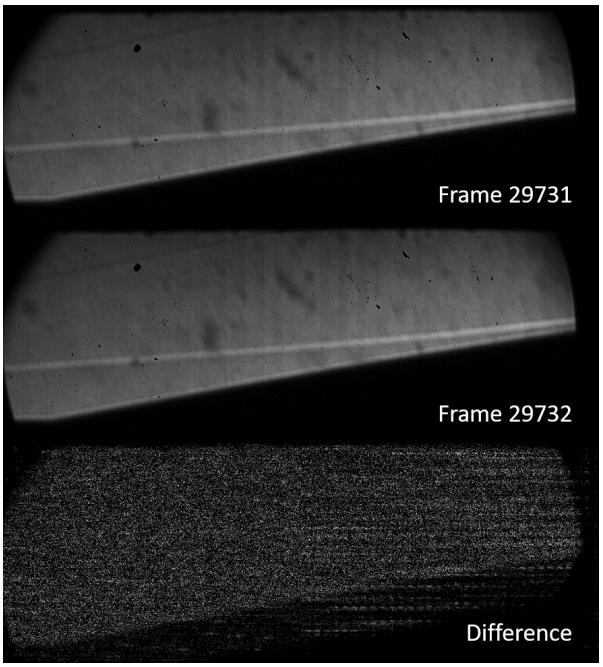

(a) Quiet flow, $Re = 11.7/m$, Run 1308

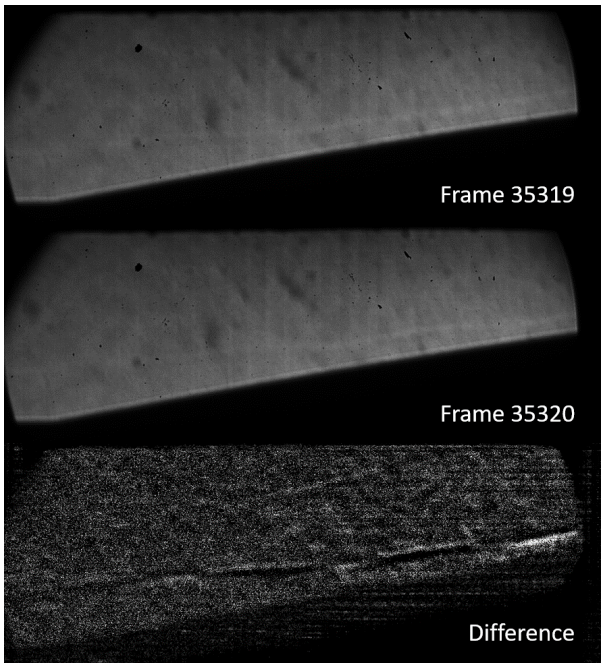

(b) Conventional noise, $Re = 2.28/m$, Run 1310

Figure 5.56. Consecutive schlieren images and their difference for two laminar cases under quiet and noisy flow.

5.3.2 Pressure Fluctuation Measurements

Figure 5.57 plots the power spectral densities for the surface pressure fluctuations along the cone and cylinder sections of the model in conventional noise. As in the quiet cases, at the two stations on the cone the second mode can be clearly seen. The gap in unit Reynolds numbers between 3.58×10^6/m and 5.36×10^6/m is due to a lack of burst diaphragms at the time of testing. As expected for second mode fluctuations, the peak frequency increases with increasing unit Reynolds number. Due to the higher amplitude of the second mode in the noisy case, second-mode harmonics can be seen between 300-450 kHz on the cone. Again, similar to the quiet flow cases, the second-mode peak amplitudes decrease along the cylinder.

Along the flare, the PSDs under conventional noise are different than those from the quiet flow cases (Figure 5.58). Low-frequency fluctuations can be seen around 25 and 30-70 kHz. In addition, some peaks can be seen around 11 kHz, but these are believed to be due to the high-pass filtering of the PCB sensors. The 25 kHz peaks do not seem to vary in frequency or amplitude consistently with unit Reynolds number, but do amplify when moving downstream. The 30-70 kHz peaks increase in frequency and amplitude with increasing unit Reynolds number, as well as when moving downstream. It is unclear if these instabilities correspond to the shear-generated waves or the second mode, or to some other instability. Similar results were seen in the Kulite measurements.

Figure 5.59 shows the cross-correlation and coherence of the PCB signals, high-pass filtered at 11 kHz. The 25 and 30-70 kHz fluctuations are significantly coherent for the PCB pairs, signifying that they may be traveling waves (Figure 5.59b). The cross-correlation between adjacent PCB pairs on the downstream portion of the flare (Figure 5.59a) peak at much lower values than in the quiet flow cases (around 0.4 compared to over 0.8 for quiet flow).

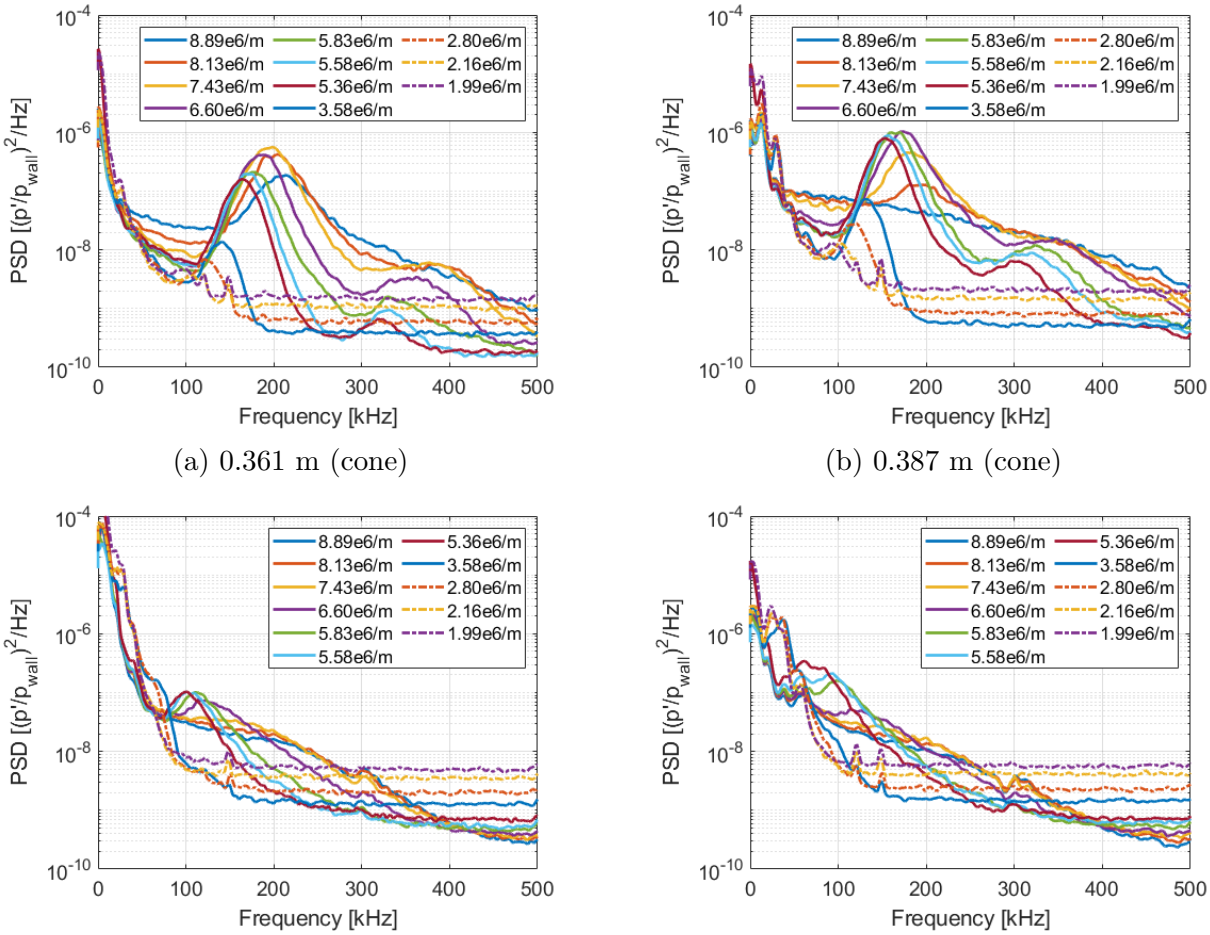

(a) 0.361 m (cone)

(b) 0.387 m (cone)

(c) 0.479 m (cylinder)

(d) 0.511 m (cylinder)

Figure 5.57. PCB PSDs along the 5° cone and the cylinder at unit Reynolds numbers between 1.99×10^6/m and 8.89×10^6/m

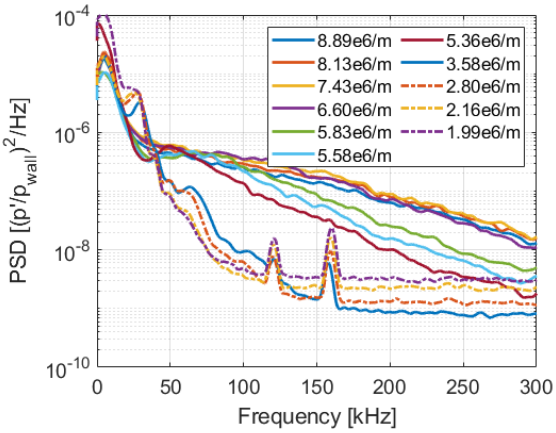

(a) 0.536 m

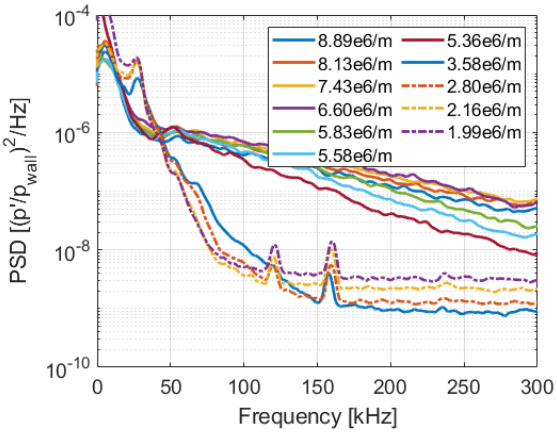

(b) 0.548 m

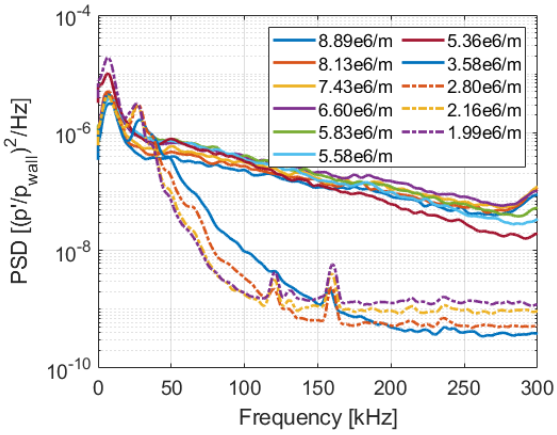

(c) 0.561 m

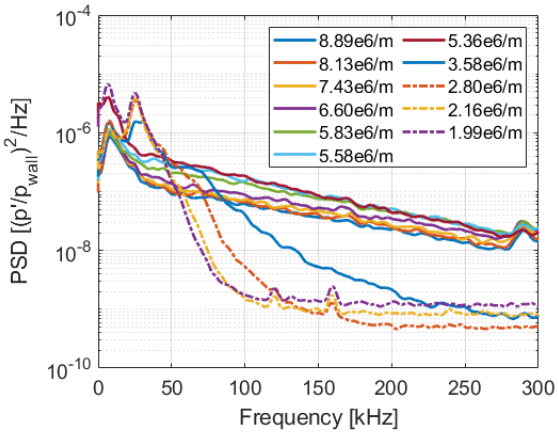

(d) 0.590 m

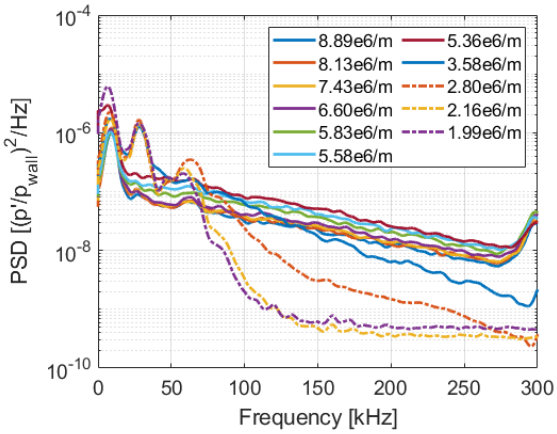

(e) 0.619 m m

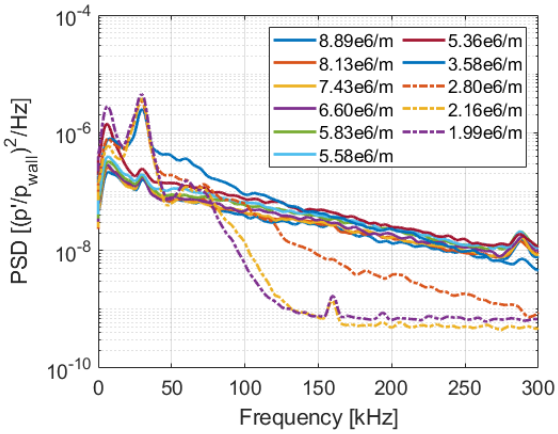

(f) 0.643 m

Figure 5.58. PCB PSDs along the 10° flare at Re between 1.99×10^6/m and 8.89×10^6/m

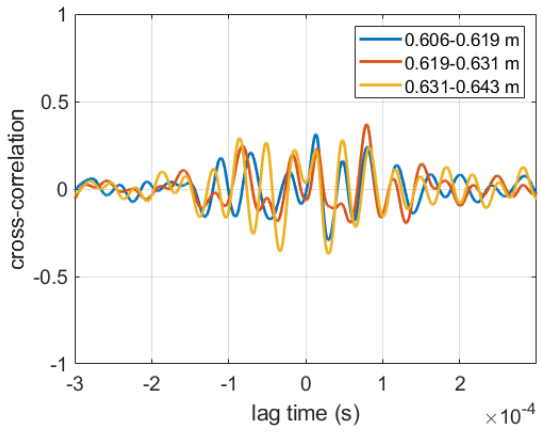

(a) Cross-correlation of adjacent PCB sensors.

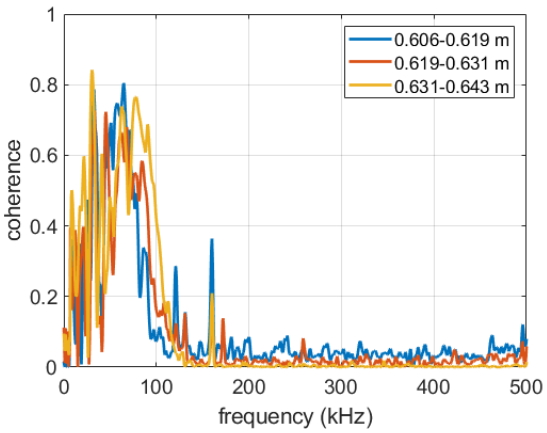

(b) Coherence of PCB pairs downstream of reattachment.

Figure 5.59. Cross-correlation and coherence between PCB sensors below the reattached boundary layer in conventional noise, $Re = 1.99 \times 10^6/\text{m}$.

5.3.3 Effect of Small Angles of Attack

Second-mode peak frequencies for the conventional-noise runs are listed in Table 5.5. The yaw-axis PCBs for the runs under conventional noise varied less than 6% from their 0.0° mean value.

Table 5.5. Second-mode peak frequencies along the cone at azimuthal angles of 0°, 90°, and 270°. The 0° and 180° PCBs are along the pitch axis, while the 90° and 270° PCBs are along the yaw axis.

Angle of Attack	0° Az.	90° Az.	180° Az.	270° Az.
-0.15°	183.4 kHz	184.1 kHz	178.1 kHz	179.1 kHz
0.0°	175.2 kHz	183.4 kHz	183.5 kHz	178.3 kHz
0.15°	162.7 kHz	181.6 kHz	194.4 kHz	182.6 kHz
0.3°	160.2 kHz	184.3 kHz	203.9 kHz	189.6 kHz
0.45°	152.2 kHz	183.2 kHz	207.6 kHz	188.5 kHz
0.6°	140.5 kHz	182.8 kHz	213.2 kHz	190.5 kHz

Figure 5.60 shows the laminar-scaled heat transfer results for conventional noise, transitional runs at small angles of attack. With these runs, the heat transfer peaks somewhere between 540 and 590 mm downstream, and reaches a peak magnitude over twice that reached in the quiet, laminar cases (see Figures 5.46 and 5.61). In this flow, heat transfer streaks indicative of streamwise vortices are visible for angles of attack up to 0.3° (see Section 5.4). As with the quiet runs, the heat transfer becomes more asymmetric with an increase in the magnitude of α. Unlike the quiet cases, the peak heat transfer seems to vary with angle of attack; the peak heat transfer generally decreases as α increases (Figure 5.61).

Figure 5.61 displays a more quantitative view of the heat transfer. As in Figure 5.46, this plots the heat transfer averaged over a streamwise strip of the model near either the windward side (near an azimuthal angle of 140°) or the leeward side (near 40°), all at the same unit Reynolds number. In general, near the windward side, the peak heat transfer occurs farther downstream as the angle of attack increases. The opposite trend is seen near the leeward side. An exception to this trend is the 0.3° case. A possible reason for the discrepancy is that, for this run, the diaphragm had difficulty bursting at the required stagnation pressure; for all other runs, the stagnation conditions were around P_0 =70 psia and T_0 =411 K, but for this case P_0 =65 psia and T_0 =393 K. Coupled with the initial stagnation temperature

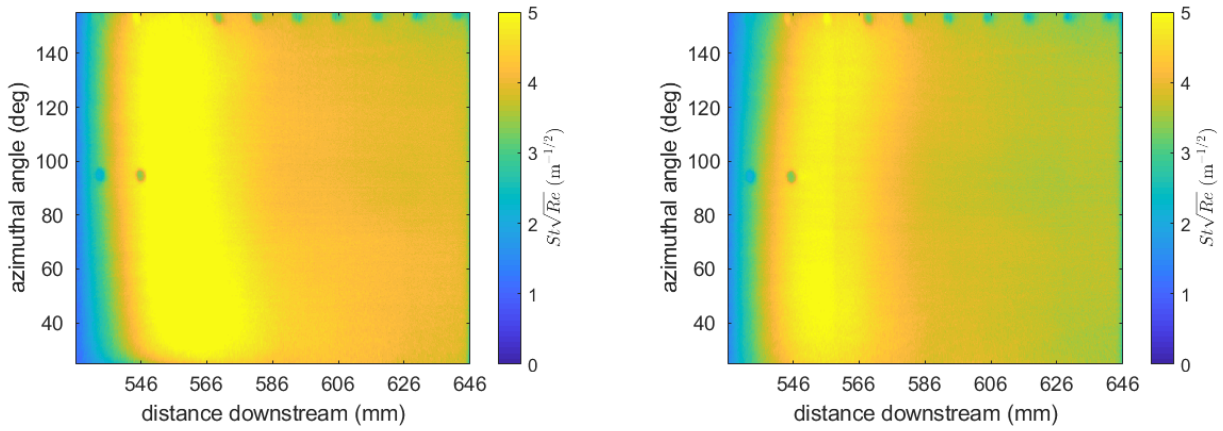

(a) -0.15°

(b) 0.0°

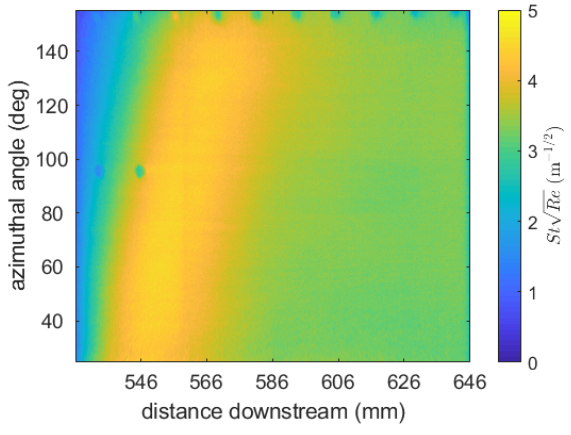

(c) 0.15°

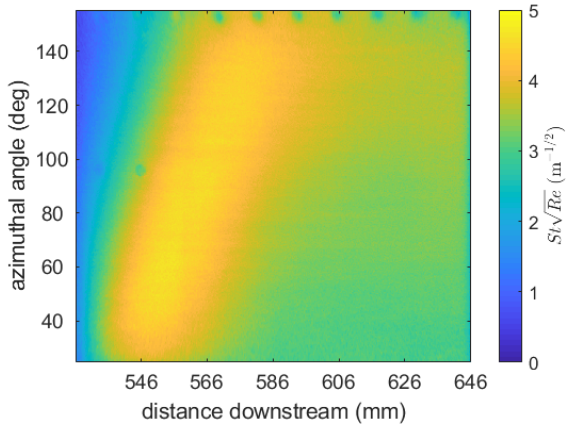

(d) 0.3°

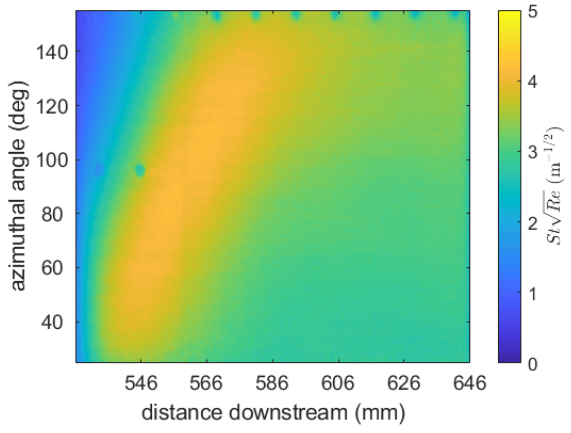

(e) 0.45°

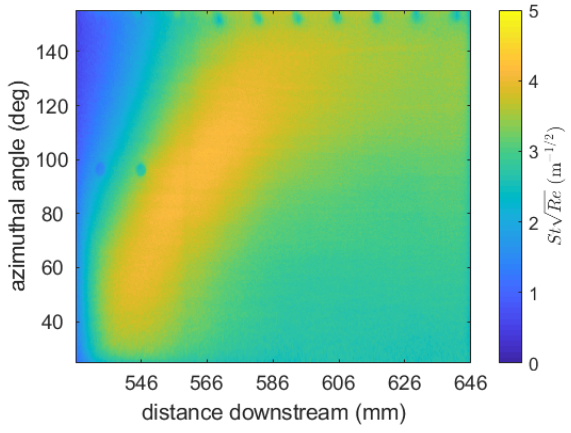

(f) 0.6°

Figure 5.60. Laminar-scaled heat transfer images on unrolled flare at small angles of attack, $Re = 6.05 \times 10^6$/m. The conventional noise flow moves from left to right. The main PCB ray was located at 180° azimuthal angle (the windward side), while the Kulite ray is at 150° and can be seen in the images.

being several degrees lower than for other cases, the desired unit Reynolds number occurred much later during the run. The remaining five cases, however, provide a good example of the small angle of attack effects. The separation bubble appears to generally increase in size with increasing angle of attack near the windward side of the model, while it seems to decrease in size near the leeward side. Large variations in peak heating occur with changes in angle of attack.

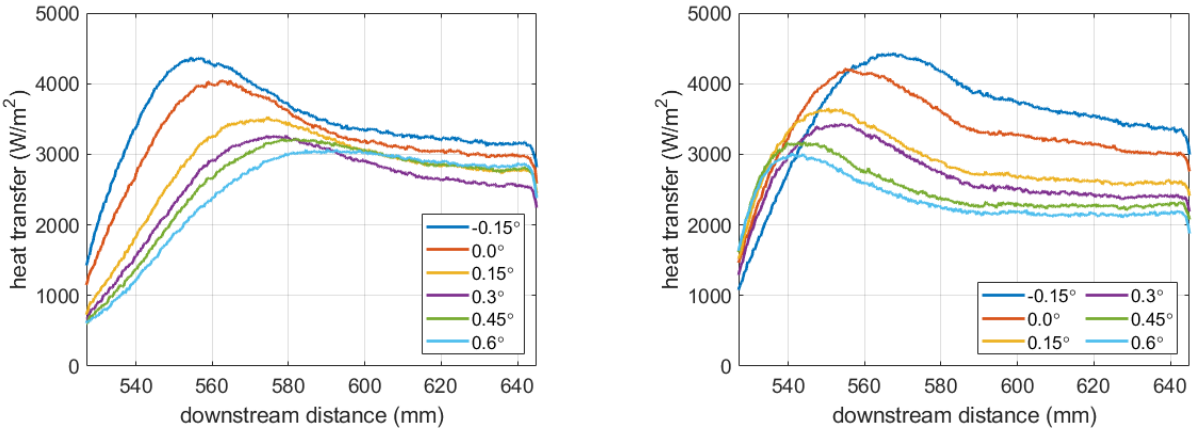

(a) Near-windward side.

(b) Near-leeward side.

Figure 5.61. Heat transfer as a function of downstream distance for the 10° flare under conventional noise flow.

As the angle of attack increases, the lines of constant heat transfer become less symmetric in azimuth. Figure 5.62 displays points extracted from the heat transfer images where $St\sqrt{Re} = 4\ (\pm\ 5 \times 10^{-4})\ \mathrm{m}^{-1/2}$, with linear fits added to the data. Since the conventional noise, transitional heat transfer has a peak rather than a plateau (the heat transfer of the quiet, laminar cases rose to a plateau), this $St\sqrt{Re}$ value occurs twice for each case. Only the upstream occurrence is plotted in Figure 5.62. The angles of the linear fits are plotted as a function of angle of attack in Figure 5.62b. The trend for the quiet, laminar cases is opposite to that for the noisy, transitional ones. As the angle of attack increases, the angle of the line of constant heat transfer also increases. Unlike for the quiet runs, it appears that the separation bubble grows on the windward side of the model as the angle of attack increases, while it shrinks on the leeward side. This trend is possibly due to the flow being transitional when entering the bubble. Previous supersonic and hypersonic separation studies have found

that laminar and transitional separation bubbles display opposite trends with changing unit Reynolds numbers; the bubble tends to grow with increasing Re for laminar cases, but shrink for transitional ones [15], [18]. These opposing trends may also hold for bubble size variations with small angles of attack.

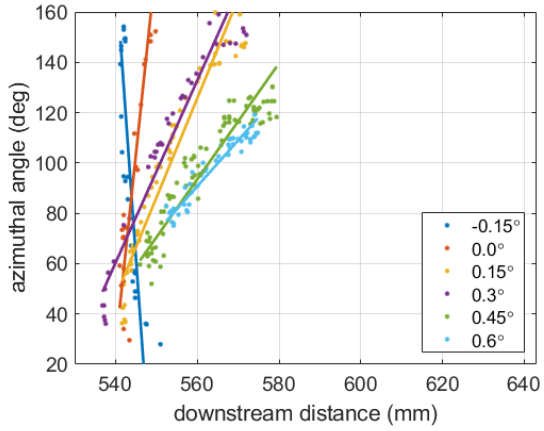

(a) Locations and linear fits for $St\sqrt{Re} = 4$ $m^{-1/2}$.

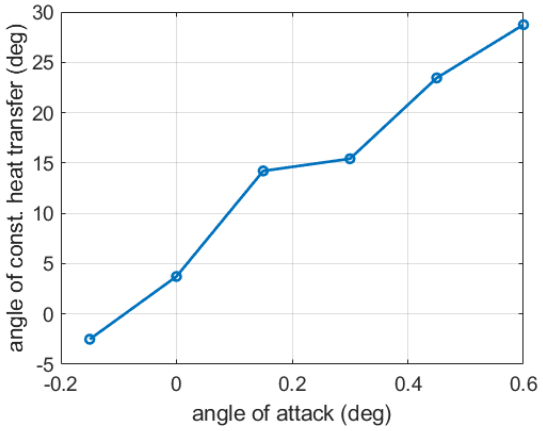

(b) Angles (determined from the slope) of linear fits as a function of angle of attack. 0.0° corresponds to a perfectly vertical line.

Figure 5.62. Linearly fitted data for $St \cdot Re^{1/2} = 4$ $m^{-1/2}$. The angle of the lines of constant heat transfer increase monotonically with angle of attack. From conventional noise runs with transitional flow.

Figure 5.63 shows schlieren images taken on the windward side of the model during a later entry at $Re = 5.45 \times 10^6$/m (P_0 =65 psia, T_0 =417 K). While at a slightly lower unit Reynolds numbers, the flow was still transitional based on surface pressure spectra. Blue dashed lines are shown over the reattachment shocks in the images, and are extrapolated to the shear layer surface. As the angle of attack increases, the reattachment point moves downstream. The reattachment shifts from 0.54 m downstream of the nosetip at 0.0° to 0.56 m by 0.6°. This trend agrees with the heat transfer measurements, where the peak in heat transfer associated with reattachment moves downstream with increasing angle of attack near the windward side. This is also the opposite of what was seen in the laminar, quiet cases, where the reattachment point moved upstream with increasing angle of attack on the windward side.

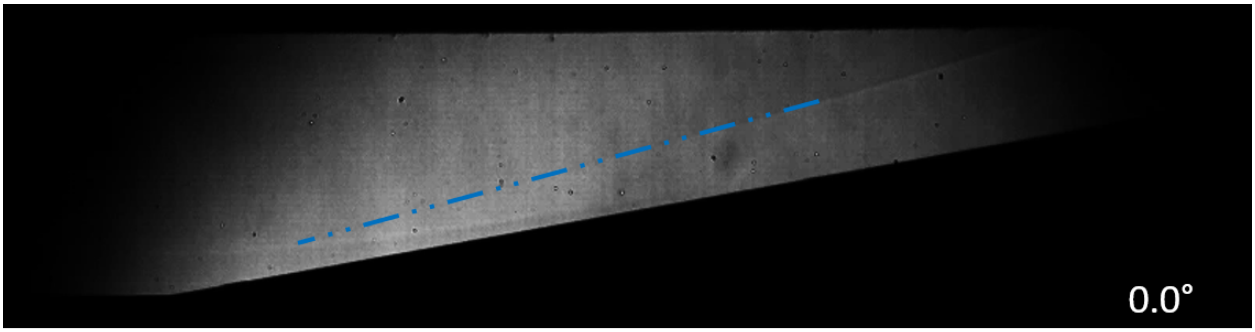

(a) 0.0°

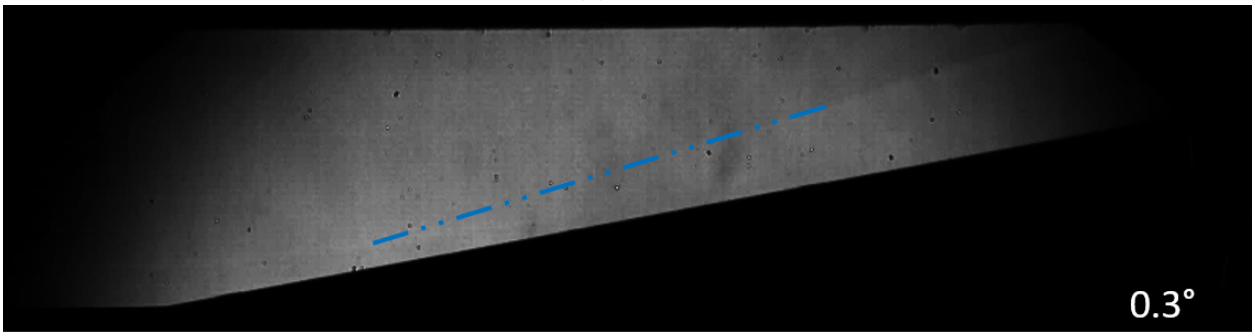

(b) 0.3°

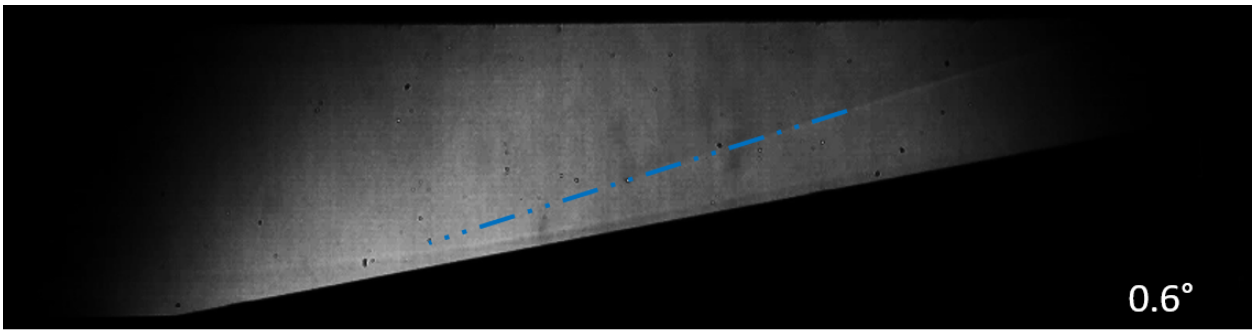

(c) 0.6°

Figure 5.63. Schlieren images of the windward side of the bubble in conventional noise at $Re = 5.45 \times 10^6$/m with 0.25 μs exposure. The reattachment shock is extrapolated with a blue dashed line to its intersection point with the shear layer. Flow is from left to right.

Figure 5.64 plots the power spectral densities for a PCB located on the cone for the different angles of attack. PCBs were located on the windward ray. Peaks between 150 and 200 kHz can be clearly seen, corresponding to the second mode. Additionally, the first harmonic for those peaks can also be seen between 300 and 400 kHz. As the angle increases, the peak frequency also increases, as expected. For the conventional noise cases, the peak amplitude decreases as α increases on the windward side. This could partially be due to the frequency dependence of the tunnel noise. Additionally, the second mode is more stable on the windward side of a model.

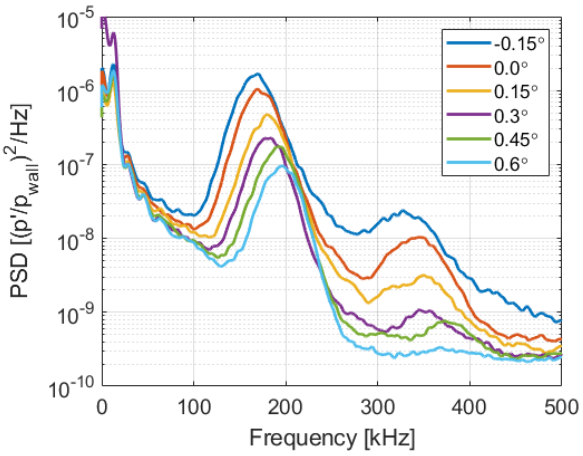

Figure 5.64. Power spectral densities for PCB sensor located on the cone, 0.387m downstream, at various small angles of attack, in conventional noise. On the windward ray.

Figure 5.65 shows PSDs for three locations on the cylinder. Unlike in quiet, laminar flow, the three cylinder PCBs in noisy, transitional flow have distinct PSDs. Moving downstream over the cylinder, the peak frequency trend changes; at 0.425 m downstream, the peak frequencies increase with increasing angle of attack, while by 0.511 m, the peak frequencies generally decrease with increasing α (Figure 5.65). However, the amplitudes are still damped over the cylinder relative to over the cone (Figure 5.64) as the flow moves through an expansion. At the first station, 0.425 m downstream, the second mode frequency peaks can be seen between 150 and 200 kHz, similar to along the cone. The flow is still believed to be attached at this point. As on the cone, the peak frequency increases with the angle

of attack. By 0.479 m downstream, these peaks are lower and now all are approximately aligned around 110 kHz. It is unclear if the flow is attached or in the separation bubble. At 0.511 m, the trend is reversed from the upstream PCB, with larger angles corresponding to lower peak frequencies. The sensors along the cylinder were found to be slightly coherent for the 50-150 kHz frequency range, potentially indicating a convective instability, possibly still the second mode.

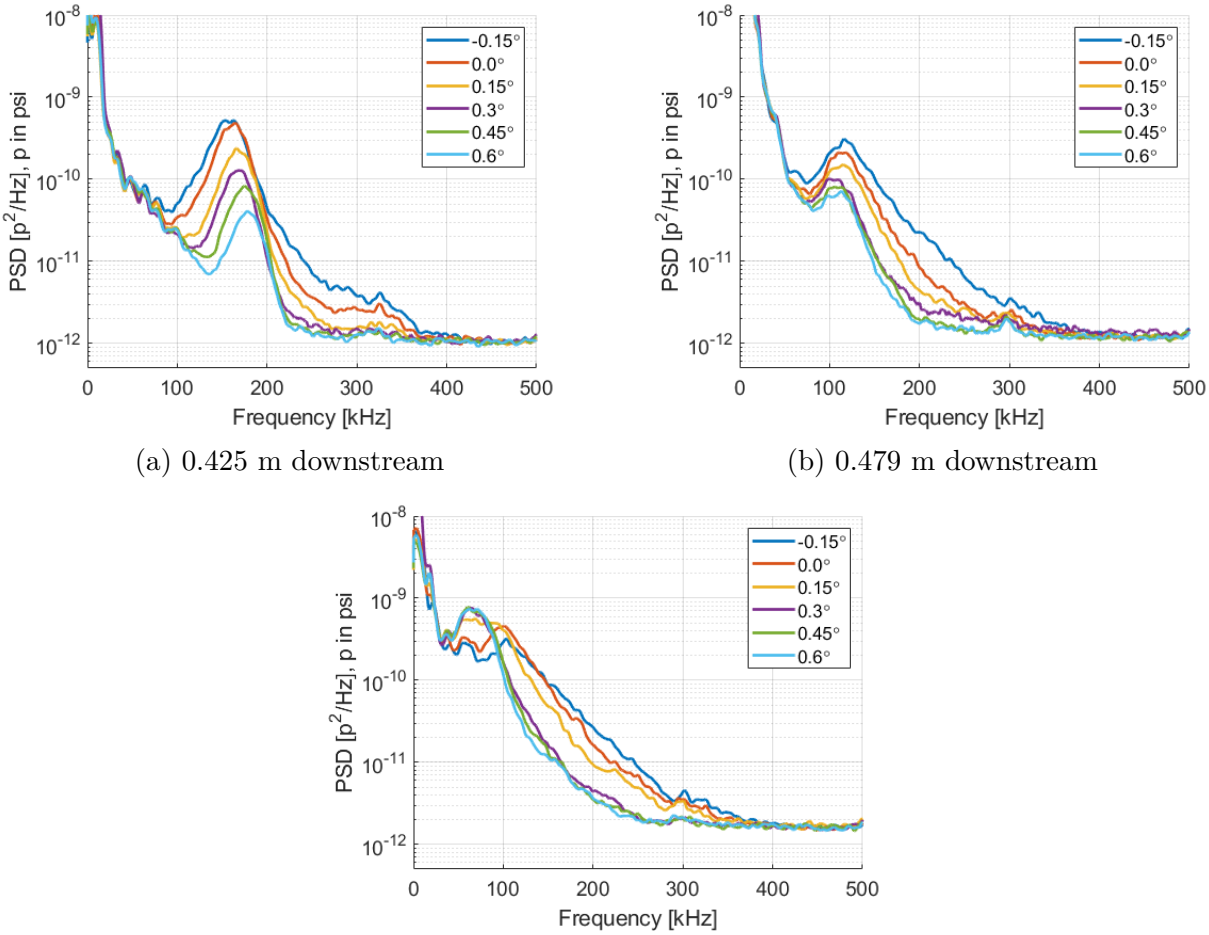

(a) 0.425 m downstream

(b) 0.479 m downstream

(c) 0.511 m downstream

Figure 5.65. Power spectral densities for PCB sensors located on the cylinder at various small angles of attack, in conventional noise. Along the windward ray. The expansion corner is located at 0.399 m downstream.

Figure 5.66 plots PSDs for PCB sensors located along the 10° flare. Each plot is for a single angle of attack, with four PCBs at varying downstream locations. For -0.15° and 0.0°, all but the upstream-most PCB have broadband signals, most likely indicating the boundary

layer is fully turbulent. Based on the heat transfer, reattachment most likely occurs upstream of the second PCB at 0.548 m. It is possible that reattachment and the end of transition are occurring simultaneously in the conventional-noise transitional flow. This is similar to what McKiernan observed on his finite-span separation model [35], [36], but is different than the quiet, laminar flow results. For higher angles of attack, the flow remains transitional up to 0.561 m as the separation bubble gets larger on the side with the sensors. For these angles, peaks around 50 kHz are visible in the sensors upstream of reattachment. These peaks have high values of coherence across adjacent sensors near this frequency, so most likely represent traveling waves rather than a local oscillation. Normalized RMS values vary between 10% and 33% of the computed surface pressure and are plotted as a function of angle of attack in Figure 5.67.

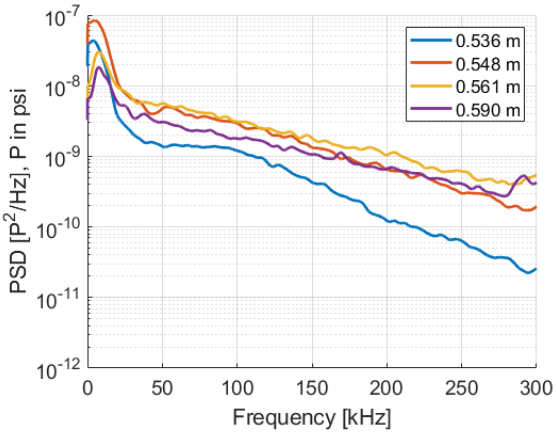

(a) -0.15°

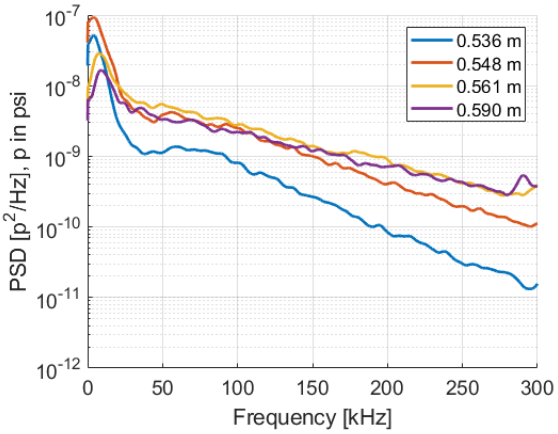

(b) 0.0°

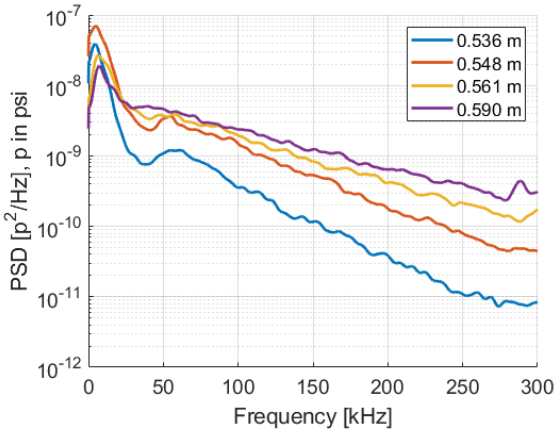

(c) 0.15°

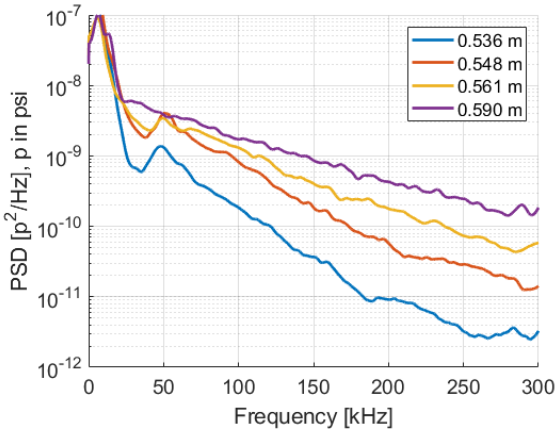

(d) 0.3°

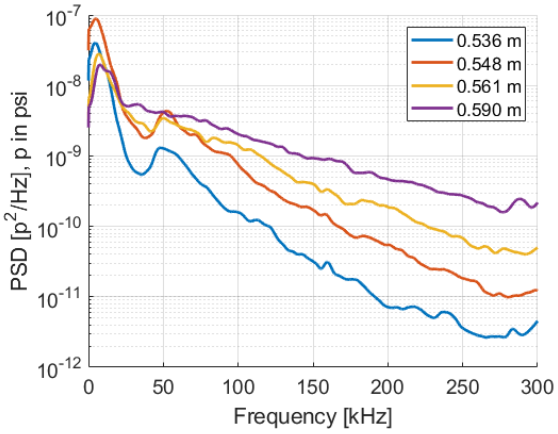

(e) 0.45°

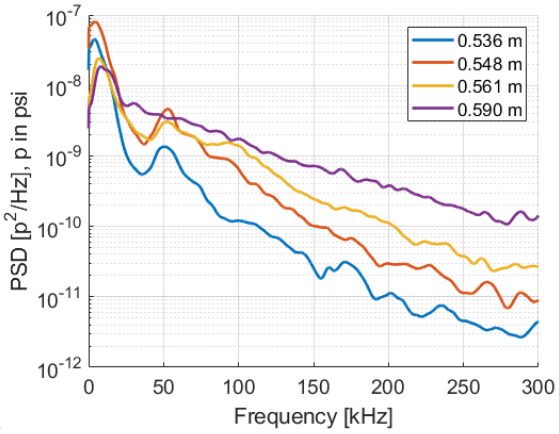

(f) 0.6°

Figure 5.66. PCB PSDs along the 10° flare at different small angles of attack, with $Re = 6.05 \times 10^6/\text{m}$. In conventional noise.

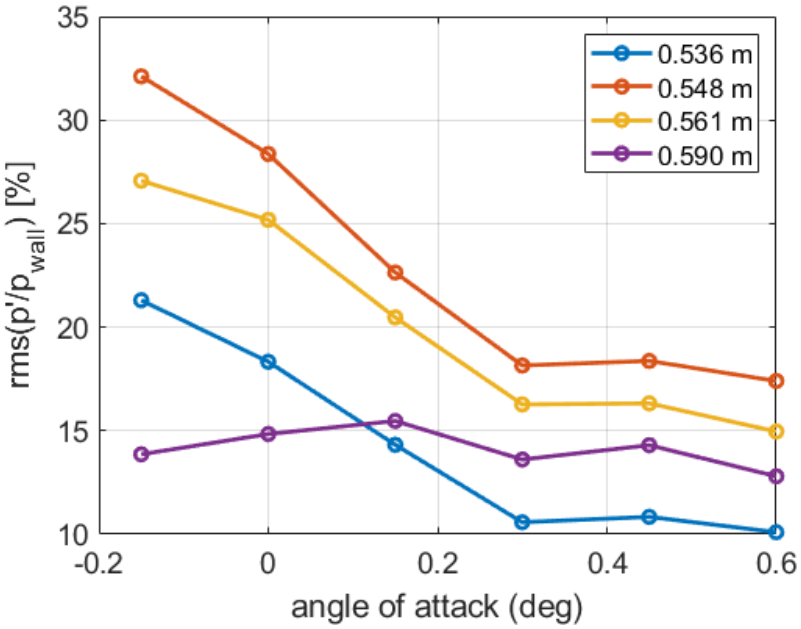

Figure 5.67. Integrated RMS amplitudes for different axial stations as a function of angle of attack. Values normalized by computed wall pressures at 0.0° angle of attack. Under conventional noise, integrated between 50-270 kHz. On the windward ray for positive α.

5.4 Streamwise Vortices Downstream of Reattachment

Work by Ginoux [17], Lugrin [21], Running [79], [80] and others with 2D or axisymmetric separations in hypersonic flow have often revealed streamwise vortices in the reattached boundary layer. The vortices are generally larger if there are larger imperfections in the leading edge, so geometries with sharp nosetips have weaker vortices [17], [20]. In this study, which used a sharp nosetip, only faint streamwise streaks indicative of vortices were seen, and only in a subset of the runs. Figures 5.68 and 5.71 highlight the vortex effects observed in the quiet and conventional-noise cases, respectively.

In quiet flow, only one case clearly showed evidence of streamwise vortices, at 0.0° angle of attack. The heat transfer image from this run is shown in Figure 5.68a with a color scale selected to highlight the streaks under the reattached boundary layer. The streaks seen in this image shift slightly in azimuth when different points in time are observed (see Figure 5.69). The purple box shows the area averaged over to plot the heat transfer fluctuations

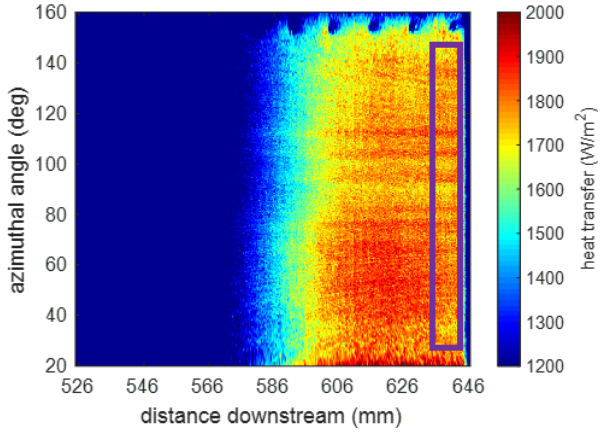

(a) Heat transfer image showing section of surface averaged over. Color values scaled to highlight evidence of vortices.

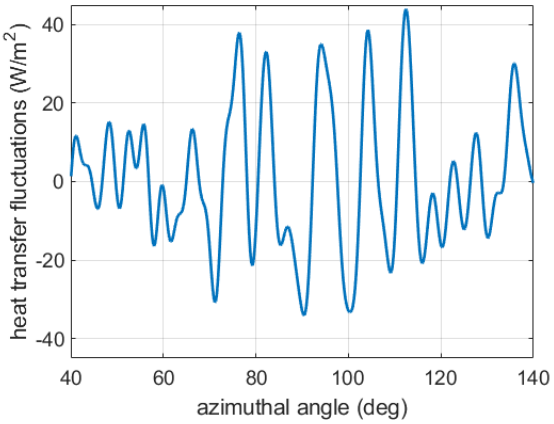

(b) Heat transfer fluctuations as function of azimuthal angle. Bandpass filtered between 0.03 and 0.30 cycles/°.

Figure 5.68. Weak streamwise vortices seen in quiet, laminar flow near the downstream edge of the flare. From Run 1040, $Re = 11.5 \times 10^6$/m.

as a function of azimuthal angle in Figure 5.68b. The heat transfer values were filtered between 0.03 and 0.30 cycles/° to remove the mean and smooth the data. In this plot, the periodic nature of the heat transfer is more apparent, and about 0.1 cycles/° (36 cycles per circumference) are present. The azimuthal power spectral densities are plotted in Figure 5.70c, showing a peak near 0.1 cycles/° only present at 0.0°. Run 1040 is believed to be the only quiet-flow case where streamwise vortices were seen because it is the quiet case to have the angle of attack closest to 0.0°. Of all the quiet flow runs conducted, this case had lines of constant heat transfer that were the closest to vertical (the heat transfer was the most axisymmetric). With slight asymmetries in the reattachment location, the streamwise vortices in heat transfer seem to disappear.

The filtered heat transfer as a function of azimuthal angle for all six angles of attack tested are plotted in Figure 5.70. Meaningful peaks are only visible for the 0.0° case. Figure 5.70b displays the RMS amplitude of the fluctuations, again highlighting the difference between the 0.0° case relative to the other angles.

Under conventional noise, the streamwise vortices were not as sensitive to asymmetric reattachment from small angles of attack, compared to the quiet flow results. Similar streaks were seen from several runs with angle of attacks from -0.15° through 0.6°. Figure 5.71a

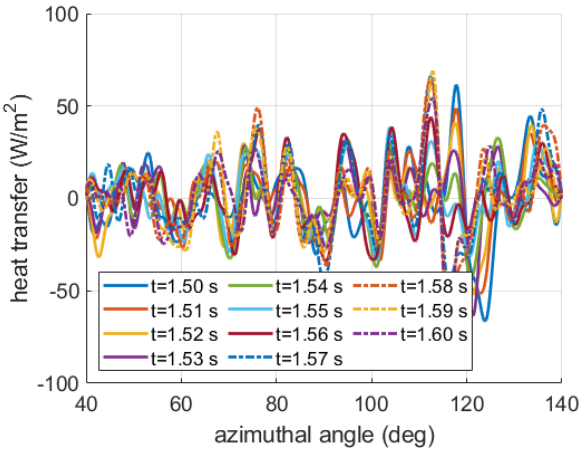

Figure 5.69. Filtered heat transfer fluctuations plotted in 0.01-second intervals. From Run 1040, $Re = 11.5 \times 10^6/\text{m}$.

shows an example of the heat transfer where streaks are evident. With conventional noise, reattachment is farther upstream. Figure 5.71b plots the heat transfer as a function of azimuthal angle again, with the values taken from averaging across the red box in Figure 5.71a. As in the quiet case, the heat transfer is periodic in azimuthal angle, with about 36 cycles per circumference.

These examples show initial evidence of streamwise vortices from a subset of the heat transfer results in quiet and noisy flow. Future work by Wagner will use controlled roughnesses to further investigate this instability [22].

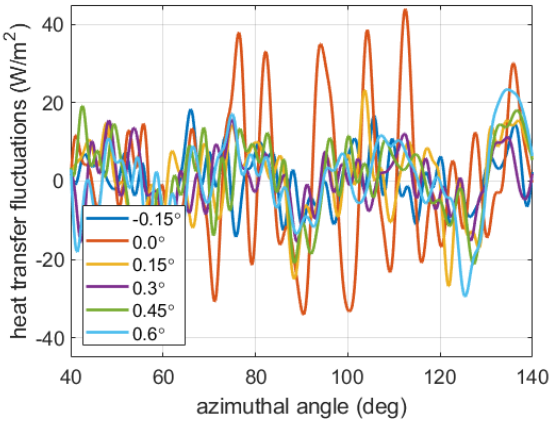

(a) Filtered heat transfer values for small angles of attack.

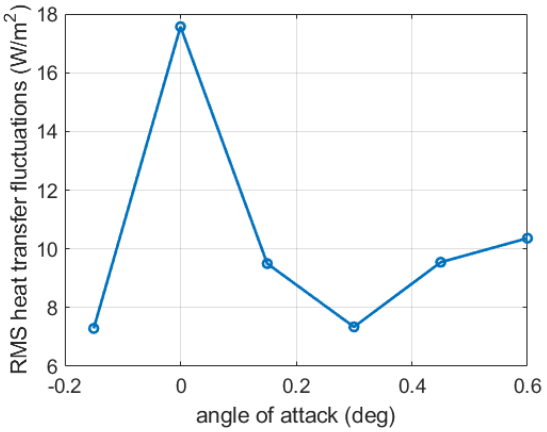

(b) Heat transfer RMS amplitudes as function of angle of attack.

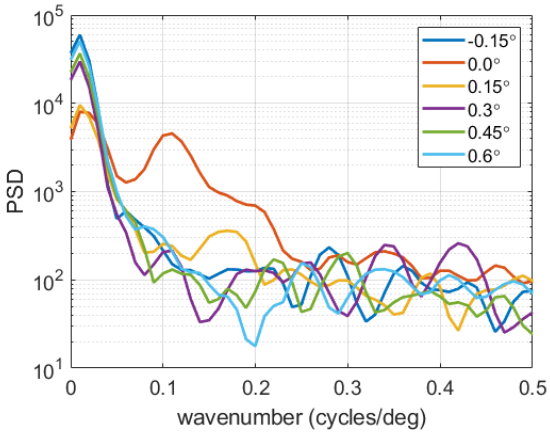

(c) Heat transfer azimuthal power spectral densities.

Figure 5.70. Streamwise vortices only appearing for 0.0° angle of attack. From Runs 1037, 1040, 1042, 1044, 1046 and 1048, $Re = 11.5 \times 10^6/\text{m}$

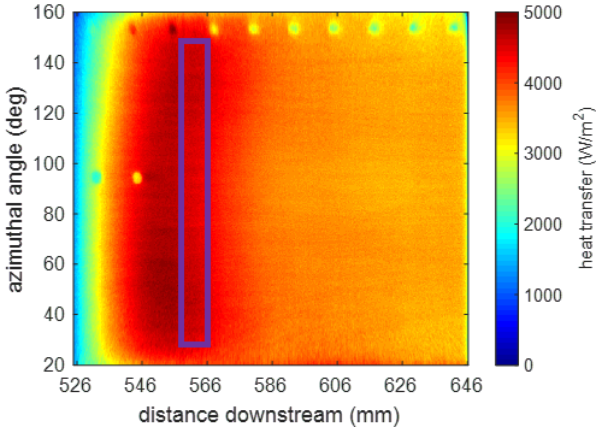

(a) Heat transfer image showing section of surface averaged over. Color values scaled to highlight evidence of vortices.

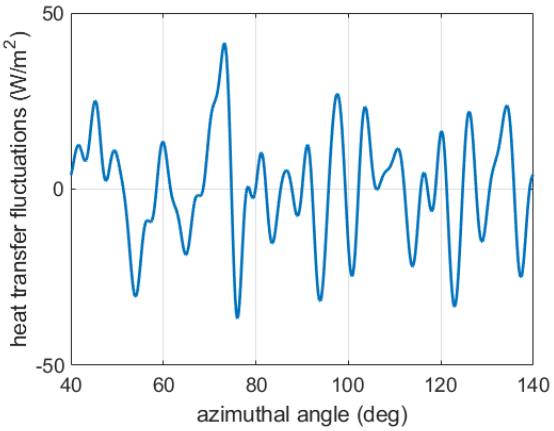

(b) Heat transfer values as function of azimuthal angle.

Figure 5.71. Weak streamwise vortices seen in conventional noise, transitional flow near the peak heat transfer. $Re = 6.05 \times 10^6/\text{m}$.

5.5 Summary of Results with a Separation Bubble

Heat transfer, schlieren images, and surface pressure and off-surface density fluctuations were obtained for a sharp cone-cylinder-flare model with the compression angle large enough to cause the boundary layer to separate. Tests were made at a variety of unit Reynolds numbers in both quiet and conventional noise flow near-0.0° angle of attack. Additionally, small non-zero angles of attack were studied for laminar, quiet flow and transitional, noisy flow.

In quiet flow, the boundary layer remained laminar for the entirety of the model. Laminar-scaled heat transfer images show a region of rapid heating followed by a plateau downstream. The increase in heating is believed to be due to reattachment of the bubble, which is supported by schlieren images. As the unit Reynolds number increased, the bubble size also increased for these laminar cases. Pressure fluctuations under the reattached boundary layer reveal two instabilities. The second mode peaks between 170 and 230 kHz depending on the unit Reynolds number, while a shear-layer instability is found between 50 and 170 kHz. This shear-layer instability is only present in the case with the separation bubble, and is first seen in the shear layer upstream of reattachment using the FLDI. It is therefore referred to as the "shear-generated" instability. These two instability convect downstream with different disturbance velocities; the second mode averaged around 81% of the freestream velocity, while the shear-generated instability was closer to 98%. Both instabilities were seen repeatably across entries. At small angles of attack, the bubble size decreased with increasing angle on the windward side of the model in laminar flow.

Under conventional noise, laminar, transitional, and turbulent flow was observed depending on the unit Reynolds number. Laminar-flow heat transfer for the noisy runs agreed well with the quiet laminar results. For transitional cases, transition seemed to occur at reattachment, where a peak in the heat transfer was observed. As the unit Reynolds number increased, the bubble size decreased for transitional runs. Surface pressure fluctuation measurements reveal peaks between 50 and 70 kHz for the laminar and some transitional cases, but it is unclear if they are from the second mode or are instead related to the shear layer.

At small angles of attack, the bubble size increased with increasing angle of attack on the windward side of the model for transitional flow.

6. CONTROLLED PERTURBATION MEASUREMENTS

A plasma perturber was integrated into the surface of the 10° cone-cylinder-flare model. The electrodes were placed 0.387 m downstream of the nosetip, towards the end of the cone but upstream of the cylinder. One-hundred nanosecond pulses at 2 kHz were generated with voltages between 7.5 and 12.5 kV. The disturbance that was generated was measured moving downstream through the separation bubble as well as after reattachment. Some of these results were published in Ref. [81].

6.1 Perturber Design and Setup

The electrode model insert for the glow perturber was designed based on previous perturbers used by Casper [82]. Two 1.78-mm-diameter stainless steel electrodes were installed in a Macor mount, with a gap between them determined by Paschen's law. This law describes the relationship between the static pressure, electrode separation, and threshold voltage necessary to cause breakdown according to the Townsend mechanism, and is described in Equation 6.1 [83].

$$V_t = F(pd) \tag{6.1}$$

In this equation, V_t is the threshold breakdown voltage (which is at least 327 V for air), p is the static pressure at the electrodes' location, d is the distance between the electrodes, and F is an empirically determined constant (433.7 V/(Pa-m) for this case). For air, the threshold voltage is reached with a Pd value of 0.754 Pa-m [82]. With the electrodes located 0.387 m downstream of the nosetip, the static pressure at their location is computed to be 1016.8 Pa for maximum quiet conditions ($P_0 = 150$ psia, $T_0 = 430$ K, $Re = 11.6 \times 10^6$/m). This corresponds to an electrode separation of 0.74 mm.

The electrodes were installed in MACOR, a machinable ceramic, and mounted directly into the surface of the model. They were located 0.387 m downstream of the nosetip, at the downstream end of the cone just upstream of the cylinder. The electrodes were placed in

line with the PCB main ray, so that disturbances generated from them would be measurable by the PCB sensors as they propagated downstream. Figure 6.1 shows a photograph of the model with the electrodes installed, as well as a drawing of the insert. Dimensioned drawings of this version of the model and the insert can be found in Appendix D.

(a) 10° cone-cylinder-flare model with perturber electrodes installed. Nosetip removed. The center of the electrodes is 387 mm downstream of the nosetip, 12.7 mm from the expansion corner.

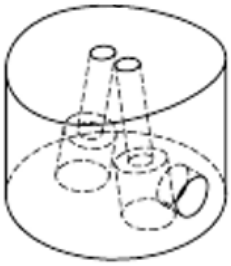

(b) Sketch of insert with electrodes.

Figure 6.1. Plasma perturber electronics setup.

An Eagle Harbor NSP-3300-20-F Pulser was used to generate the controlled disturbances. This is the same device used by McKiernan for the artificial disturbances used in his dissertation [35]. It was triggered by a Stanford Research Systems DG535 delay generator, which itself was triggered off the HBM data acquisition system. The delay generator provided 300 pulses at a rate of 2 kHz, with pulse widths of 100 ns. The pulse train was set to begin 1.5 seconds after the start of the run, so that the artificial disturbances occurred during the quiet and uniform portion of the flow. The Eagle Harbor pulser was powered with a TDK-Lambda power supply, which generates voltages between 0-600 V. The pulser outputs a voltage between 0-25 kV that is linearly related to the power supply output. The pulses passed through a resistor bank on the way to the electrodes, to limit the maximum volt-

age to 20 kV. The voltage was measured with two Tektronix P6015A high voltage probes, one connected to each wire attached to the exit of the pulser. The current was measured with a Magnelab CT-D1.0 current transformer located around one of the wires exiting the resistor bank. A Keysight Technologies DSO9104A oscilloscope was used to record both the voltage and current for the majority of the runs, and was also triggered off the HBM DAQ. This oscilloscope has a 1 GHz bandwidth with 12-bit vertical resolution. The electronics for the perturber were provided by Prof. Sally Bane. They are generally used for plasma experiments such as in [84], [85]. Photographs of the perturber setup can be seen in Figure 6.2.

Pulser voltages of 7.5, 10.0, and 12.5 kV were used with the plasma perturber at a freestream unit Reynolds number of 11.6×10^6/m in quiet flow. The 12.5 kV voltage was then used at a variety of stagnation pressures to see the effect of unit Reynolds number on wave-packet amplification. The stagnation pressures range from a case where no waves are naturally seen to near the maximum quiet pressure. The Reynolds sweep also includes FLDI measurements of the shear layer above the bubble. Table 6.1 summarizes the run conditions and pulser settings used for this study.

Table 6.1. Run conditions and pulser settings for plasma perturber study.

Run	Re (m^{-1})	Pulse Duration (ns)	Frequency (kHz)	Number of Pulses	Voltage (kV)
1232	11.6×10^6	100	2	300	7.5
1211	11.6×10^6	100	2	300	10.0
1228	11.6×10^6	100	2	300	12.5
1231	10.3×10^6	100	2	300	12.5
1230	8.91×10^6	100	2	300	12.5
1229	7.39×10^6	100	2	300	12.5

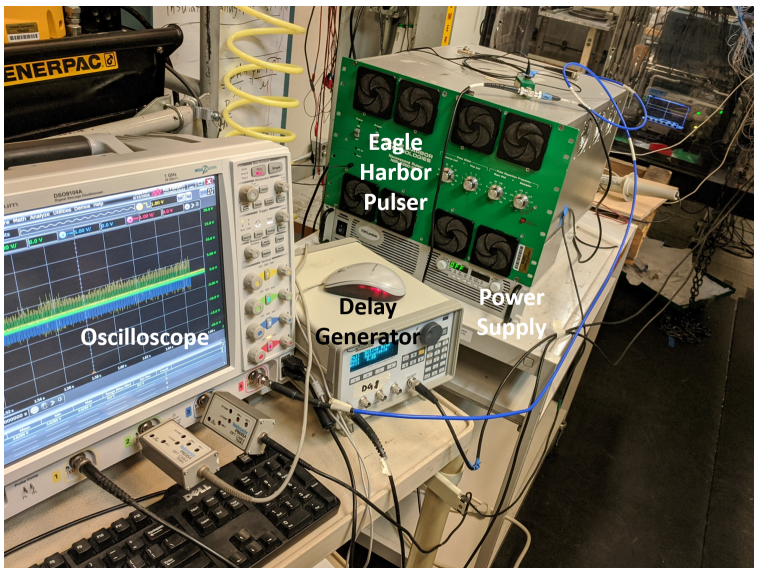

(a) Front of pulser, oscilloscope, and delay generator.

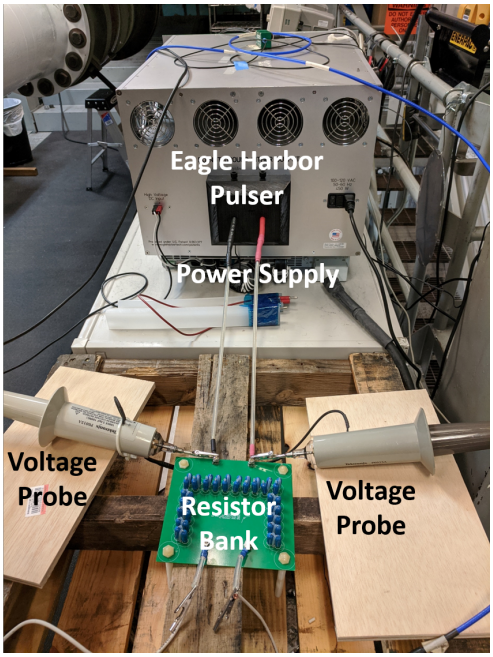

(b) Back of pulser, resistor bank, and probes.

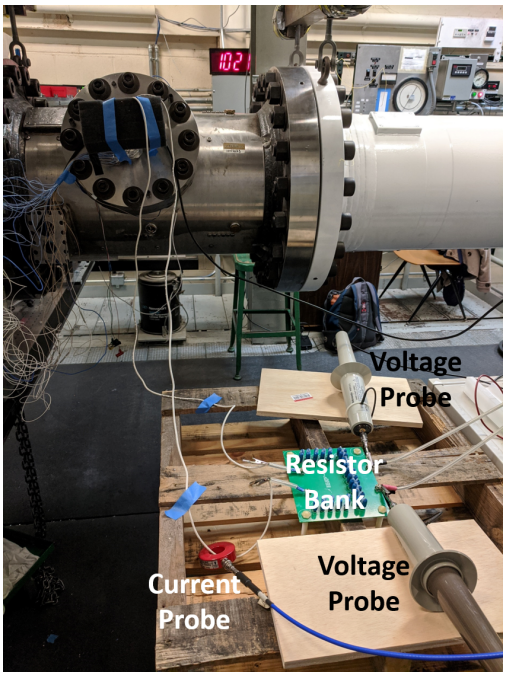

(c) Tunnel with high-voltage wires exiting, resistor bank, and probes.

Figure 6.2. Plasma perturber electronics setup.

6.2 Pulse Statistics

The voltage exiting the pulser and the current exiting the resistor bank were measured for each run. The data were recorded at 50 MHz to capture all pulses during a run. The pulse statistics for the runs highlighted in this chapter are summarized in Table 6.2. For each run, the variation in pulse voltage stayed below 13%, while the variation in current was below 27%. These values are comparable to what McKiernan measured using a similar perturber [35].

Table 6.2. Electronic statistics for runs with the plasma perturber.

Run	Mean V_{rms} (kV)	Stand. Dev. V_{rms} (kV)	Max. Var. V_{rms} (%)	Mean I_{rms} (A)	Stand. Dev. I_{rms} (A)	Max. Var. I_{rms} (%)
1232	2.23	0.103	12.6	2.68	0.231	26.8
1211	3.05	0.123	8.2	3.78	0.516	26.3
1228	3.44	0.154	11.0	4.68	0.483	24.2
1231	3.40	0.158	10.8	4.75	0.332	17.4
1230	3.26	0.134	11.8	4.67	0.352	23.5
1229	3.34	0.127	10.2	4.49	0.421	26.6

Figure 6.3 shows some sample pulses and a histogram of all pulses for Run 1228. In Figure 6.3a, three individual pulses as well as the ensemble average current are shown. While there was some variation in the peak current, the pulse width was highly consistent. A histogram of the RMS current for the pulses is shown in Figure 6.3b. The majority of the pulses were within 4.0 to 5.5 A. In Figure 6.3c, the same three individual pulses and the ensemble average voltage can be seen. The voltage of the pulses was more consistent in waveform, and again highly repeatable in pulse width. The corresponding histogram is in Figure 6.3d. The pulse voltages were between 3 and 4 kV.

To get a better idea of the general pulse shape, a few pulses were generated with no flow in the tunnel, at atmospheric pressure. These pulses were captured with a higher sampling rate of 2 GHz. They were measured at without flow because the data capture period was

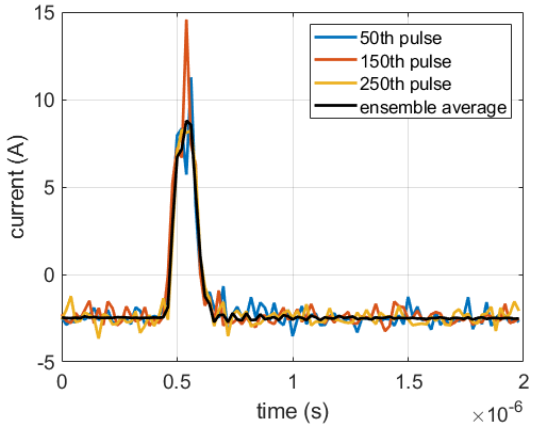

(a) Individual pulses and averaged current.

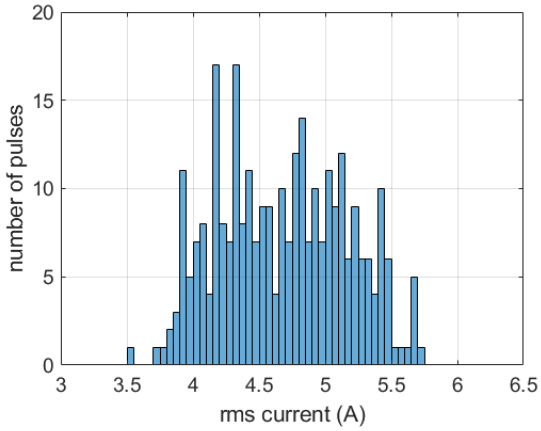

(b) RMS integrated current distribution.

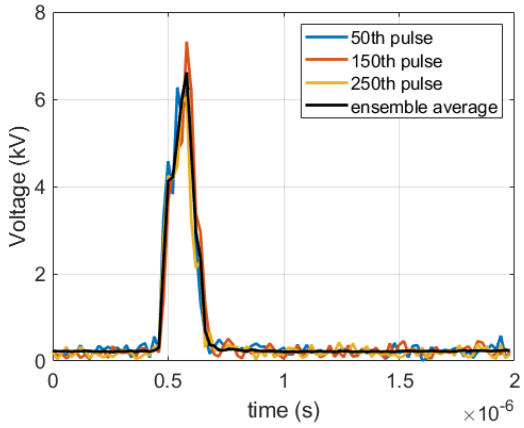

(c) Individual pulses and averaged voltage.

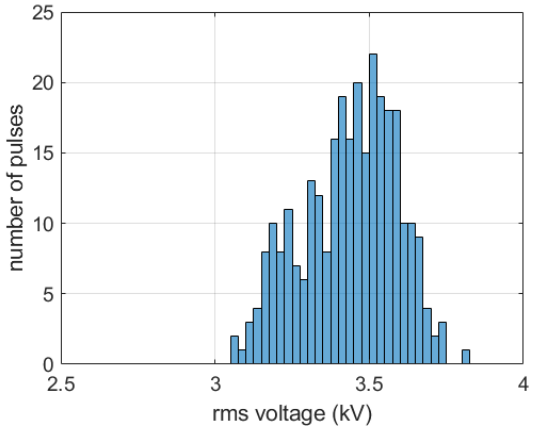

(d) RMS integrated voltage distribution.

Figure 6.3. Plasma perturber pulse samples and distributions for Run 1228, with $Re = 11.6 \times 10^6/\text{m}$.

shorter with the higher sampling rate, which makes it challenging to synchronize with the start of quiet flow in the tunnel. The current and voltage for one of these pulses is plotted in Figures 6.4a and 6.4b, respectively. A sample pulse from Run 1228 is also plotted along the same axes, to compare the higher-resolution pulse generated at atmospheric pressure to one generated during a run (in this case, with $Re = 11.6 \times 10^6/\text{m}$). The current from both pulses are similar, with pulse widths of around 150 ns. The voltages, however, differ in both peak height and width. The atmospheric pulse reaches nearly 10 kV and has a width of only about 100 ns, while the pulse from Run 1228 only goes to about 6 kV and is closer to 150 ns. FFTs for both pulses are shown in Figures 6.4c and 6.4d. The current

FFTs are similar for the atmospheric and Run 1228 pulses, with a first lobe ending around 10 MHz. The atmospheric voltage FFT also had a first lobe that ends around 10 MHz, while the Run 1228 voltage FFT drops off by 9 MHz. Importantly, the frequency response for the two pulses is essentially flat up to 2 MHz for both current and voltage. These pulses excite a large band of frequencies including the natural instabilities previously seen between 50-170 kHz and 170-290 kHz. Therefore, the pulses are sufficiently short enough to excite the shear-layer and boundary-layer instabilities of this model. While not conducted during this dissertation, future work with the perturber should include FLDI measurements of the aerodynamic disturbance generated at the electrodes. This would allow for direct measurements of the pulse generated in the air rather than relying on current and voltage measurements.

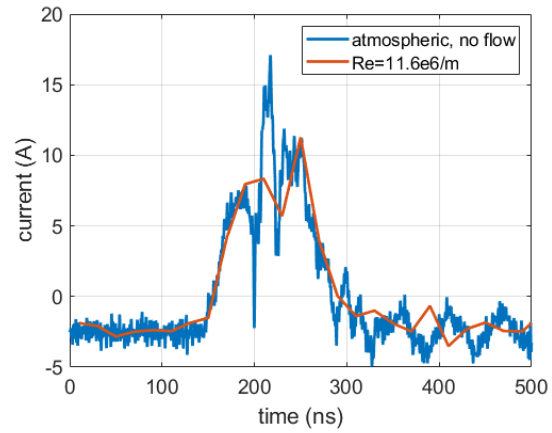

(a) Individual pulses, current.

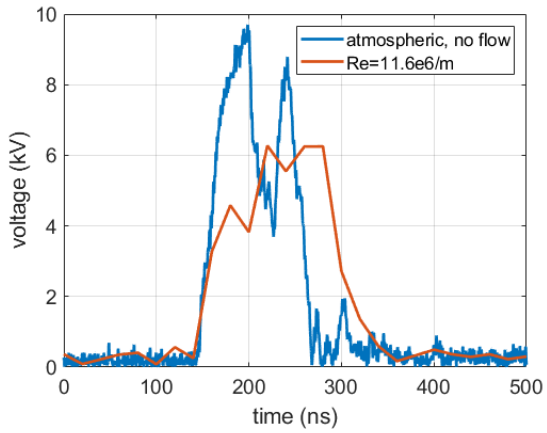

(b) Individual pulses, voltage.

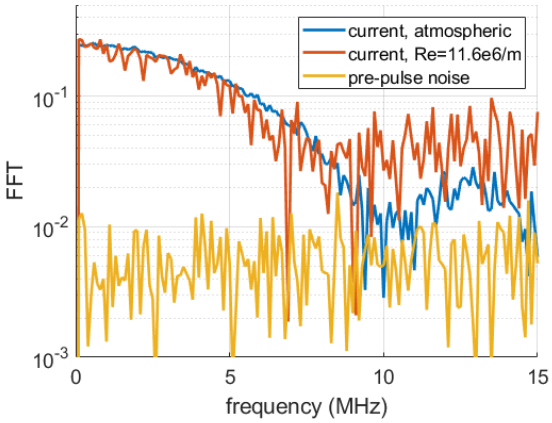

(c) Current FFT.

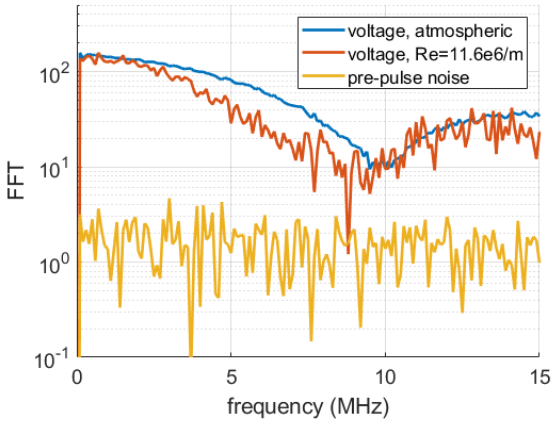

(d) Voltage FFT.

Figure 6.4. Plasma perturber pulse examples. High sampling rate pulse data taken at atmospheric pressure with no flow, while lower sampling rate pulse data taken from Run 1228 with $Re = 11.6 \times 10^6/\text{m}$.

6.3 Noise Filtering Methods

Each time the perturber sent a pulse, a large noise spike was visible in all sensors. These noise spikes created broadband noise in the power spectral densities, which could obfuscate a lower-amplitude signal. To reduce this effect, McKiernan looked at using a PSD of the ensemble average or using a Hampel filter to remove the noise [35]. He found that the PSD of the ensemble average produced lower amplitudes due to the averaging out of intermittent signals, while the Hampel filter produced power values similar to the unfiltered data when a signal was present, but with lower noise levels. The Hampel filter uses a moving median

average to remove outliers from the data. It does effectively lower the noise floor, but depending on the settings may leave some of the noise spike or remove some of the wave packet if the frequency is high enough (in some cases as low as 250 kHz). Since the frequency at which the noise spikes appear is known, it is possible to instead directly replace the spike with the local mean. This works similarly to the Hampel filter, except that the times when the replacement is taking place are predetermined rather than dynamically searched for. This technique is only possible because the pulser is instructed to fire at a given frequency, here 2.000 kHz (accurate to 0.03 Hz), so the time of each associated noise spike is therefore known. By directing the data replacement, only the noise spikes are removed and the generated wave packets are left undisturbed.

Figure 6.5 shows an example comparing the Hampel filter and the method of directly removing the noise spikes. In Figure 6.5a, the raw unfiltered pressure fluctuations are plotted in blue. A large, narrow spike can be seen between 1.5300 and 1.5301 seconds. This spike corresponds to electronic noise from the perturber firing. The Hampel filtered data is shown in red. It greatly reduces the amplitude of the noise spike, but still has some residual noise present. The direct replacement data is in yellow. This time trace completely removes the noise spike and replaces it with a constant equal to the local mean. The generated wave packet can be seen just after 1.5303 seconds. It is the same for all three time traces. The corresponding power spectral densities for the three series of data are shown in Figure 6.5b. The raw, unfiltered pressure fluctuations show a peak around 100 kHz, and the spectra remains above 1×10^{-11}/Hz for the 500 kHz range shown. By comparison, the prerun electronic noise is level is around 2×10^{-13}/Hz at 500 kHz. The Hampel filtered data maintains the amplitude of the 100 kHz peak, but then drops down to around 1×10^{-12}/Hz by 500 kHz. Finally, the pressure fluctuations where the noise is directly cut still has the 100 kHz peak, but then drops down to the level of the electronic noise by 500 kHz. Due to the superior noise reduction without loss of signal amplitude, the direct cut method is used for the processing of the perturber data.

Future work with this data set will include conducting a wavelet analysis. More quantitative spectra will also be built by excluding time series data without the artificially-generated disturbances.

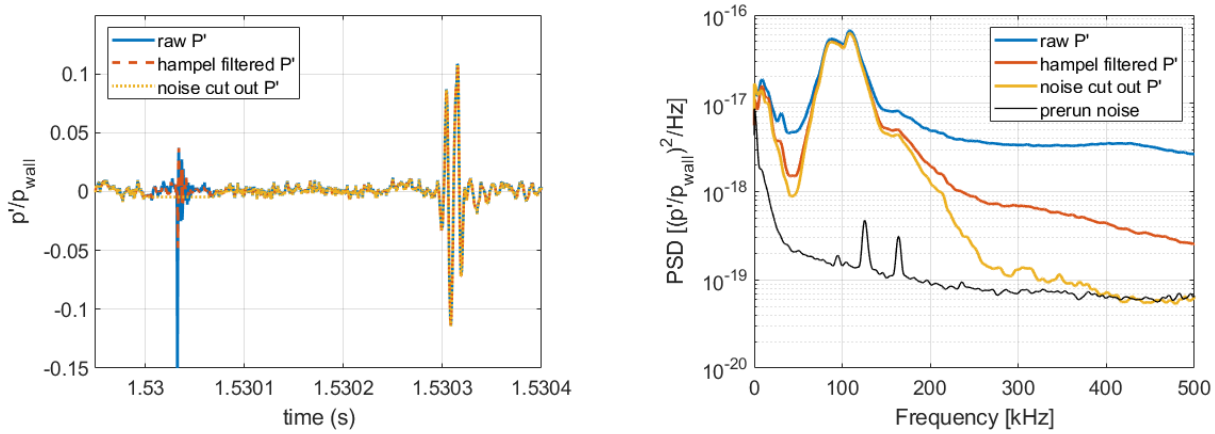

(a) Pressure time series highlighting different filtering methods.

(b) Pressure PSDs for each filtering method.

Figure 6.5. Noise filtering methods used with the perturber.

6.4 Instability Measurements with the Plasma Perturber

The effects of controlled disturbances were studied in the reattached boundary layer using PCB sensors. Additionally, FLDI measurements were made in the shear layer just upstream of reattachment.

6.4.1 Amplitude Effects

Perturber voltages of 7.5, 10.0, and 12.5 kV were tested with a unit Reynolds number of 11.6×10^6/m to see the effect of voltage on disturbance amplification. The resulting power spectral densities for the five PCB sensors under the reattached boundary layer are shown in Figure 6.6. The PSDs for the three voltages are displayed, as well as for no perturbation, and the prerun electronic noise. In general, as the voltage increases, the resulting disturbance is larger. Additionally, the instability peaks of the higher voltages tend to broaden upstream of those from lower voltages, indicating that higher voltage corresponds to earlier transition along the model at the same unit Reynolds number.

By plotting the perturbed and unperturbed PSDs on the same axes, the frequencies amplified by the perturber and those amplified naturally can be compared. Two instabilities are generally seen naturally with this geometry. The apparent second mode is found between

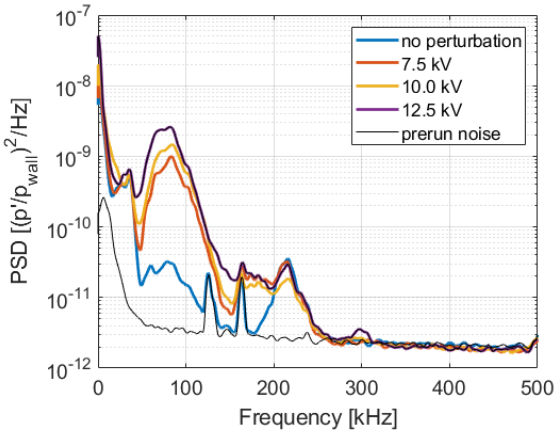

(a) 0.590 m downstream

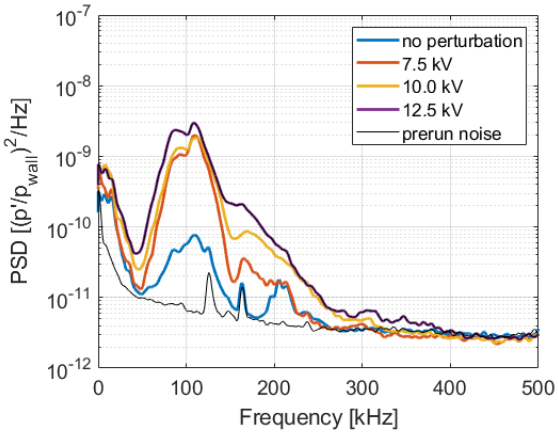

(b) 0.606 m downstream

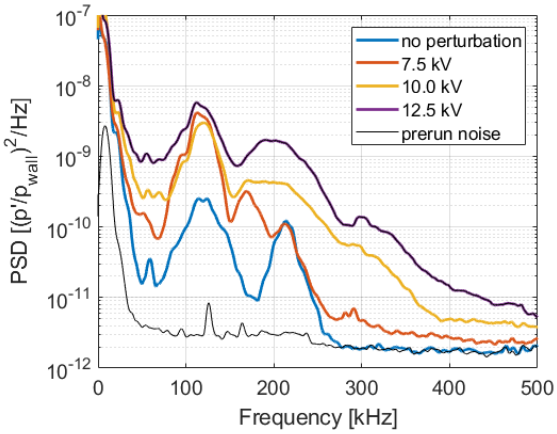

(c) 0.619 m downstream

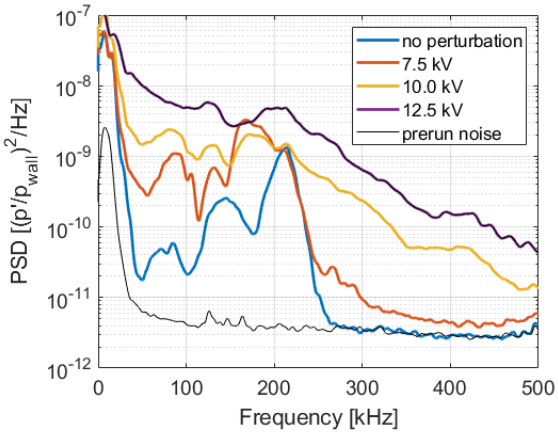

(d) 0.631 m downstream

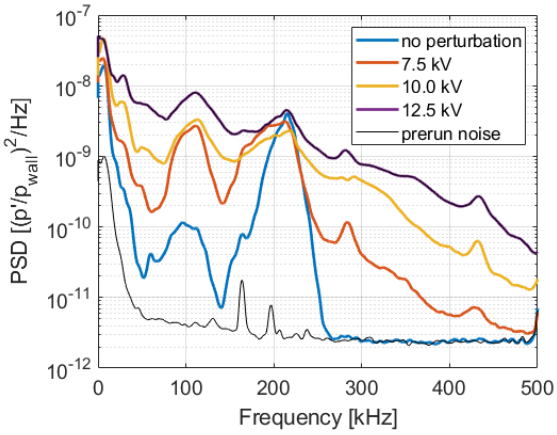

(e) 0.643 m downstream

Figure 6.6. Power spectral densities for PCBs along the flare under the reattached boundary layer with different pulser voltages. From Runs 1232, 1211, and 1228 for 7.5, 10.0, and 12.5 kV, respectively. $Re = 11.6 \times 10^6/\text{m}$.

170 and 290 kHz, while the shear-generated waves are between 50 and 170 kHz. Since the artifical disturbances excite a broad range of frequencies through several megahertz, the natural disturbances should be amplified by the shear layer and boundary layer that they traverse through. McKiernan demonstrated the natural amplification of the second mode with his tests on a 7° sharp cone [35]. The perturber electrodes were located on the end of the cone, downstream of where most of the second-mode waves are amplified, but upstream of the separation bubble. Therefore, it would be expected that the shear-generated waves are amplified due to the larger initial disturbances provided by the perturber. The PSDs in the reattached boundary layer support this hypothesis. In Figure 6.6a, the second-mode peak amplitudes (between 170-290 kHz) are relatively constant across the unperturbed and perturbed spectra. However, the shear-generated instability (between 50-170 kHz) is noticeably larger with the input disturbances.

Figure 6.7 highlights the peak frequencies and integrated amplitudes for the unperturbed and perturbed cases at $Re = 11.6 \times 10^6/\text{m}$. The peak frequencies, plotted as function of downstream distance in Figure 6.7a, increase moving downstream until 0.631 m for all runs. They remain within 10% of the unperturbed values for all voltages throughout the reattached boundary layer. The RMS values (integrated between 50 and 270 kHz) are plotted in Figure 6.7b. As the voltage increases, so does the RMS amplitude. For the highest voltage level, however, a peak amplitude is reached 0.631 m downstream, potentially indicating the boundary layer has fully transitioned.

Based on these results, a voltage of 12.5 kV was selected for the unit Reynolds sweep. This value should provide the largest amplitudes of the shear-generated waves.

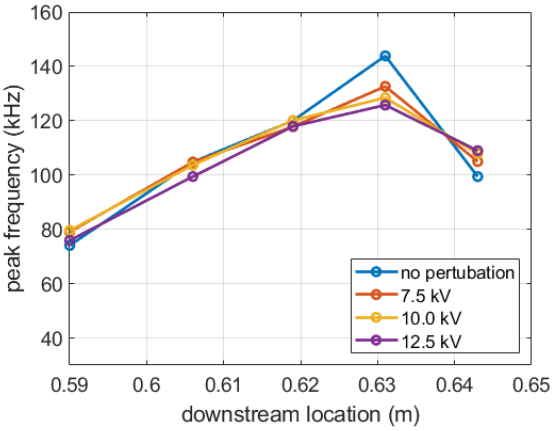

(a) Peak frequencies of the shear-generated waves as a function of downstream distance.

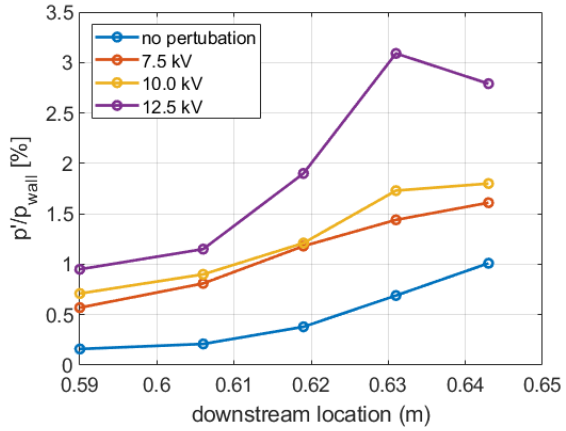

(b) Integrated RMS amplitudes (between 50-270 kHz) as a function of downstream distance.

Figure 6.7. Peak frequencies and integrated RMS amplitudes, highlighting effects of perturber voltage.

6.4.2 Reynolds Number Effects

Unit Reynolds numbers between 7.39×10^6/m and 11.58×10^6/m were tested with the pulser set to a voltage of 12.5 kV. This range was selected to span values from where the natural instabilities were below the electronic noise to where natural instabilities were largest.

Wave packets were observed for all unit Reynolds numbers that were tested. Figure 6.8 displays a sample wave packet propagating downstream at each unit Reynolds number. The wave packets had approximately the same velocity, found by cross-correlating the signals in the reattached boundary layer. This value, about 97% of the freestream velocity, is similar to the natural velocity of the shear-generated disturbances (see Section 5.2.2.2). As the wave convects downstream, it appears to increase in frequency for all unit Reynolds numbers. This trend agrees with the natural shear-generated waves, as well as the artificial ones seen by McKiernan with his finite-span separation [35].

For the lowest two unit Reynolds numbers, shown in Figures 6.8a and 6.8b, the wave packets remain approximately sinusoidal at each PCB station. At $Re = 10.33 \times 10^6$/m (Figure 6.8c), the waveform at the downstream-most PCB has become irregular and jagged, potentially indicating a turbulent spot. By $Re = 11.58 \times 10^6$/m (Figure 6.8d), the two

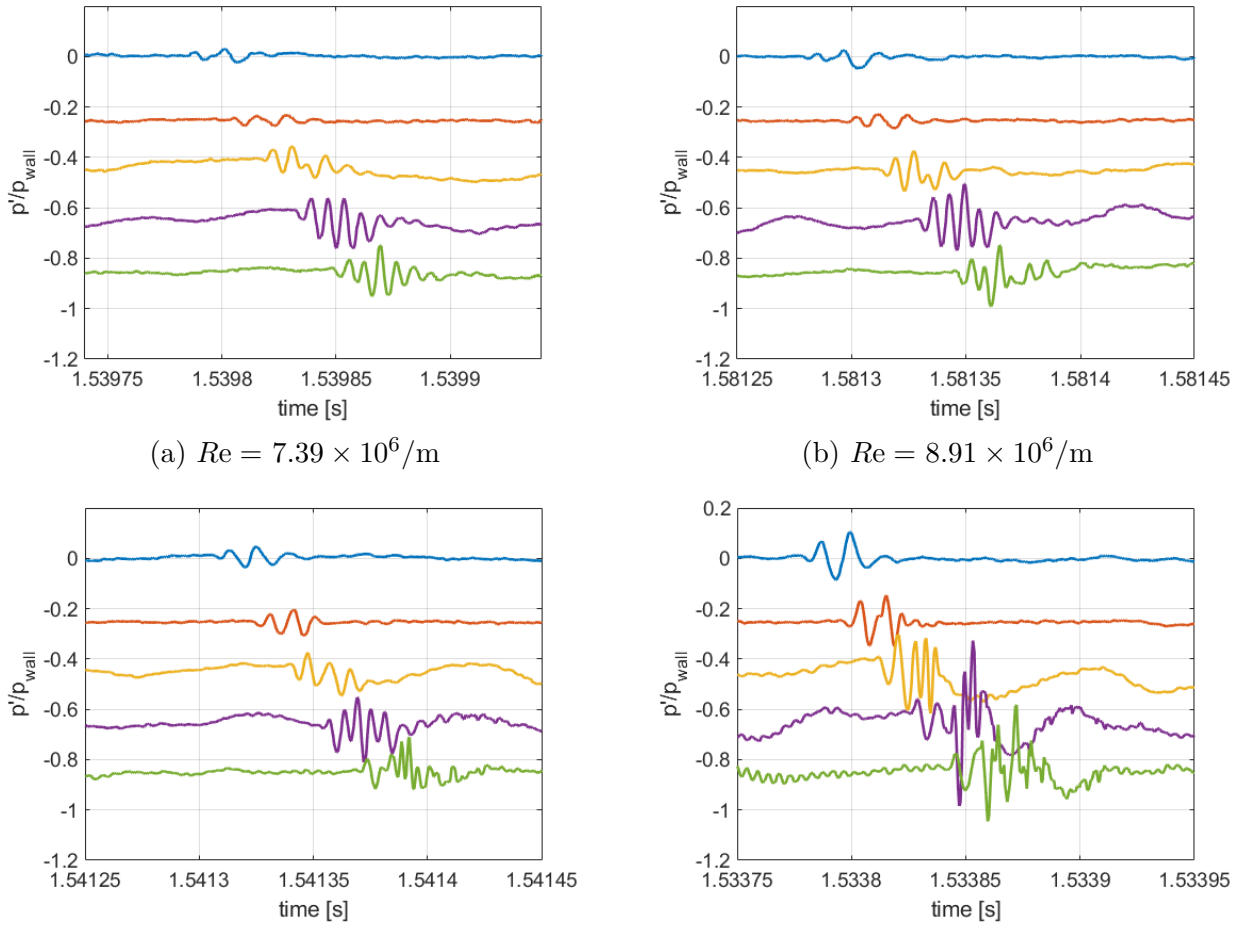

(a) $Re = 7.39 \times 10^6/\text{m}$

(b) $Re = 8.91 \times 10^6/\text{m}$

(c) $Re = 10.3 \times 10^6/$

(d) $Re = 11.6 \times 10^6/\text{m}$

Figure 6.8. Sample wave packets from PCBs in the reattached boundary layer at different unit Reynolds numbers with controlled disturbances. From Runs 1228-1231.

farthest-downstream sensors now have this irregular appearance, and have a much larger amplitude. Additionally, naturally-generated waves also appear before the artificially-generated waves for the latter three sensors. In general, as the unit Reynolds number increased, the amplitude of the generated waves also increased.

Figure 6.9 plots the power spectral densities for the same data that include the wave packets in Figure 6.8. The spectra reinforce what was seen in the time series. Higher unit Reynolds numbers correspond to higher peak amplitudes. Larger unit Reynolds numbers also correspond to spectra that broaden farther upstream. For example, the spectra for

$Re = 11.58 \times 10^6$/m is already broadening by 0.619 m downstream of the nosetip, while $Re = 10.33 \times 10^6$/m does not begin broadening until 0.631 m downstream.

The integrated RMS values for the instabilities are presented in Figure 6.10a. Similar results from McKiernan's perturber experiments are shown in Figure 6.10b for comparison. For the axisymmetric cone-cylinder-flare, the unperturbed amplitudes did not begin increasing above the noise until around $Re_x = 6.1 \times 10^6$. However, the perturbed amplitudes begin increasing above the noise for sensor Reynolds numbers as low as 4.2×10^6. The integrated amplitudes for the perturbed results were always greater than those for the unperturbed results at a given Reynolds number. For the finite-span cone-slice-flap, on the other hand, the unperturbed amplitudes begin increasing around $Re_x = 8.2 \times 10^5$. The perturbed results had a much higher noise floor, and did not begin increasing until around 11.0×10^5, where they agreed well with the unperturbed values. McKiernan concluded that the mechanism for transition under quiet flow with his cone-slice-flap is independent of the shear-generated waves he observed with the perturber, due to the similarity between the perturbed and unperturbed amplitudes once the noise floor was crossed. The cone-cylinder-flare, however, behaves differently when artificial disturbances are generated. The instability amplification is visible at lower length Reynolds numbers when the larger initial disturbances from the perturber are present than when they are not.

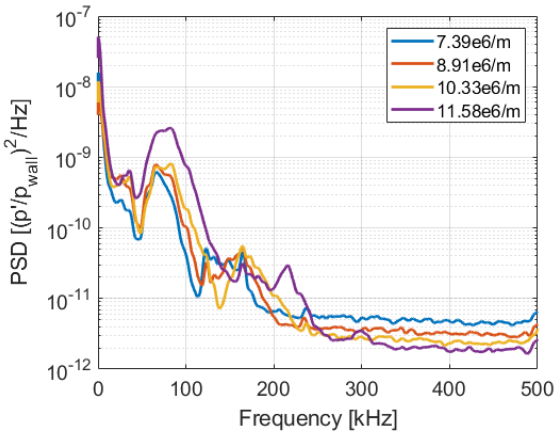

(a) 0.590 m downstream

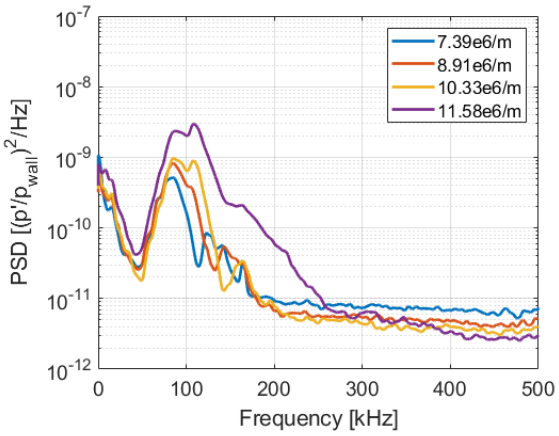

(b) 0.606 m downstream

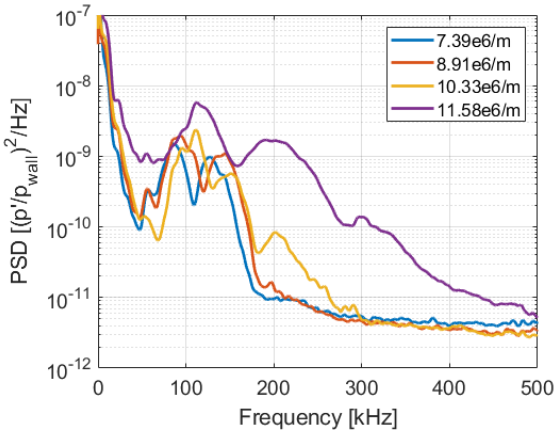

(c) 0.619 m downstream

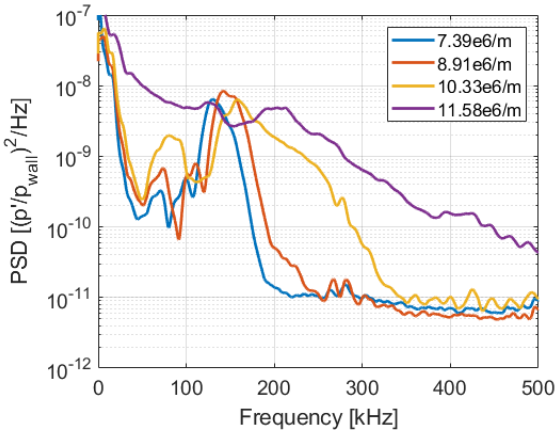

(d) 0.631 m downstream

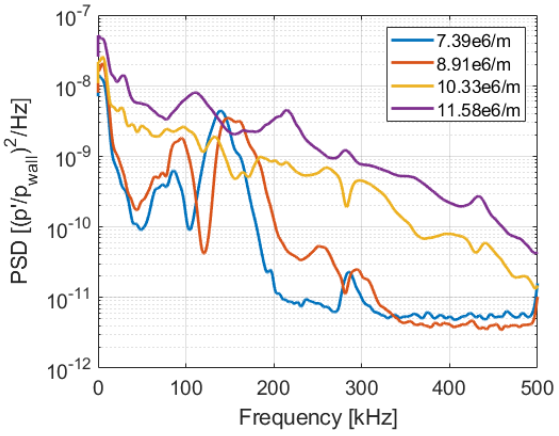

(e) 0.643 m downstream

Figure 6.9. Power spectral densities for PCBs in the reattached boundary layer at different unit Reynolds numbers with controlled disturbances. From Runs 1228-1231.

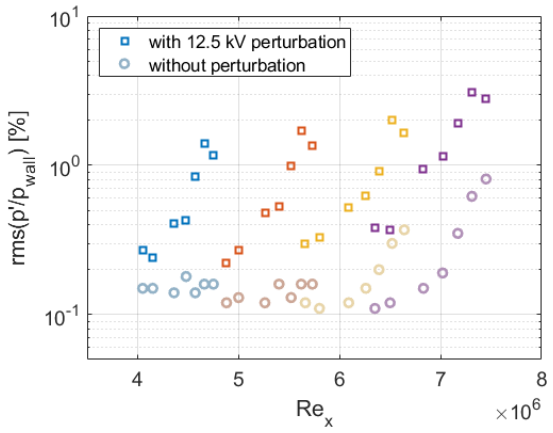

(a) Cone-cylinder-flare, integrated between 50-270 kHz.

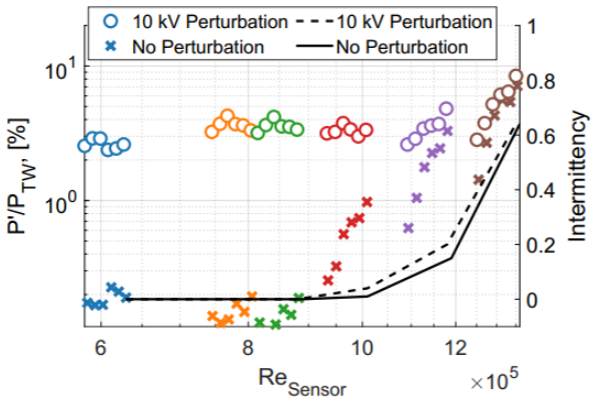

(b) Cone-slice-flap, integrated between 15-200 kHz. Reproduced with permission from Ref. [35].

Figure 6.10. Integrated RMS amplitudes (between 50-270 kHz) as a function of Reynolds number at the sensor.

6.4.2.1 FLDI Measurements

FLDI measurements were taken approximately 3 mm off the surface of the model and 0.578 m downstream of the nosetip, in the shear layer above the separation bubble. The 3 mm offset was selected because it is the location of the peak density fluctuations for that axial position when $Re = 11.5 \times 10^6$/m (see Figure 5.33b). These FLDI measurements were made simultaneously with the PCB measurements. The FLDI measurements were noisier than the PCBs, but were still able to detect the wave packets generated by the perturber. Figure 6.11a plots sample time-series data from the FLDI capturing a generated wave packet at each of the four unit Reynolds numbers studied. When the time-series were averaged over the full ensemble of pulses, the wave packets become more apparent (Figure 6.11b).

Power spectral densities were computed for the FLDI results immediately before the perturbations began, as well as during the perturbations. The results are shown in Figure 6.12. Without perturbations (Figure 6.12a), only the second mode is evident in the PSDs, and only for the two highest unit Reynolds numbers. The naturally-occuring shear-generated waves as seen in Figure 5.33b are most likely obscured by the slightly higher noise floor during this test. The lower unit Reynolds cases do not show any clear frequency peaks. With the

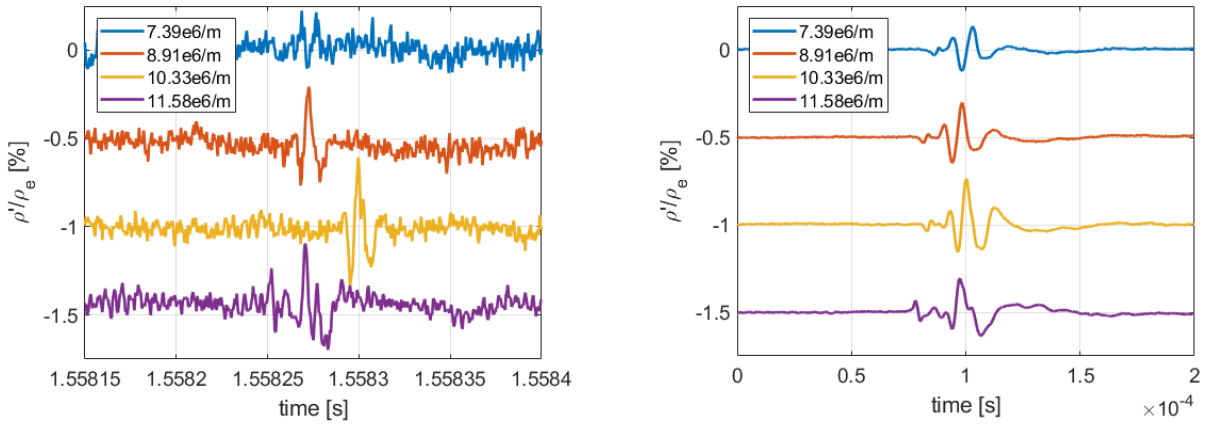

(a) FLDI time series data.

(b) Ensemble averaged FLDI time series.

Figure 6.11. FLDI time series data, showing both sample pulses as well as the ensemble averages.

perturbations (Figure 6.12b), however, all four cases show clear instabilities in the PSDs. For $Re = 7.39 \times 10^6$, 8.91×10^6, and 10.33×10^6/m, a peak around 100 kHz appears, which is consistent with the shear-generated instability. At $Re = 11.58 \times 10^6$/m, a series of peaks between 50-180 kHz are seen (around 50 kHz, 100 kHz, and 150 kHz). The reason for these multiple peaks at the highest unit Reynolds number is uncertain, although the bicoherence does show significant nonlinear interactions at frequencies below 200 kHz (Figure 6.13). The second-mode frequency peaks at the two highest unit Reynolds numbers are unchanged from their unperturbed values.

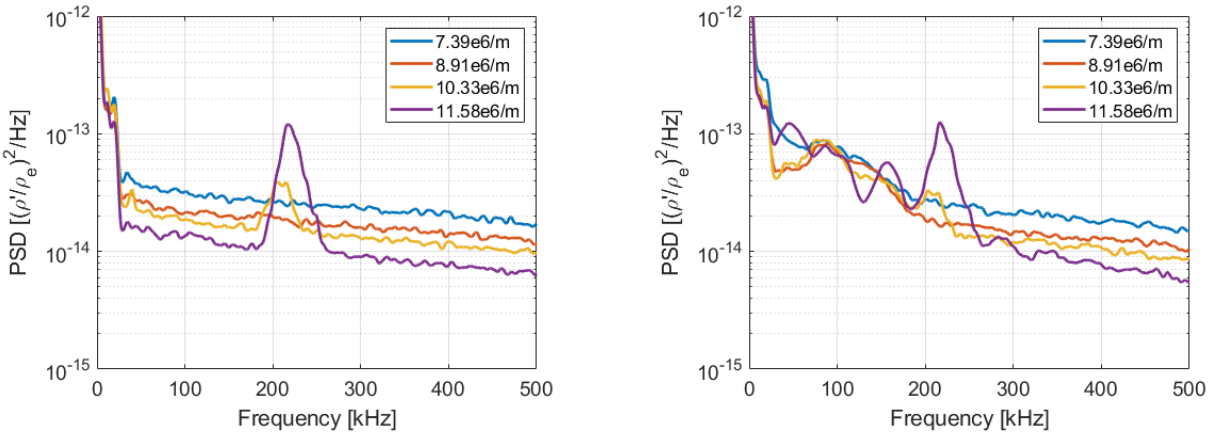

(a) FLDI PSD without perturbation.

(b) FLDI PSD with 12.5 kV perturbation.

Figure 6.12. FLDI PSDs with and without perturbation.

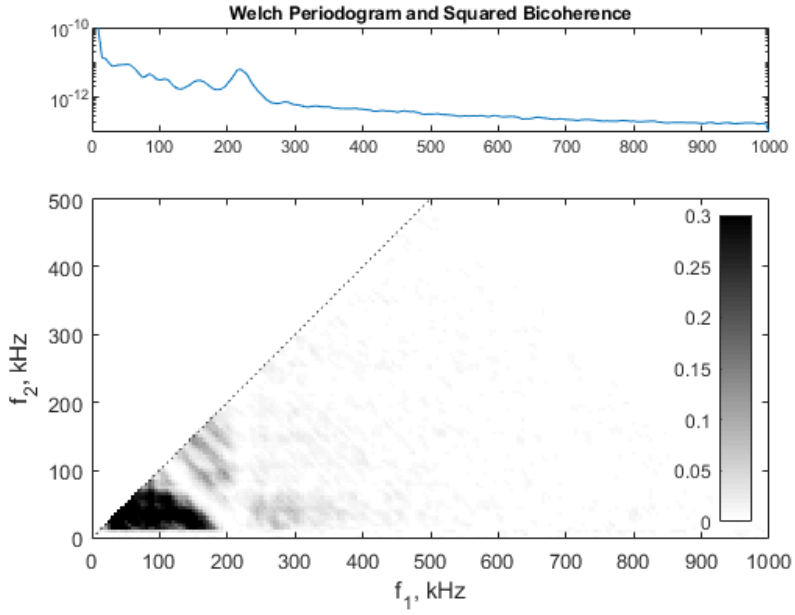

Figure 6.13. FLDI bicoherence from Run 1228, 0.578 m downstream and 3 mm off the surface. Significant nonlinear interactions are seen for frequencies below 200 kHz. $Re = 11.58 \times 10^6/\text{m}$.

6.5 Summary of Controlled Perturbation Measurements

A plasma perturber was used to insert controlled disturbances into the boundary layer upstream of the separation bubble. Due to its location, the shear-generated instability ampli-

fied the larger initial disturbances provided by the perturber, which was downstream of the main region of second-mode amplification. The generated waves were studied and compared to the naturally amplified waves. Higher perturber voltages corresponded to greater amplitudes at the same unit Reynolds number. Higher unit Reynolds numbers also corresponded to greater amplitudes with the same perturber voltage. Amplification moving downstream was seen in the perturber results for all unit Reynolds numbers, even when the unperturbed values were below the noise floor. FLDI measurements picked up the shear-generated instability in the shear layer when the perturber was active, but only the second-mode when it was not. The second-mode instability amplitudes were not changed when using controlled disturbances.

The perturber experiments provide additional evidence that the second mode is neutrally stable in the shear layer. The shear-generated instability, however, amplifies as it convects through the shear layer. With a larger initial disturbance relative to the naturally-generated waves, wave packets from the perturber began to transition to turbulent spots in the reattached boundary layer. This provides an initial illustration of transition influenced by the shear-generated instability under quiet flow.

7. SUMMARY AND RECOMMENDATIONS

7.1 Summary and Conclusions

Shock/boundary-layer interactions (SBLIs) are common occurrences along hypersonic vehicles that can cause the flow to separate from the surface. Previous studies in low-speed regimes have noted traveling waves generated in the shear layer above a separation as a possible mechanism of transition [25]. Some evidence of similar traveling waves was seen in hypersonic tests with generated disturbances by McKiernan [35]. This dissertation presents the first evidence of such waves occurring naturally in quiet hypersonic flow. The purpose of this work is to study traveling waves associated with a hypersonic separation bubble. An axisymmetric cone-cylinder-flare geometry was studied with measurements taken both on- and off-the-surface of the model in the Boeing/AFOSR Mach 6 Quiet Tunnel (BAM6QT).

To obtain off-the-surface measurements in the flow, a focused laser differential interferometer (FLDI) first needed to be developed to work with the unique challenges posed by the BAM6QT. A traditional FLDI was first assembled and tested using a small-diameter jet to determine its spatial sensitivity. A new configuration was then developed with the assistance of a ray-tracing simulation to work with the contoured Plexiglas™ tunnel windows. This BAM6QT configuration underwent the same tests as the traditional FLDI with the windows in the system. The BAM6QT version had a wider sensitivity region, most likely due to the irregular beam profiles produced by the laser traversing the Plexiglas™. However, it was still sufficiently small to significantly reduce any signals from the nozzle-wall boundary layer. This FLDI was tested in the tunnel with a 7° sharp cone to validate its performance with a well-understood geometry. The BAM6QT FLDI was used to measure phase shifts due to density fluctuations within the boundary layer. The experimental measurements agreed well with the computed FLDI phase shifts.

Initial testing was conducted in quiet flow on a cone-cylinder-flare with a 3.5° flare, designed to have an axisymmetric compression corner that does not cause the boundary layer to separate. The second mode was observed amplifying along the cone, dampening out over the cylinder, and then amplifying again along the flare. Amplification rates along the downstream portion of the flare agreed well with computational estimates, as did second-

mode peak frequencies. The boundary layer appeared to be laminar for all unit Reynolds numbers available in quiet flow.

More extensive tests were conducted on a cone-cylinder-flare with a 10° flare under quiet flow. This geometry produced an axisymmetric separation bubble that was observed in schlieren images. Under quiet flow, the boundary layer again remained laminar for all unit Reynolds numbers available. Heat transfer measurements along the flare showed an increasing value under the separation bubble that plateaued after reattachment. Surface pressure fluctuations under the reattached boundary layer had the second mode present, as well as another instability. This instability is referred to as the "shear-generated" instability, as it appears to be either generated or amplified by the shear layer above the separation bubble. The shear-generated waves convect downstream at a faster velocity than the second mode, and are not present with the 3.5° flare model. FLDI measurements taken in and above the separation bubble show that the second mode is present but not amplifying in the shear layer, and the shear-generated instability first appears just upstream of reattachment. Downstream of reattachment, FLDI measurements indicate both the shear-generated instability and the second mode at higher amplitudes than upstream of reattachment, with peak amplitudes located off-the-surface of the model. Paredes et al. offer a probable explanation of the shear-generated instability through oblique waves [74]. Small angles of attack were observed to have a significant effect on the symmetry of the separation bubble, with the bubble shrinking on the windward side of the model with increasing angles of attack under laminar, quiet flow.

In conventional noise (as opposed to quiet flow), laminar, transitional, and turbulent boundary layers were observed for the 10° cone-cylinder-flare. Laminar flow heat transfer agreed well with heat transfer measurements made under quiet flow. When transition occurred along the flare, it appeared to occur at reattachment, creating a localized heat transfer peak. Surface pressure spectra indicated two frequency peaks at much lower frequencies than observed under quiet flow, although it is unclear whether they are caused by the same instabilities. Bubble symmetry with small angles of attack under transitional, noisy flow followed the opposite trend of that under laminar, quiet flow, with the bubble growing on the windward side of the model with increasing angles of attack.

In both quiet and noisy flow, streamwise streaks indicative of Görtler-like vortices were present under the reattached boundary layer. Under conventional noise, these streaks were present even at small, non-zero angles of attack. In quiet flow, however, they only appeared when the angle of attack was near 0.0°.

A plasma electrode induced perturbations on the 10° flare model. The electrodes were placed at the end of the cone, downstream of the region of second-mode amplification but upstream of the separation bubble. The location was selected because it is downstream of the main region where the second mode is amplified, but upstream of the separation bubble. The disturbances naturally amplified downstream of the electrodes should have greater amplitudes with the perturbation than without it. Therefore, the perturber can be used to determine if the second mode is amplified as it traverses downstream through the shear layer and whether or not the shear-generated instability is in fact amplified or generated in the shear layer. Surface pressure measurements under the reattached boundary layer and FLDI measurements of the shear layer just upstream of reattachment indicated that the shear-generated instability, but not the second mode, was larger due to the larger initial disturbances from the perturber. Higher voltages and larger unit Reynolds numbers created larger-amplitude instabilities. Wavepackets in the reattached boundary layer initially appeared sinusoidal, but became irregular as they convected downstream at the highest voltage and unit Reynolds number tested.

This research was able to examine a traveling instability generated or amplified by the shear layer over an axisymmetric separation bubble in quiet flow. This "shear-generated" instability was not seen in surface-pressure-fluctuation measurements on a cone-cylinder-flare without separation, but was present in PCB, Kulite, and FLDI measurements of the model with separation across a variety of conditions. Controlled disturbances generated downstream of the second-mode amplification region but upstream of the separation bubble resulted in amplified shear-generated peaks, but did not impact the second-mode amplitudes. Unfortunately, the quiet flow stagnation pressures available during this work were not sufficiently high to cause natural transition, although results with the plasma perturber may indicate the generation of turbulent spots from the amplification of the controlled disturbances.

Overall, with the 10° flare configuration there are at least three instabilities: the second mode, the shear-generated instability, and the Görtler-like instability. Which of these is the dominant instability will depend on the conditions of the flow. With the sharp-nose, axisymmetric geometry near 0.0° angle of attack studied in this case, the Görtler-like instability is lower. For a hypersonic vehicle in flight, with varying conditions such as angle of attack, Mach number, and wall temperature, the dominant instability remains to be determined.

In conclusion, this work provides measurements that can be used in the development and validation of computational tools that include hypersonic axisymmetric separation bubbles. Essentially, the goal is to provide useful information to vehicle designers who will need to understand how such separation bubbles will impact the vehicle's controllability and survivability. However, this dissertation is only a starting point. More work is necessary to understand how the shear-generated instability impacts transition.

7.2 Open Questions and Future Work

Many open questions remain:

7.2.1 FLDI Instrumentation

1. *Develop and test multi-beam FLDI.*

   Current FLDI advancements have involved splitting the laser beams multiple times to get several simultaneous measurements in the test flow [64], [86]–[89]. Closely-spaced beams allow disturbance phase speeds to be measured as well as density fluctuations across multiple locations. A Double-FLDI (D-FLDI) was designed towards the end of experimentation for this research, and was tested with the shock tube. This work can be extended to get additional measurements simultaneously. A more powerful laser is necessary for a useful signal-to-noise ratio for use with the BAM6QT, based on initial testing during this work with D-FLDI.

2. *Quantify FLDI frequency response.*

   It was assumed in this work that the FLDI frequency response time is limited only by the photodetector and that the frequency response is generally flat. This assumption was not experimentally validated, and the frequency response of the FLDI as a system was not measured.

7.2.2 Instabilities of Hypersonic Separated Flows

1. *What is the dominant mechanism for transition in flows with axisymmetric separation?*

   Under quiet flow, the boundary layer remained laminar for the entirety of the model. Instability amplification was observed, but breakdown to turbulence was not seen in quiet flow without use of the plasma perturber. Transition was forced with the perturber, but the same mechanism is not necessarily naturally dominant. Running a larger flare angle under quiet flow may allow for natural transition. Additionally, the dominant mechanism likely depends on the conditions of the flow.

2. *What is the role and behavior of the streamwise streaks seen in the reattached boundary layer?*

   Some evidence of streamwise streaks was seen in the heat transfer results of the 10° cone-cylinder-flare. The vortices causing these streaks should be looked at in more detail to determine their effect on transition. This instability is also likely to depend on flow conditions. This problem is currently being addressed by Lauren Wagner [22].

3. *What causes the difference in transition mechanism between flow with axisymmetric and finite-span separations?*

   McKiernan performed an extensive study of a finite-span separation bubble for his dissertation [35]. On his cone-slice-flap geometry, transition occurred naturally in quiet flow, and was described by a broadband rise in the surface-pressure power spectra. Plasma perturbations introduced to the flow resulted in traveling waves similar to the shear-generated waves seen in this work. However, the transition Reynolds number remained the same with and without the artificial disturbances, indicating that some

other mechanism is responsible for the boundary-layer transition on that geometry at the flow conditions tested. This differs from the cone-cylinder-flare, which did not transition naturally in quiet flow even at higher unit Reynolds numbers.

4. *What is the role of oblique waves in the shear-generated instability?*

   Preliminary analysis by Dr. Pedro Paredes et al. at Langley indicates that oblique waves explain the shear-generated waves [74]. More off-axis measurements are needed to look into the role of such waves experimentally.

5. *How do the radii of curvature at the model corners (cone-cylinder and cylinder-flare intersections) affect measured instabilities?*

   The STABL computations assumed perfectly sharp corners at the cone-cylinder and cylinder-flare intersections of the model, while the physical model actually has non-zero radii of curvature at these points. Zygo measurements of the expansion corner resulted in an average radius of curvature of 3.11 mm. The compression corner had a measured radius of 0.451 mm for the 10° flare. It is unknown what, if any, effect these non-zero radii of curvature have on the hypersonic instabilities measured.

6. *What is the role, if any, of the second-mode waves on the generation and growth of the shear-generated instability?*

   The cone-cylinder-flare geometry includes a significant region of second-mode amplification along the cone. While damped through the expansion to the cylinder, the second-mode continues to convect at a lower amplitude through the shear layer. It is possible that the presence of the second mode is necessary for the development of the shear-generated instability. Future measurements should be made on a geometry that either does not contain or successfully removes the second mode prior to the separation bubble.

REFERENCES

[1] F. White, *Viscous Fluid Flow*, 3rd edition. McGraw-Hill Higher Education, New York, NY, 2011.

[2] A. Martellucci, R. Neff, and W. True, "An Experimental Investigation of Boundary Layer Transition on a Cone at Angle of Attack," Space and Missile Systems Organization, Tech. Rep. 69-383, Sep. 1969, DTIC citation AD-A-864-331.

[3] S. Schneider and R. Bowersox, "Hypersonic Transition and Turbulence," in *Encyclopedia of Aerospace Engineering*, R. Blockley and W. Shyy, Eds., John Wiley & Sons, Ltd., 2010, ISBN: 978-0-470-68665-2.

[4] S. Schneider, "Hypersonic Laminar-Turbulent Transition on Circular Cones and Scramjet Forebodies," *Progress in Aerospace Sciences*, vol. 40, no. 1-2, pp. 1–50, Feb. 2004. DOI: 10.1016/j.paerosci.2003.11.001.

[5] S. Schneider, "Effects of High-Speed Tunnel Noise on Laminar-Turbulent Transition," *Journal of Spacecraft and Rockets*, vol. 38, no. 3, pp. 323–333, May 2001. DOI: 10.2514/2.3705.

[6] K. Casper, H. Johnson, and S. Schneider, "Effect of Freestream Noise on Roughness-Induced Transition for a Slender Cone," *Journal of Spacecraft and Rockets*, vol. 48, no. 3, pp. 406–413, May 2011. DOI: 10.2514/1.48300.

[7] R. Wagner, D. Maddalon, and L. Weinstein, "Influence of Measured Freestream Disturbances on Hypersonic Boundary-Layer Transition," *AIAA Journal*, vol. 8, no. 9, pp. 1664–1670, Sep. 1970. DOI: 10.2514/3.5962.

[8] H. Babinsky and J. Harvey, *Shock Wave-Boundary-Layer Interactions*. Cambridge University Press, 2014.

[9] G. Settles, "An Experimental Study of Compressible Turbulent Boundary Layer Separation at High Reynolds Numbers," Ph.D. dissertation, Princeton University, Princeton, New Jersey, 1976.

[10] K. Stewartson and P. Williams, "Self-Induced Separation," vol. 312, no. 1509, pp. 181–206, Sep. 1969, in *Proceedings of the Royal Society of London. Series A, Mathematical and Physical Sciences*. DOI: 10.1098/rspa.1969.0148.

[11] D. Chapman, D. Kuehn, and H. Larson, "Investigation of Separated Flows in Supersonic and Subsonic Streams with Emphasis on the Effect of Transition," NACA, Tech. Rep. 1356, Jan. 1958, NTRS number 19930092343.

[12] J. Becker and P. Korycinski, "Heat Transfer and Pressure Distribution at a Mach Number of 6.8 on Bodies with Conical Flares and Extensive Flow Separation," NACA, Tech. Rep. RM L56F22, Apr. 1956, DTIC citation AD0274584.

[13] H. Larson and S. Keating, "Transition Reynolds Numbers of Separated Flows at Supersonic Speeds," NASA, Tech. Rep. D-349, Dec. 1960, NTRS number 19980227089.

[14] J. Schaefer and H. Ferguson, "Investigation of Separation and Associated Heat Transfer and Pressure Distribution on Cone-Cylinder-Flare Configurations at Mach Five," *ARS Journal*, vol. 32, no. 5, pp. 762–770, May 1962, ISSN: 1936-9972. DOI: 10.2514/8.6146.

[15] D. Needham and J. Stollery, "Boundary Layer Separation in Hypersonic Flow," *AIAA*, Oct. 1966, Paper 66-455. DOI: 10.2514/6.1966-455.

[16] A. Demetriades, "Transition in High-Speed Free Shear Layers," in *Instability and Transition Volume 1. ICASE/NASA LaRC Series*, M. Hussaini and R. Voigt, Eds., Springer, 1990, pp. 52–67.

[17] J. Ginoux, "Investigation of Flow Separation over Ramps at M_∞=3," Von Karman Gas Dynamics Facility, Arnold Engineering Development Center, Tech. Rep. AEDC-TR-65-273, Dec. 1965.

[18] K. Heffner, A. Chpoun, and J. Lengrand, "Experimental Study of Transitional Axisymmetric Shock-Boundary Layer Interactions at Mach 5," *AIAA*, Jul. 1993, Paper 93-3131. DOI: 10.2514/6.1993-3131.

[19] A. Dwivedi, S. Gs, G. Candler, J. Nichols, and M. Jovanovic, "Input-Output Analysis of Shock Boundary Layer Interaction," *AIAA*, Jun. 2018, Paper 2018-3220. DOI: 10.2514/6.2018-3220.

[20] M. Leinemann, R. Radespiel, F. Muñoz, S. Esquieu, G. McKiernan, and S. Schneider, "Boundary Layer Transition on a Generic Model of Control Flaps in Hypersonic Flow," *AIAA*, Jan. 2019, Paper 2019-1908. DOI: 10.2514/6.2019-1908.

[21] M. Lugrin, S. Beneddine, C. Leclercq, E. Garnier, and R. Bur, "Transition Scenario in Hypersonic Axisymmetrical Compression Ramp Flow," *Journal of Fluid Mechanics*, vol. 907, A6, 2021. DOI: 10.1017/jfm.2020.833.

[22] L. Wagner, "Streamwise Vortices in Separated Flow at Mach 6," M.S. thesis, Purdue University, West Lafayette, Indiana, To be completed Dec. 2021.

[23] G. Inger, "Three-Dimensional Disturbances in High Speed Boundary Layer Flows," AFOSR, Tech. Rep. 82-0110, Aug. 1981, DTIC citation ADA120251.

[24] D. Dolling, "Wall Pressure Fluctuations in a Supersonic Separated Compression Ramp Flowfield," *AIAA*, Jun. 1982, Paper 82-0986. DOI: 10.2514/6.1982-986. [Online]. Available: http://arc.aiaa.org/doi/10.2514/6.1982-986.

[25] A. Dovgal, V. Kozlov, and A. Michalke, "Laminar Boundary Layer Separation: Instability and Associated Phenomena," *Progress in Aerospace Sciences*, vol. 30, no. 1, pp. 61–94, Jan. 1994, ISSN: 03760421. DOI: 10.1016/0376-0421(94)90003-5.

[26] L. Vandomme, B. Chanetz, R. Benay, and J. Parraud, "Shock Wave Transitional Boundary Layer Interaction in Hypersonic Flow," *AIAA*, Dec. 2003, Paper 2003-6966. DOI: 10.2514/6.2003-6966.

[27] R. Benay, B. Chanetz, B. Mangin, L. Vandomme, and J. Perraud, "Shock Wave/Transitional Boundary-Layer Interactions in Hypersonic Flow," *AIAA Journal*, vol. 44, no. 6, pp. 1243–1254, Jun. 2006. DOI: 10.2514/1.10512.

[28] P. Balakumar, H. Zhao, and H. Atkins, "Stability of Hypersonic Boundary Layers over a Compression Corner," *AIAA Journal*, vol. 43, no. 4, pp. 760–767, Apr. 2005. DOI: 10.2514/1.3479.

[29] D. Estruch-Samper, B. Ganapathisubramani, L. Vanstone, and R. Hiller, "Axisymmetric Flare-Induced Separation of High-Speed Transitional Boundary Layers," *AIAA*, Jan. 2012, Paper 2012-0067. DOI: 10.2514/6.2012-67.

[30] L. Vanstone, D. Estruch-Samper, R. Hillier, and B. Ganapathisubramani, "Shock Induced Separation in Transitional Hypersonic Boundary Layers," *AIAA*, Jun. 2013, Paper 2013-2736. DOI: 10.2514/6.2013-2736.

[31] L. Vanstone, D. Estruch-Samper, R. Hillier, and B. Ganapathisubramani, "Establishment Times of Hypersonic Shock-Wave/Boundary-Layer Interactions in Intermittent Facilities," *AIAA Journal*, vol. 55, no. 9, pp. 2875–2887, Sep. 2017. DOI: 10.2514/1.J055575.

[32] L. Vanstone and N. Clemens, "Unsteadiness Mechanisms of a Swept Compression-Ramp Shock/Boundary Layer Interaction at Mach 2," *AIAA*, Jan. 2019, Paper 2019-0095. DOI: 10.2514/6.2019-0095.

[33] J. Edelman, B. Chynoweth, G. McKiernan, C. Sweeney, and S. Schneider, "Instability Measurements in the Boeing/AFOSR Mach-6 Quiet Tunnel," *AIAA*, Jun. 2016, Paper 2016-3343. DOI: 10.2514/6.2016-3343.

[34] B. Chynoweth, J. Edelman, K. Gray, G. McKiernan, and S. Schneider, "Measurements in the Boeing/AFOSR Mach-6 Quiet Tunnel on Hypersonic Boundary-Layer Transition," *AIAA*, Jun. 2017, Paper 2017-3632. DOI: 10.2514/6.2017-3632.

[35] G. McKiernan, "Instability of the Shear Layer on a Sliced Cone with Finite Span Compression Ramps at Mach 6," Ph.D. dissertation, Purdue University, West Lafayette, Indiana, May 2020.

[36] G. McKiernan and S. Schneider, "Instability and Transition on a Cone with a Slice and Ramp at Mach 6," *AIAA*, Jan. 2021, Paper 2021-0249. DOI: 10.2514/6.2021-0249.

[37] W. Oberkampf and D. Aeschliman, "Joint Computational/Experimental Aerodynamics Research on a Hypersonic Vehicle, Part I: Experimental Results," *AIAA Journal*, vol. 30, no. 8, pp. 2000–2009, Aug. 1992, ISSN: 0001-1452. DOI: 10.2514/3.11172.

[38] C. Butler and S. Laurence, "Interaction of Hypersonic Boundary-Layer Instability Waves with Axisymmetric Compression and Expansion Corners," *AIAA*, Jun. 2020, Paper 2020-3071. DOI: 10.2514/6.2020-3071.

[39] E. Malkiel and R. Mayle, "Transition in a Separation Bubble," *Journal of Turbomachinery*, Oct. 1996. DOI: 10.1115/1.2840931.

[40] J. Edelman, "Nonlinear Growth and Breakdown of the Hypersonic Crossflow Instability," Ph.D. dissertation, Purdue University, West Lafayette, Indiana, 2019.

[41] K. Gray, "Flowfield Characterization of the Boeing/AFOSR Mach-6 Quiet Tunnel," M.S. thesis, Purdue University, West Lafayette, Indiana, Dec. 2018.

[42] D. Turbeville, "Measurements of Transition in the Corner Formed by a Highly-Swept Fin and a Cone at Mach 6," Ph.D. dissertation, Purdue University, West Lafayette, Indiana, To be completed Dec. 2021.

[43] D. Berridge, "Generating Low-Pressure Shock Waves for Calibrating High-Frequency Pressure Sensors," Ph.D. dissertation, Purdue University, West Lafayette, Indiana, 2015.

[44] M. Wason, "Calibration of High-Frequency Pressure Sensors Using Low-Pressure Shock Waves," M.S. thesis, Purdue University, West Lafayette, Indiana, 2019.

[45] J. Edelman, "Secondary Instabilities of Hypersonic Stationary Crossflow Waves," M.S. thesis, Purdue University, West Lafayette, Indiana, 2016.

[46] N. Parziale, "Reflected Shock Tunnel Noise Measurement by Focused Differential Interferometry," *AIAA*, Jun. 2012, Paper 2012-3261. DOI: 10.2514/6.2012-3261.

[47] N. Parziale, "Slender-Body Hypervelocity Boundary-Layer Instability," Ph.D. dissertation, California Institute of Technology, Pasadena, California, 2013.

[48] N. Parziale, J. Shepherd, and H. Hornung, "Observations of Hypervelocity Boundary-Layer Instability," *Journal of Fluid Mechanics*, vol. 781, pp. 87–112, Oct. 2015. DOI: 10.1017/jfm.2015.489.

[49] M. Fulghum, "Turbulence Measurements in High-Speed Wind Tunnels Using Focusing Laser Differential Interferometry," Ph.D. dissertation, The Pennsylvania State University, State College, Pennsylvania, 2014.

[50] T. Salyer, "Laser Differential Interferometry for Supersonic Blunt Body Receptivity Experiments," Ph.D. dissertation, Purdue University, West Lafayette, Indiana, 2002.

[51] B. Schmidt and J. Shepherd, "Analysis of Focused Laser Differential Interferometry," *Applied Optics*, vol. 54, no. 28, pp. 8459–8472, Oct. 2015. DOI: 10.1364/ao.54.008459.

[52] F. Pedrotti, L. Pedrotti, and L. Pedrotti, *Introduction to Optics*. Pearson Prentice Hall, 2007.

[53] J. Lawson, M. Neet, I. Grossman, and J. Austin, "Characterization of a Focused Laser Differential Interferometer," *AIAA*, Jan. 2019, Paper 2019-2296. DOI: 10.2514/6.2019-2296.

[54] J. Gladstone and T. Dale, "Researches on the Refraction, Dispersion, and Sensitiveness of Liquids," *Proceedings of the Royal Society of London*, vol. 12, pp. 317–343, Jan. 1863. DOI: 10.1098/rspl.1862.0097.

[55] A. Franzen, *ComponentLibrary*, Creative Commons licensed. [Online]. Available: http://www.gwoptics.org/ComponentLibrary/.

[56] M. Zaccara, S. Cerasuolo, G. Cardone, J. Edelman, and S. Schneider, "Infrared Thermography Data Reduction Technique for Heat Transfer Measurements in the Boeing/AFOSR Mach-6 Quiet Tunnel," *AIAA*, Jan. 2019, Paper 2019-0894. DOI: 10.2514/6.2019-0894.

[57] H. Yates, M. Tufts, and T. Juliano, "Analysis of the Hypersonic Cross-Flow Instability with Experimental Wavenumber Distributions," *Journal of Fluid Mechanics*, vol. 883, A50, 2020. DOI: 10.1017/jfm.2019.864.

[58] B. Wheaton, "Roughness-Induced Instabilities in a Mach-6 Laminar Boundary Layer," Ph.D. dissertation, Purdue University, West Lafayette, Indiana, 2012.

[59] E. Benitez, *Handbook on the BAM6QT Data Acquisition System (DAQ)*, Internal BAM6QT Research Group Report, Jun. 2020.

[60] E. Benitez, J. Jewell, and S. Schneider, "Focused Laser Differential Interferometry for Hypersonic Flow Instability Measurements with Contoured Tunnel Windows," *AIAA*, Jan. 2020, Paper 2020-1282. DOI: 10.2414/6.2020-1282.

[61] E. Benitez, J. Jewell, and S. Schneider, "Focused Laser Differential Interferometry with Contoured Tunnel Windows," *AIAA Journal*, no. 2, pp. 419–429, Feb. 2020. DOI: 10.2514/1.J060081.

[62] G. Settles and M. Fulghum, "The Focusing Laser Differential Interferometer, an Instrument for Localized Turbulence Measurements in Refractive Flows," *Journal of Fluids Engineering*, vol. 138, Oct. 2016. DOI: 10.1115/1.4033960.

[63] A. Ceruzzi and C. Cadou, "Turbulent Air Jet Investigation Using Focused Laser Differential Interferometry," *AIAA*, Jul. 2017, Paper 2017-4834. DOI: 10.2514/6.2017-4834.

[64] J. Jewell, A. Hameed, N. Parziale, and S. Gogineni, "Disturbance Speed Measurements in a Circular Jet via Double Focused Laser Differential Interferometry," *AIAA*, Jan. 2019, Paper 2019-2293. DOI: 10.2514/6.2019-2293.

[65] H. Johnson and G. Candler, "Hypersonic Boundary Layer Stability Analysis using PSE-Chem," *AIAA*, Jun. 2005, Paper 2005-5023. DOI: 10.2514/6.2005-5023.

[66] M. Wright, G. Candler, and D. Bose, "Data-Parallel Line Relaxation Method for the Navier–Stokes Equations," *AIAA Journal*, vol. 36, no. 9, Sep. 1998. DOI: 10.2514/2.586.

[67] L. Mack, "Linear Stability Theory to the Problem of Supersonic Boundary-Layer Transition," *AIAA Journal*, vol. 13, no. 3, pp. 278–289, Mar. 1975. DOI: 10.2514/3.49693.

[68] B. Chynoweth, "Measurements of Transition Dominated by the Second-Mode Instability at Mach 6," Ph.D. dissertation, Purdue University, West Lafayette, Indiana, 2018.

[69] S. Esquieu, E. Benitez, S. Schneider, and J. Brazier, "Flow and Stability Analysis of a Hypersonic Boundary-Layer over an Axisymmetric Cone-Cylinder-Flare Configuration," *AIAA*, Jan. 2019, Paper 2019-2115. DOI: 10.2514/6.2019-2115.

[70] K. Gray, S. Schneider, and J. Jewell, "Flow-Induced Vibrations Measured on a Slender Cone in Mach-6 Quiet Flow," *AIAA*, Aug. 2021, Accepted for Aviation Forum 2021.

[71] A. Federov, "Receptivity of a High-Speed Boundary Layer," *Journal of Fluid Mechanics*, pp. 101–129, Sep. 2003. DOI: 10.1017/S0022112003005263.

[72] E. Benitez, J. Jewell, S. Schneider, and S. Esquieu, "Instability Measurements on an Axisymmetric Separation Bubble at Mach 6," *AIAA*, Jun. 2020, Paper 2020-3072. DOI: 10.2414/6.2020-3072.

[73] E. Benitez, J. Jewell, and S. Schneider, "Separation Bubble Variation Due to Small Angles of Attack for an Axisymmetric Model at Mach 6," *AIAA*, Jan. 2021, Paper 2021-0245.

[74] P. Paredes, A. Scholten, M. Choudhari, F. Li, E. Benitez, and J. Jewell, "Boundary-Layer Instabilities Over a Cone-Cylinder-Flare Model at Mach 6," *AIAA*, Jan. 2022, Submitted for AIAA SciTech, 2022.

[75] C. Sweeney, "Characterization of a Hypersonic Quiet Wind Tunnel Nozzle," M.S. thesis, Purdue University, West Lafayette, Indiana, 2016.

[76] D. Mullen, personal communication to F. Drew Turbeville, Sep. 2019.

[77] K. Stetson, E. Thompson, J. Donaldson, and L. Siler, "Laminar Boundary Layer Stability Experiments on a Cone at Mach 8. III - Sharp Cone at Angle of Attack," *AIAA*, Jan. 1985, Paper 1985-492. DOI: 10.2514/6.1985-492.

[78] F. Ji, X. Liu, Q. Wang, X. Yuan, and Q. Shen, "Stability Analysis of Hypersonic Boundary Layer over a Cone at Small Angle of Attack," *Advances in Mechanical Engineering*, Feb. 2015. DOI: 10.1155/2014/217976.

[79] C. Running, T. Juliano, J. Jewell, M. Borg, and R. Kimmel, "Hypersonic Shock-Wave/Boundary-Layer Interactions on a Cone/Flare," *Experimental Thermal and Fluid Science*, vol. 109, Dec. 2019. DOI: 10.1016/j.expthermflusci.2019.109911.

[80] C. Running, T. Juliano, M. Borg, and R. Kimmel, "Characterization of Post-shock Thermal Striations on a Cone/Flare," *AIAA*, vol. 58, no. 5, pp. 2352–2358, May 2020. DOI: 10.2514/1.J059095.

[81] E. Benitez, J. Jewell, and S. Schneider, "Propagation of Controlled Disturbances through an Axisymmetric Separation Bubble at Mach 6," *AIAA*, Aug. 2021, Paper 2021-2844.

[82] K. Casper, "Pressure Fluctuations Beneath Instability Wave Packets and Turbulent Spots in a Hypersonic Boundary Layer," Ph.D. dissertation, Purdue University, West Lafayette, Indiana, 2012.

[83] D. Ladoon, "Wave Packets Generated by a Surface Glow Discharge on a Cone at Mach 4," Ph.D. dissertation, Purdue University, West Lafayette, Indiana, 1998.

[84] B. Singh, L. Rajendran, P. Vlachos, and S. Bane, "Two Regime Cooling in Flow Induced by a Spark Discharge," *Phys. Rev. Fluids*, vol. 5, p. 014 501, 1 Jan. 2020. DOI: 10.1103/PhysRevFluids.5.014501.

[85] B. Singh, L. Rajendran, J. Zhang, P. Vlachos, and S. Bane, "Vortex Rings Drive Entrainment and Cooling in Flow Induced by a Spark Discharge," *Phys. Rev. Fluids*, Jul. 2020, accepted, arXiv:2007.11065. [Online]. Available: https://arxiv.org/abs/2007.11065.

[86] A. Ceruzzi and C. Cadou, "Simultaneous Velocity and Density Gradient Measurements using Two-point Focused Laser Differential Interferometry," *AIAA*, Jan. 2019, Paper 2019-2295. DOI: 10.2514/6.2019-2295.

[87] J. Jewell, N. Parziale, K. Lam, B. Hagen, and R. Kimmel, "Disturbance and Phase Speed Measurements for Shock Tubes and Hypersonic Boundary-Layer Instability," *AIAA*, Jun. 2016, Paper 2016-3112. DOI: 10.2514/6.2016-3112.

[88] B. Bathel, J. Weisberger, G. Herring, R. Jagannathan, C. Johansen, S. Jones, and A. Cavone, "Analysis of the Amplitude Response of a Two-Point and a Multi-Point Focused Laser Differential Interferometer," *AIAA*, Jan. 2021, Paper 2021-0598. DOI: 10.2514/6.2021-0598.

[89] M. Gragston, T. Price, K. Davenport, J. Schmisseur, and Z. Zhang, "An m × n FLDI Array for Single-Shot, Multipoint Disturbance Measurements in High-Speed Flows," *AIAA*, Jan. 2021, Paper 2021-0599. DOI: 10.2514/6.2021-0599.

[90] B. Hildebrand, *Introduction to Numerical Analysis*, 2nd ed. Dover Publications, Inc. New York, NY, 1987, ISBN: 0-486-65363-3.

[91] M. Greenspan and K. Reddy, "A Laser Deflection Technique for Sensitive Measurements of a Reduced-Density Channel in Neutral Gas," *Applied Physics Letters*, vol. 40, no. 7, pp. 576–578, Jan. 1982. DOI: 10.1063/1.93185.

[92] C. Enloe, M. Brake, and T. Repetti, "Laser Deflection through a Spark," *American Journal of Physics*, vol. 58, no. 4, pp. 400–403, Apr. 1990. DOI: 10.1119/1.16484.

[93] J. Stricker and O. Kafri, "A New Method for Density Gradient Measurements in Compressible Flows," *AIAA Journal*, vol. 20, no. 6, pp. 820–823, Jun. 1982, Paper 82-4144. DOI: 10.2514/3.7946.

[94] I. Glatt and O. Kafri, "Moiré Deflectometry Ray Tracing Interferometry," *Optics and Lasers in Engineering*, vol. 8, no. 3-4, pp. 277–320, 1988. DOI: 10.1016/0143-8166(88)90041-3.

A. COMPLETE SETUP FOR THE BAM6QT FLDI

This Appendix contains a complete set of instructions for replicating the BAM6QT FLDI used in this work. Section A.1 is a list of every component including the manufacturer and part number of each item. Section A.2 displays comprehensive illustrations of how to assemble the components, as well as a list of what is used to mount each labeled optical device.

A.1 List of Components

Table A.1. Complete list of BAM6QT FLDI components

#	Component	Manufacturer	Description	Part Number	Quant.
1	Laser	Research Electro-Optics (REO), Inc.	1.5 mW linearly polarized, frequency-stabilized 633 nm laser system	32734	1
2	Photodetector	Ultrafast Sensors	amplified Si (1000 - 350 nm) dual photodetector, mod: 3.00 mm photodiodes	SDX318	1
3	Polarizer	Newport	multiorder waveplate, 1/4 wave 632.8 nm, 1/2in mlar coated	05RP14-24	2
4	Birefringent Prism	United Crystals, Inc.	quartz Wollaston prism(optical glue), 20x20mm, splitting angle	custom	2
5	Birefringent Prism	ThorLabs	wollaston prism, 20° beam separation, 350-2300 nm, uncoated calcite	WP10	1

Table A.1. (continued)

6	Lens	ThorLabs	ϕ12.7 F=-15.0 N-SF11 bi-concave lens	LD2060	1
7	Lens	ThorLabs	f = 250.00 mm, H = 60.00 mm, L = 62.0 mm, N-BK7 Plano-Convex Cylindrical Lens, Antireflection Coating: 350-700 nm	LJ1267L1-A	1
8	Lens	ThorLabs	f = 300.00 mm, H = 60.00 mm, L = 62.0 mm, N-BK7 Plano-Convex Cylindrical Lens, Antireflection Coating: 350-700 nm	LJ1996L1-A	1
9	Lens	Newport	visible achromatic doublet lens, 25.4 mm, 125 mm EFL, 400-700 nm	PAC055	1
10	Lens	Newport	visible achromatic doublet lens, 25.4 mm, 120.2 mm EFL, 400-700 nm	similar to PAC055	1
11	Mirror	Newport	pyrex flat mirror, 50.8 mm diameter, 1/10 wave, R¿99% 0-45, 632.8 nm	20D20DM.4	
12	Laser Mount	Newport	cylindrical laser mount, 1.0-1.75 in., high-resolution AJS adjusters	ULM-TILT	1
13	Polarizer/Prism Mount	Newport	360° continuous rotation stage, 1 in aperture, fine adjust knob, 8-32 and M4	RSP-1T	3

Table A.1. (continued)

14	Prism Mount	ThorLabs	rotation mount for ϕ2" optics, 8-32 tap	RSP2	1
15	Prism Mount	Newport	360° continuous rotation stage, 2 in aperture, fine adjust knob, 8-32 and M4	RSP-2T	1
16	Lens Mount	ThorLabs	lens mounting ring for 0.5" dia optic	LMR05	1
17	Lens Mount	ThorLabs	fixed cylindrical lens mount, max optic height: 2.60" (66.0 mm)	CH2B	2
18	Lens Mount	Newport	XY lens positioner, 2.0 in. (50.8 mm) diameter	LP-2A-XY	1
19	Lens Mount	Newport	XY lens positioner, 1.0 in. (25.4 mm) diameter	LP-1A-XY	1
20	Mirror Mount	Newport	Ultima center mirror mount, 2.0 in., 2 locking knob adjustment	U200-AC2K	4
21	Optical Rail	Newport	precision optical rail, 24.28 in. length, 3.93 in. width, 36 in. scale	PRL-24	3
22	Support Rod	Newport	optical support rod, 24 in., 1.5 in. diameter	42	3
23	Rail Carrier	Newport	rail carrier, 3.0 in. length, 1/4-20 thread, PRL series	PRC-3	9
24	Rod Clamp	Newport	rod clamp, for 1.5 in. diameter models 40, 41, 42, 45, 1/4-20	340-RC	1

Table A.1. (continued)

25	Rod Clamp	Newport	rack-and-pinion rod clamp, 1.5 in. rod models 70, 71, 72, 75, 1/4-20	370-RC	4
26	Rod Platform	Newport	rod platform, three machined mounting surfaces	300-P	1
27	Platform	Newport	solid aluminum optical bread-board, 4 x 6 in., 1 in. 1/4-20 hole grid	SA2-04x06	1
28	Stage	Newport	low profile linear stage, vacuum compatible, 1.0 in. travel, 8-32 and 1/4-20	9067-COM-V	1
29	Stage	Newport	double-row ball bearing linear stage, 2.01 in. travel, 8-32 and 1/4-20	UMR8.51	2
30	Stage	Newport	high-performance linear stage, low-profile, ball bearings, 1.0 in., 1/4-20	423	2
31	Stage	Newport	ULTRAlign precision XYZ linear stage, 13 mm travel, req. 3 actuators	562-XYZ	1
32	Stage	Newport	high-performance linear stage, low-profile, ball bearings, 4.0 in., 1/4-20	443-4	1
33	Micrometer	Newport	vernier micrometer, 13 mm travel, 9 lb load capacity, 50.8 TPI	SM-13	3

Table A.1. (continued)

34	Micrometer	Newport	vernier micrometer, 50 mm travel, 23 lb load capacity, 50.8 TPI	SM-50	2
35	Micrometer	Newport	motorized linear actuator, 2 in. travel	850F	2
36	Riser	Newport	modular riser plates, 4 in. x 4 in. x 1 in., 1/4-20 thread	MRP4-1	7
37	Riser	Newport	modular riser plates, 4 in. x 4 in. x 0.5 in., 1/4-20 thread	MRP4-0.5	2
38	Riser	Newport	modular riser plates, 4 in. x 4 in. x 0.25 in., 1/4-20 thread	MRP4-0.25	3
39	Post Holder	Newport	no slip optical post holder, 2 in., 0.5 in. diameter posts, 1/4-20	VPH-2	2
40	Post Holder	Newport	no slip optical post holder, 1 in., 0.5 in. diameter posts, 1/4-20	VPH-1	1
41	Post	Newport	optical mounting post, 2.0 in., 0.5 in. dia. stainless, 8-32 & 1/4-20	SP-2	2
42	Post	Newport	optical mounting post, 1.5 in., 0.5 in. dia. stainless, 8-32 & 1/4-20	SP-1.5	5
43	Post	Newport	optical mounting post, 1.0 in., 0.5 in. dia. stainless, 8-32 & 1/4-20	SP-1	1

A.2 Complete Drawing

A.2.1 Source Side

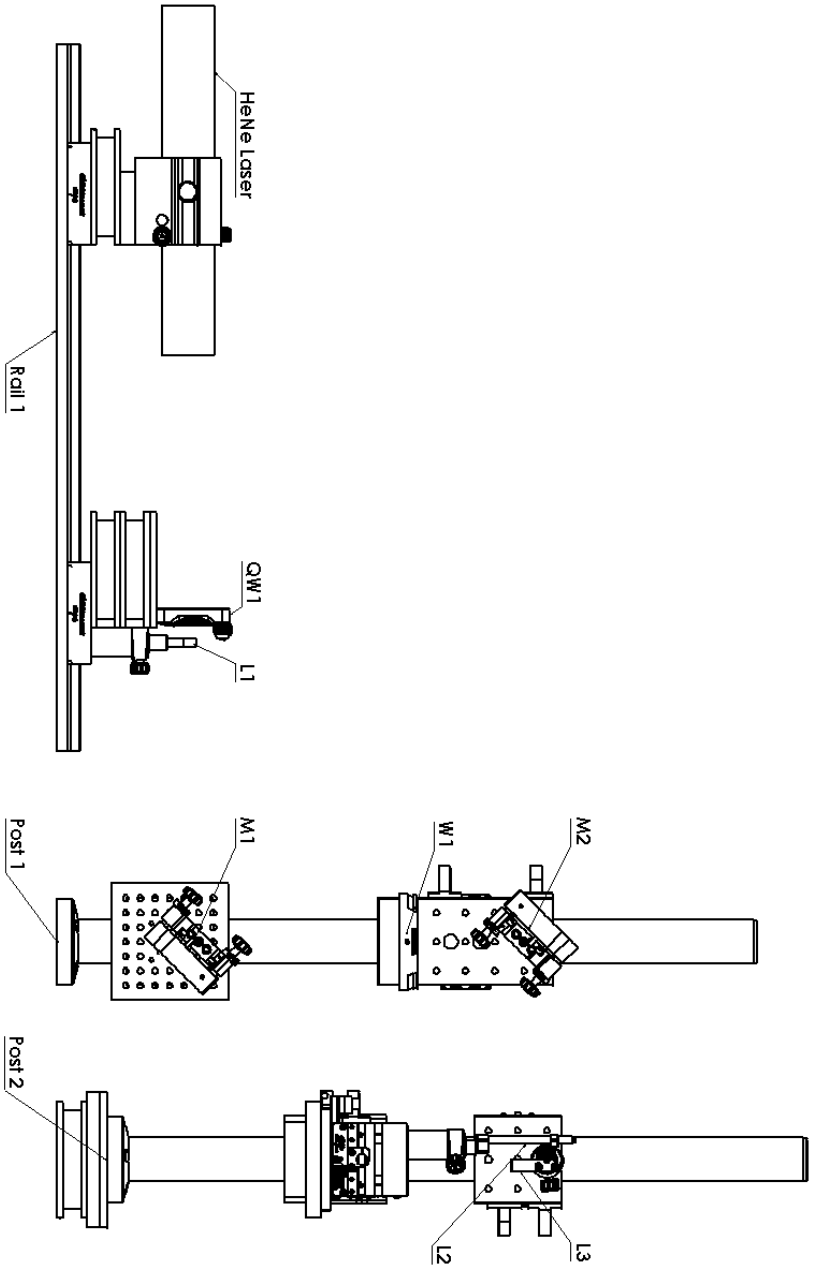

Table A.2. Mounting Information for Source Side of BAM6QT FLDI (generally listed from central component outward). Component number from Table A.1.

Label	**Name (Component #)**	**Mounted With Component #s (quantity in brackets if greater than 1)**
Rail 1 (component 21)		
HeNe Laser	HeNe Laser (1)	12, 28, 36, 23
QW1	Quarter-Wave Plate 1 (3)	13, 38, 36 [2], 23
L1	Lens 1 (6)	16, 41, 39, 23 (same as for QW1)
Post 1 (component 22)		
M1	Mirror 1 (11)	20, 42, 36, 25
W1	Wollaston 1 (4)	14, 42, 32, 25
M2	Mirror 2 (11)	20, 42, 32 (same as for W1), 25 (same as for W1)
Post 2 (component 22, mounted on 29 and 36)		
L2	Lens 2 (8)	17, 41, 39, 31, 27, 26
L3	Lens 3 (7)	17, 41, 39, 32, 25

A.2.2 Receiver Side

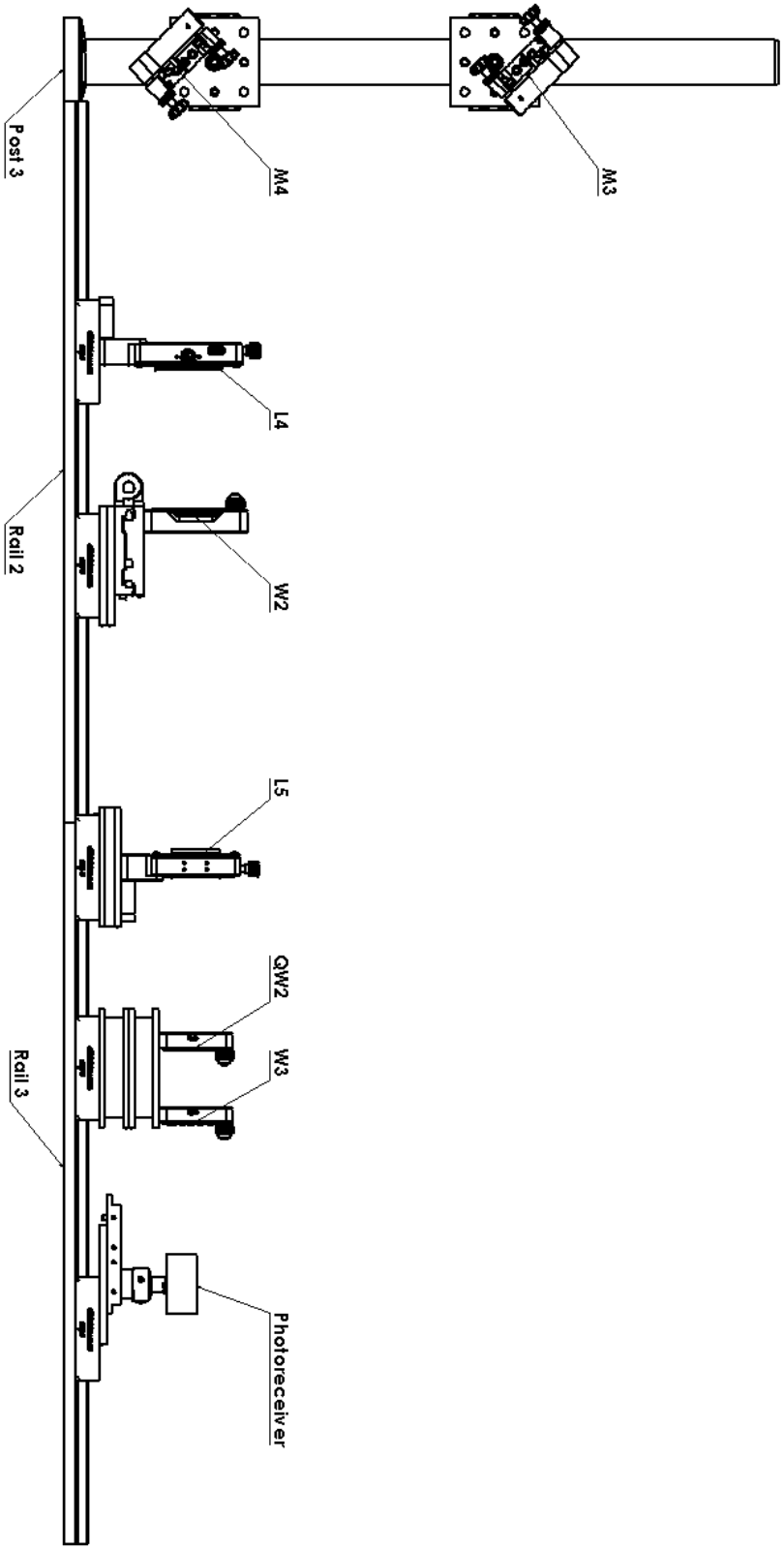

Table A.3. Mounting Information for Receiver Side of BAM6QT FLDI (generally listed from central component outward). Component number from Table A.1.

Label	**Name (Component #)**	**Mounted With Component #s (quantity in brackets if greater than 1)**
Post 3 (component 22)		
M3	Mirror 3 (11)	20, 42, 25
M4	Mirror 4 (11)	20, 42, 25
Rail 2 (component 21)		
L4	Lens 4 (10)	18, 23
W2	Wollaston 2 (4)	15, 30, 38, 23
Rail 3 (component 21)		
L5	Lens 5 (9)	19, 38, 37, 23
QW2	Quarter-Wave Plate 2 (3)	13, 36 [2], 23
W3	Wollaston 3 (5)	13, 36 [2] (same as for QW2), 23 (same as for QW2)
Photoreceiver	Photoreceiver (2)	43, 40, 37, 38, 23

B. INSTRUCTIONS FOR USING THE BAM6QT FLDI

This appendix contains a comprehensive set of instructions for how to use the BAM6QT FLDI. It is assumed that the FLDI components listed in Appendix A.1 are already assembled as shown in the drawings in Appendix A.2. There should be three optical rails:

- Rail 1, which will include the laser, first quarter-wave plate (QW1), and biconcave lens (L1)
- Rail 2, which will include a spherical convex lens (L4), the second Wollaston prism (W2), and another spherical convex lens (L5)
- Rail 3, which will include the second quarter-wave plate (QW2), third Wollaston prism (W3), and the photoreceiver

Rail 2 and Rail 3 will be placed sequentially such that the optical components can slide freely between them. There should also be three optical posts:

- Post 1, which will include two mirrors (M1 and M2) and the first Wollaston prism (W1)
- Post 2, which will include the two cylindrical lenses (L2 and L3)
- Post 3, which will include two more mirrors (M3 and M4)

These three rails and three posts should all be bolted to an optical breadboard with mounting holes spaced at 1 inch intervals. Rail 1, Post 1, and Post 2 all go on the source side of the tunnel, while Post 3, Rail 2, and Rail 3 should all be on the receiver side. Post 1 and Post 2 should be about 12.5 inches from each other.

Part of the alignment procedure also involves using a ThorLabs CCD Beam Profiler. This profiler is used to circularize the beam foci, as well as measure their widths and calibrate the beam translation. It should be mounted on the sting prior to beginning alignment. The ThorLabs software needs to be installed on a nearby computer to use the profiler.

As a reminder, in these instructions the z-direction is taken to be along the laser path (along the optical axis), while the x-direction is vertical and the y-direction is horizontal and

perpendicular to the optical axis. The two FLDI beams are located in the y-z plane, while their profiles are in the x-y plane.

1. Turn on the REO HeNe laser. The laser takes about 20 minutes to stabilize; while stabilizing, its indicator light will blink at a constant rate, and this light will stop blinking once stable.

2. Place the rail carrier with QW1 and L1 on Rail 1. Use the adjustment knobs on the laser mount to center the beam through QW1 and L1.

3. Place the rod clamp with M1 and as well as the one with W1 and M2 on Post 1. Tilt and shift M1 until the beams bounce up vertically between the two mirrors. Tilt M2 until they then become parallel to the breadboard after reflecting off that mirror.

4. Place the rod clamps with L2 and with L3 on Post 2. Shift the rod clamps with W1 and M2 on Post 1 and with L2 and L3 on Post 2 up on their respective posts until beams reach the height of the beam profiler aperture. Shift the beam profiler using optical posts until the beams enter the aperture.

5. Slide the rail carrier with L1 until it is about 16 inches from W1. Adjust the z-direction location of L2 and L3 until the foci of the beams are close to the z-location of the beam profiler. The profiler will later be used to confirm the location of each beam's focus.

6. Open the ThorLabs beam profiler software. Two spots of equal intensity should be seen that correspond to the two laser beams. If only one spot is seen, or if the spots seem to have different intensities, rotate QW1 until the two spots are of equal intensity. Next, rotate W1 until the two spots lie along the horizontal plane (the y-direction in the software, as the beam profiler is rotated 90° on the posts). This orientation places one beam upstream of the other for maximum signal response.

7. Shift L1, L2, and L3 in small increments until the two spots are roughly circular and are also as small as possible (indicating that the beam profiler camera is at the focus of each beam).

8. Move the profiler out of the beam paths temporarily to check that the beams exit the tunnel at the same height they entered at. If not, shift L1 until they do. Return the profiler to the beam paths.

9. Using the measuring tool in the software, determine the distance between the two spots as well as the height and width of the spots. This information can be useful for comparing the experimental results to FLDI simulations.

10. Next is the beam traversal calibration. Use the measuring tool to mark the current location of the two beams with the ThorLabs software. Then, move W2, M2, and L2 0.5 mm. Mark the new location of the beams and find the distance they travelled from their previous location. Repeat this process for several more intervals of 0.5 mm. The distances travelled by the beams for each shift in the optics should be similar; average them to determine how much the beams move at their foci for 0.5 mm shifts of the micrometers. This value allows the relative positions of the beams to be determined from adjustments in the locations of W2, M2, and L2 made during the entry.

11. Now remove the beam profiler and close the test section with the model installed inside. After closing the tunnel, shift W2, M2, and L2 to move the beams until they just touch the model surface. This will be location 0, with future shifts moving the beam off the surface in the flow of the boundary layer and freestream above that.

12. Place the rod clamp with M3 and the one with M4 on Post 3. Tilt and shift M3 as necessary until the beams bounce down from the test section to M4. Place the rail carriers with L4, W2, L5, QW2, and W3 on Rails 2 and 3. Then, tilt and shift M4 so the beams are parallel to the breadboard and travel through the center of the optics on the receiving side of the FLDI.

13. Slide W2 until is about 26 inches from the tunnel window. Then, place a plain white sheet of paper towards the end of the receiving side of the FLDI and shift L5 such that the laser spots are large enough to see the interference fringe patterns on the paper. Rotate W2 until these fringes are vertical.

14. Now it is necessary to "zoom in" to the fringe until infinite fringe spacing is achieved. Shift W2 towards or away from L4 so that the fringe lines get wider and wider. Stop when the interference pattern "flips" over; this should be the point of "infinite" fringe. It is important to check that the fringe spacing is still infinite before each run, as over time it tends to shift.

15. Remove the sheet of paper. Shift the rail carrier with QW2 and W3 until the beam spots are the same distance apart as the photodiodes on the photoreceiver. Shift L5 until the two beam profiles are as small as possible on the photodiodes. If necessary, rotate W3 so that the beam spots align with the centers of the photodiodes.

16. Now the FLDI needs to be calibrated. This and the following steps must be performed before each run. Two pieces of information need to be collected: the single photodiode equivalent baseline voltage V_c and the interference offsets V_{i1} and V_{i2}. V_{i1} and V_{i2} can be measured by shifting W2 in the y-direction for a full interference cycle. The voltages of the full interference cycle should be recorded and saved as "run_#_cal1.isf" (or .wfm, depending on which scope is used to record), where # is replaced by the particular run number of the entry. Next, V_c can be found by using a finger to block the beam from each photodiode separately. The maximum amplitude of the voltages measured should be equivalent for each photodiode. The data from the V_c calibration test should be recorded and saved as "run_#_cal2.isf". The voltages for each of these two tests should be recorded prior to a run.

17. Lastly, the FLDI must be set to the linear region of the interference pattern. Shift W2 in the y-direction until equal intensity is achieved in each photodiode. This is determined by a voltage output of 0 V, as the difference between the two inputs should be zero at the linear portion of the fringe. Shift W2 in the y-direction until 0 voltage is achieved on the scopes.

C. DOUBLE FLDI (D-FLDI)

By splitting the initial laser beam with an 0.5° Wollaston prism, the FLDI can be converted into a double-FLDI (D-FLDI) configuration (see Figure C.1). The additional prism (W0) is located just before the first quarter-wave plate and 2 arcminute Wollaston prism, that splits the beams into two beam pairs. The beams pairs will traverse the same optics for the majority of their path. They are fully separated by a mirror prism located at their final focal point after they are recombined in space by the second 2 arcminute Wollaston prism. Each beam is then passed through 40 mm convex lens to refocus it through the final quarter-wave plate and 20° Wollaston, before their intensities are measured at a balanced photoreceiver. The D-FLDI variation was tested with the Purdue 3-inch shock tube. However, when tested with the BAM6QT, the signal-to-noise ratio was too low to see any instabilities in quiet flow with the additional beam split. A more power laser is needed.

The D-FLDI was created by splitting the initial laser beam with an 0.5° Wollaston prism. This split resulted in two beam pairs measured to be 2.6 mm apart. Figure C.2 shows an image of the beam profiles near the focal points.

The Purdue 3-inch shock tube was utilized to see if the D-FLDI could accurately measure disturbance speed. The beam pairs were oriented in the streamwise direction. The relative locations of the 0.5° Wollaston and the 2-arcminute Wollaston result in the two beam pairs being 180° out-of-phase. Therefore, the voltages of one pair were inverted relative to the other.

Voltage time traces from the D-FLDI with the shock tube are shown in Figure C.3. By cross-correlating the voltages around the disturbance of interest, the time difference between the signals can be determined. By finding the lag time at maximum cross-correlation magnitude and dividing the known beam-pair separation by it, a disturbance velocity can be computed. In addition to the D-FLDI, two PCB sensors at downstream positions 6 inches apart were installed in the shock tube wall upstream of the D-FLDI beams. This second set of measurements provides a comparison for the D-FLDI results. The velocities of the shock and reflection for each sensor type are summarized in Table C.1. The D-FLDI provided shock and reflection velocities that were less than 2% off of the PCB speeds.

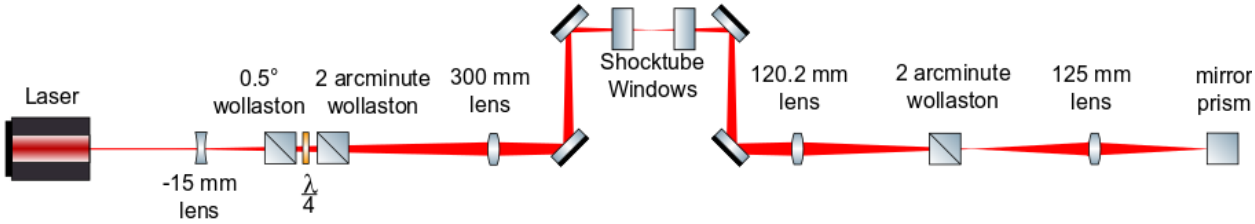

(a) D-FLDI view from side (similar to configurations in Figure 2.10)

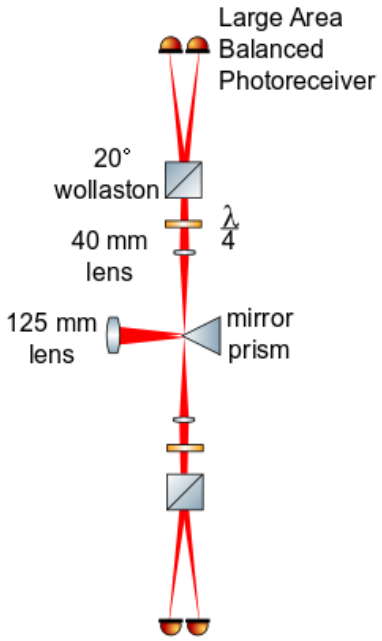

(b) D-FLDI view from above, beginning with 125 mm lens and showing beam paths to each photoreceiver

Figure C.1. D-FLDI optical setup

Figure C.2. D-FLDI beam profiles near focal points

Table C.1. Shock and reflection speeds measured by PCBs and D-FLDI

Sensor Type	Shock Velocity (m/s)	Reflection Velocity (m/s)
PCB	493	315
D-FLDI	490	319
% Difference	0.62%	1.10%

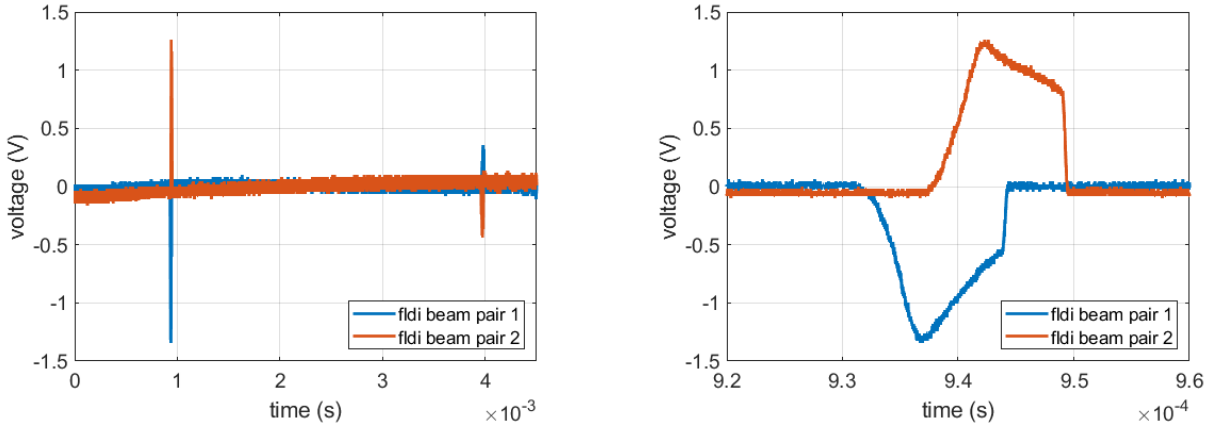

(a) Time traces of shock and reflection

(b) Enhanced view of shock

Figure C.3. D-FLDI voltages for each beam pair

D. DRAWINGS OF MODELS

D.1 Cone-Cylinder with a 3.5° Flare

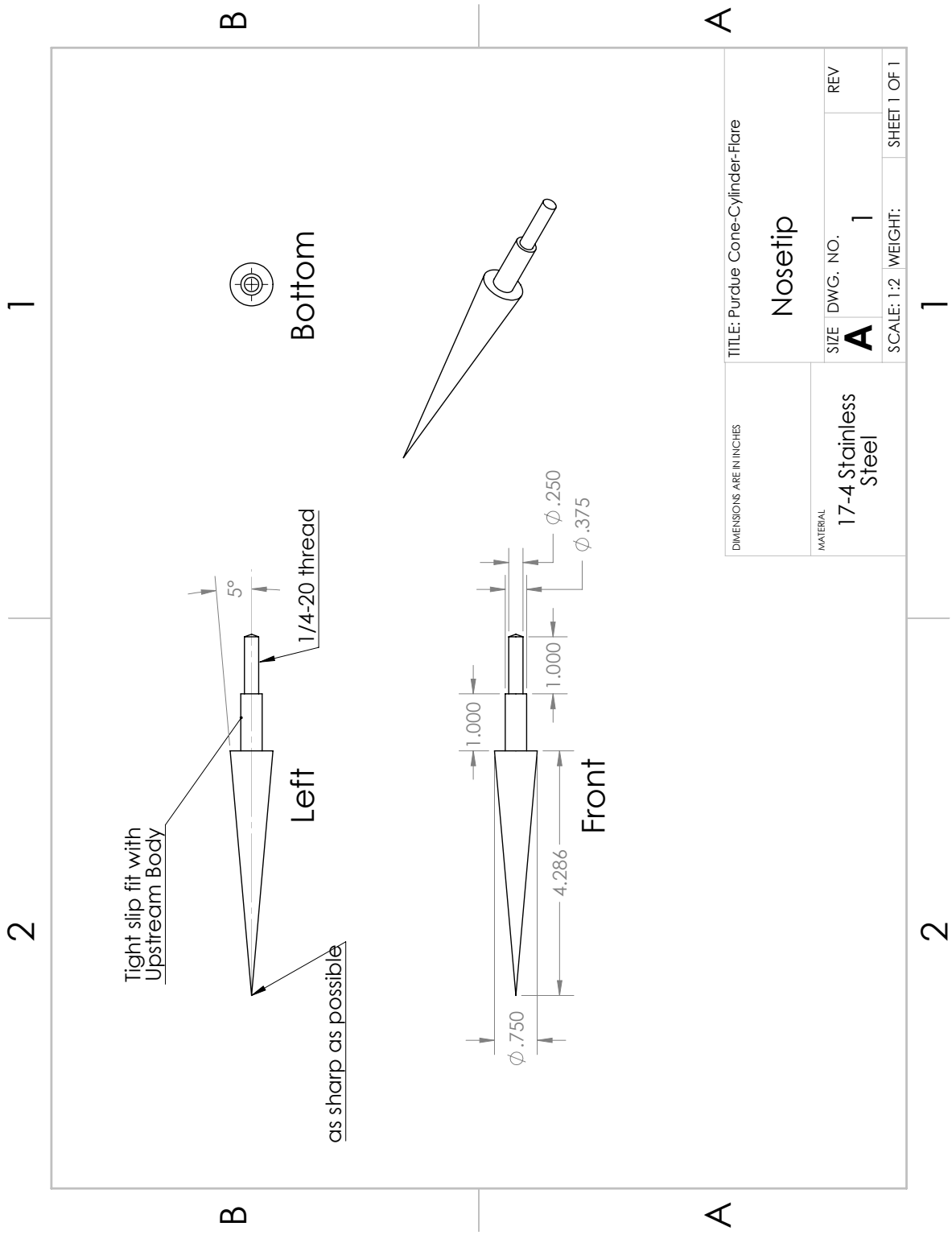

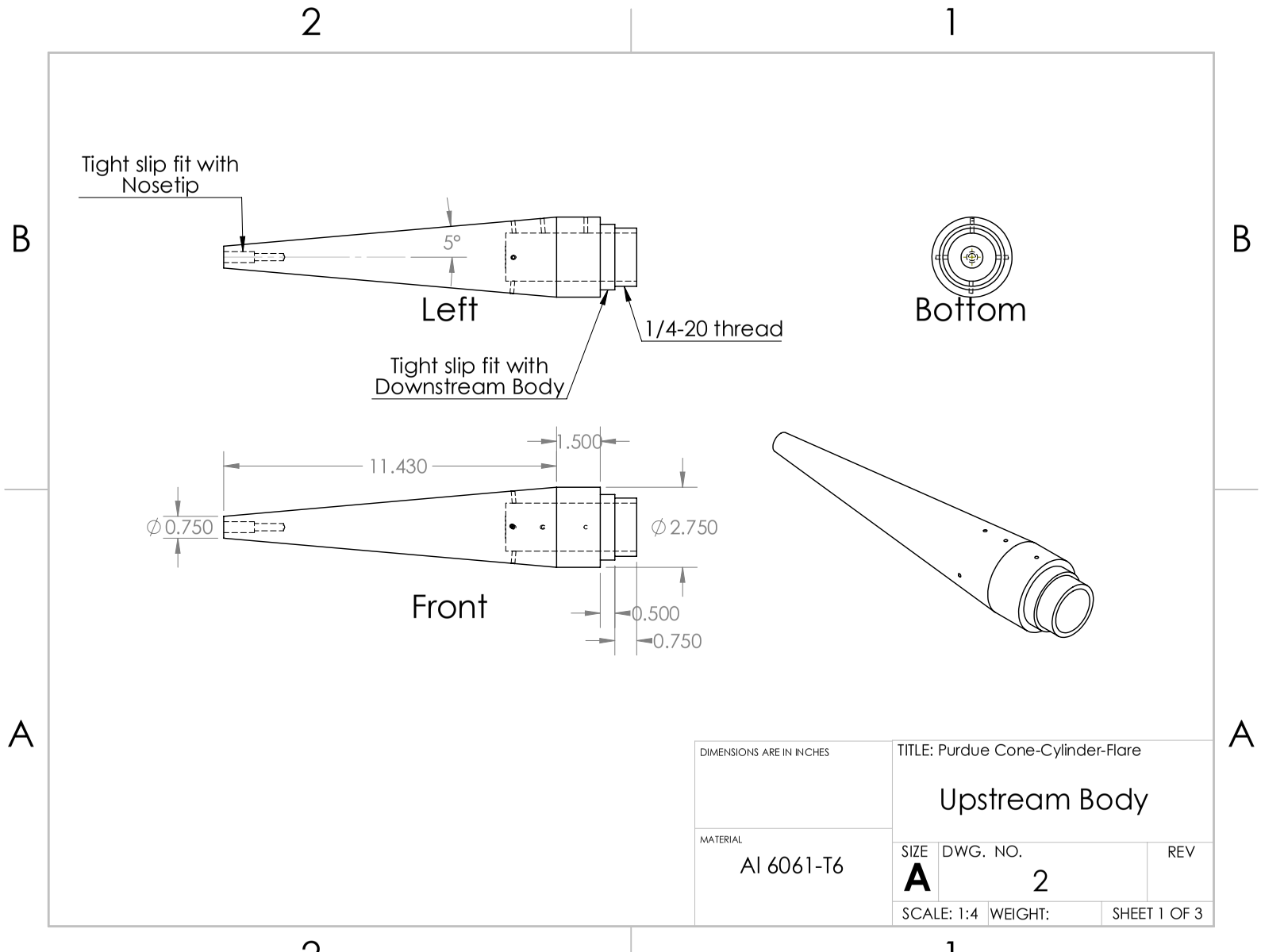
2
1
B
A
Tight slip fit with
Nosetip
5°
Left
1/4-20 thread
Tight slip fit with
Downstream Body
Bottom
1.500
11.430
∅0.750
∅2.750
Front
0.500
0.750
DIMENSIONS ARE IN INCHES
MATERIAL
Al 6061-T6
TITLE: Purdue Cone-Cylinder-Flare
Upstream Body
SIZE
A
DWG. NO.
2
REV
SCALE: 1:4
WEIGHT:
SHEET 1 OF 3

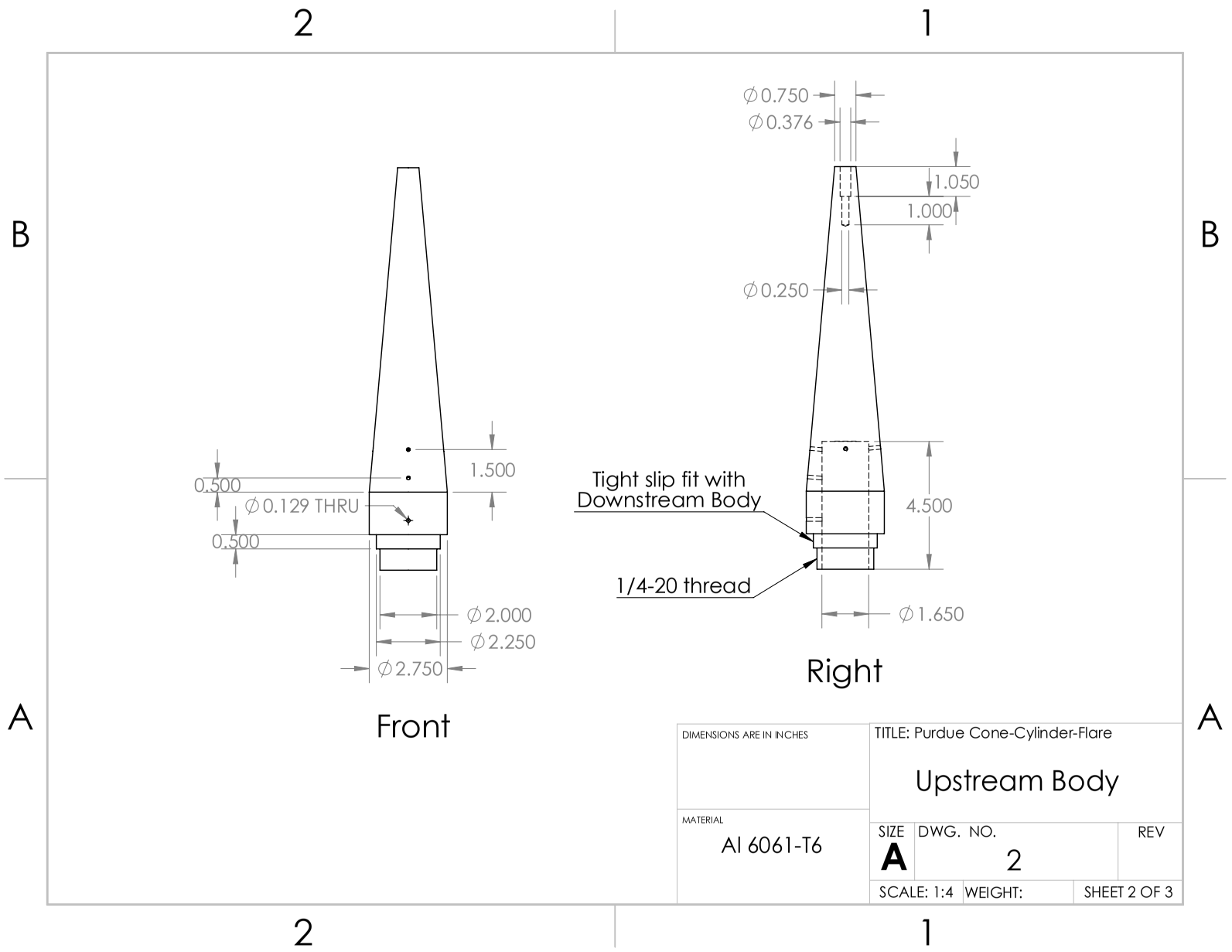
2
1
B
A
0.500
0.129 THRU
0.500
1.500
2.000
2.250
2.750
Front
0.750
0.376
1.050
1.000
0.250
Tight slip fit with
Downstream Body
1/4-20 thread
4.500
1.650
Right
DIMENSIONS ARE IN INCHES
MATERIAL
Al 6061-T6
TITLE: Purdue Cone-Cylinder-Flare
Upstream Body
SIZE
A
DWG. NO.
2
REV
SCALE: 1:4
WEIGHT:
SHEET 2 OF 3

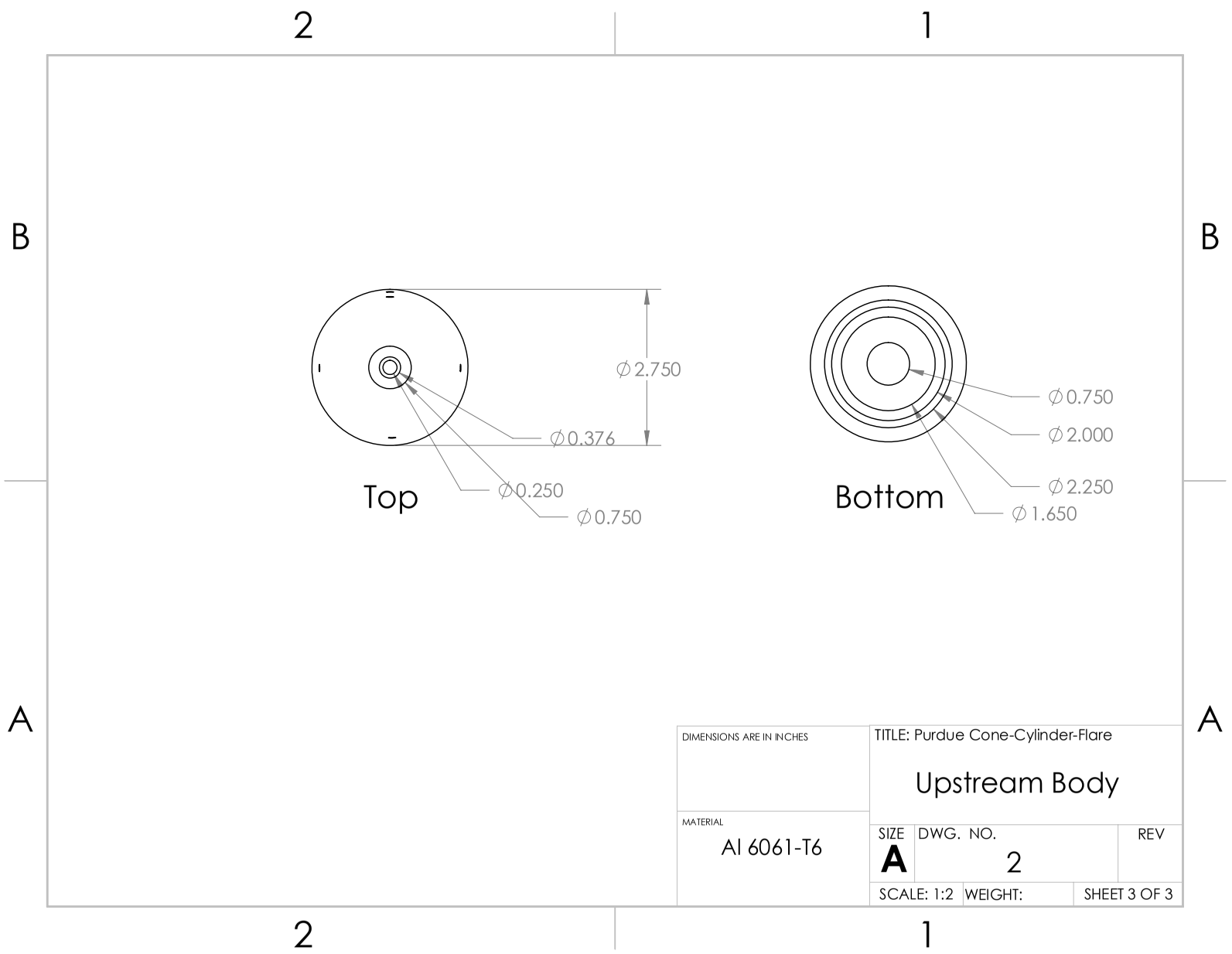
2
1
B
A
280
∅2.750
∅0.376
∅0.250
∅0.750
Top
∅0.750
∅2.000
∅2.250
∅1.650
Bottom
DIMENSIONS ARE IN INCHES
MATERIAL
Al 6061-T6
TITLE: Purdue Cone-Cylinder-Flare
Upstream Body
SIZE
A
DWG. NO.
2
REV
SCALE: 1:2
WEIGHT:
SHEET 3 OF 3

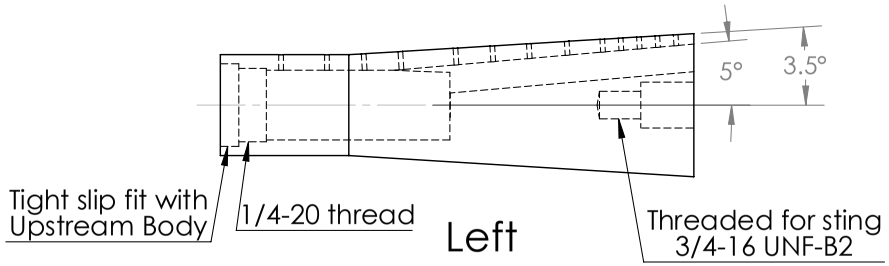

Left

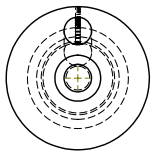

Bottom

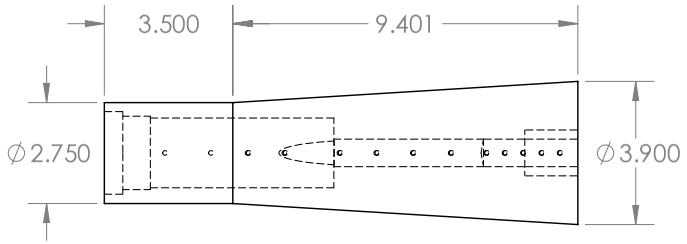

Front

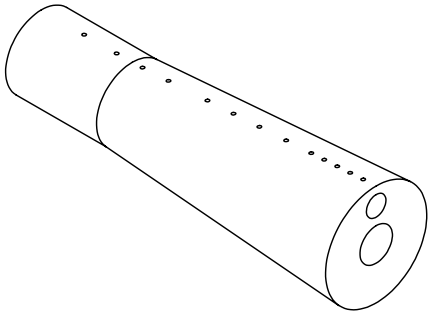

DIMENSIONS ARE IN INCHES	TITLE: Purdue Cone-Cylinder-Flare 3.5 Deg. Downstream Body	
MATERIAL PEEK	SIZE A	DWG. NO. 3
	SCALE: 1:4	WEIGHT:
		SHEET 1 OF 3

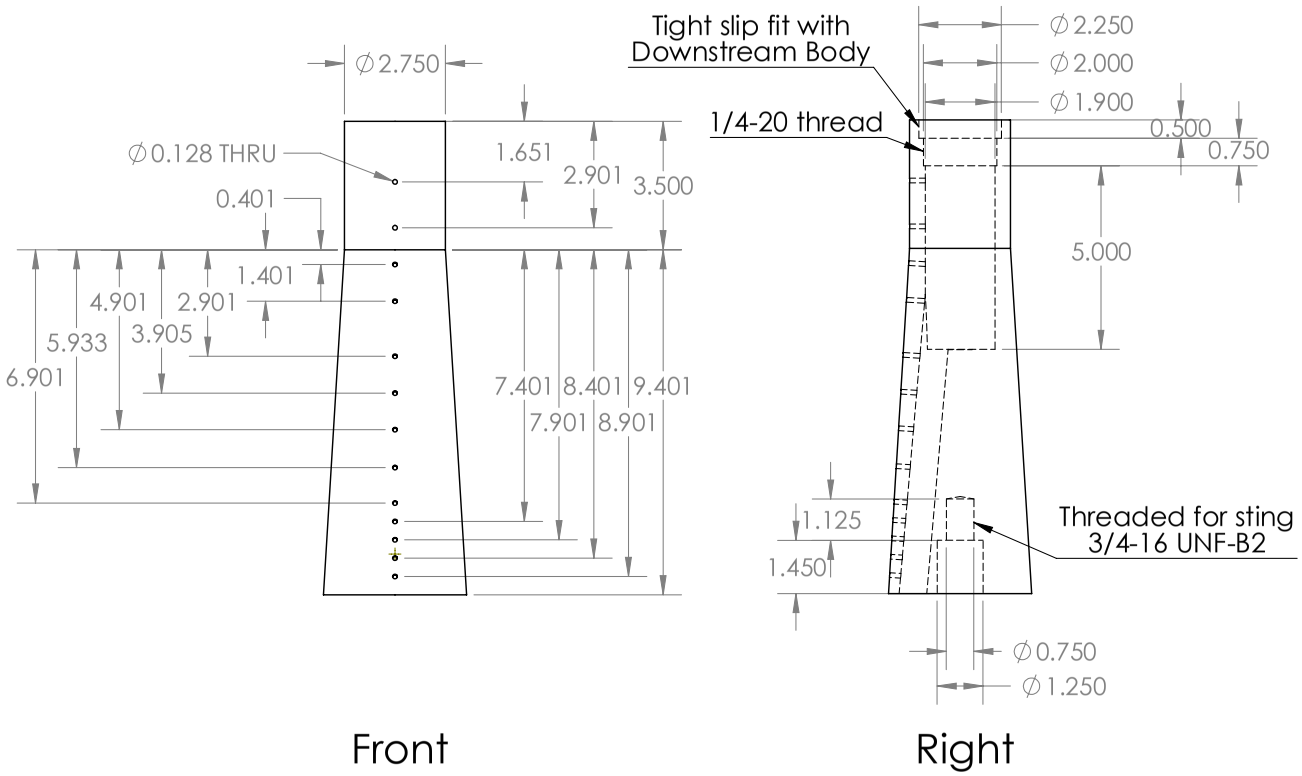

DIMENSIONS ARE IN INCHES	TITLE: Purdue Cone-Cylinder-Flare 3.5 Deg. Downstream Body
MATERIAL PEEK	SIZE A | DWG. NO. 3 | REV
	SCALE: 1:4 | WEIGHT: | SHEET 2 OF 3

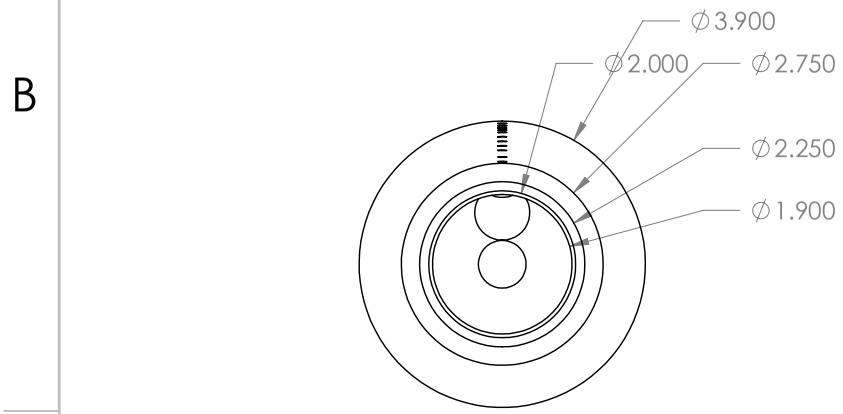

Top

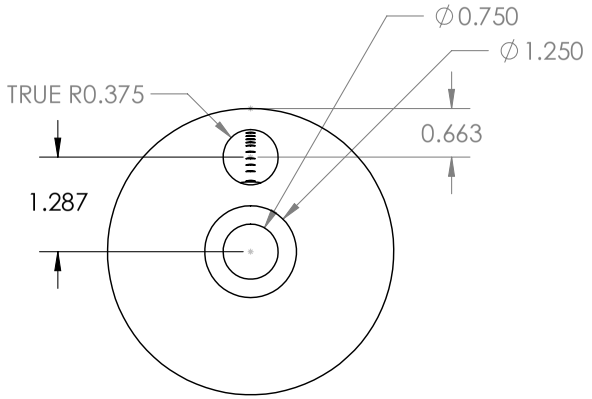

Bottom

DIMENSIONS ARE IN INCHES	TITLE: Purdue Cone-Cylinder-Flare 3.5 Deg. Downstream Body	
MATERIAL PEEK	SIZE A	DWG. NO. 3 / REV
	SCALE: 1:2	WEIGHT: / SHEET 3 OF 3

D.2 Cone-Cylinder with a 10° Flare Base

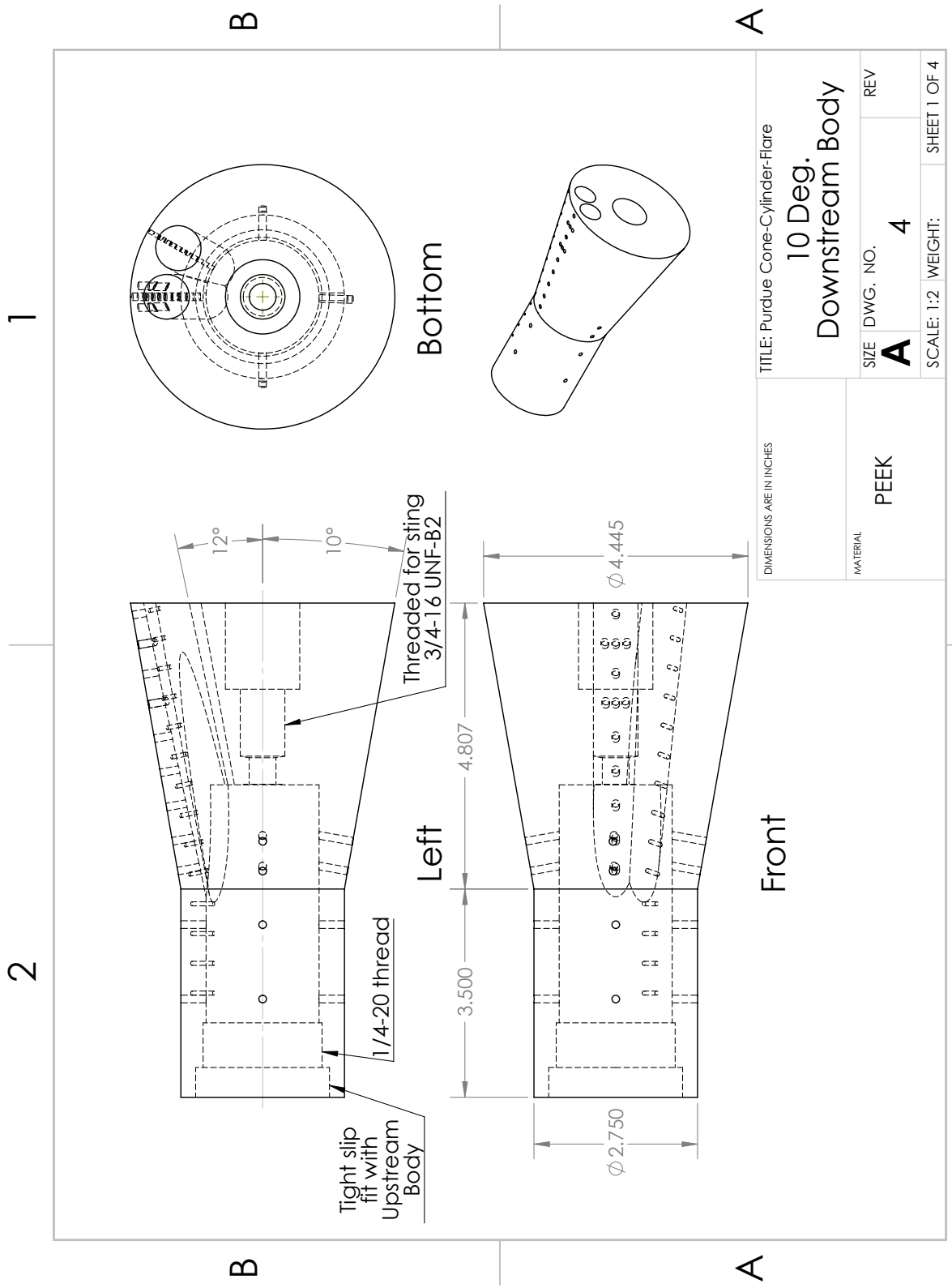

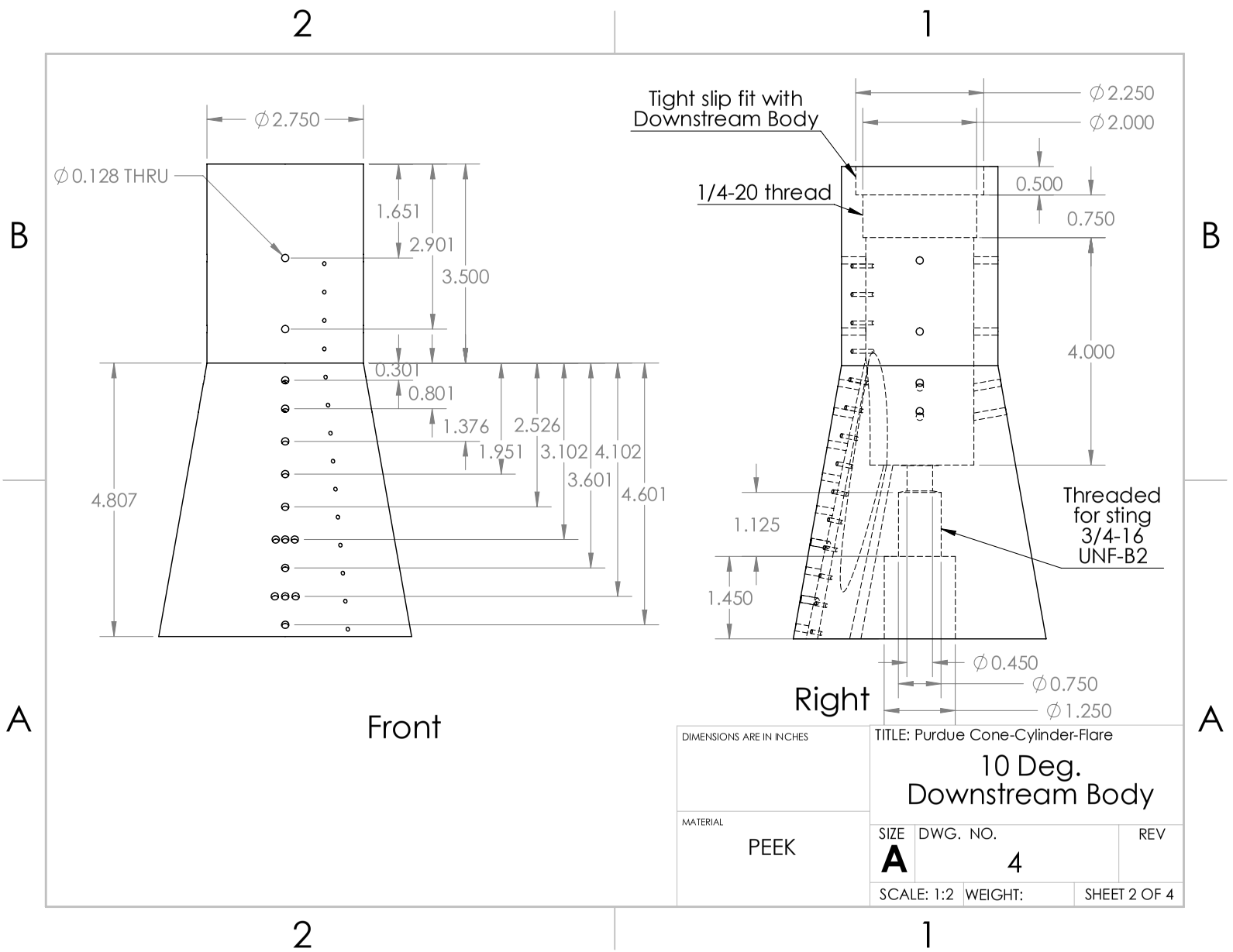
2
1
B
A
∅2.750
∅0.128 THRU
1.651
2.901
3.500
0.301
0.801
1.376
2.526
1.951
3.102
4.102
3.601
4.601
4.807
Front
Tight slip fit with
Downstream Body
1/4-20 thread
∅2.250
∅2.000
0.500
0.750
4.000
Threaded
for sting
3/4-16
UNF-B2
1.125
1.450
∅0.450
∅0.750
∅1.250
Right
DIMENSIONS ARE IN INCHES
MATERIAL
PEEK
TITLE: Purdue Cone-Cylinder-Flare
10 Deg.
Downstream Body
SIZE
A
DWG. NO.
4
REV
SCALE: 1:2
WEIGHT:
SHEET 2 OF 4

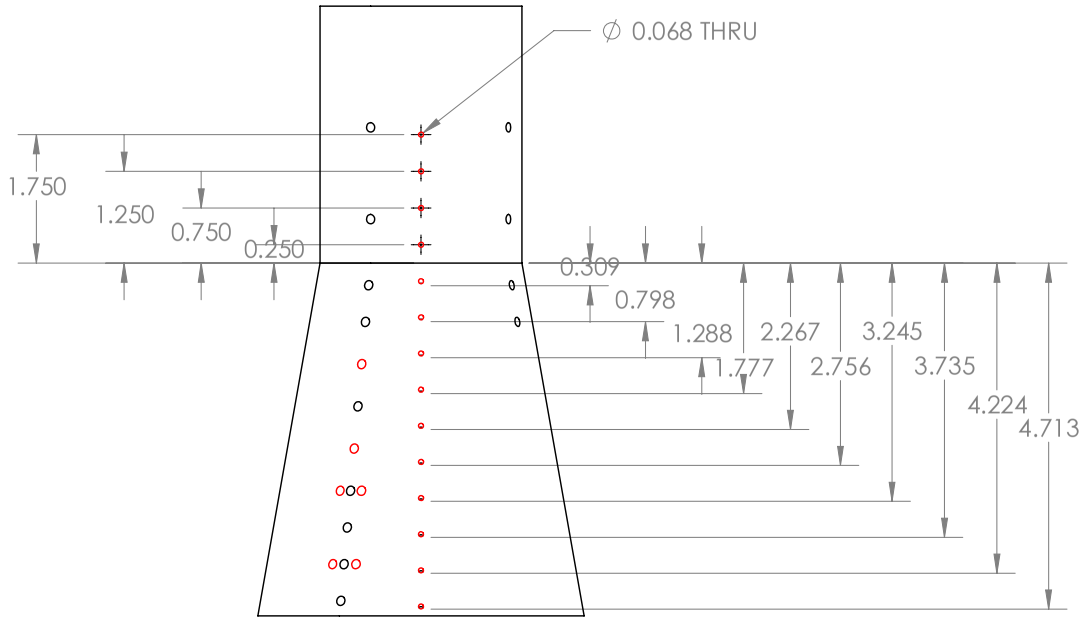

DIMENSIONS ARE IN INCHES	TITLE: Purdue Cone-Cylinder-Flare 10 Deg. Downstream Body
MATERIAL PEEK	SIZE A | DWG. NO. 4 | REV
	SCALE: 1:2 | WEIGHT: | SHEET 3 OF 4

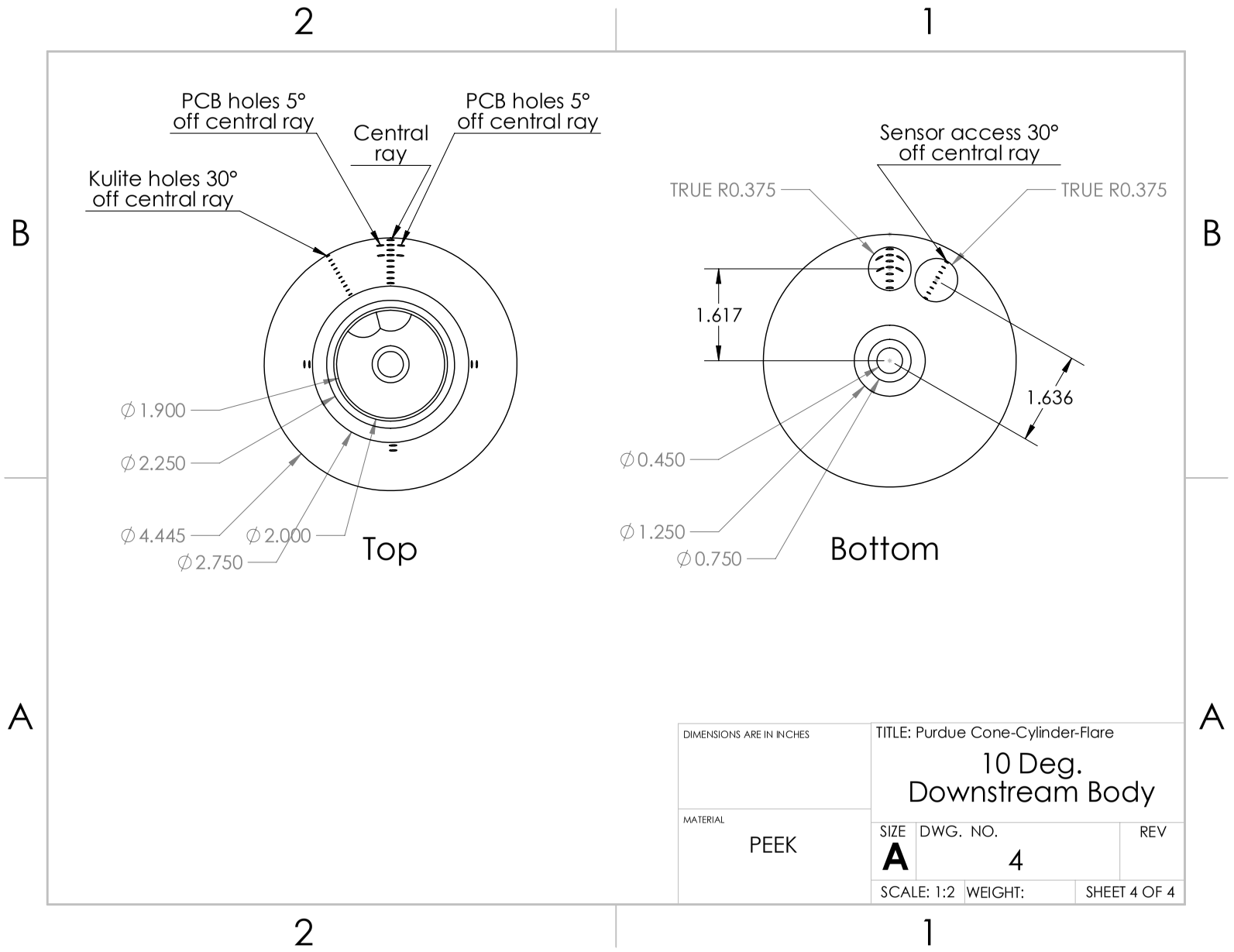
2
1
B
A
PCB holes 5°
off central ray
Central
ray
PCB holes 5°
off central ray
Kulite holes 30°
off central ray
∅1.900
∅2.250
∅4.445
∅2.000
∅2.750
Top
Sensor access 30°
off central ray
TRUE R0.375
TRUE R0.375
1.617
1.636
∅0.450
∅1.250
∅0.750
Bottom
DIMENSIONS ARE IN INCHES
MATERIAL
PEEK
TITLE: Purdue Cone-Cylinder-Flare
10 Deg.
Downstream Body
SIZE
A
DWG. NO.
4
REV
SCALE: 1:2
WEIGHT:
SHEET 4 OF 4

D.3 Plasma Perturber Electrodes and Cone-Cylinder Section

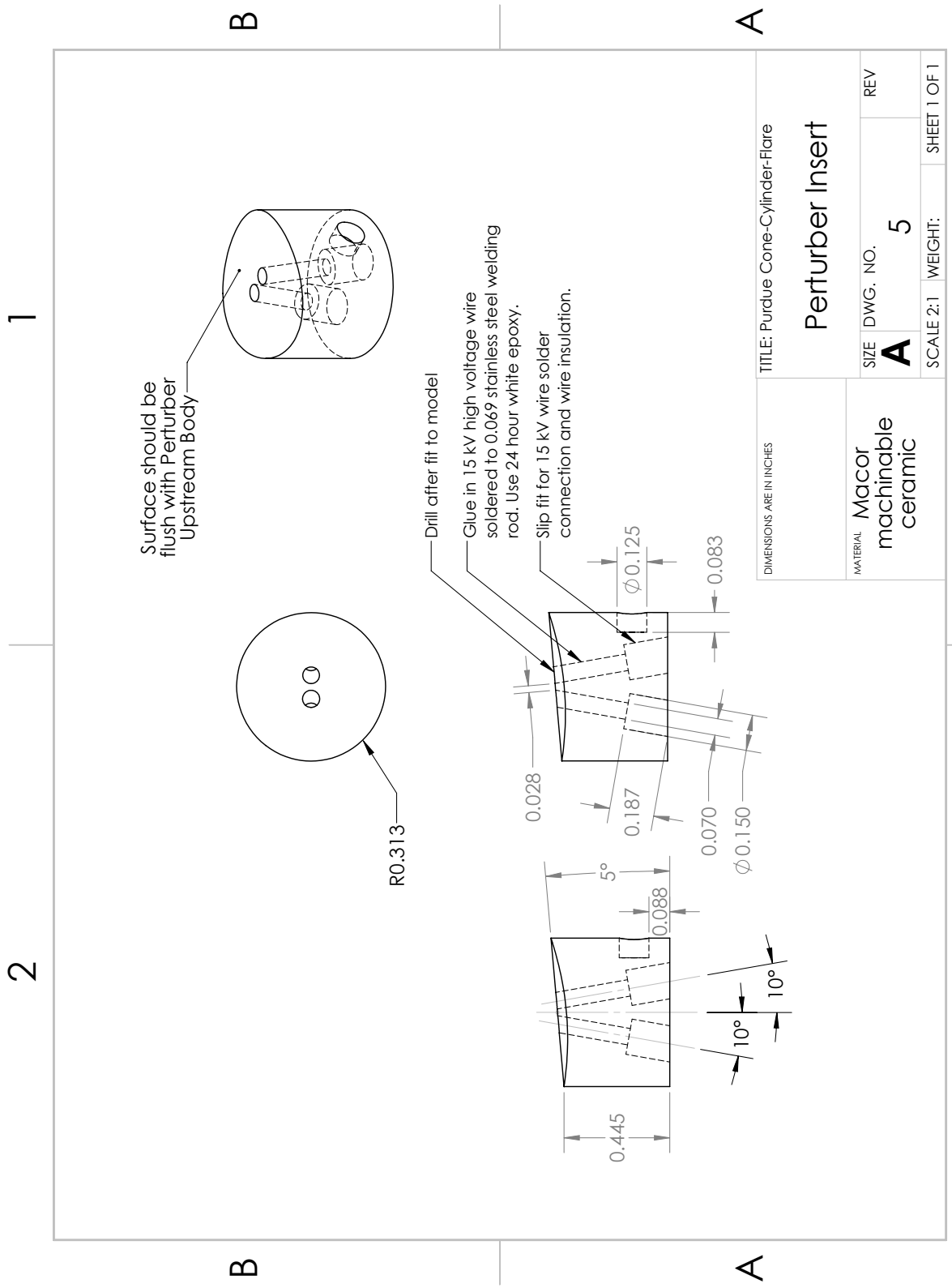

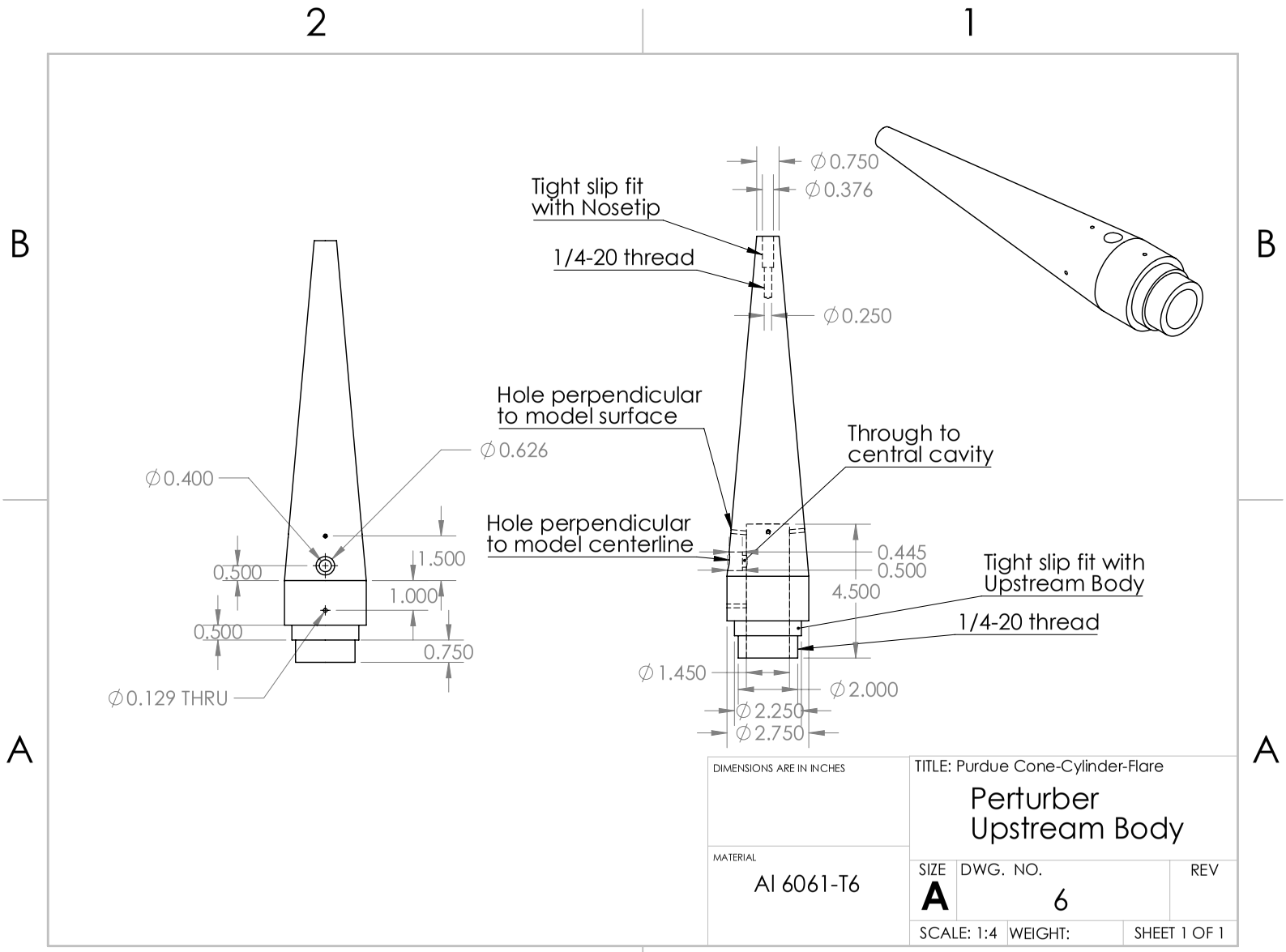
2
1
B
A
Tight slip fit
with Nosetip
1/4-20 thread
∅0.750
∅0.376
∅0.250
Hole perpendicular
to model surface
Through to
central cavity
Hole perpendicular
to model centerline
Tight slip fit with
Upstream Body
1/4-20 thread
∅0.626
∅0.400
0.500
1.500
1.000
0.500
0.750
∅0.129 THRU
0.445
0.500
4.500
∅1.450
∅2.000
∅2.250
∅2.750
DIMENSIONS ARE IN INCHES
MATERIAL
Al 6061-T6
TITLE: Purdue Cone-Cylinder-Flare
Perturber
Upstream Body
SIZE
A
DWG. NO.
6
REV
SCALE: 1:4
WEIGHT:
SHEET 1 OF 1

E. FLDI PROCESSING CODE AND DOCUMENTATION

The primary script used for processing the FLDI voltage data is fldi_analysis.m, which is included in this appendix. This script is used for both acquiring the calibration constants and processing the run data. Features of the script include:

- Determining calibration values from voltage data
- Calibrating FLDI run and prerun data from raw voltages to convert to single photodiode voltages, phase change values, or density fluctuations
- Computing power spectral densities from data
- Finding frequency peaks in specified frequency range of power spectra
- Creating spectrograms of the data to view both frequency and time information
- Playing back and saving audio from the FLDI voltages
- Plotting a variety of other information related to the data

E.1 Obtaining Calibration Values

For an individual run, the script must be used at least three times and a calibration file called FLDI_Calibrations.csv should exist. This file should have 8 columns, the final 4 to be filled with data computed from the script. Until the values are known, fill in each column with a placeholder to prevent the script from ignoring partial entries. Table E.1 summarizes the columns of the calibration file. Note that the first row of the file is not read in, and is instead reserved for comments. If the data acquisition system is used instead of oscilloscopes, fill columns 3 and 4 with zeros as placeholders.

Table E.1. FLDI_Calibrations.csv Columns

Column #	Information
1	Run number
2	Scope number

Table E.1. (continued)

3	Channel number for DC data
4	Channel number for AC data
5	V_{i1}
6	V_{i2}
7	V_c
8	$d\phi_0$

The first time the script is run is to obtain the single photodiode equivalent baseline voltage, V_c. Therefore, the value for CALIBRATION should be set to 2 (to read in the corresponding calibration file, run_#_cal2.isf or run_#_cal2.wfm where the data was recorded) and AC should be set to 0. The value for V_c should print to the console; enter that value in the calibration file, as it is necessary to obtain the remaining calibration values.

Next, the interference offsets V_{i1} and V_{i2} need to be determined, so CALIBRATION should be set to 1 (to read from run_#_cal1.isf or run_#_cal1.wfm), and AC again set to 0. After these values are displayed, enter them in the calibration file.

Finally, the script can be called for the actual run data. CALIBRATION should now be set to 0, but AC should remain at 0 for this script call. Using the DC data allows $d\phi_0$ to be obtained (it is printed to the console), so it can be entered in the calibration file. Once $d\phi_0$ is known, the AC data can be used instead if the DC fluctuations are causing quantization issues.

E.2 Options

There are several options for the user to input in the upper portion of the script. Table E.2 below includes a detailed list of the options, what they mean, and any extra information required.

Table E.2. Matlab Script Options

Option	Class	Description
`main_path`	String	Path to scope or DAQ data and FLDI_Calibrations.csv file
`PRERUN_NOISE`	Boolean	Toggle to look at prerun data (before $t = 0$) instead of run data
`CALIBRATION`	Integer	Determine which (if any) calibration file to process 0 = run data (not a calibration file; if TYPE is not 0, requires V_{i1}, V_{i2}, and V_c to be known) 1 = V_{i1} and V_{i2} computation from run_#_cal1 (requires V_c to be known) 2 = V_c computation from run_#_cal2
`RUNS`	Integer Array	List of run numbers to process
`TIME`	Double Array	List of times to process at (if only one time is present, all runs will use that time; otherwise, the list of times should be the same length as the list of run numbers)
`AC`	Boolean	Toggle to look at AC voltages as opposed to DC voltages (note that to obtain V_c, V_{i1}, V_{i2}, and $d\phi_0$ this must be set to 0)
`LINEAR`	Boolean	Toggle to assume that the data is perfectly centered in the linear region of the fringe (forces $d\phi_0 = -\pi/2$)
`TYPE`	Integer	Determine how data should be processed: 0 = balanced photoreceiver voltages (raw voltage data, V_{pr}) 1 = single photodiode equivalent voltages ($V = V_{pr}/2 + V_c$)

Table E.2. (continued)

		2 = phase change ($d\phi$) in radians 3 = optical path change (difference in optical distance travelled by each beam) in meters 4 = density change in kg/m^3
DAQ	Boolean	Toggle to use data acquired from DAQ (as opposed to oscilloscopes)
PLOT_VOLTS	Boolean	Toggle to plot raw voltage time trace
PLOT_DATA	Boolean	Toggle to plot calibrated data time trace
COMPUTE_PSD	Boolean	Toggle to compute power spectral densities (PSDs) or power spectra
PLOT_PSD	Boolean	Toggle to plot PSDs or power spectra
FIND_ERR	Boolean	Toggle to estimate error offsets of calibrated data caused by divergence from center of linear region of the fringe
POWER	Boolean	Toggle to compute power spectra as opposed to PSDs (equal to PSD scaled by the noise bandwidth from the window used with pwelch)
SPECTROGRAM	Boolean	Toggle to compute and plot a spectrogram of the data to see both time and frequency information in one plot
same_plot	Boolean	Toggle to plot the PSDs/power spectra of multiple runs in one figure
prange	Double Array	Frequency range in which to look for potential frequency peaks in PSD/power spectrum (and empty array will skip this process and not return any peak information)

Table E.2. (continued)

PLOT_PRANGE	Boolean	Display beginning and end of frequency range defined in prange and denote frequency peaks in PSD/power spectrum plots
peak_dec	Double	Scaling factor between 0 and 1 used to find edge frequencies of frequency peak, corresponding to the percent of the maximum value to search for - this value should be closer to 1 for small peaks and closer to 0 for large, clear ones
PLAY_SOUND	Boolean	Toggle to play audio from voltage data
SAVE_SOUND	String	Name to save audio data as a .wav file (use empty string to not save)
factor	Double	Value to scale plotted data by (helps fit multiple types of data in same axes)
width	Double	Line width for plotted data
freq_reso	Double	Frequency resolution for PSD or power spectrum in Hz
freq_bins	Integer	Number of frequency bins for spectrogram in bins/Hz
time_bins	Integer	Number of time bins for spectrogram in bins/s
desired_time	Double	Starting time for data to be analyzed in seconds
process_time	Double	Amount of time of data to process in seconds

E.3 Peak Frequency Determination

Figure E.1 shows a sample PSD of some FLDI phase change data with the peak frequency and amplitude found by the FLDI_analysis.m code. For this particular example, `prange` was set to [85 135], `peak_dec` was set to 0.3 and `freq_reso` was set to 2 kHz. The limits defined by `prange` are shown as black dotted lines in the plot.

The frequency at which a peak occurs in the PSD or power spectrum is determined by first finding the maximum amplitude within the frequency range defined by prange (this point is shown as the red star in Figure E.1). The value of the maximum is then scaled by `peak\_dec`, and this scaled value is found on either side of the maximum (shown as black stars in the figure). The two frequencies these scaled values occur at are then averaged to define the computed peak frequency. Finally, the amplitude of the PSD or power spectrum at this frequency is found and noted as the peak amplitude (marked by the red circle in the plot). To obtain actual power values, the area under the curve is integrated between the limits defined by `prange`.

For the example shown in Figure E.1, the maximum was at a frequency of 109.0 kHz and an amplitude of 1.147×10^{-10}. The scaled values were at frequencies of 99.1 kHz and 116.9 kHz and both had a value near 3.442×10^{-11}. The computed peak frequency was at 108.0 kHz, and had an amplitude of 1.123×10^{-10}. The power of this peak was computed at 1.341e-3 by integrated between the frequency limits.

This peak-finding method was compared to a parabolic approximation using interpolation described by Hildebrand [90]. It was determined that the peak frequency found by the averaging the frequencies of the scaled values on either side of the maximum (the method used in this code) was within 0.001% of that found by Hildebrand's method in most cases when using the same three points (the maximum, the lower scaled value, and the upper scaled value). The largest error seen between the two methods was 0.5%. Therefore, the averaging method described here was used for peak finding analysis of both FLDI and PCB data.

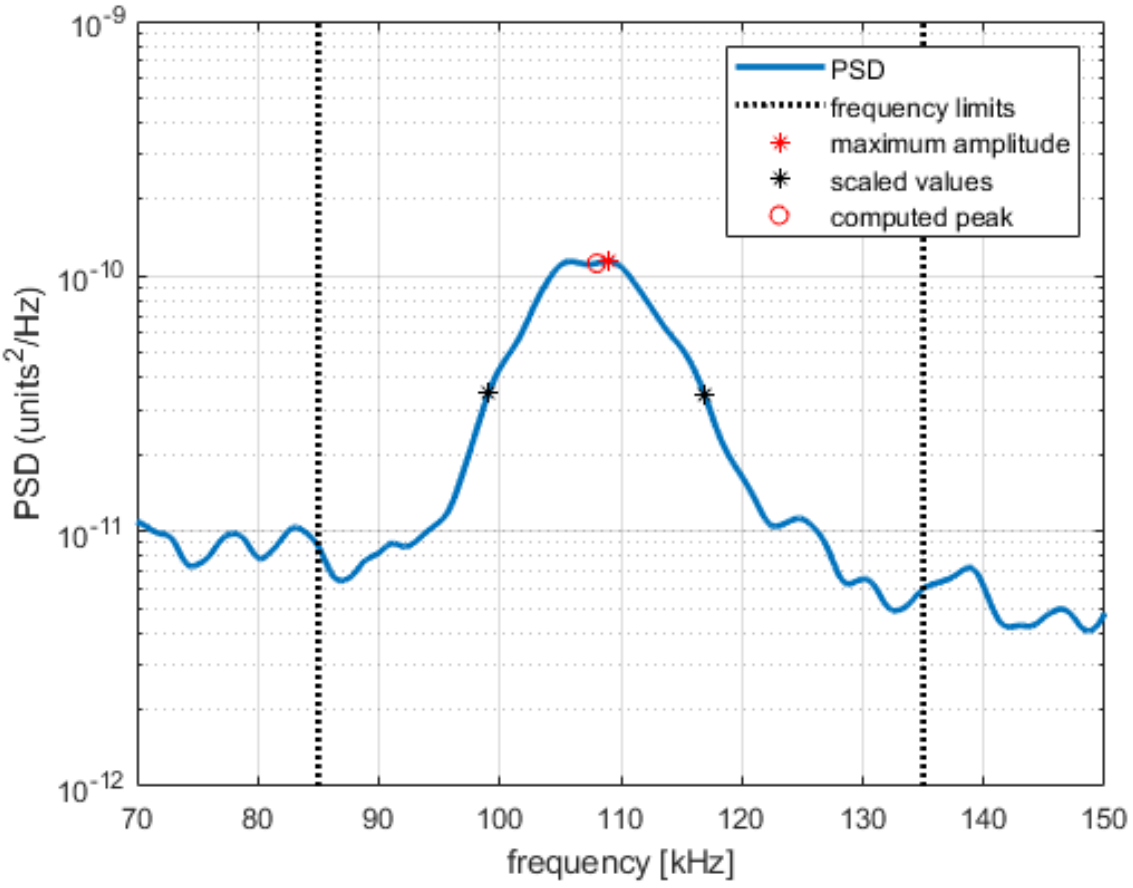

Figure E.1. Example of frequency peak determination

E.4 Matlab Code

```
%% FLDI Data Analysis Script
% By: Elizabeth Benitez
% Last Modified: 24 April 2019
% Reads in FLDI data and processes it
clear all; clc;
close all;
addpath('PCB_quick_look');

%% options
main_path = 'E:\entry1\scope_data\'      % location of input FLDI
    data

PRERUN_NOISE = 0;                        % get output on prerun data
    (t = -0.5 s)
CALIBRATION = 0;                         % 0 = regular data, 1 = Vi
    data, 2 = Vc data
BENCH_TEST = 0;                          % 0 = tunnel data, 1 = other
    data
RUNS = [1];                              % run number(s) to analyze
TIME = [1.5];                            % time(s) during run to
    analyze

```

```
AC = 0;                                 % 1 = AC voltages, 0 = DC voltages
LINEAR = 0;                             % 0 = compute phase offset d_phi0
                                        % 1 = assume linear portion of fringe
                                        % (d_phi0 = pi/2)
TYPE = 2;                               % voltages (balanced)   = 0
                                        % voltages (single)     = 1
                                        % phase change          = 2
                                        % optical path change   = 3
                                        % density change        = 4
DAQ = 0;                                % 0 = oscilloscopes, 1 = DAQ

PLOT_VOLTS = 0;                         % plot voltages
PLOT_DATA = 0;                          % plot calibrated data
COMPUTE_PSD = 1;                        % compute PSD/power data
PLOT_PSD = COMPUTE_PSD;                 % plot PSD
FIND_ERR = 0;                           % compute error extremes due to being outside
                                        % linear region
POWER = 0;                              % computer power instead of PSD (equal to PSD
                                        % scaled by noise bandwidth of window)
SPECTROGRAM = 0;                        % plot spetrogram of data
same_plot = 1;                          % use same figure number for different runs

prange = [150 250];                     % frequency range of potential peaks
                                        % (use [] if not looking for peak frequencies
                                        % or peak amplitudes)
PLOT_PRANGE = 0;                        % show frequency range and peak locations on
                                        % plots
peak_dec = 0.5;                         % peak frequency cutoff value as fraction of
                                        % maximum amplitude

PLAY_SOUND = 0;                         % play audio data
SAVE_SOUND = '';                        % save audio data as .wav (leave as blank
                                        % string to not save)
factor = 1;                             % factor to scale plotted data by
width = 2;                              % linewidth of plotted data

if COMPUTE_PSD || SPECTROGRAM
    freq_reso = 4e3;                    % frequency resolution for PSD, Hz
    freq_bins = 100e3;                  % number of frequency bins for spectrogram,
                                        % bins/Hz
    time_bins = 2e5;                    % number of time bins for spectrogram, bins/s
end

if PRERUN_NOISE
    desired_time = -0.3;                % time to look at prerun noise
    process_time = 0.1;                 % time to process prerun noise
else
    desired_time = TIME;                % time to look at flow data
    if CALIBRATION == 1 || CALIBRATION == 2
        desired_time = -5;
        process_time = 10;              % time to process flow data
    else
        process_time = 0.1;             % time to process flow data
```

```
    end
end

T = 295;                                    % room temperature, K

%% calibration and scope information
try
    % read in information from csv file
    FLDI_Calibrations = csvread([main_path,'FLDI_Calibrations.csv'],1,0);
    Vi1 = FLDI_Calibrations(RUNS,5);
    Vi2 = FLDI_Calibrations(RUNS,6);
    Vc = FLDI_Calibrations(RUNS,7);
    SCOPE = ones(1,length(RUNS)).*FLDI_Calibrations(RUNS,2);
    if AC
        CH = ones(1,length(RUNS)).*FLDI_Calibrations(RUNS,4);
        d_phi0 = FLDI_Calibrations(RUNS,8);
    else
        CH = ones(1,length(RUNS)).*FLDI_Calibrations(RUNS,3);
    end
catch
    % if no csv file, use hardcoded values
    Vc = 4.6847.*ones(1,length(RUNS));  % baseline voltage, V
    Vi1 = 4.6825.*ones(1,length(RUNS));  % max from interference, V
    Vi2 = Vc;
    warning(['No FLDI_Calibrations.csv file found, using hard-coded values of ' ...
        ' Vc = ' Vc(1) ' and Vi = ' Vi1(1)]);
    SCOPE = ones(1,length(RUNS)).*3;    % scope number
    if AC
        CH = ones(1,length(RUNS)).*2;   % AC channel number
    else
        CH = ones(1,length(RUNS)).*1;   % DC channel number
    end
end
V0 = Vc;


%% constants
R = 8.314;                                  % gas constant, J/(molK)
lambda = 632.8e-9;                          % wavelength, m
K = 2.257e-4;                               % gladstone-dale constant, m^3/kg
L = 15e-3;                                  % optical path length, m
eps = 0.5;                                  % error tolerance
style = {'-','--','.-',':'};                % plot line styles

%% script
% get file(s)
n = length(RUNS);
for i=1:n
    run_num = RUNS(i)
    scope_num = SCOPE(i);
    ch_num = CH(i);
    run = num2str(run_num);

    % import data (x = photoreceiver voltage, V; t = time, s)
    if CALIBRATION == 1
        name = [main_path 'run' run '/run' run '_cal1']
    elseif CALIBRATION == 2
        name = [main_path 'run' run '/run' run '_cal2']
    elseif BENCH_TEST
        if run_num < 10
            run = ['00' num2str(run_num)];
        elseif run_num < 100
            run = ['0' num2str(run_num)];
        elseif run_num < 1000
            run = num2str(run_num);
        else
            error('run number > 1000');
        end
        name = [main_path 'tek0' run 'CH' num2str(ch_num)];
    else
        name = [main_path 'run' run '/run' run '_scope' num2str(scope_num) '_Ch' ...
            num2str(ch_num)]
    end
```

```
144
145     if ~DAQ || CALIBRATION ~= 0
146         WFM_exist = exist([name,'.wfm'],'file');
147         ISF_exist = exist([name,'.isf'],'file');
148         CSV_exist = exist([name,'.csv'],'file');
149         if WFM_exist == 2
150             filename = [name,'.wfm'];
151             [x,t] = wfm2read(filename);
152             if DFLDI
153                 filename2 = [name2,'.wfm'];
154                 [x2,t2] = wfm2read(filename2);
155             end
156         elseif ISF_exist == 2
157             filename = [name,'.isf'];
158             [x,t] = isfread(filename);
159             if DFLDI
160                 filename2 = [name2,'.isf'];
161                 [x2,t2] = isfread(filename2);
162             end
163         elseif CSV_exist == 2
164             filename = [main_path 'tek0' run '.csv']
165             y = csvread(filename,22,0);
166             y(~any(~isnan(y(:,2)),2),:)=[];
167             x = y(:,2);
168             t = y(:,1);
169         else
170             error(['could not find file: ' name]);
171         end
172     else
173         if run_num < 10
174             fname = [main_path 'run' run filesep 'Run00' run '.mat'
                    ];
175         elseif run_num < 100
176             fname = [main_path 'run' run filesep 'Run0' run '.mat'];
177         else
178             fname = [main_path 'run' run filesep 'Run' run '.mat'];
179         end
180 %         if run_num < 10
181 %             fname = [main_path filesep 'Run00' run '.mat'];
182 %         elseif run_num < 100
183 %             fname = [main_path filesep 'Run0' run '.mat'];
184 %         else
185 %             fname = [main_path filesep 'Run' run '.mat'];
186 %         end
187         load_data;
188         if AC
189             sensor = ['FLDI_AC'];
190         else
191             if DFLDI == 1
192                 sensor = ['D_FLDI_1'];
193             elseif DFLDI == 2
194                 sensor = ['D_FLDI_2'];
195             else
196                 sensor = ['FLDI_DC'];
197             end
198         end
199         try
200             x = eval(sensor);
201         catch
202             x = eval('D_FLDI_1');
203         end
204         t_ind = 1;
205         t_var = ['t_' num2str(t_ind)];
206         while true
207             if length(eval(t_var)) == length(x)
208                 t = eval(t_var);
209                 break;
210             end
211             t_ind = t_ind + 1;
212             t_var = ['t_' num2str(t_ind)];
213         end
214     end
215
216     fs = (length(t) + 1)/((t(end) - t(1)));
217     v = x/2 + Vc(i);                    % voltage equivalent to
        single photodiode
218     if CALIBRATION == 1
219         cal(i,1) = (max(v) - min(v))/2;
```

```
220         cal(i,2) = (max(v) + min(v))/2;
221         disp(['Vc = ' num2str(Vc(i))]);
222     elseif CALIBRATION == 2
223         cal(i,1) = max(abs(x));
224         disp(['Vi = ' num2str([Vi1(i) Vi2(i)])]);
225     else
226         cal(i,:) = [Vi1(i) Vc(i)];
227         disp(['Vi = ' num2str([Vi1(i) Vi2(i)]) ', Vc = ' num2str(Vc(
                i))]);
228     end
229     disp(['Max absolute voltage: ' num2str(max(abs(x)))]);
230
231     % find subset of data
232     N = length(x);
233
234     t_offset = -t(1);                   % Find the offset from
            trigger
235     sample_rate = round(1/(t(2)-t(1)));
236     data_offset = t_offset*sample_rate;
237     sample_length = sample_rate*process_time;
238
239     if length(desired_time) > 1
240         des_time = desired_time(i);
241     else
242         des_time = desired_time;
243     end
244     Astart = data_offset+des_time*sample_rate+1; %In samples
245     if Astart < 1
246         warning(['Start time before data begins at ' num2str(t(1))
                ...
247             ', resetting to start time.']);
248         Astart = 1;
249     end
250     Aend   = sample_length + Astart-1;  % Sets length of the sample
            window
251     if Aend > N
252         warning(['End time after data ends at ' num2str(t(end)) ...
253             ', resetting to end time.']);
254         Aend = N;
255     end
256
257     % data conversion
258     if LINEAR
259 %         d_phi = asin(v/V0(i) - 1);    % phase change (Parziale
        2013)
260         d_phi = asin((v - Vi2(i))./Vi1(i));     % phase change (
                Lawson et al. 2019)
261         d_phi0(i) = -pi/2;              % phase offset
262         perc_err(i) = 0;                % percent error based on
                distance from linear
263                                         % region
264     else
265         Vint(i) = mean(v(Astart:Aend)); % photodiode mean voltage
266         if ~AC
267             d_phi0(i) = -acos((Vint(i) - Vi2(i))/Vi1(i));  % phase
                    offset
268         end
269         perc_err(i) = 1 - cos(pi/2 + d_phi0(i));        % percent
                error based on
270                                                         % distance
                                                              from
                                                              linear
                                                              region
271
272         d_phi = acos((v - Vi2(i))./Vi1(i)) + d_phi0(i); % phase
                change (Lawson et al.
273                                                         % 2019)
274         disp(['d_phi0 = ' num2str(d_phi0(i))]);
275     end
276     d_rho = lambda/(2*pi*K*L)*d_phi;    % density change
277
278     if FIND_ERR
279         x_max = (x(Astart:Aend) - mean(x(Astart:Aend)))./(1 -
                perc_err(i)) + ...
280             mean(x(Astart:Aend));
281         x_min = (x(Astart:Aend) - mean(x(Astart:Aend)))./(1 +
                perc_err(i)) + ...
282             mean(x(Astart:Aend));
```

```
283
284         v_max(i,:) = (v(Astart:Aend) - mean(v(Astart:Aend)))./(1 -
                perc_err(i)) + ...
285              mean(v(Astart:Aend));
286         v_min(i,:) = (v(Astart:Aend) - mean(v(Astart:Aend)))./(1 +
                perc_err(i)) + ...
287              mean(v(Astart:Aend));
288
289         d_phi_max = acos((v_max(i,:) - Vi2(i))./Vi1(i)) + d_phi0(i);
290         d_phi_min = acos((v_min(i,:) - Vi2(i))./Vi1(i)) + d_phi0(i);
291
292         d_rho_max = lambda/(2*pi*K*L)*d_phi_max;
293         d_rho_min = lambda/(2*pi*K*L)*d_phi_min;
294     end
295
296     if TYPE==0
297         data = x;
298         if FIND_ERR
299             data_max = x_max;
300             data_min = x_min;
301         end
302     elseif TYPE == 1
303         data = v;
304         if FIND_ERR
305             data_max = v_max(i,:);
306             data_min = v_min(i,:);
307         end
308     elseif TYPE == 2
309         data = d_phi;
310         if FIND_ERR
311             data_max = d_phi_max;
312             data_min = d_phi_min;
313         end
314     elseif TYPE == 3
315         data = d_phi/(2*pi/lambda);
316         if FIND_ERR
317             data_max = d_phi_max/(2*pi/lambda);
318             data_min = d_phi_min/(2*pi/lambda);
319         end
320     else
321         data = d_rho;
322         if FIND_ERR
323             data_max = d_rho_max;
324             data_min = d_rho_min;
325         end
326     end
327
328     A = data(Astart:Aend);                % Gets data to be analyzed
329     if FIND_ERR
330         A_max = data_max;
331         A_min = data_min;
332     end
333     A_mean = mean(A)
334     A_less_mean = A-A_mean;
335
336     if PLOT_VOLTS
337         figure(run_num*10+1);
338         plot(t,x*factor,'linewidth',width);
339         grid on; hold on;
340         plot(t(Astart:Aend),x(Astart:Aend)*factor,'linewidth',width)
                ;
341         xlabel('time (s)');
342         ylabel('voltage (V)');
343         if FIND_ERR
344             plot(t(Astart:Aend),x_max*factor,'linewidth',1);
345             plot(t(Astart:Aend),x_min*factor,'linewidth',1);
346         end
347     end
348     if PLOT_DATA
349         figure(run_num*10+2)
350         plot(t(Astart:Aend),A_less_mean,'linewidth',width);
351         grid on;    hold on;
352         xlabel('time (s)');
353         if TYPE == 0
354             ylabel('balanced photoreceiver voltage (V)');
355         elseif TYPE == 1
356             ylabel('single photodiode voltage (V)');
357         elseif TYPE == 2
```

```
            ylabel('\Delta\phi');
        else
            ylabel('\Delta\rho (kg/m^3)');
        end
        if FIND_ERR
            plot(t(Astart:Aend),A_max,'linewidth',1);
            plot(t(Astart:Aend),A_min,'linewidth',1);
        end
    end

    rms_total(i) = rms(A_less_mean);
    mean_total(i) = mean(A_less_mean);
    disp(['RMS: ' num2str(rms_total(i))]);

    if SPECTROGRAM && ~CALIBRATION
        figure(i*10+4);
        [s,f,t,spsd] = spectrogram(A_less_mean,sample_rate/time_bins
            ,0,freq_bins, ...
            fs,'yaxis','power');
        imagesc(t+TIME(i),f,mag2db(spsd));
        colormap jet;   h = colorbar;   ylabel(h,'power (dB)');
        set(gca,'YDir','normal');
        set(gcf,'position',[113 558 1762 420]);
        xlabel('time (s)');
        ylabel('frequency (Hz)');
    end

    if COMPUTE_PSD && ~CALIBRATION
        PercentOverlap = [];
        nfft = length(A_less_mean);

        if freq_reso == 0
            freq_reso = 1/(t(Aend:Aend)-t(Astart:Astart));
        end
        WindowSize = hamming(sample_rate/freq_reso);
        if ~POWER
            [ppsd,fpsd] = pwelch(abs(A_less_mean),WindowSize,
                PercentOverlap,nfft, ...
                sample_rate,'psd');
            if FIND_ERR
                [ppsd_max,fpsd_max] = pwelch(A_max-mean(A_max),
                    WindowSize, ...
                    PercentOverlap,nfft,sample_rate,'psd');
                [ppsd_min,fpsd_min] = pwelch(A_min-mean(A_min),
                    WindowSize, ...
                    PercentOverlap,nfft,sample_rate,'psd');
            end
        else
            [ppsd,fpsd] = pwelch(A_less_mean,WindowSize,
                PercentOverlap,nfft, ...
                sample_rate,'power');
            if FIND_ERR
                [ppsd_max,fpsd_max] = pwelch(A_max-mean(A_max),
                    WindowSize, ...
                    PercentOverlap,nfft,sample_rate,'power');
                [ppsd_min,fpsd_min] = pwelch(A_min-mean(A_min),
                    WindowSize, ...
                    PercentOverlap,nfft,sample_rate,'power');
            end
        end

        if PLOT_PSD
            if same_plot
                figure(1)
                semilogy(fpsd./1e3,ppsd,style{floor(i/8)+1},'
                    linewidth',2)
                grid on; hold on;
                if FIND_ERR
                    semilogy(fpsd_max./1e3,ppsd_max,style{floor(i/8)
                        +1}, ...
                        'linewidth',1)
                    semilogy(fpsd_min./1e3,ppsd_min,style{floor(i/8)
                        +1}, ...
                        'linewidth',1)
                end
            else
```

```
424                 figure(run_num*10+3)
425                 semilogy(fpsd./1e3,ppsd,style{1},'linewidth',2)
426                 grid on; hold on;
427                 if FIND_ERR
428                     semilogy(fpsd_max./1e3,ppsd_max,style{1},'
                        linewidth',1)
429                     semilogy(fpsd_min./1e3,ppsd_min,style{1},'
                        linewidth',1)
430                 end
431             end
432             xlabel('frequency [kHz]');
433             if ~POWER
434                 ylabel('PSD (units^2/Hz)');
435             else
436                 ylabel('Power');
437             end
438             title(['Run ' num2str(run_num)]);
439             xlim([0 300])
440         end
441
442         if ~isempty(prange)
443             % integrate start to end of noted frequency peaks
444             start_freq = min(prange);
445             end_freq = max(prange);
446             start_int = start_freq*1000*process_time;
447             end_int = end_freq*1000*process_time;
448             peak_int(1,(i)) = run_num;
449             peak_int(2,(i)) = sqrt(trapz(fpsd(start_int:end_int), ...
450                 ppsd(start_int:end_int)));
451             peak_int(3,(i)) = max(abs(A));
452
453             format short
454
455             freq_peak = find(ppsd == max(ppsd(start_int:end_int)));
456             freq_peak_freq(i) = fpsd(freq_peak(1));
457             freq_peak_amp(i) = ppsd(freq_peak(1));
458             freq_peak_amp_2 = freq_peak_amp(i)*peak_dec;
459             freqpeak = find(ppsd(start_int:end_int) >
                freq_peak_amp_2) + start_int;
460             peakrange_min(i) = fpsd(min(freqpeak));
461             peakrange_min_a(i) = ppsd(min(freqpeak));
462             peakrange_max(i) = fpsd(max(freqpeak));
463             peakrange_max_a(i) = ppsd(max(freqpeak));
464             peak_amp(i) = ppsd(floor(mean(freqpeak)));
465
466             if FIND_ERR
467                 peak_amp_max(i) = ppsd_max(floor(mean(freqpeak)));
468                 peak_amp_min(i) = ppsd_min(floor(mean(freqpeak)));
469             end
470
471             min_amp = min(ppsd);
472             max_amp = max(ppsd);
473
474             if PLOT_PRANGE
475                 hold on;
476                 plot([start_freq,start_freq],[min_amp max_amp],'k:',
                    'linewidth',2)
477                 plot([end_freq,end_freq],[min_amp max_amp],'k:','
                    linewidth',2)
478
479                 plot(peakrange_min./1000,peakrange_min_a,'k*')
480                 plot(peakrange_max./1000,peakrange_max_a,'k*')
481             end
482
483             labels=['Run Number:           ';...
484                     'Min Freq (kHz):       ';...
485                     'Max Freq (kHz):       ';...
486                     'Peak Freq (kHz):      ';...
487                     'Peak \delta\phi:      ';...
488                     'Peak \int\delta\phi: '];
489             disp(['FLDI results'; '************']);
490             disp([labels, num2str([peak_int(1,:); peakrange_min
                ./1000; ...
491                 peakrange_max./1000; (peakrange_min + peakrange_max)
                    ./2000; ...
```

```
                peak_amp; peak_int(2,:)])])
            if FIND_ERR
                labels=['Percent error:          ';...
                        'Peak \delta\phi max:    ';...
                        'Peak \delta\phi min:    ';...
                        '\delta\phi upper err:   ';...
                        '\delta\phi lower err:   '];
                disp([labels, num2str([perc_err.*100; peak_amp_max;
                    peak_amp_min; ...
                     peak_amp_max - peak_amp; peak_amp - peak_amp_min
                        ])])
            end
            format long
        end
    end

    if PLAY_SOUND
        fsN = fs/1e5;
        if fsN > 1
            xint = x(1:fsN:end);
            soundsc(xint,fs/fsN)
        else
            xint = x;
            soundsc(xint,fs)
        end

        if ~isempty(SAVE_SOUND)
            audiowrite(SAVE_SOUND,xint,int32(fs));
        end
    end
end
rms_total = rms_total';
mean_total = mean_total';
```

F. BEAM DEFLECTIONS DUE TO DENSITY GRADIENTS

It is important to determine the amount of deflection the FLDI beams experience at the focal point due to traversing large density gradients such as those in the bow shock and boundary layer around the cone. The beam deflection can alter the position of the beams relative to the model surface.

The deflecting effect of light crossing a density gradient has been experimentally studied for a variety of applications. Greenspan and Reddy in 1982 [91] and Enloe, Brake, and Repetti in 1990 [92] used position-sensitive photodiodes to measure laser deflection through shocks caused by sparks. Stricker and Kafri in 1982 [93] and Glatt and Kafri in 1987 [94] studied Moiré deflectometry and how it can be used to quantitatively measure density fields. Glatt and Kafri include a concise equation to find deflection angles for light traversing an axisymmetric density gradient about a circular cone at zero angle of attack:

$$\theta_d(x,y) = x\int_x^\infty \frac{\delta n(r,y)}{\delta r}(r^2-x^2)^{-1/2}dr \tag{F.1}$$

Note that in equation F.1 the origin is at the center of the model cross-section, which is defined one the x-z plane with x pointed upward and z parallel to the laser beams. The variable r is the distance from the origin, defined by $r=\sqrt{x^2+z^2}$, and the y-axis is in the direction of the flow. θ_d is the beam deflection angle at the focal point.

DPLR was used to compute the axisymmetric density profile from the surface of a 7° sharp cone model through its bow shock. The Gladstone-Dale relationship can then be used to find the index of refraction derivative with Equation F.2 (determined from Equation 2.22):

$$\frac{\delta n}{\delta r} = K\frac{\delta \rho}{\delta r} \tag{F.2}$$

Figure F.1 plots the density profile and the index of refaction derivative used in this computation. The particular case plotted is for a stagnation pressure of 130 psia.

Inserting the computed values for density, the deflection values for a variety of beam distances from the model surface (h) can be studied. The results are summarized in Figure F.2. The peak deflection occurs when the beam is about 1.4 mm from the surface, with

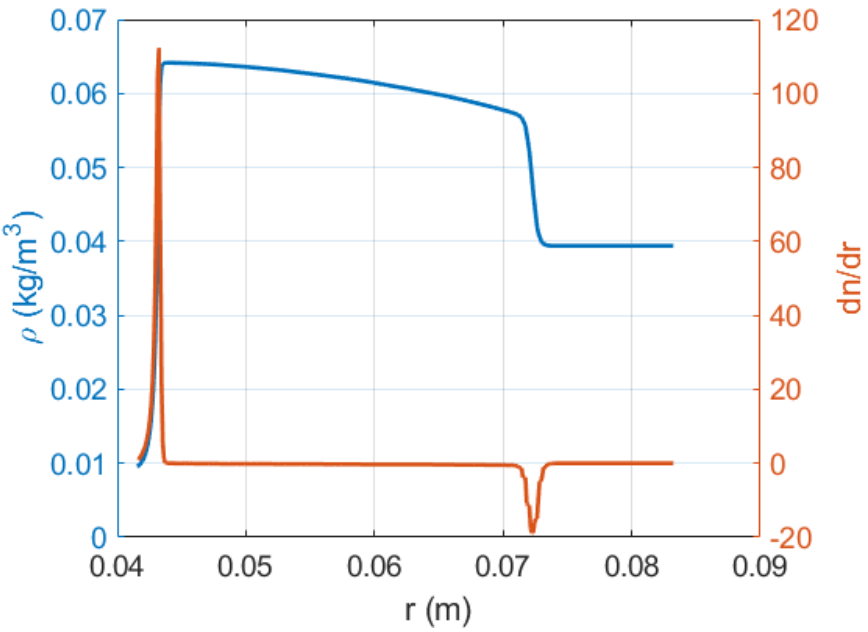

Figure F.1. Density profile and index of refraction derivative with respect to r for 7° straight cone 0.3383 m downstream.

a deflection angle of 89.7 μrad and an overall displacement of 7.55 μm at the focus. This displacement is less than 1% of the overall distance from the model surface, so the effect of laser beam deflection due to density gradient traversal can be considered negligible.

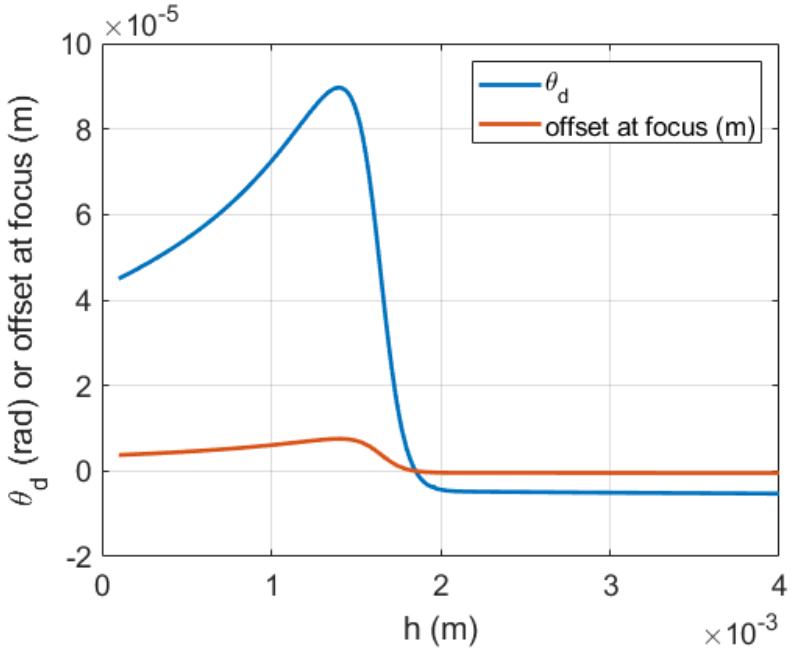

Figure F.2. Displacement in beam location normal to model surface due to density variations across beam path.

G. TUNNEL ENTRIES AND SELECTED RUN CONDITIONS

The tunnel entries made to collect the data for this dissertation are summarized in Table G.1. For all entries, the model was at a nominal 0° angle of attack and used one of two available sharp nosetips. For the cone-cylinder-flare (CCF) models, the angle refers to the flare angle (the same 5° cone-cylinder section was used for both variations). When FLDI measurements were made, two large rectangular Plexiglas™ windows were used for optical access unless otherwise noted in parentheses. All entries were made in the BAM6QT unless otherwise noted in brackets.

Throughout the dissertation, run numbers are given in the form $EERR$, where EE refers to the two-digit entry number and RR to the specific two-digit run in that entry.

Table G.1. Tunnel Entries

Entry #	Model	Type of Measurements Made
1	3.5° CCF	PCB and TSP
2	7° straight cone	PCB and FLDI (Plexiglas™ porthole window)
3	3.5° CCF	PCB, TSP, and FLDI
4	7° straight cone	PCB and FLDI
5	10.0° CCF	PCB and IR
6	10.0° CCF	PCB and Schlieren
7	10.0° CCF	PCB and FLDI
8	10.0° CCF	PCB and Schlieren [AFRL Mach 6 Ludweig Tube]
9	10.0° CCF	PCB and FLDI
10	10.0° CCF	PCB, Kulite, and IR
11	3.5° CCF	PCB and IR
12	10.0° CCF with perturber	PCB and FLDI
13	10.0° CCF	PCB, Kulite, and Schlieren (large sapphire windows)

Table G.1. (continued)

14	10.0° CCF	PCB, Kulite, and Schlieren (large sapphire windows)

Specific runs described in this dissertation are summarized in Table G.2. Values correspond to conditions at the time data was taken. For all entries, the model was at a nominal 0° angle of attack unless otherwise specified. One of two available sharp nosetips (both with a radius of 0.1 mm) were used for each run. Throughout the dissertation, run numbers are given in the form $EERR$, where EE refers to the two-digit entry number and RR to the specific two-digit run in that entry.

Table G.2. Selected Run Conditions

Run #	Flow	T_0 (K)	P_0 (psia)	Re ($\times 10^6$/m)	Notes
0228	Quiet	423.4	145.0	11.1	
0404	Noisy	420.6	80.01	6.66	
0405	Noisy	420.8	79.91	6.64	
0406	Noisy	417.6	80.13	6.75	
0407	Noisy	418.7	80.05	6.71	
0410	Noisy	416.9	80.08	6.76	
0411	Noisy	418.0	80.09	6.74	
0412	Noisy	417.8	79.95	6.73	
0416	Noisy	417.6	79.97	6.74	
0427	Quiet	413.0	134.9	11.6	
0506	Quiet	419.0	141.11	11.0	
0507	Quiet	418.7	131.95	10.3	
0508	Quiet	420.3	122.67	9.49	
0510	Quiet	422.6	104.04	7.98	

Table G.2. (continued)

0511	Quiet	422.8	94.25	7.22	
0512	Quiet	421.5	85.45	6.58	
0519	Quiet	421.7	155.7	12.0	
0521	Quiet	420.0	112.01	8.68	
0704	Quiet	413.8	144.1	11.5	
0705	Quiet	413.1	144.3	11.5	
0706	Quiet	413.4	143.9	11.5	
0708	Quiet	414.1	144.5	11.5	
0712	Quiet	416.0	144.7	11.5	
0713	Quiet	414.9	144.7	11.5	
0714	Quiet	416.9	147.5	11.5	
0716	Quiet	412.6	144.0	11.5	
0718	Quiet	413.5	144.0	11.5	
0722	Quiet	419.3	149.4	11.5	
0723	Quiet	418.4	148.0	11.5	
0724	Quiet	418.0	148.1	11.5	
0725	Quiet	416.2	146.0	11.5	
0728	Quiet	414.5	144.6	11.5	
0729	Quiet	414.3	144.7	11.5	
0730	Quiet	415.2	144.6	11.5	
0731	Quiet	414.5	144.7	11.5	
0732	Quiet	414.5	144.7	11.5	
0922	Quiet	414.1	145.0	11.5	
0923	Quiet	414.3	145.0	11.5	
0924	Quiet	414.3	145.0	11.5	
0925	Quiet	414.1	145.0	11.5	

Table G.2. (continued)

0926	Quiet	414.2	144.8	11.5	
0928	Quiet	414.4	145.1	11.5	
0929	Quiet	419.2	147.8	11.5	
0930	Quiet	417.4	146.8	11.5	
0931	Quiet	416.9	146.5	11.5	
0932	Quiet	414.6	145.0	11.5	
0933	Quiet	412.6	143.9	11.5	
0934	Quiet	413.3	144.6	11.5	
0938	Quiet	412.7	144.4	11.5	
1027	Noisy	422.1	79.76	6.60	
1028 (a)	Noisy	421.4	70.29	5.83	
1028 (b)	Noisy	411.4	64.63	5.58	
1028 (c)	Noisy	402.4	59.82	5.36	
1029	Noisy	418.4	33.39	2.80	
1030 (a)	Noisy	411.1	25.03	2.16	
1030 (b)	Noisy	392.9	21.35	1.99	
1031	Noisy	415.2	42.13	3.58	
1033	Noisy	420.1	89.09	7.43	
1034	Noisy	420.3	97.58	8.13	
1035	Noisy	420.5	106.75	8.89	
1037	Quiet	415.8	145.8	11.5	-0.15° angle of attack
1038	Noisy	416.3	71.53	6.05	-0.15° angle of attack
1039	Noisy	414.5	70.88	6.05	
1040	Quiet	422.0	149.7	11.5	
1041	Noisy	410.8	69.88	6.05	0.15° angle of attack
1042	Quiet	419.2	147.6	11.5	0.15° angle of attack
1043	Noisy	393.5	65.23	6.05	0.3° angle of attack

Table G.2. (continued)

1044	Quiet	418.9	147.7	11.5	0.3° angle of attack
1045	Noisy	409.5	69.54	6.05	0.45° angle of attack
1046	Quiet	418.6	147.5	11.5	0.45° angle of attack
1047	Noisy	408.3	69.19	6.05	0.6° angle of attack
1048	Quiet	418.6	147.5	11.5	0.6° angle of attack
1104	Quiet	419.1	148.1	11.5	
1105	Quiet	419.3	139.5	10.8	
1107	Quiet	418.0	129.7	10.1	
1108	Quiet	418.3	121.5	9.48	
1110	Quiet	416.8	112.6	8.84	
1111	Quiet	416.9	104.0	8.15	
1112	Quiet	415.6	94.97	7.49	
1113	Quiet	415.0	85.85	6.79	
1114	Quiet	415.4	77.12	6.09	
1115	Quiet	415.4	67.70	5.34	
1116	Noisy	422.6	117.6	9.71	
1119	Noisy	421.6	89.53	7.42	
1120	Noisy	420.8	98.35	8.18	
1121	Noisy	419.5	80.25	6.71	
1123	Noisy	422.7	64.80	5.22	
1124	Noisy	416.9	52.59	4.44	
1125	Noisy	416.7	43.78	3.70	
1126	Noisy	412.0	34.16	2.94	
1127	Noisy	412.0	25.09	2.16	
1129	Noisy	418.2	107.6	9.04	
1132	Quiet	417.0	146.8	11.5	
1142	Noisy	417.1	69.09	5.83	

Table G.2. (continued)

1211	Quiet	416.2	148.0	11.6	
1228	Quiet	418.8	148.8	11.6	
1229	Quiet	416.9	94.20	7.39	
1230	Quiet	415.5	113.0	8.91	
1231	Quiet	416.6	131.6	10.3	
1232	Quiet	417.0	148.0	11.6	
1308	Quiet	420.2	151.3	11.7	
1310	Noisy	414.7	26.86	2.29	
1311	Noisy	413.3	45.19	3.87	
1313	Noisy	414.3	63.27	5.40	
1314	Quiet	414.4	147.7	11.7	
1316	Quiet	419.7	32.90	2.55	
1318	Quiet	414.4	32.19	2.55	
1319	Quiet	414.9	148.1	11.7	
1320	Quiet	411.4	31.85	2.55	
1321	Quiet	418.0	149.9	11.7	
1323	Quiet	424.0	153.4	11.7	
1324	Quiet	421.6	152.1	11.7	
1413	Quiet	416.7	118.4	9.29	
1415	Noisy	417.4	62.79	5.26	
1416	Quiet	415.9	125.2	9.92	

VITA

Elizabeth K. Benitez was born on Long Island, NY. She graduated from East Meadow High School in 2009. For her undergraduate studies, she attended the Massachusetts Institute of Technology where she obtained a B.S. in Aerospace Engineering with Information Technology in 2013. During her studies, she completed internships at Northrop Grumman and NASA Dryden Flight Research Center and was a NASA Aeronautics Scholar.

Upon graduation, she took a job as a research engineer with the Georgia Tech Research Institute in Dayton, OH, where she worked in modeling and simulation of electronic warfare systems with the Air Force Life Cycle and Management Center and the Air Force Research Laboratory Sensors Directorate (AFRL/RY). While working, she obtained her M.S. in Aerospace Engineering at Georgia Institute of Technology in 2015. In 2017 she started her Ph.D. at Purdue University, which she completed in 2021. During her doctoral studies, she was a National Defense Science and Engineering Graduate (NDSEG) Fellow, and also received the Amelia Earhart Fellowship, the AIAA Orville and Wilbur Wright Graduate Award, and the Purdue Forever Fellowship. Elizabeth has accepted a position as an NRC Research Associate at AFRL/RQHF.

PUBLICATIONS

Publications related to work from this dissertation, in reverse chronological order:

1. E.K. Benitez and J.S. Jewell. “Simulated Focused Laser Differential Interferometry of Time-Varying Signals.” *AIAA SciTech 2022*, January 2022, San Diego. *Submitted*.

2. P. Paredes, A. Scholten, M. M. Choudhari, F. Li, E.K. Benitez, and J.S. Jewell. “Boundary Layer Instabilities in a Cone-Cylinder-Flare Model at Mach 6.” *AIAA SciTech 2022*, January 2022, San Diego. *Submitted*.

3. E.K. Benitez, J.S. Jewell, and S.P. Schneider. ”Propagation of Controlled Disturbances through an Axisymmetric Separation Bubble at Mach 6.” *AIAA Aviation 2021*, August 2021, Virtual. AIAA 2021-2844.

4. E.K. Benitez, J.S. Jewell, and S.P. Schneider. “Focused Laser Differential Interferometry with Contoured Tunnel Windows.” *AIAA Journal*, Vol. 59, No. 2 (2021), pp. 419-429. doi: 10.2514/1.J060081.

5. E.K. Benitez, J.S. Jewell, and S.P. Schneider. ”Separation Bubble Variation Due to Small Angles of Attack for an Axisymmetric Model at Mach 6.” *AIAA SciTech 2021*, January 2021, Virtual. AIAA 2021-0245.

6. E.K. Benitez, S. Esquieu J.S. Jewell, and S.P. Schneider. ”Instability Measurements on an Axisymmetric Separation Bubble at Mach 6.” *AIAA Aviation 2020*, June 2020, Virtual. AIAA 2020-3072.

7. E.K. Benitez, J.S. Jewell, and S.P. Schneider. ”Focused Laser Differential Interferometry for Hypersonic Flow Instability Measurements with Contoured Tunnel Windows.” *AIAA SciTech 2020*, January 2020, Orlando, FL. AIAA 2020-1282.

8. S. Esquieu, E.K. Benitez, S.P. Schneider, and J.-P. Brazier. ”Flow and Stability Analysis of a Hypersonic Boundary Layer over an Axisymmetric Cone Cylinder Flare Configuration.” *AIAA SciTech 2019*, January 2019, San Diego, CA. AIAA 2019-2115.